

**Search for the rare decays of Z and Higgs bosons to
J/ ψ plus photon at $\sqrt{s} = 13$ TeV**

by

Hao-Ren Jheng

at the

NATIONAL CENTRAL UNIVERSITY

June 2018

© National Central University 2018. All rights reserved.

Author..... Hao-Ren Jheng

Department of Physics and Center of high energy of high field
physics, National Central University, Taiwan
Thursday 6th September, 2018

Certified by

Chia-Ming Kuo
Associate Professor
Thesis Supervisor

**Search for the rare decays of Z and Higgs bosons to J/ ψ plus
photon at $\sqrt{s} = 13$ TeV**

by

Hao-Ren Jheng

Abstract

A search for decays of Z and Higgs bosons to a J/ ψ meson and a photon, with the subsequent decay of the J/ ψ to $\mu^+ \mu^-$, is presented. The analysis uses a data sample of proton-proton collisions corresponding to an integrated luminosity of 35.9 fb^{-1} at $\sqrt{s} = 13$ TeV collected with the CMS detector at the LHC in 2016. The observed (expected) upper limit on the $Z \rightarrow J/\psi \gamma$ decay branching fraction, assuming that the J/ ψ is produced unpolarized, is $1.4 (1.6^{+0.7}_{-0.5}) \times 10^{-6}$ at 95% confidence level, which corresponds to 15 (18) times the standard model prediction. The subscript and superscript stand for the range of 68% central quantiles of upper limits with background-only hypothesis. For the extreme polarization scenarios the observed (expected) limit varies from -13.6 (-13.5) to +8.6 (+8.2)%. The observed (expected) upper limit on the branching fraction for $H \rightarrow J/\psi \gamma$ with $m_H = 125 \text{ GeV}$ is $7.6 (5.2^{+2.4}_{-1.6}) \times 10^{-4}$, 260 (170) times the standard model prediction, at 95% confidence level. The J/ ψ meson from the Higgs boson decay is assumed to be fully transversely polarized. The results for the Higgs boson decay are combined with the results from proton-proton collisions at $\sqrt{s} = 8$ TeV corresponding to 19.7 fb^{-1} , and this yields an observed (expected) upper limit on the branching fraction for $H \rightarrow J/\psi \gamma$ of 220 (160) times the standard model prediction.

Thesis Supervisor: Chia-Ming Kuo
Title: Associate Professor

Acknowledgments

This is the acknowledgements section. You should replace this with your own acknowledgements.

Contents

1	Introduction	9
1.1	The standard model of particle physics	9
1.1.1	Gauge invariance	10
1.1.2	Weak interaction and the electroweak unification	14
1.1.3	The Higgs mechanism	21
1.1.4	The production of the Higgs boson and its decays	29
1.1.5	The measurement of the Higgs coupling	37
1.2	The rare decays $Z/H \rightarrow J/\psi \gamma$	44
1.2.1	Overview	44
1.2.2	Features of the decays	46
1.2.3	Previous results from the ATLAS and CMS Collaborations .	47
2	Experimental apparatus	51
2.1	Large Hadron Collider	51
2.2	Compact Muon Solenoid	53
2.3	Object reconstruction	60
2.3.1	Particle-Flow algorithm	60
2.3.2	Pile-up & Primary vertex	66
3	Analysis procedures	69
3.1	Data and simulated samples	69
3.1.1	Data sample	69
3.1.2	Simulated samples	70

3.2	Trigger	78
3.3	Object identification	89
3.3.1	Muon identification	89
3.3.2	Photon identification	97
3.4	Event Selection	98
3.5	Background modeling	117
3.5.1	F-test	118
3.5.2	Bias study	120
3.6	Signal modeling	133
3.7	Systematic uncertainties	133
3.8	Statistical method	141
4	Results and conclusion	149
4.1	Limits on decay branching fraction	149
4.2	Conclusion	151
4.3	Outlook	152
A	Additional materials for the bias study	155
A.1	Linearity	155
A.1.1	$H \rightarrow J/\psi \gamma$	156
A.1.2	$Z \rightarrow J/\psi \gamma$ Cat1	158
A.1.3	$Z \rightarrow J/\psi \gamma$ Cat2	160
A.1.4	$Z \rightarrow J/\psi \gamma$ Cat3	162
A.2	Pseudo-event	164
A.2.1	Pseudo-events for $H \rightarrow J/\psi \gamma$	165
A.2.2	Pseudo-events for Cat1 of $Z \rightarrow J/\psi \gamma$	166
A.2.3	Pseudo-events for Cat2 of $Z \rightarrow J/\psi \gamma$	167
A.2.4	Pseudo-events for Cat3 of $Z \rightarrow J/\psi \gamma$	168
B	Discussion on the systematic uncertainties	171
Bibliography		177

¹ Chapter 1

² Introduction

³ The thesis is organized as follows. The theoretical background, from the concept
⁴ of the gauge invariance, the electroweak theory to the Higgs mechanism, will be
⁵ introduced. The experimental perspective and an overview of the searched decays
⁶ $Z/H \rightarrow J/\psi \gamma$ are followed. Chapter 2 will briefly mention the experiment ap-
⁷ paratus, with the object reconstruction. In Chapter 3, the analysis procedure and
⁸ methods, including data and simulated samples, the object identification, back-
⁹ ground and signal models construction, systematic uncertainties estimation, and
¹⁰ the statistical methods, are described in detail. Chapter 4 represents the results of
¹¹ this analysis, as well as the possible improvements.

¹² 1.1 The standard model of particle physics

¹³ The standard model (SM) of particle physics provides so far the most effective
¹⁴ and appropriate theory framework to describe the fundamental constituents of
¹⁵ the Universe, and the interactions between them, the force¹, which are carried by
¹⁶ the gauge boson. The last piece of the SM is the Higgs boson, which is the mani-
¹⁷ festation of the mechanism by which particles acquire masses.

¹⁸ There are twelve fundamental fermions in the SM, and are categorized into

¹The interactions here do not include the gravitational force. In the following text, "the interactions in the SM" will simply refer to the electromagnetic, weak, and strong forces.

19 quarks and leptons by the types of interactions they experience. All the fermions
 20 involve in the weak interaction, which is mediated by the W^\pm and Z bosons. Ex-
 21 cept for the electrically neutral neutrinos, the remaining nine fermions participate
 22 in the electromagnetic interaction, which is mediated by the photon γ . The theory
 23 of the electromagnetic interaction is the Quantum Electrodynamics (QED), which
 24 is the most accurately tested physics theory. The above two interactions can be
 25 unified into the Electro-Weak theory (EW), and will be described later in the text.
 26 Only the quarks carry the color charge and undergo the strong interaction, which
 27 is mediated by the gluons g . The theory for the strong interaction is the Quan-
 28 tum Chromodynamics (QCD). The color is a label for the three orthogonal states
 29 in the $SU(3)$ symmetry group of the QCD. Quarks are always bound together to
 30 form hadrons, which can either be mesons (consist of a quark and a anti-quark) or
 31 baryons (consist of three quarks). This is the nature of the QCD, called color con-
 32 finement – quarks are always observed to be confined to bound colorless states.
 33 An overview of QCD can be found in the lecture [1] and will not be discussed in
 34 this thesis. The elementary particles, and their basic properties, are summarized in
 35 Fig. 1-1.

36 **1.1.1 Gauge invariance**

37 In the context of Quantum Field Theory (QFT), particles are described by exci-
 38 tations of a quantum field which satisfies the quantum field equation. In a con-
 39 tinuous system, the *field* represents the generalized coordinates at each point in
 40 space-time, and therefore is written in the form of a continuous function. The dy-
 41 namics of the field is often expressed by the Lagrangian density $\mathcal{L}(\phi_i, \partial_\mu \phi_i)$ where
 42 ϕ_i is the field. Later in the text a simplified term "the Lagrangian" will be used to
 43 replace the Lagrangian density. The equation of motion describing the dynamics
 44 of the field can be derived from the Euler-Lagrange equation

$$\partial_\mu \left(\frac{\partial \mathcal{L}}{\partial (\partial_\mu \phi_i)} \right) - \frac{\partial \mathcal{L}}{\partial \phi_i} = 0. \quad (1.1)$$

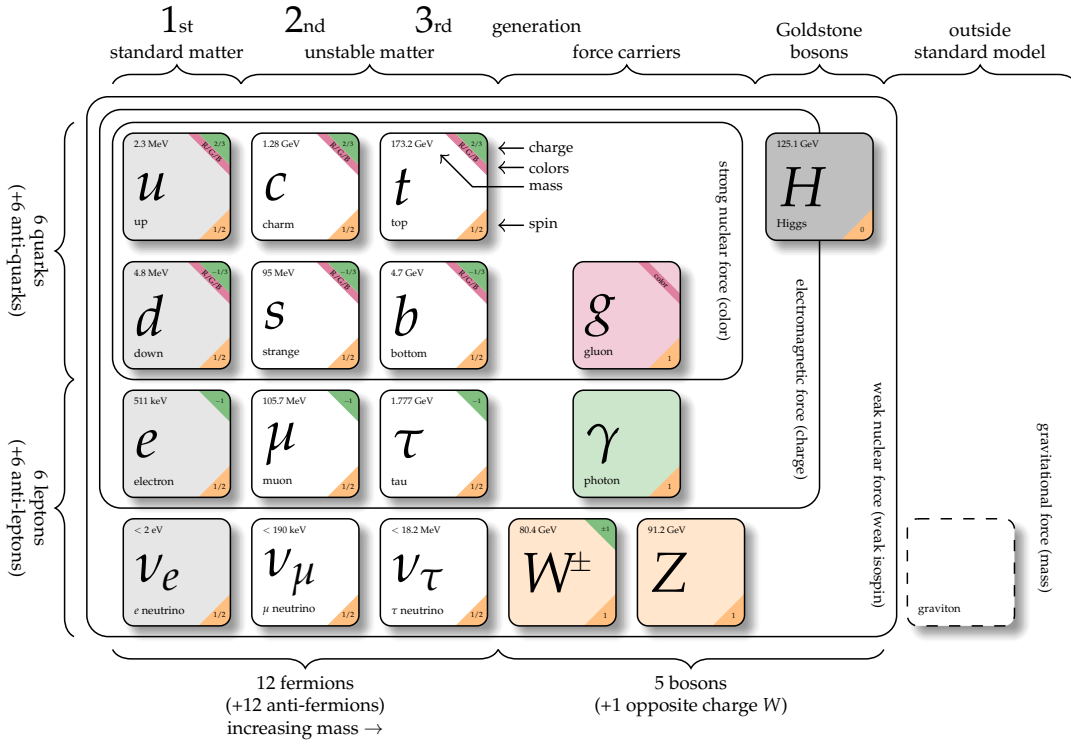


Figure 1-1: The elementary particles of SM, with the three generations of fermions, four gauge bosons, and the Higgs boson.

45 The three interactions, QED, weak, and QCD, can be derived by requiring the
 46 *local gauge invariance*: the Lagrangian is invariant under the *local phase transformation* of the fields,

$$\psi(x) \rightarrow \psi'(x) = U(x)\psi(x) = e^{iq\chi(x)}\psi(x). \quad (1.2)$$

48 The Lagrangian for a free spin- $\frac{1}{2}$ particle (referred to as free Lagrangian)

$$\mathcal{L}_{\text{free}} = i\bar{\psi}\gamma^\mu\partial_\mu\psi - m\bar{\psi}\psi. \quad (1.3)$$

49 With the $U(1)$ local gauge transformation, Eq. 1.3 becomes

$$\mathcal{L}_{\text{free}} \rightarrow \mathcal{L}'_{\text{free}} = \mathcal{L}_{\text{free}} - q\bar{\psi}\gamma_\mu(\partial_\mu\chi)\psi. \quad (1.4)$$

⁵⁰ The free Lagrangian is obviously not invariant under U(1) local gauge transformation.
⁵¹ The solution to deal with the extra term in Eq. 1.4 is to replace the derivative
⁵² ∂_μ in the free Lagrangian with the *covariant derivative* D_μ ,

$$\partial_\mu \rightarrow D_\mu = \partial_\mu + iqA_\mu, \quad (1.5)$$

⁵³ with the introduction of a new field A_μ . After the replacement, the new field A_μ
⁵⁴ transforms in coordination with the local phase transformation of the ψ as

$$A_\mu \rightarrow A'_\mu = A_\mu - \partial_\mu\chi, \quad (1.6)$$

⁵⁵ The invariance of the Lagrangian can be preserved. It is worth noting that Eq. 1.6
⁵⁶ is actually the concept of gauge transformation of the electromagnetic vector po-
⁵⁷ tential A_μ in the classical electromagnetism. The requirement of the U(1) local
⁵⁸ invariance of the Lagrangian takes price, which is to introduce a vector field that
⁵⁹ couples to the spin- $\frac{1}{2}$ particles. The full Lagrangian should include this newly in-
⁶⁰ troduced vector field. The corresponding terms in the Lagrangian is known as the
⁶¹ Proca Lagrangian

$$\mathcal{L}_{\text{Proca}} = -\frac{1}{4}F^{\mu\nu}F_{\mu\nu} + \frac{1}{2}m_A^2 A^\mu A_\mu. \quad (1.7)$$

⁶² where the $F_{\mu\nu} \equiv (\partial_\mu A_\nu - \partial_\nu A_\mu)$ is the field-strength tensor. However, the $F_{\mu\nu}$ is
⁶³ invariant under Eq. 1.6 while the $A^\mu A_\mu$ term transforms as

$$\frac{1}{2}m_A^2 A^\mu A_\mu \rightarrow \frac{1}{2}m_A^2 (A_\mu - \partial_\mu\chi)(A^\mu - \partial^\mu\chi) \neq \frac{1}{2}m_A^2 A^\mu A_\mu, \quad (1.8)$$

⁶⁴ which is certainly not invariant. A conclusion can be drawn that the U(1) local
⁶⁵ gauge symmetry can only be satisfied with the *massless* gauge boson of the inter-
⁶⁶ action. The Lagrangian describing the QED takes the form

$$\mathcal{L}_{\text{QED}} = (i\bar{\psi}\gamma^\mu\partial_\mu\psi - m\bar{\psi}\psi) - (q\bar{\psi}\gamma_\mu\psi)A_\mu - \frac{1}{4}F^{\mu\nu}F_{\mu\nu}. \quad (1.9)$$

⁶⁷ The introduction of the new field not only exhibits the observed gauge invari-

⁶⁸ ance of classical electromagnetism, but also corresponds to a wave equation with
⁶⁹ an interaction term of the form

$$q\gamma^\mu A_\mu \psi. \quad (1.10)$$

This is the QED interaction potential, and its vertex is shown in Fig. 1-2. The re-

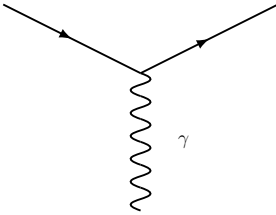


Figure 1-2: The Feynman diagram of the QED vertex.

⁷⁰
⁷¹ quirement of the physics to be invariant under local U(1) phase transformations
⁷² implies that a gauge field must exist, and the excitation of this field is now com-
⁷³ monly identified as the massless gauge boson – the photon.

⁷⁴ The same construction can be applied to the weak and the strong interactions
⁷⁵ (QCD, quantum chromodynamics), of which the underlying symmetry is the in-
⁷⁶ variance under SU(2) and SU(3) local phase transformations respectively,

$$\psi(x) \rightarrow \psi'(x) = \exp \left[ig_S \boldsymbol{\alpha}(x) \cdot \mathbf{M} \right] \psi(x), \quad (1.11)$$

⁷⁷ with the corresponding replacements of the partial derivatives to covariant deriva-
⁷⁸ tives,

$$\partial_\mu \rightarrow D_\mu = \partial_\mu + ig_{W(S)} \mathbf{M} \cdot \mathbf{G}_\mu(x), \quad (1.12)$$

⁷⁹ where $g_{W(S)}$ is the coupling constant of weak (strong) interaction, \mathbf{M} are the gen-
⁸⁰ erators of SU(2) (SU(3)) symmetry group, and \mathbf{G} are the three (eight) new gauge
⁸¹ fields of weak (stron) interaction. The well-known representations of the SU(2)
⁸² group are the Pauli matrices and of the SU(3) are the Gell-Mann matrices.

⁸³ In the following paragraphs, the weak interaction will be introduced a bit deeper.

⁸⁴ **1.1.2 Weak interaction and the electroweak unification**

⁸⁵ The weak interaction at first was proposed to explain the beta decay. Fermi (1933)
⁸⁶ treated the process as a contact interaction, which takes place at a single space-time
⁸⁷ point and does not require mediating particles. Nowadays, it is widely known that
⁸⁸ the Fermi's model is the low energy approximation and will fail at high energy
⁸⁹ regime.

⁹⁰ At the beginning, this theory only includes the charged-current weak interaction
⁹¹ which can be associated with invariance under SU(2) local phase transformation
⁹²

$$\psi(x) \rightarrow \psi'(x) = \exp \left[ig_W \chi(x) \cdot \mathbf{M} \right] \psi(x), \quad (1.13)$$

⁹³ where \mathbf{M} are the three generators of the SU(2) symmetry group, of which the representation
⁹⁴ is the Pauli matrix,

$$\mathbf{M} = \frac{1}{2} \boldsymbol{\sigma}. \quad (1.14)$$

⁹⁵ The local gauge invariance is satisfied with the three introduced fields, W_μ^k with
⁹⁶ $k = 1, 2, 3$, corresponding to three gauge bosons $W^{(1)}$, $W^{(2)}$, and $W^{(3)}$. Since the
⁹⁷ SU(2) generators are represented by 2×2 matrices, the wavefunction must have
⁹⁸ two additional degrees of freedom. Furthermore, only left-handed (LH) chiral
⁹⁹ particles and right-handed (RH) chiral antiparticles couple to the weak charged-
¹⁰⁰ current interaction, LH particles and RH antiparticles are placed in weak isospin
¹⁰¹ doublets. On the other hand, RH particles and LH antiparticles are put into weak
¹⁰² isospin singlets and hence will not be affected by the transformation of Eq. 1.13.
¹⁰³ Consequently, the wave functions can be interpreted as

$$\psi(x) = \begin{pmatrix} \mu_i \\ \ell_i \end{pmatrix}_L, \begin{pmatrix} u_i \\ d_i \end{pmatrix}_L, (u_i)_R, (d_i)_R, (\ell_i)_R, \quad (1.15)$$

¹⁰⁴ where $i = 1, 2, 3$ for the three families of fermions. Again, the requirement of
¹⁰⁵ the local gauge invariance necessitates the modification of the Dirac equation to

¹⁰⁶ include a new interaction term

$$ig_W T_k \gamma^\mu W_\mu^k \psi_L = ig_W \frac{1}{2} \sigma_k \gamma^\mu W_\mu^k \psi_L, \quad (1.16)$$

¹⁰⁷ where ψ_L stands for the weak isospin doublet of LH particles. From this form of
¹⁰⁸ interaction, three weak currents can be associated with Pauli matrices,

$$j_1^\mu = \frac{g_W}{2} \bar{\psi}_L \gamma^\mu \sigma_i \psi_L, \quad (1.17)$$

¹⁰⁹ where $i = 1, 2, 3$. The actual charged-currents relate to the isospin raising the low-
¹¹⁰ ering operators, $\sigma_\pm = \frac{1}{2}(\sigma_1 \pm i\sigma_2)$, and read as

$$j_\pm^\mu = \frac{1}{\sqrt{2}} \left(j_1^\mu \pm ij_2^\mu \right) = \frac{g_W}{\sqrt{2}} \bar{\psi}_L \gamma^\mu \sigma_\pm \psi_L. \quad (1.18)$$

¹¹¹ In the case of the doublet formed by the LH electron and electron neutrino, the
¹¹² currents j_\pm^μ , corresponding to the exchange of the physical W^\pm bosons, are

$$j_+^\mu = \frac{g_W}{\sqrt{2}} (\bar{\nu}_L \bar{e}_L) \gamma^\mu \begin{pmatrix} 0 & 1 \\ 0 & 0 \end{pmatrix} \begin{pmatrix} \nu_l \\ e_L \end{pmatrix} = \frac{g_W}{\sqrt{2}} \bar{\nu} \gamma^\mu \frac{1}{2} (1 - \gamma^5) e, \quad (1.19)$$

¹¹³

$$j_-^\mu = \frac{g_W}{\sqrt{2}} (\bar{\nu}_L \bar{e}_L) \gamma^\mu \begin{pmatrix} 0 & 0 \\ 1 & 0 \end{pmatrix} \begin{pmatrix} \nu_l \\ e_L \end{pmatrix} = \frac{g_W}{\sqrt{2}} \bar{e} \gamma^\mu \frac{1}{2} (1 - \gamma^5) \nu, \quad (1.20)$$

¹¹⁴ consistent with the experimental observation of the vector minus axial vector (V-A)
¹¹⁵ structure. The physical W bosons are identified as

$$W_\mu^\pm = \frac{1}{\sqrt{2}} \left(W_\mu^{(1)} \mp i W_\mu^{(2)} \right). \quad (1.21)$$

¹¹⁶ The $SU(2)_L$ does not only give two weak charged-currents, but also implies the
¹¹⁷ existence of a weak neutral-current

$$j_3^\mu = g_W \bar{\psi}_L \gamma^\mu \frac{1}{2} \sigma_3 \psi_L. \quad (1.22)$$

₁₁₈ In the case of the fermion doublet (again, the LH electron and electron neutrino are
₁₁₉ used as an example), it reads as

$$j_3^\mu = g_W \frac{1}{2} (\bar{\nu}_L \bar{e}_L) \gamma^\mu \begin{pmatrix} 1 & 0 \\ 0 & -1 \end{pmatrix} \begin{pmatrix} \nu_L \\ e_L \end{pmatrix} = g_W \frac{1}{2} \bar{\nu}_L \gamma_L^\nu - g_W \frac{1}{2} \bar{e}_L \gamma^\mu e_L \quad (1.23)$$

₁₂₀ or in a more compact form

$$j_3^\mu = I_W^{(3)} g_W \bar{f} \gamma^\mu \frac{1}{2} (1 - \gamma^5) f, \quad (1.24)$$

₁₂₁ where f represents the fermion doublet and $I_W^{(3)}$ is the third component of the weak
₁₂₂ isospin. The property that RH particles and LH antiparticles do not couple to the
₁₂₃ weak interaction is preserved, as they possess $I_W^{(3)} = 0$. (One should not mix this
₁₂₄ weak neutral-current with the SM Z boson that currently known, as the reason will
₁₂₅ be stated in the following paragraphs.)

₁₂₆ There is another evidence and argument that the weak neutral-current must
₁₂₇ exist: the cross-section of the W boson pair production in the electron-positron col-
₁₂₈ lisions do not converge if there is no neutral-current interaction. Fig. 1-3 shows the
₁₂₉ leading order diagrams of the $e^+e^- \rightarrow W^+W^-$ process. The left most diagram is
₁₃₀ the charged-current process. The middle one is the electromagnetic process as it is
₁₃₁ mediated by the photon, and there is also a γWW vertex indicating that the γ can
₁₃₂ couple with W boson since they carry electric charge. In the right most diagram, a
₁₃₃ neutral boson, which is now known as the Z boson, acts as the mediator. Fig. 1-4
₁₃₄ shows the predicted $e^+e^- \rightarrow W^+W^-$ cross-sections of three cases: only the ν_e dia-
₁₃₅ gram included; only ν_e and γ diagrams included; all diagrams included [2]. With
₁₃₆ only the first two diagrams, the cross-section will increase without limit. The inclu-
₁₃₇ sion of the neutral-current interaction makes the calculated cross-section converge
₁₃₈ and consistent with the experimental observation.

₁₃₉ The cancellation that preserves the unitary of $e^+e^- \rightarrow W^+W^-$ indicates that
₁₄₀ the coupling of the γ , charged- and neutral-currents are related. A unification of
₁₄₁ the electromagnetic and weak interaction was proposed, and a unified electroweak

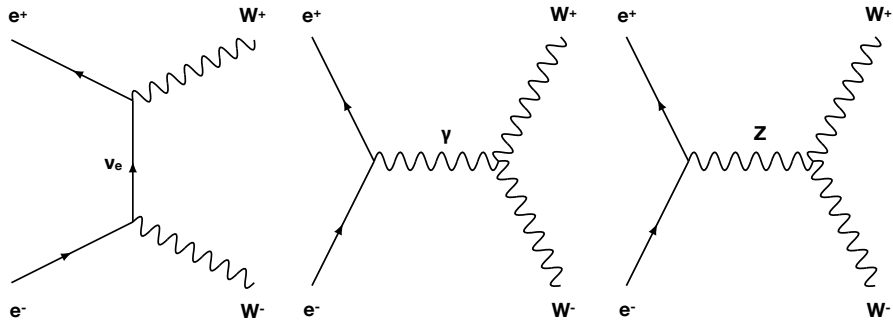


Figure 1-3: The leading order diagrams of the $e^+e^- \rightarrow W^+W^-$ process.

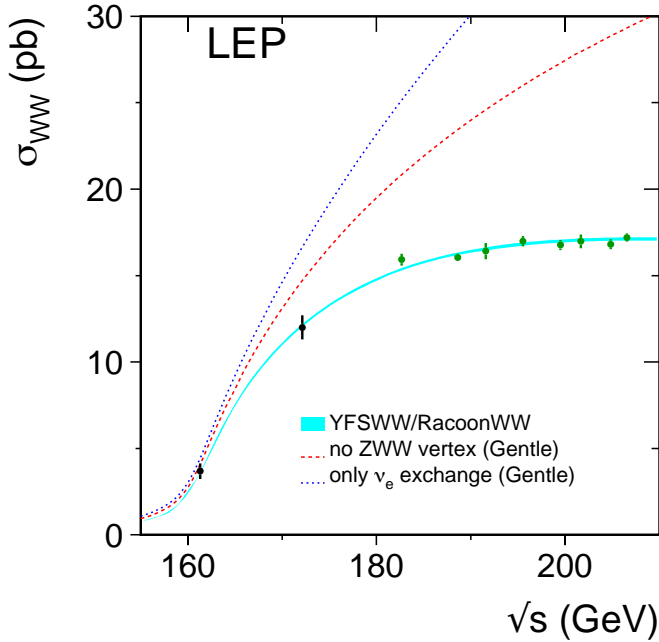


Figure 1-4: Measurements of the W-pair production cross-section, compared to the different predictions. The shaded area represents the uncertainty on the theoretical predictions [2].

¹⁴² model was completed by Sheldon Glashow, Abdus Salam, and Steven Weinberg,
¹⁴³ and now it is called GSW model.

¹⁴⁴ One thing that must be incorporated in the unification is the correspondence
¹⁴⁵ between the weak neutral-current and the physical Z boson. The neutral-current

₁₄₆ previously stated does not couple to RH particles/LH antiparticles, which is in
₁₄₇ contrast to the experimental evidence that the neutral Z boson couples, not equally,
₁₄₈ to both LH and RH particles. At the first step, a $U(1)_Y$ local gauge symmetry is in-
₁₄₉ troduced to replace the $U(1)$ gauge group of the electromagnetism with the trans-
₁₅₀ formation

$$\psi(x) \rightarrow \psi'(x) = U(x)\psi(x) = \exp\left[ig'\frac{Y}{2}\chi'(x)\right]\psi(x), \quad (1.25)$$

₁₅₁ with a new field B_μ and a new weak hypercharge Y . This new symmetry yields
₁₅₂ the same interaction term as the $U(1)$ symmetry of the QED in Eq. 1.10,

$$g'\frac{Y}{2}\gamma^\mu B_\mu \psi. \quad (1.26)$$

₁₅₃ The physical photon γ and Z boson are expressed as,

$$A_\mu = +B_\mu \cos \theta_W + W_\mu^{(3)} \sin \theta_W, \quad (1.27)$$

₁₅₄

$$Z_\mu = -B_\mu \sin \theta_W + W_\mu^{(3)} \cos \theta_W, \quad (1.28)$$

₁₅₅ where the θ_W is the weak mixing angle. The physical QED and weak neutral-
₁₅₆ current are therefore,

$$j_{em}^\mu = j_Y^\mu \cos \theta_W + j_3^\mu \sin \theta_W, \quad (1.29)$$

₁₅₇

$$j_Z^\mu = -j_Y^\mu \sin \theta_W + j_3^\mu \cos \theta_W, \quad (1.30)$$

₁₅₈ with the weak neutral-current j_3 of Eq. 1.23 and the current associated with the
₁₅₉ interaction term j_Y of Eq. 1.26

$$j_Y^\mu = \frac{1}{2}g'Y_{e_L}\bar{e}_L\gamma^\mu e_L + \frac{1}{2}g'Y_{e_R}\bar{e}_R\gamma^\mu e_R + \frac{1}{2}g'Y_{\nu_L}\bar{\nu}_L\gamma^\mu \nu_L + \frac{1}{2}g'Y_{\nu_R}\bar{\nu}_R\gamma^\mu \nu_R \quad (1.31)$$

₁₆₀ On the other hand, the electromagnetic current (of the electron doublet) is simply

$$j_{em}^\mu = Q_e e \bar{e}_L \gamma^\mu e_L + Q_e e \bar{e}_R \gamma^\mu e_R. \quad (1.32)$$

161 The underlying symmetry group of the electroweak sector, as described in GSW
 162 model, is $U(1)_Y \times SU(2)_L$. In order to preserve the invariance under $U(1)_Y$ and
 163 $SU(2)_U$ local gauge transformation, the hypercharges of particles in a weak isospin
 164 doublet should be the same. Having this argument and equating each component
 165 of the Eq. 1.29 with j_3^μ and j_Y^μ substituted and Eq. 1.32, the weak hypercharge can
 166 be expressed as a linear combination of the electromagnetic charge Q and the third
 167 component of weak isospin $I_W^{(3)}$

$$Y = 2(Q - I_W^{(3)}), \quad (1.33)$$

168 Relations between the weak coupling g_W , the hypercharge coupling g' and the
 169 electric charge can be derived

$$e = g_W \sin \theta_W = g' \cos \theta_W. \quad (1.34)$$

170 The GSW model successfully bridges the couplings of QED, weak, and the hyper-
 171 charge with the simple relation. The measurement of the weak mixing angle, in
 172 convention, provides the value of $\sin^2 \theta_W$, which is also the ratio of the weak to
 173 electromagnetic coupling constant

$$\sin^2 \theta_W = \frac{\alpha}{\alpha_W} = \frac{e^2}{g_W^2} \sim 0.23. \quad (1.35)$$

174 The coupling of the physical Z boson can be determined similarly. From Eq. 1.30,
 175 the current of the interaction between the Z boson and a fermion (with flavor f)
 176 can be written as

$$\begin{aligned} j_Z^\mu &= g_Z(I_W^{(3)} - Q_f \sin^2 \theta_W) \bar{u}_L \gamma^\mu u_L - g_Z(Q_f \sin^2 \theta_W) \bar{u}_R \gamma^\mu u_R \\ &\equiv g_Z(c_L \bar{u}_L \gamma^\mu u_L + c_R \bar{u}_R \gamma^\mu u_R) \end{aligned} \quad (1.36)$$

177 where $u_{L(R)}$ is the spinor of LH (RH) states, $c_L = I_W^{(3)} - Q_f \sin^2 \theta_W$ and $c_R =$
 178 $-Q_f \sin^2 \theta_W$ indicating the strengths of the coupling, and the coupling of the phys-

¹⁷⁹ ical Z boson defined as

$$g_Z = \frac{g_W}{\cos \theta_W} = \frac{e}{\sin \theta_W \cos \theta_W}. \quad (1.37)$$

¹⁸⁰ As stated previously, the physical Z boson does couple to LH and RH particles,
¹⁸¹ however, unequally. This is intuitively reasonable, as the current associated with
¹⁸² the Z boson is the mixture of the weak and $U(1)_Y$ interactions, where the former
¹⁸³ one couples only to LH particles but the latter one equally couples to LH and RH
¹⁸⁴ particles.

¹⁸⁵ In 1967, Steven Weinberg obtained the formula for the W and Z boson masses [3],
¹⁸⁶ with the θ_W which had not yet been determined then. In the following years, the
¹⁸⁷ θ_W was measured in various experiments, and in 1982 the masses of the W and
¹⁸⁸ Z bosons were predicted to be $m_W = 82 \pm 2 \text{ GeV}/c^2$ and $m_Z = 92 \pm 2 \text{ GeV}/c^2$. In
¹⁸⁹ 1983, Carlos Rubbia and his group discovered the W and the Z boson [4, 5] with
¹⁹⁰ measured masses $m_W = 80.403 \pm 0.029 \text{ GeV}/c^2$ and $m_Z = 91.188 \pm 0.002 \text{ GeV}/c^2$.
¹⁹¹ Experiments later on also confirmed the couplings. The GSW model is now con-
¹⁹² sidered as one of the most important successes in the SM.

¹⁹³ Despite the triumph of the electroweak unification, it did have some questions
¹⁹⁴ regarding the whole mechanism. First of all, Eq. 1.27 and 1.28 demonstrate that
¹⁹⁵ the fields of $U(1)_Y$ and $SU(2)_L$ are mixed to give physical bosons. The underlying
¹⁹⁶ nature of this mixture was unclear. Secondly, four electroweak gauge bosons have
¹⁹⁷ different masses, especially when comparing the photon with other three massive
¹⁹⁸ particles. This fact seems to contradict the physical picture that both electromag-
¹⁹⁹ netic and weak interactions are manifestations of a more fundamental electroweak
²⁰⁰ interaction. The problem with the masses happens also on the fermions. In Eq. 1.9,

201 the mass term in the QED Lagrangian can be expressed in the chiral states

$$\begin{aligned}
 -m\bar{\psi}\psi &= -m\bar{\psi} \left[\frac{1}{2}(1 - \gamma^5) + \frac{1}{2}(1 + \gamma^5) \right] \psi \\
 &= -m\bar{\psi} \left[\frac{1}{2}(1 - \gamma^5)\psi_L + \frac{1}{2}(1 + \gamma^5)\psi_R \right] \\
 &= -m(\bar{\psi}_R\psi_L + \bar{\psi}_L\psi_R).
 \end{aligned} \tag{1.38}$$

202 In the $SU(2)_L$ gauge transformation of the weak interaction, LH particles transform
203 as doublets while RH particles as singlets. Eq. 1.38 obviously does not follow the
204 required gauge invariance. Thirdly, a problem was found: the unitarity violation
205 of the scattering process $W^+W^- \rightarrow W^+W^-$. An overview of the WW scatter-
206 ing process can be found in Ref. [6]. The original calculation for the amplitude
207 included the diagrams, shown in Fig. 1-5. The unitarity violation results from the
208 longitudinal polarized states of W boson and the process $W_LW_L \rightarrow W_LW_L$. The is-
209 sue is solved by introducing a new scalar particle to mediate the WW process. The
210 diagrams are shown in Fig. 1-6. All the above three problems necessitate a new
211 mechanism, which is now called the Higgs mechanism, with its manifestation, the
Higgs boson.

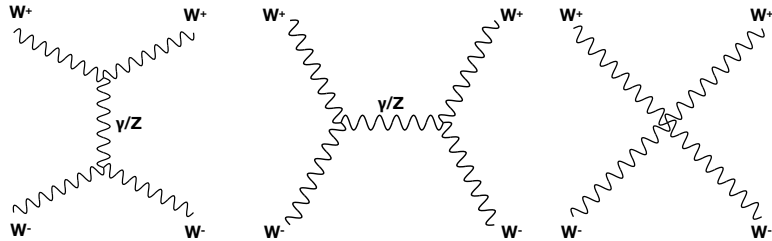


Figure 1-5: The leading order diagrams for $W^+W^- \rightarrow W^+W^-$ scattering process.

212

213 1.1.3 The Higgs mechanism

214 The Higgs mechanism was proposed back to 1964 by Robert Brout and François
215 Englert, Peter Higgs, and Gerald Guralnik, C. R. Hagen, and Tom Kibble [7, 8, 9].

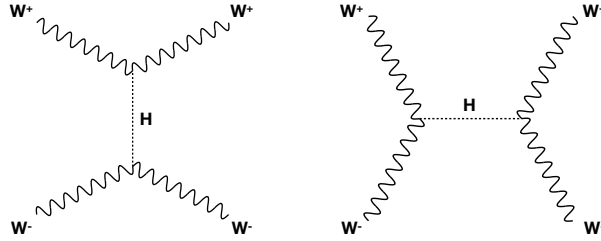


Figure 1-6: The diagrams for $W^+W^- \rightarrow W^+W^-$ scattering process with a scalar boson as mediator.

Before formally introducing the Higgs mechanism in the SM, a single scalar field ϕ is used as an example to illustrate the concept. Consider the potential of the form

$$V(\phi) = \frac{1}{2}\mu^2\phi^2 + \frac{1}{4}\lambda\phi^4. \quad (1.39)$$

The corresponding Lagrangian is given by

$$\begin{aligned} \mathcal{L}_{ex} &= \frac{1}{2}(\partial_\mu\phi)(\partial^\mu\phi) - V(\phi) \\ &= \frac{1}{2}(\partial_\mu\phi)(\partial^\mu\phi) - \frac{1}{2}\mu^2\phi^\mu - \frac{1}{4}\lambda\phi^4. \end{aligned} \quad (1.40)$$

In this example Lagrangian, the term of $(\partial_\mu\phi)(\partial^\mu\phi)$ can be associated with the kinematic energy of the scalar particle. The term of ϕ^2 can be read as the mass of the particle (strictly to say, when $\mu^2 > 0$, it is the coefficient of the ϕ^2 term that associates to the mass). The ϕ^4 term is identified as self-interactions of the scalar field.

The vacuum state is the lowest energy state of the field. In the field theory, the particles state (or the excitations of the field) can be obtained by applying perturbations of the field around the vacuum state. In order to have minima for the potential, the λ must be positive. When $\mu^2 > 0$, the minimum of the potential happens to be at $\phi = 0$. When $\mu^2 < 0$, the term can no longer be interpreted as mass, and the potential now has two degenerate minima at $\phi = \pm v = \pm |\sqrt{\frac{-\mu^2}{\lambda}}|$. One needs to arbitrarily select one of the degenerate states as the ground state, then the ground state no longer preserves the symmetry of the Lagrangian. This way to

²³³ obtain the asymmetric vacuum state is known as *spontaneous symmetry breaking*.

²³⁴ In the SM, the Higgs mechanism is embedded in the $U(1)_Y \times SU(2)_L$ local gauge
²³⁵ symmetry of the electroweak sector. As the Higgs mechanism is required to gener-
²³⁶ ate masses of the electroweak gauge bosons, one of the scalar fields must be neutral
²³⁷ (therefore termed as ϕ^0), and the other must be charged (ϕ^+ and $\phi^- = (\phi^+)^*$) to
²³⁸ give the longitudinal polarization states of the W bosons². The simplest Higgs
²³⁹ model, which has four degrees of freedom and consists of two complex scalar
²⁴⁰ fields, is placed in a weak isospin doublet,

$$\phi = \begin{pmatrix} \phi^+ \\ \phi^0 \end{pmatrix} = \frac{1}{\sqrt{2}} \begin{pmatrix} \phi_1 + i\phi_2 \\ \phi_3 + i\phi_4 \end{pmatrix}. \quad (1.41)$$

²⁴¹ The Lagrangian of this doublet of fields is

$$\mathcal{L} = (\partial_\mu \phi)^\dagger (\partial^\mu \phi) - V(\phi), \quad (1.42)$$

²⁴² To preserve the invariance under the $U(1)_Y \times SU(2)_L$ local gauge transformation,
²⁴³ the derivative in the Lagrangian should be replaced by the covariant derivative of
²⁴⁴ the form

$$\partial_\mu \rightarrow D_\mu = \partial_\mu + ig_W \mathbf{T} \cdot \mathbf{W}_\mu + ig' \frac{Y}{2} B_\mu, \quad (1.43)$$

²⁴⁵ where $\mathbf{T} = \frac{1}{2}\sigma$ are the three generators of the $SU(2)$ group. The Higgs potential is
²⁴⁶ of the form

$$V(\phi) = \mu^2 \phi^\dagger \phi + \lambda (\phi^\dagger \phi)^2, \quad (1.44)$$

²⁴⁷ where λ is positive. The visualization of the Higgs field is shown in Fig. 1-7. The
²⁴⁸ potential is spherically symmetric, and thus the original Lagrangian is spherically
²⁴⁹ symmetric. For $\mu^2 < 0$, the potential has infinite degenerate minima

$$\phi^\dagger \phi = \frac{1}{2} (\phi_1^2 + \phi_2^2 + \phi_3^2 + \phi_4^2) = \frac{v^2}{2} = -\frac{\mu^2}{2\lambda}. \quad (1.45)$$

²Before the Higgs mechanism, the gauge bosons do not have masses. Hence, they can only have transverse polarization states. After acquiring the masses, gauge bosons become massive particles, which can have longitudinal polarization state.

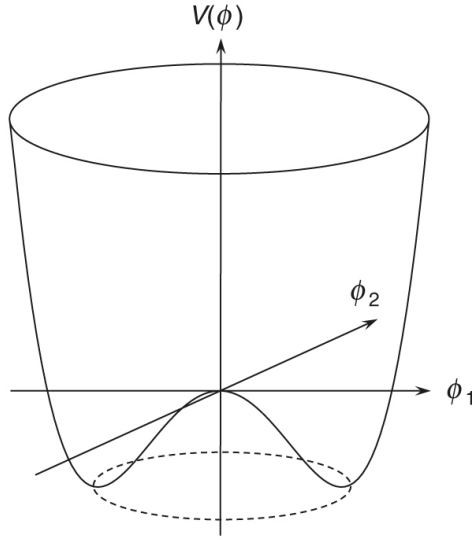


Figure 1-7: The Higgs potential for $\mu^2 < 0$.

250 For the neutral photon to be massless after the symmetry breaking, the vacuum
251 state is chosen to be

$$\phi^{\text{vacuum}} = \frac{1}{\sqrt{2}} \begin{pmatrix} 0 \\ v \end{pmatrix}. \quad (1.46)$$

252 The symmetry of the original Lagrangian is broken, given that a particular ground
253 state is selected among the degenerate states. A field η is introduced when apply-
254 ing the perturbation around the vacuum state

$$\phi^{\text{vacuum}} = \frac{1}{\sqrt{2}} \begin{pmatrix} \phi_1 + i\phi_2 \\ v + \eta + i\phi_4 \end{pmatrix}. \quad (1.47)$$

255 By substituting Eq. 1.47 into the Lagrangian, however, will produce massless Gold-
256 stone bosons and terms associated with the couplings between the massive gauge
257 fields and the Goldstone fields. An important fact is that every choice of the gauge
258 transformation, as long as it follows correct form, will not break the symmetry of
259 the Lagrangian. Therefore, a clever way to eliminate the Goldstone fields from
260 the Lagrangian is to choose a gauge transformation called *Unitary gauge*, and after
261 which the complex scalar fields will be entirely real. The Higgs doublet after the

²⁶² Unitary gauge is written as

$$\phi^{\text{vacuum}} = \frac{1}{\sqrt{2}} \begin{pmatrix} 0 \\ v + h \end{pmatrix}, \quad (1.48)$$

²⁶³ where η is replaced by h , which represents the physical field. After expanding all
²⁶⁴ the terms of the Lagrangian, the masses of gauge bosons can be identified as the
²⁶⁵ coefficients of the quadratic in the gauge fields.

²⁶⁶ In the Higgs doublet, the lower component is neutral ($Q = 0$) and has $I_W^{(3)} =$
²⁶⁷ $-\frac{1}{2}$, therefore the whole doublet has weak hypercharge $Y = 1$. Expanding the term
²⁶⁸ $(D_\mu \phi)^\dagger (D^\mu \phi)$

$$(D_\mu \phi)^\dagger (D^\mu \phi) = \frac{1}{2} (\partial_\mu h) (\partial^\mu h) + \frac{1}{8} g_W^2 (W_\mu^{(1)} + i W_\mu^{(2)}) (W^{(1)\mu} - i W^{(2)\mu}) (v + h)^2 + \frac{1}{8} (g_W W_\mu^{(3)} - g' B_\mu) (g_W W^{(3)\mu} - g' B^\mu) (v + h)^2. \quad (1.49)$$

²⁶⁹ one can identify the quadratic terms as

$$\frac{1}{8} v^2 g_W^2 \left(W_\mu^{(1)} W^{(1)\mu} + W_\mu^{(2)} W^{(2)\mu} \right) + \frac{1}{8} v^2 \left(g_W W_\mu^{(3)} - g' B_\mu \right) \left(g_W W^{(3)\mu} - g' B^\mu \right) \quad (1.50)$$

²⁷⁰ Identify the mass of the W boson by comparing

$$\frac{1}{2} m_W^2 W_\mu^{(1)} W^{(1)\mu} = \frac{1}{8} v^2 g_W^2 W_\mu^{(1)} W^{(1)\mu}, \quad (1.51)$$

²⁷¹ therefore

$$m_W = \frac{1}{2} g_W v. \quad (1.52)$$

²⁷² The mass the physical W boson is determined by the coupling constant of the
²⁷³ $SU(2)_L$ gauge interaction g_W and the vacuum expectation value of the Higgs field
²⁷⁴ v .

²⁷⁵ The second term in Eq. 1.50 is associated with the neutral $W^{(3)}$ and B fields,

²⁷⁶ and can be written as

$$\frac{1}{8}v^2 \left(g_W W_\mu^{(3)} - g' B_\mu \right) \left(g_W W^{(3)\mu} - g' B^\mu \right) = \frac{1}{8}v^2 \begin{pmatrix} W_\mu^{(3)} & B_\mu \end{pmatrix} \begin{pmatrix} g_W^2 & -g_W g' \\ -g_W g' & g'^2 \end{pmatrix} \begin{pmatrix} W^{(3)\mu} \\ B^\mu \end{pmatrix} \quad (1.53)$$

²⁷⁷ The matrix (referred to as mass matrix) appearing in the equation is non-diagonal,
²⁷⁸ showing that the off-diagonal elements couple the $W^{(3)}$ and B fields and allow
²⁷⁹ them to mix. The physical boson fields (termed as Z_μ and A_μ) correspond to the
²⁸⁰ eigenstates of the mass matrix, which can be obtained by solving the characteristic
²⁸¹ equation

$$\det(\mathbf{M} - \lambda I) = (g_W^2 - \lambda)(g'^2 - \lambda) - g_W^2 g'^2 = 0. \quad (1.54)$$

²⁸² As a result, the eigenvalues $\lambda = 0$ or $g_W^2 + g'^2$ with the eigenstates

$$A_\mu = \frac{g' W_\mu^{(3)} + g_W B_\mu}{\sqrt{g_W^2 + g'^2}}, \quad m_A = 0 \text{ (photon)} \quad . \quad (1.55)$$

$$Z_\mu = \frac{g_W W_\mu^{(3)} - g' B_\mu}{\sqrt{g_W^2 + g'^2}}, \quad m_Z = \frac{1}{2}v\sqrt{g_W^2 + g'^2} \text{ (Z boson)}$$

²⁸³ Now, by defining the ratio of the coupling as

$$\frac{g'}{g_W} = \tan \theta_W, \quad (1.56)$$

Eq. 1.55 can be expressed as

$$A_\mu = +B_\mu \cos \theta_W + W_\mu^{(3)} \sin \theta_W$$

$$Z_\mu = -B_\mu \sin \theta_W + W_\mu^{(3)} \cos \theta_W.$$

²⁸⁴ Eq. 1.27 and 1.28 are retained. With Eq. 1.56, the mass of the physical Z boson is

$$m_Z = \frac{1}{2} \frac{g_W}{\cos \theta_W} v. \quad (1.57)$$

²⁸⁵ Combining with the W boson mass from Eq. 1.52, one would obtain

$$\frac{m_W}{m_Z} = \tan \theta_W. \quad (1.58)$$

²⁸⁶ The mass of the Higgs boson m_H can be identified as the quadratic term in the
²⁸⁷ Higgs boson field which is generated by the potential $V(\phi)$ in the Lagrangian,

$$m_H^2 = 2\lambda v^2. \quad (1.59)$$

²⁸⁸ In Eq. 1.49, the gauge boson fields appears in the form of $VV(v + h)^2$, where
²⁸⁹ V stands for gauge fields. The VVv^2 terms relate to the mass of the gauge bosons,
²⁹⁰ and the $VVvh$ and $VVhh$ terms represent the triple and quartic couplings between
²⁹¹ the Higgs bosons and the gauge bosons. From the weak theory, the physical W
²⁹² bosons are constructed as linear combination of the $W^{(1)}$ and $W^{(2)}$, as shown in
²⁹³ Eq. 1.21. Hence, the second term in Eq. 1.49 associated with the $W^{(1)}$ and $W^{(2)}$ can
²⁹⁴ be rewritten as

$$\frac{1}{4}g_W^2 W_\mu^- W^{+\mu} (v + h)^2 = \frac{1}{4}g_W^2 v^2 W_\mu^- W^{+\mu} + \frac{1}{2}g_W^2 v W_\mu^- W^{+\mu} h + \frac{1}{4}g_W^2 W_\mu^- W^{+\mu} hh. \quad (1.60)$$

²⁹⁵ The first terms gives the masses of W boson as stated previous, the second term
²⁹⁶ represents the triple HW^+W^- coupling, and the third term gives rise to the quartic
²⁹⁷ HHW^+W^- coupling. The coupling strength of the HW^+W^- vertex is

$$g_{HWW} = \frac{1}{2}g_W^2 v = g_W m_W. \quad (1.61)$$

²⁹⁸ Similarly, the coupling HZZ can be derived $g_{HZZ} = \frac{g_W}{\cos \theta_W} m_Z \equiv g_Z m_{cPZ}$. *The cou-*
²⁹⁹ *plings of the Higgs boson and the gauge bosons are proportional to the mass of the gauge*
³⁰⁰ *bosons.*

³⁰¹ As mentioned previously, the fermion mass term $-m\bar{\psi}\psi = -m(\bar{\psi}_R\psi_L + \bar{\psi}_L\psi_R)$
³⁰² is not invariant under $SU(2)_L \times U(1)_Y$ transformation, since the RH and LH fermions

303 transform differently

$$\begin{aligned} \text{LH doublet fermions : } \psi_L &\rightarrow \psi'_L = \psi_L e^{ig_W T \cdot W + ig' \frac{Y}{2} B} \\ \text{RH singlet fermions : } \psi_R &\rightarrow \psi'_R = \psi_R e^{ig' \frac{Y}{2} B} \end{aligned} . \quad (1.62)$$

304 The solution is to construct a *singlet* under $SU(2)_L \times U(1)_Y$ in the Lagrangian. Con-
 305 sider an infinitesimal $SU(2)$ local transformation on the $SU(2)$ doublet ϕ of the Higgs
 306 fields,

$$\phi \rightarrow \phi' = (I + ig_W \epsilon(x) \cdot T)\phi, \quad (1.63)$$

307 where T are generators of the $SU(2)$ group. The LH doublets L undergoes the same
 308 transformation

$$\begin{aligned} L &\rightarrow L' = (I + ig_W \epsilon(x) \cdot T)L \\ \bar{L} &= L^\dagger \gamma^0 \rightarrow \bar{L}' = \bar{L}(I - ig_W \epsilon(x) \cdot T) \end{aligned} \quad (1.64)$$

309 It is clear that a term of $\bar{L}\phi$ is invariant under the $SU(2)_L$ transformation, or in
 310 other word, a singlet under $SU(2)_L \times U(1)_Y$. The effects of the transformation on
 311 the ϕ and \bar{L} compensate to each other. Combining the $\bar{L}\phi$ with RH singlet R also
 312 results in a singlet under $SU(2)_L \times U(1)_Y$ (The conjugate of the combination is also
 313 a singlet). Consequently, a term in the Lagrangian of the form $-y_f(\bar{L}\phi R + \bar{R}\phi^\dagger L)$
 314 possesses the $SU(2)_L \times U(1)_Y$ gauge symmetry. The Lagrangian, after spontaneous
 315 symmetry breaking and in the unitary gauge, is now

$$\mathcal{L}_{\text{fermion mass}} = -\frac{y_f}{\sqrt{2}} v (\bar{\ell} f_R + \bar{f}_R \ell) - \frac{y_f}{\sqrt{2}} (\bar{\ell} f_R + \bar{f}_R \ell). \quad (1.65)$$

316 where y_f is a constant known as *Yukawa coupling*. The first term corresponds to
 317 the fermion masses, $m_\ell = \frac{y_f v}{\sqrt{2}}$, representing the coupling of the fermions to the
 318 Higgs field through the non-zero vacuum expectation value. The second term cor-
 319 responds to the interaction between the fermions and the physical Higgs boson.

320 The non-zero vacuum expectation value appears only in the lower component
 321 of the Higgs doublet, thus only fermions in the lower component of the $SU(2)$

322 doublet (charged fermions and down-type quarks) can acquire masses, which is
323 obviously not the case. The way to give masses to up-type quarks is to construct
324 the conjugate doublet of the Higgs field ϕ_c which transforms in the same way as
325 the doublet ϕ

$$\phi_c = -i\sigma_2\phi^* = \begin{pmatrix} -\phi^{0*} \\ \phi^- \end{pmatrix} = \begin{pmatrix} -\phi_3 + i\phi_4 \\ \phi_1 - i\phi_2 \end{pmatrix} \quad (1.66)$$

326 The Lagrangian of the up-type quark masses is the same as Eq. 1.65 except ϕ now
327 is replaced by ϕ_c . Consequently, the Lagrangian, after the symmetry breaking, is

$$\mathcal{L}_{\text{up-type quark masses}} = -\frac{y_{f, \text{up}}}{\sqrt{2}} v (\bar{u} u_R + \bar{u}_R u) - \frac{y_{f, \text{up}}}{\sqrt{2}} (\bar{u} u_R + \bar{u}_R u). \quad (1.67)$$

328 where the up-type quark masses can be identified as $m_{\text{up}} = \frac{y_{f, \text{up}} v}{\sqrt{2}}$. The Yukawa
329 coupling of the fermions to the Higgs field is jointly written as

$$y_f = \frac{\sqrt{2}m_f}{v}, \quad (1.68)$$

330 and its value is determined to be consistent with the observed fermion masses.

331 The neutrino masses are yet another story. The possible mechanism to account
332 for the neutrino masses was first introduced in Ref. [10, 11], and is now known as
333 the seesaw mechanism. This mechanism will not be discussed in this thesis.

334 A review of the Higgs boson production at the LHC will be introduced in the
335 next sub-section.

336 1.1.4 The production of the Higgs boson and its decays

337 The main production processes at the hadron collider are gluon-gluon fusion (ggF),
338 vector boson fusion (VBF, or qqH), associated vector boson production (VH), and
339 associated top quark pair production (ttH). The diagrams for these production
340 modes are shown in Fig. 1-8 and the Higgs boson production cross-sections at
341 the center-of-mass frame energy $\sqrt{s} = 13$ TeV are shown in Fig. 1-9 [12]. The
342 profound results of the deep inelastic scattering experiments showed that the mo-

343 momentum of the proton is not only carried by its three valence quarks, but also by
 344 the gluons that mediate the strong interaction between the quarks. In such a high
 345 energy collision at the LHC, the majority of energy is the carried by gluons, and
 346 hence the hard processes are dominantly produced by the gluon-gluon interac-
 347 tions.

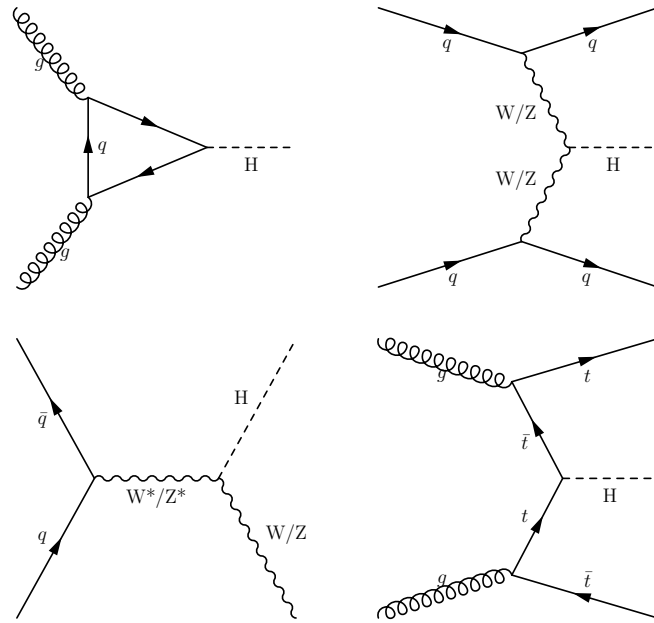


Figure 1-8: The diagrams for dominant production modes. (Top left) gluon-gluon fusion; (Top right) vector boson fusion; (Bottom left) associated vector boson production; (Bottom right) associated top quark pair production.

348 Since the Higgs boson is the manifestation of the Higgs mechanism which gives
 349 fundamental particles masses, in principal it can decay into all particles, if it is
 350 kinematically allowed. The decay probability is interpreted as branching ratio.
 351 The branching ratio of the most important decay channels as function of the Higgs
 352 boson mass are shown in Fig.1-10. In the following paragraphs, I will discuss the
 353 main decay channels of the Higgs boson.

354 The Higgs boson cannot decay into top quarks as the top quark is too heavy [13].
 355 The coupling between the Higgs boson and the top quark y_t is then realized in
 356 terms of the ttH production and loops of virtual top quarks in the ggF produc-

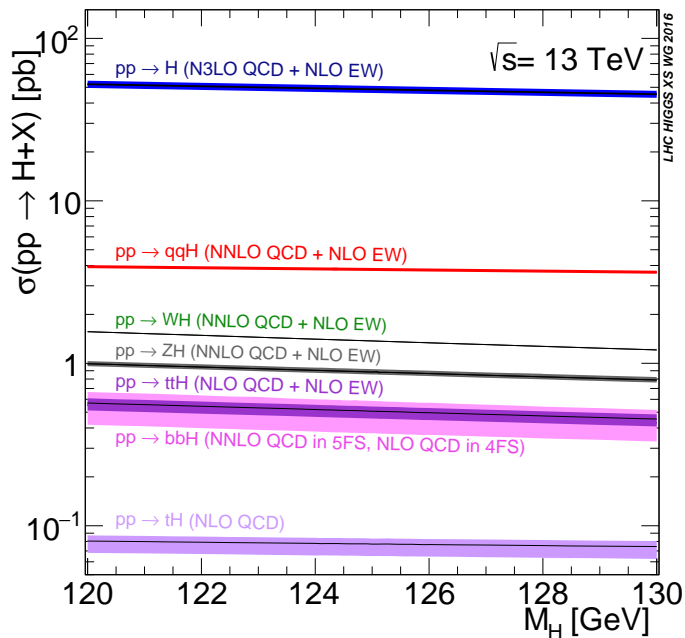


Figure 1-9: The SM Higgs boson production cross sections at $\sqrt{s} = 13 \text{ TeV}$ as a function of the Higgs boson mass [12].

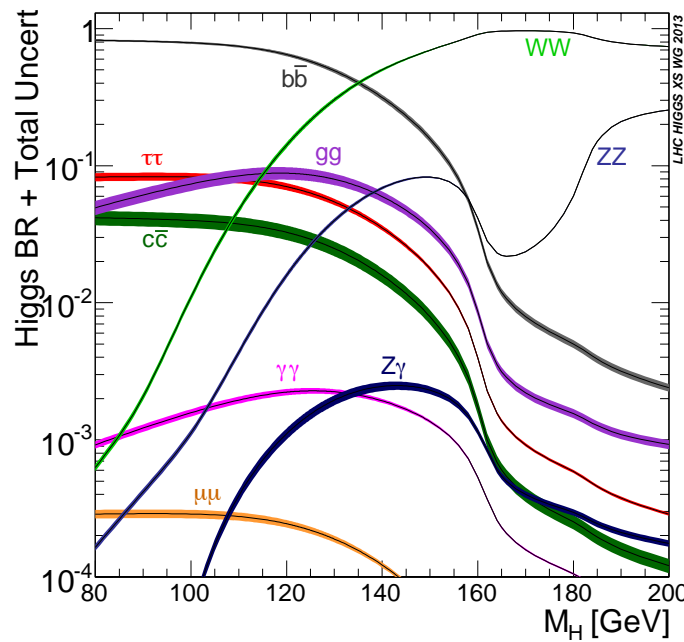


Figure 1-10: The SM Higgs boson decay branching ratios [12].

tion or in the decays to the massless particles, such as $H \rightarrow \gamma\gamma$ and $H \rightarrow gg$.
The combined measurement of the rate of Higgs boson production through gluon-gluon fusion and of the $H \rightarrow \gamma\gamma$ decay with LHC Run1 data suggested that the Higgs boson coupling to top quarks is consistent with SM prediction within uncertainties [14]. A measurement of the production rate of the tree-level ttH process can provide further information as to whether there exists non-SM particles in the loops that introduce terms compensating for other deviations from the SM. The analysis is very difficult, as the top-quark decays to a W bosons and b-quark, and shortly afterwards the W decays hadronically to two jets or leptonically to a lepton and a neutrino. Both the ATLAS and CMS Collaboration have recently observed this production channel, and established the confirmation of the tree-level coupling of the Higgs boson to top quarks with the combined analyses of datasets collected at $\sqrt{s} = 7, 8$, and 13 TeV [15, 16]. The best-fit signal strength $\hat{\mu}$ from the ATLAS measurement is $1.32^{+0.28}_{-0.26}(\text{Total}) \pm 0.18(\text{Stat.})^{+0.21}_{-0.19}(\text{Syst.})$, and from the CMS is $1.26^{+0.31}_{-0.26}(\text{Total}) \pm 0.16(\text{Stat.})^{+0.27}_{-0.22}(\text{Syst.})$. The ATLAS obtained a significance of 6.3 standard deviations (σ) relative to the background-only hypothesis, where the expected significance is 5.1σ . The CMS also obtained the observed significance of 5.2σ with the expected significance is 4.2σ . The Higgs-top coupling can also be probed in the search for the production of Higgs boson in association with a single top quark. The production cross-section of this process is not only sensitive to the absolute values of the modifiers of the Higgs-top coupling, κ_t , and the coupling of vector bosons to the Higgs boson, κ_V , but also to their relative signs with respect to those predicted in the SM. Hence, it provides additional information toward the nature of the Higgs boson. The CMS Collaboration performed this search with data collected in 2016 [17], and the results showed that the observed data favor positive sign of the coupling.

The largest branching ratio of the Higgs boson of mass $m_H = 125$ GeV is to bottom quarks, with $\mathcal{BR}(H \rightarrow b\bar{b}) \approx 58.2\%$. The measurement of the rate of the $H \rightarrow b\bar{b}$ decay offers a direct test to the magnitude of Hbb coupling, while the relative sign of the coupling can be determined by the decay process $H \rightarrow Y + \gamma$,

where the Y is the bound state of the b quarks [18]. In order to suppress the QCD backgrounds, the analysis is designed to search for the VH production where a W or Z boson decays leptonically, corresponding to five independent channels: $Z(\ell\ell)H$, $W(\ell\nu)H$, and $Z(\nu\nu)H$ where $\ell = e, \mu$. A multivariate regression technique [19, 20, 21] is applied to calibrate the measured energy of the b-tagged jets to improve the dijet mass resolution, after which the mass resolution is approximately 10–15%. The CMS Collaboration performs the search, and the combination with Run1 measurement results in an observed (expected) significance is $3.8 (3.8)\sigma$. The corresponding signal strength $\hat{\mu} = 1.06^{+0.31}_{-0.29}$ [22]. The ATLAS Collaboration announces the first observation of this channel with data corresponding to an integrated luminosity of 79.8 fb^{-1} collected in Run2 at $\sqrt{s} = 13 \text{ TeV}$ [23]. A combination with other production modes of the Higgs boson is performed for $H \rightarrow b\bar{b}$ decay mode, which yields an observed (expected) significance of $5.4 (5.5)\sigma$. The signal strength $\hat{\mu} = 1.01^{+0.20}_{-0.20}$.

The $H \rightarrow \tau^+\tau^-$ decay mode has been considered as the only accessible leptonic decay mode that probes the coupling of the Higgs boson to the fermionic sector. It can also be used to constrain CP violation in the VBF production [24] and provide sensitivity to CP violation in the Higgs boson coupling to leptons [25]. This decay benefits from a favorable signal-to-background conditions than the $H \rightarrow b\bar{b}$ decay, however, slightly worse mass resolution of $\approx 10 - 20\%$, resulting from the inaccuracy of the momentum reconstruction of the τ lepton. The τ lepton can decay leptonically as $\tau \rightarrow \nu_\tau \ell \bar{\nu}_l$ where $\ell = e, \mu$, and hadronically to charged or neutral pions. The analyses from both the ATLAS and CMS utilizes the four most sensitive $\tau\tau$ final states: $e\mu$, $e\tau_h$, $\mu\tau_h$, and $\tau_h\tau_h$, where τ_h denotes the hadronic decay. The ATLAS Collaboration reports the signal strength $\hat{\mu} = 1.09^{+0.36}_{-0.30}$ with an observed (expected) significance of $6.4 (5.4)\sigma$ with a combined analysis with $\sqrt{s} = 7, 8$, and 13 TeV data [26]. The CMS Collaboration also obtains the signal strength $\hat{\mu} = 1.09^{+0.27}_{-0.26}$ with an observed (expected) significance of $5.9 (5.9)\sigma$ in combination with Run1 data [27].

Prior to the discovery of the Higgs boson, the decay mode $H \rightarrow WW$ was con-

sidered the most sensitive channel in the mass range around the WW threshold of 160 GeV, and thus was important to the exclusion in such range. The $H \rightarrow WW^* \rightarrow \ell\nu\ell\nu$ analysis profits from the fact that it has large branching fraction and has a relatively low-background final state. As a result, this decay channel has very good sensitivity to most production processes, in particular ggF and VBF. However, the presence of neutrinos in the final state prevents the full reconstruction of the Higgs boson mass, and hence worse mass resolution of $\approx 20\%$. The different-flavor leptonic decay mode $e\mu$ has the largest branching fraction, is the least affected by background processes, and therefore is the most sensitive channel of the analysis. The ATLAS Collaboration provides results of ggF and VBF production with 2016 data separately [28]. For the ggF production the signal strength $\hat{\mu} = 1.21^{+0.22}_{-0.21}$ with an observed (expected) significance of 6.3 (5.2) σ , while for the VBF the signal strength $\hat{\mu} = 0.62^{+0.37}_{-0.36}$ with an observed (expected) significance of 1.9 (2.7) σ . The CMS Collaboration reports the signal strength $\hat{\mu} = 1.28^{+0.18}_{-0.17}$ with an observed (expected) significance of 9.1 (7.1) σ , combining all considered channels [29].

The $H \rightarrow ZZ^* \rightarrow 4\ell$ ($\ell = e$ or μ) decay has low branching fraction, but fortunately has the lowest background contamination, resulting in very good sensitivity. It provides the direct probe in constraining the HZZ coupling. The precise reconstruction of the final state products allows the complete determination of the kinematics of the reconstructed Higgs boson with mass resolution of $\approx 1 - 2\%$, which makes it one of the most important channels to measure the properties of the Higgs boson. The ATLAS and CMS Collaborations have both performed analyses for this channel with the Run1 data to determine the mass and spin-parity of the boson [30, 31, 32, 33, 34], its width [35, 36, 37], the fiducial cross sections [22, 23], and the tensor structure of its interaction with a pair of neutral gauge bosons [32, 34, 36]. These measurements provided results that are so far consistent with the SM predictions. The CMS Collaboration provides results, based on the combined data collected in 2016 and 2017, of the signal strength $\hat{\mu} = 1.06^{+0.15}_{-0.13}$ [38]. The ATLAS Collaboration reports the signal strength $\hat{\mu} = 1.18^{+0.13}_{-0.13}$ [39]. A model-independent measurement of the Higgs boson width is performed by the CMS

447 Collaboration with 2016 data using the $m_{4\ell}$ distribution in the range $105 < m_{4\ell} <$
448 140 GeV , and is able to constrain the width to be $\Gamma_H < 1.10$ (1.60) GeV at 95%
449 confidence level (CL) for observed (expected) value [40].

450 Despite the small branching fraction predicted by the SM, the $H \rightarrow \gamma\gamma$ decay
451 provides a clean final state, two energetic photons, with an invariant mass peak
452 that can be reconstructed with high precision with mass resolution of $\approx 1 - 2\%$.
453 Consequently, this channel was one of the most important channels for the Higgs
454 boson discovery and first measurements of its properties [41, 42]. Since the $H \rightarrow$
455 $\gamma\gamma$ decay proceeds mainly through W- and top-loop processes, interference effects
456 make its branching fraction sensitive to the relative sign of the fermion and vector
457 boson couplings. The differential cross sections enables us to test the perturbative
458 QCD predictions for Higgs boson production, and can be used to probe the spin
459 and CP properties of the Higgs boson. The CMS Collaboration provides the re-
460 sults using 2016 data of the signal strength $\hat{\mu} = 1.18^{+0.17}_{-0.14}$ [43], while the ATLAS
461 Collaboration obtains $\hat{\mu} = 0.99^{+0.14}_{-0.14}$. The interpretation of the coupling measure-
462 ments from both collaborations shows that the observed data favors the positive
463 sign of the coupling [44, 45]. The ATLAS Collaboration also tries to investigate the
464 strength and tensor structure of the Higgs boson interactions using an effective La-
465 grangian, which introduces additional CP-even and CP-odd interactions [45], but
466 no significant new physics contributions are observed.

467 The decay of $H \rightarrow Z/\gamma^* + \gamma$ shares almost the same diagrams as that of the
468 $H \rightarrow \gamma\gamma$ decay, where in the former one a Z boson or a virtual photon γ^* is radi-
469 ated from the loop. Measurement of this rare decay can enhance the current under-
470 standing of the nature of the Higgs boson, and can also provide an alternative way
471 to test if there is any beyond standard model (BSM) couplings induced in the loop
472 diagrams. A brief summary of these extension of SM can be found in Ref. [46, 47].
473 If there exists BSM that is manifested through CP violation, one can also observe
474 the anomaly though a measurement of the forward-backward asymmetry. The AT-
475 LAS Collaboration sets an observed (expected) exclusion upper limit on the pro-
476 duction cross section times the branching ratio of the $H \rightarrow Z\gamma$ decay of 6.6 (5.2)

477 times the SM prediction at 95% CL for a Higgs boson mass $m_H = 125.09$ GeV, while
478 the upper limits from the CMS Collaboration varies between 6.1 and 11.4 (3.9 and
479 9.1) times the SM value in the mass range of $120 < m_H < 130$ GeV [46, 47]. The
480 CMS Collaboration also provides so far the most stringent limit on the $H \rightarrow \gamma^* \gamma$
481 decay, varying between 1.4 and 4.0 (2.1 and 2.3) times the SM prediction in the
482 range of $120 < m_H < 130$ GeV [46].

483 The rare decay $H \rightarrow \mu\mu$ offers the best possibility to measure the Higgs cou-
484 pling to second-generation fermions at the LHC. The expected branching fraction
485 for a Higgs boson mass $m_H = 125.09$ GeV is $\mathcal{BR}(H \rightarrow \mu\mu) \approx 2.2 \times 10^{-4}$ [48] which
486 is roughly one order of magnitude smaller than the $H \rightarrow Z/\gamma^* + \gamma$ decay, owing
487 to the small Yukawa coupling of the muon to the Higgs field. The CMS Collabo-
488 ration sets the observed (expected) upper limit on the signal strength of 2.92 (2.16)
489 times the SM prediction, with combination of 7, 8, and 13 TeV data [49], while the
490 ATLAS Collaboration reports an upper limit of 2.1 (2.0) times the SM values [50].

491 The other decay of the Higgs boson to second-generation fermions that was
492 searched for is the $H \rightarrow c\bar{c}$ process. It is commonly considered impossible to dis-
493 cover this channel even in high luminosity run of the LHC (HL-LHC) due to the
494 small branching fraction, large background in hadron collider, and jet flavor iden-
495 tification inefficiency [51, 52]. Nevertheless, direct search for the $H \rightarrow c\bar{c}$ decay is
496 important in the long-term perspective, as the development of the charm-tagging
497 technique and the direct constraint of the Higgs-charm coupling would be valua-
498 ble inputs to the next generation of particle colliders. The ATLAS Collaboration
499 presents the first search for this process with data collected in 2016, utilizing the ZH
500 production with the subsequent decay of the Z boson to dilepton. The observed
501 (expected) upper limit on the production cross-section $\sigma(pp \rightarrow ZH) \times \mathcal{BR}(H \rightarrow$
502 $c\bar{c})$ is found to be 2.7 ($3.9^{+2.1}_{-1.1}$) pb at the 95% CL, corresponding to an observed
503 (expected) upper limit on the signal strength $\hat{\mu} < 110$ (150^{+80}_{-40}) [53].

504 1.1.5 The measurement of the Higgs coupling

505 The ATLAS and CMS Collaborations both reported the observation of a new bo-
 506 son with a mass of $m_H = 125.09 \pm 0.21(\text{stst.}) \pm 0.11(\text{syst.}) \text{ GeV}$ [54] in 2012, and
 507 subsequent measurements revealed its Higgs-boson-like properties [31, 32, 55, 56,
 508 57, 58, 59, 60]. One of the important analyses, and most related to this thesis, is the
 509 measurement of the Higgs coupling. A combined measurement were performed
 510 by ATLAS and CMS with data collected at 7 and 8 TeV [14], and the CMS Collabo-
 511 ration provides the latest results with 13 TeV data [61]. The results from CMS with
 512 13 TeV data will be shown in the following paragraphs.

513 The inputs of the analysis are the four main production processes introduced
 514 previously, decay channels to bosons $H \rightarrow ZZ$, WW , $\gamma\gamma$, and to fermions $H \rightarrow$
 515 $\tau\tau$, $b\bar{b}$, $\mu\mu$. In this work, a so-called κ -framework [62] is used³. Within the
 516 framework, there are assumptions made such that the production and decay of
 517 the Higgs boson can be factorized and parametrized as

$$\sigma_i \cdot \mathcal{BR}^f = \frac{\sigma_i(\vec{\kappa}) \cdot \Gamma^f(\vec{\kappa})}{\Gamma_H}, \quad (1.69)$$

518 where Γ_H is the total width of the Higgs boson and Γ^f is the partial width for Higgs
 519 boson decay to the final state f . Coupling modifiers, $\vec{\kappa}$, are introduced in order
 520 to test deviations in the couplings of the Higgs boson to other particles, and are
 521 defined as

$$\kappa_j^2 = \frac{\sigma_j}{\sigma_{j\text{SM}}} \text{ or } \kappa_j^2 = \frac{\Gamma_j^f}{\Gamma_{j\text{SM}}^f}, \quad (1.70)$$

522 where all $\kappa_j = 1$ in the SM and j denotes the tested production or decay mode.
 523 Tree-level Higgs boson couplings, such as the $H - Z$, $H - W$, $H - t$, $H - b$, $H -$
 524 τ , and $H - \mu$, are introduced as individual coupling modifiers. For those processes
 525 that occur at leading-order (LO) involving box or triangular loop diagrams, the
 526 loops are resolved in terms of the corresponding coupling modifiers, weighted by
 527 their individual contribution. Interference effects between the different diagrams

³It was referred to as Interim framework in the cited reference.

528 provide sensitivity to the relative signs of the Higgs boson couplings to differ-
529 ent particles. The coupling modifiers κ_c and κ_s are allowed to vary as function of
530 other modifiers, provided that current LHC data are insensitive to these couplings.
531 The constraint on κ_c will be introduced separately later. Other coupling modifiers
532 κ_u , κ_d , and κ_e are not included in combination given that their magnitudes are
533 marginal.

534 There are two parametrization schemes. One is defined such that two addi-
535 tional effective coupling modifiers, κ_g and κ_γ , which describe the loop processes
536 for ggF production and $H \rightarrow \gamma\gamma$ decay, are introduced to account for the situation
537 that BSM particles may be present in these loops. The other one is to resolve the
538 ggF and $H \rightarrow \gamma\gamma$ processes as function of remaining coupling modifiers. Fig. 1-
539 11 shows the summary plots for the κ -framework model with the resolved loop
540 scheme and the assumption $\mathcal{BR}_{BSM} = 0$. The points indicate the best fit values
541 while the thick and thin horizontal bars show the 1σ and 2σ CL intervals, respec-
542 tively. Without loss of generality, the value of κ_t is restricted to be positive. For
543 this model, both positive and negative values of κ_W , κ_Z , and κ_b are considered.
544 The result shows that negative values of κ_W are disfavored by more than 2σ . The
545 interference between diagrams of the ZH production leads to the break of the de-
546 generacy between signs, and indicates that a positive value of κ_Z is favored. A
547 negative value of κ_b is preferred in this model, however, the difference between
548 the best-fit point and the minimum in the positive region is small. Fig. 1-12 shows
549 the summary plots with effective couplings scheme. In the left figure the constraint
550 $\mathcal{BR}_{BSM} = \mathcal{BR}_{inv} + \mathcal{BR}_{undet} = 0$ is imposed, and both positive and negative val-
551 ues of κ_W and κ_Z are considered. In the right figure a constraint $|\kappa_V| \leq 1$, where
552 κ_V denotes κ_Z or κ_W , is imposed (same sign of κ_Z and κ_W), while $\mathcal{BR}_{inv} > 0$ and
553 $\mathcal{BR}_{undet} > 0$ are free parameters. The preferred sign of the κ_W , opposite to the
554 first scheme, is negative. In Fig. 1-13, left plot shows the scan of the test statistic
555 as a function of \mathcal{BR}_{inv} , and the right plot shows the 68% and 95% CL contours
556 for \mathcal{BR}_{inv} vs. \mathcal{BR}_{undet} , indicating the 95% CL upper limits of $\mathcal{BR}_{inv} < 0.22$ and
557 $\mathcal{BR}_{undet} < 0.36$.

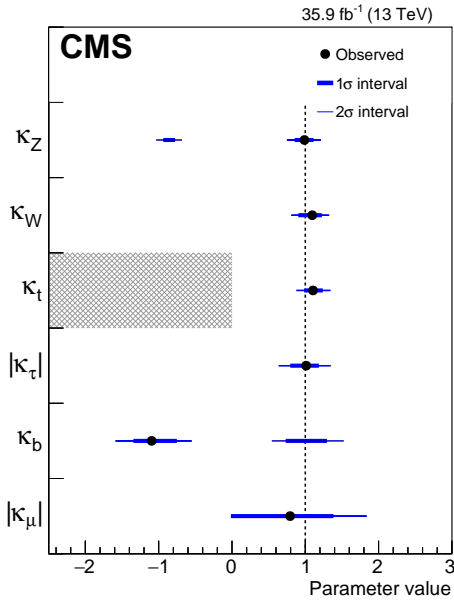


Figure 1-11: Summary for the κ -framework model with the resolved loop scheme [61].

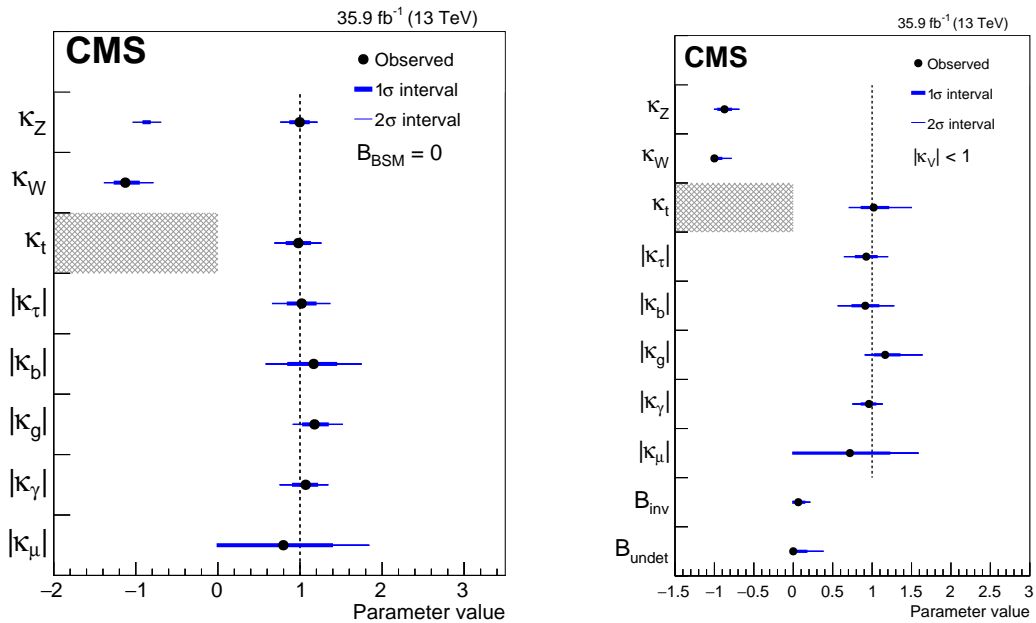


Figure 1-12: Summary for the κ -framework model with the effective couplings scheme [61].

558 Another fit is performed using a phenomenological parameterization relating
559 the masses of the fermions and vector bosons to the corresponding modifiers with

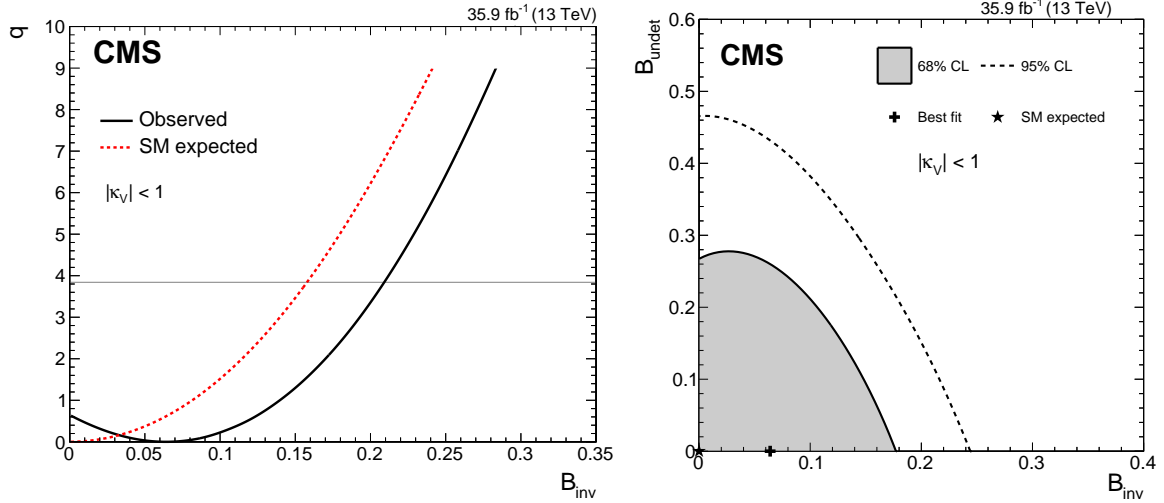


Figure 1-13: Scan of the test statistic as a function of $\mathcal{BR}_{\text{inv}}$ (left), and 68% and 95% CL regions for $\mathcal{BR}_{\text{inv}}$ vs. $\mathcal{BR}_{\text{undet}}$ (right) [61].

two parameters, M and ϵ [63, 64]. In this parametrization, the coupling modifiers, M and ϵ are related as $\kappa_F = \frac{v \cdot m_f^\epsilon}{M^{1+\epsilon}}$ for fermions and $\kappa_V = \frac{v \cdot m_V^{2\epsilon}}{M^{1+2\epsilon}}$ for vector bosons, where $v = 246.22 \text{ GeV}$ is the vacuum expectation value [65]. The SM expectation of $\kappa = 1$, corresponds to $(M, \epsilon) = (v, 0)$. The left plot in Fig. 1-14 shows the 1σ and 2σ CL regions in the (M, ϵ) fit, and the results of the fit using the six modifiers are plotted versus the particle masses on the right-hand side, as well as the result of the (M, ϵ) fit. A "reduced" vector boson coupling $\frac{\sqrt{\kappa_V \cdot m_V}}{v}$ is shown to represent the couplings of the vector bosons in the same plot. As one can see, the couplings of these six particles to the Higgs boson are consistent within uncertainties with the SM predictions.

570 The Higgs-charm coupling

As stated previously, a sensitive measurement of Higgs-charm coupling is not feasible in the environment of the LHC. There are still ways to constrain the size of the coupling. Since c- and b-jets share rough similarities, jets originating from charm quarks may be mistagged as b- jets. Hence, with the tagging efficiency of c- and b-jets, one can recast the existing analyses of $H \rightarrow b\bar{b}$ to constrain the

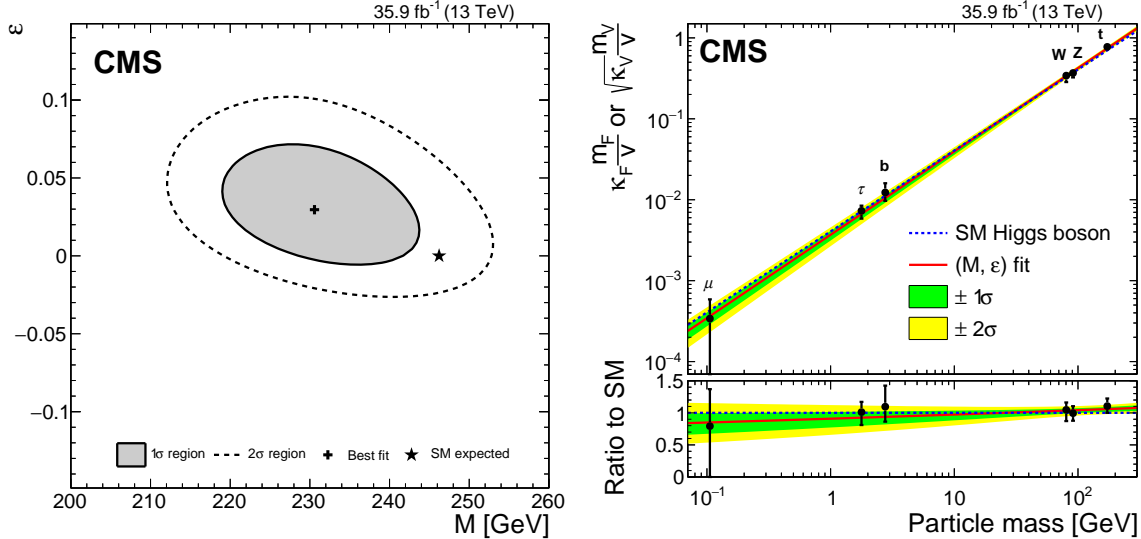


Figure 1-14: (Left) Likelihood scan in the $M - \epsilon$ plane. The best fit point and the 1σ and 2σ CL regions are shown, along with the SM prediction. (Right) Result of the phenomenological (M, ϵ) fit with the loop-resolved scheme of κ -framework model [61].

576 H \rightarrow $c\bar{c}$ rate [51]. This results in a model-independent bound on the charm signal
 577 strength of $\mu_c = 95^{+90}_{-95}$ with the results of the H $\rightarrow b\bar{b}$ search in VH production
 578 from both ATLAS and CMS Collaborations. Both ATLAS and CMS Collaboration
 579 give a model-independent bound on the Higgs total width from the invariant-mass
 580 distribution of the H $\rightarrow ZZ^*$ and H $\rightarrow \gamma\gamma$ in the Run1 analyses. This bound on the
 581 total width can be used to constrain the Higgs-charm coupling by assuming the
 582 entire Higgs width is formed by H $c\bar{c}$. With this method, the upper bounds at 95%
 583 CL with the CMS results is $\kappa_c < 120$ and with the ATLAS results is $\kappa_c < 150$. A
 584 method that relies on the measurements of transverse momentum distributions of
 585 Higgs boson was proposed to determine the limit on the coupling modifier κ_c [66].
 586 Fig. 1-15 shows the impact of the coupling modifier κ_c on the normalized p_T^H spec-
 587 trum in inclusive Higgs production. This letter takes the p_T spectrum from the
 588 ATLAS combined measurement of H $\rightarrow \gamma\gamma$ and H $\rightarrow ZZ^*$ decays with Run1
 589 $\sqrt{s} = 8$ TeV data, and obtains the bounds on κ_c at 95% CL of $\kappa_c \in [-16, 18]$. The
 590 spectrum of the p_t^H at $\sqrt{s} = 13$ TeV is expected to be slightly harder than that of

591 $\sqrt{s} = 8 \text{ TeV}$, thus will enhance the sensitivity to κ_c at ongoing LHC runs as well
 592 as possible future hadron colliders at higher energies. The CMS Collaboration ap-
 593 plies this method with the distributions from $H \rightarrow \gamma\gamma$ and $H \rightarrow ZZ^*$ analyses
 594 using data collected in 2016 to set limit on the constrain of κ_c [67]. Fig. 1-16 shows
 595 the simultaneous fit results for κ_b and κ_c . On the left plot, 1 and 2σ deviation con-
 596 tours for the combined ($H \rightarrow \gamma\gamma$ and $H \rightarrow ZZ^*$) fit to data and for $H \rightarrow \gamma\gamma$ and
 597 $H \rightarrow ZZ^*$ separately, assuming coupling dependency of the branching fractions,
 598 while the right plot assumes freely floating branching fractions in the fit. The ob-
 599 served (expected) constraints on κ_c are

$$-4.3 < \kappa_c < 4.3 \quad (-5.4 < \kappa_c < 5.3) \text{ (coupling dependent } \mathcal{BR}), \quad (1.71)$$

600
 – $-18.0 < \kappa_c < 22.9 \quad (-15.7 < \kappa_c < 19.3) \text{ (freely floating } \mathcal{BR}). \quad (1.72)$

601 If the branching fractions are fixed to the SM expectations, the expected constraint
 602 will be

$$-8.7 < \kappa_c < 10.6 \text{ (SM branching fractions).} \quad (1.73)$$

603 Rare exclusive decays of the Higgs boson to mesons in association with a pho-
 604 ton can be used to explore these couplings. For example, the $H \rightarrow J/\psi \gamma$ decay can
 605 probe the Higgs boson coupling to the charm quark [18]. This decay is the focus in
 606 the thesis, and will be discuss in the next section. Using Run1 results of the upper
 607 limit on $H \rightarrow J/\psi \gamma$, the bound at 95% CL is set at $\kappa_c < 220$.

608 In some extensions to the SM, modified $Hc\bar{c}$ couplings can arise [68]. For ex-
 609 ample, within the context of the effective field theory [69, 70, 71] the $Hc\bar{c}$ cou-
 610 pling is modified in the presence of dimension-six operator, leading to only an
 611 enhancement of the coupling with respect to the SM at the cutoff scale Λ , of or-
 612 der tens of TeV, and leaving no other signature of new physics at the LHC. In the
 613 two Higgs doublet model with minimal flavor violation [72, 73], the $Hc\bar{c}$ coupling
 614 can be significantly enhanced by breaking the flavor symmetry, while other cou-
 615 plings are not severely affected. The composite pseudo-Nambu-Goldstone boson

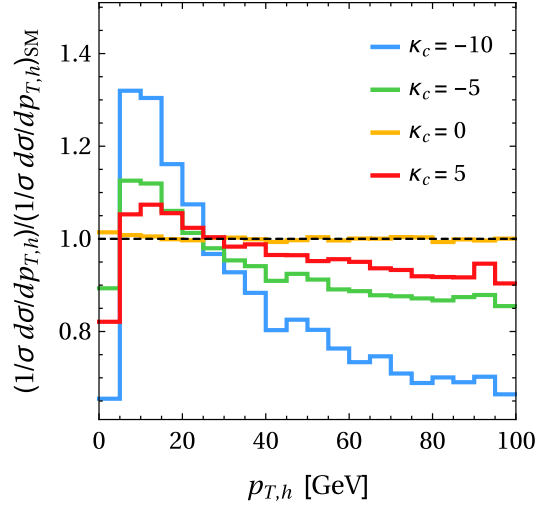


Figure 1-15: The normalized p_T^H spectrum of inclusive Higgs production at $\sqrt{s} = 8$ TeV with different values of κ_c [18].

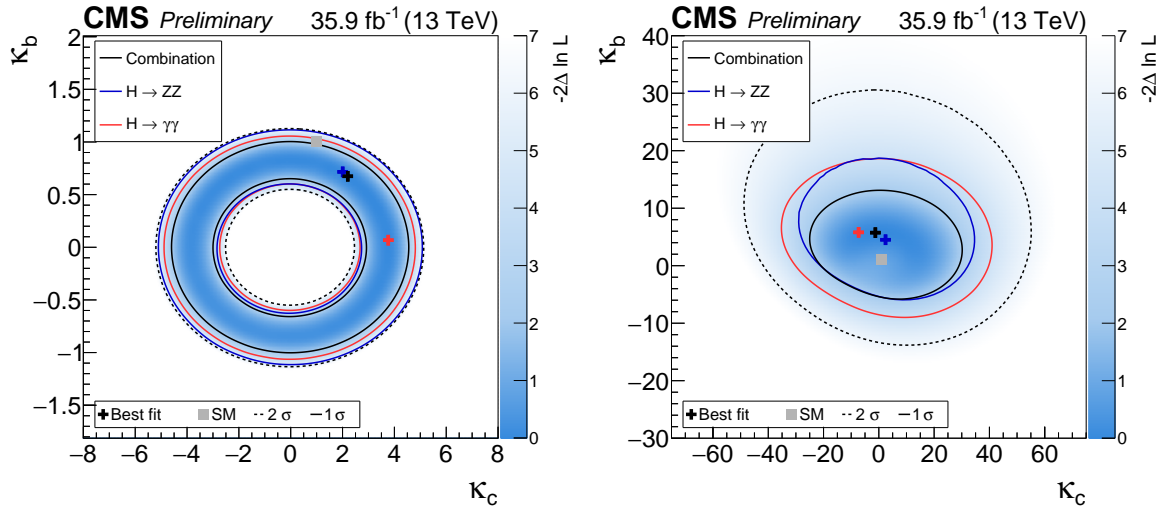


Figure 1-16: Simultaneous fit results for κ_b and κ_c [67].

616 model [74] parametrizes the coupling by the degree of compositeness and compo-
617 siteness scale, which can be experimentally constrained by the direct search for the
618 charm partner [75].

619 **1.2 The rare decays $Z/H \rightarrow J/\psi \gamma$**

620 **1.2.1 Overview**

621 The rare decay of $H \rightarrow J/\psi \gamma$ is one of the proposed ways to probe the Higgs-
 622 charm coupling. The corresponding decay of the Z boson, $Z \rightarrow J/\psi \gamma$, can be
 623 used as an experimental benchmark for the $H \rightarrow J/\psi \gamma$ search, given that the
 624 mass of the Z boson is not far from that of the Higgs boson, and to test various
 625 QCD factorization approaches that are being used in the estimation of branching
 626 fractions for hadronic radiative decays of bosons [76, 77, 78].

627 Both the Higgs and Z boson decays have contributions from direct and indirect
 628 processes. In the direct mechanism, Z and Higgs bosons couple to charm quarks,
 629 and charm quarks then hadronize to form J/ψ mesons. In the indirect mechanism,
 630 the Higgs and Z bosons decay through the quark and W boson loops to $\gamma\gamma^*$, and
 631 the γ^* then converts to a $c\bar{c}$ resonant state. The Feynman diagrams for these decay
 632 modes are shown in Fig. 1-17. The widths of the decays are expected to be

$$\begin{aligned}\Gamma_{H \rightarrow J/\psi \gamma} &= \frac{1}{8\pi} \frac{m_H - m_{J/\psi}}{m_H} |\mathcal{A}_{\text{direct}} + \mathcal{A}_{\text{indirect}}|^2 \\ &= \left[(11.71 \pm 0.17) - [(0.659^{+0.085}) - i(0.073^{+0.035})] \kappa_c \right] \times 10^{-10} \text{ GeV} \\ &= 1.221^{+0.042}_{-0.041} \times 10^{-8} \text{ GeV},\end{aligned}\tag{1.74}$$

633

$$\Gamma_{Z \rightarrow J/\psi \gamma} = \frac{m_Z^3}{96\pi m_{J/\psi}^2} |\mathcal{A}_{\text{direct}} + \mathcal{A}_{\text{indirect}}|^2 = 2.236^{+0.377}_{-0.344} \times 10^{-7} \text{ GeV},\tag{1.75}$$

634 where in Eq. 1.74 the equality and numerical results are taken from Ref. [18, 79],
 635 and those in Eq. 1.75 are from Ref. [80]. In these theoretical calculations, a frame-
 636 work of the nonrelativistic QCD (NRQCD) factorization [81] is used, where the
 637 nonperturbative effects are parametrized in terms of the quarkonium light-cone
 638 distribution amplitudes (LCDAs) [82, 83]. These computations will not be dis-
 639 cussed in detail here. With the total widths of both the Higgs $\Gamma_H = 4.20 \text{ MeV}$ and

640 Z boson $\Gamma_Z = 2.4952 \text{ GeV}$ and $\kappa_c = 1$ in the SM, the branching fractions of both
641 decays are then:

$$\mathcal{B}_{\text{SM}}(H \rightarrow J/\psi \gamma) = (3.0_{-0.2}^{+0.2}) \times 10^{-6}. \quad (1.76)$$

642

$$\mathcal{B}_{\text{SM}}(Z \rightarrow J/\psi \gamma) = (9.0_{-1.4}^{+1.5}) \times 10^{-8}, \quad (1.77)$$

643 The direct and indirect amplitudes interfere destructively in both decays. In the
644 Higgs decay, the contribution from the indirect process is larger. Only direct pro-
645 cess included in the calculation leads to a brancing fractions of 5.28×10^{-8} , while
646 only indirect diagrams included results in a brancing fractions of 3.25×10^{-6} . The
647 branching fraction of the Z decay, compared to the Higgs decay, is smaller by 1-2
648 orders of magnitude. This results from the suppression of the indirect amplitude,
649 which is less than 1% of the magnitude of direct amplitude, in the Z decay. One
650 qualitative explanation uses the Landau-Yang theorem [84], which states that the
651 Z boson does not decay to two on-shell photon. This requires that the indirect
652 amplitude tends to zero in the limit $m_{J/\psi} \rightarrow 0$.

653 With the branching fractions shown above, one can obtain

$$\begin{aligned} \sigma(pp \rightarrow H) \times \mathcal{B}_{\text{SM}}(H \rightarrow J/\psi \gamma \rightarrow \mu\mu\gamma) &= \\ 55 \text{ pb} \times 3.0 \times 10^{-6} \times 0.059 &= 9.8 \times 10^{-3} \text{ fb}, \end{aligned} \quad (1.78)$$

654

$$\begin{aligned} \sigma(pp \rightarrow Z) \times \mathcal{B}_{\text{SM}}(Z \rightarrow J/\psi \gamma \rightarrow \mu\mu\gamma) &= \\ 5.7 \times 10^4 \text{ pb} \times 9.0 \times 10^{-8} \times 0.059 &= 3.0 \times 10^{-1} \text{ fb}. \end{aligned} \quad (1.79)$$

655 where the cross-section of the Higgs boson are summed over the ggF, VBF, VH,
656 and ttH productions, and taken from Ref. [48]. The cross-section of the Z boson are
657 calculated using FEWZ 3.1.b2 program [85].

658 Deviations from the SM predictions for the couplings can affect the interference
659 terms and may result in changes in the branching fractions. For example, the shift
660 in the branching fraction for $H \rightarrow J/\psi \gamma$ can be more than 100% if the $Hc\bar{c}$ cou-
661 pling deviates from its SM value by more than a factor of 2, as shown in Fig. 1-18.
662 Measurements of the direct decay of $H \rightarrow c\bar{c}$ leave the overall signs of the cou-

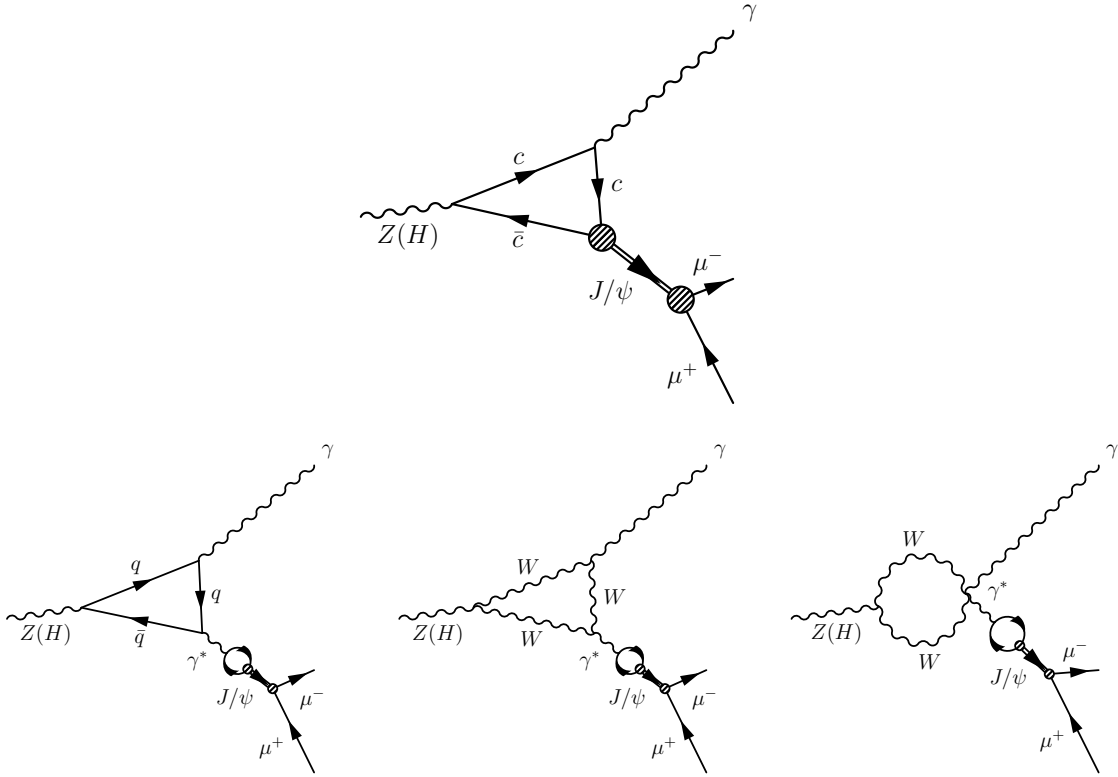


Figure 1-17: Feynman diagrams for $Z(H) \rightarrow J/\psi \gamma$ decay. The top diagram shows the direct process and the remaining diagrams show the indirect processes.

plings undetermined. This ambiguity can be resolved by the interference terms in
 $H \rightarrow J/\psi \gamma$, providing us with additional information about the Higgs properties.

1.2.2 Features of the decays

Due to the relatively heavy Z and Higgs boson, the J/ψ and γ from their decays will have high transverse momenta p_T and energy E_T (boosted). The high- E_T photon will be produced back-to-back to the J/ψ particle, and hence can be distinguished from backgrounds easily and be identified as an isolated photon. Since the J/ψ meson from Z (Higgs) boson decay is boosted, the p_T of the two muons from its decay are anti-correlated. Further, these two muons are very close to each other spatially. Therefore, dedicated strategies for trigger algorithms and both offline reconstruction are needed. The photon should be well separated from each muon.

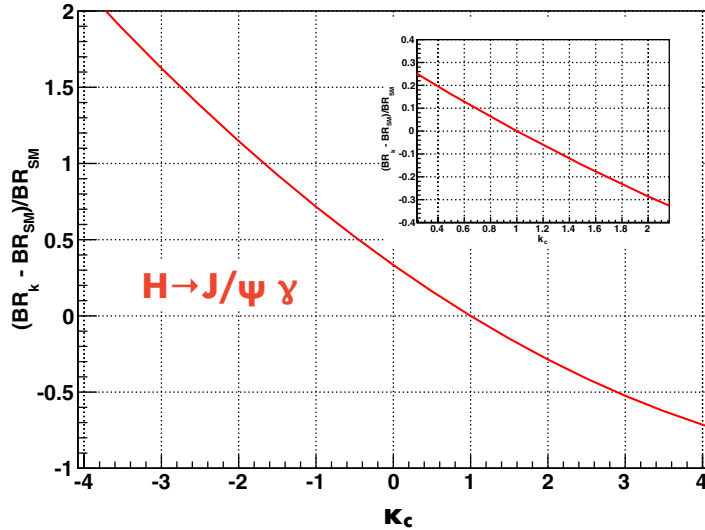


Figure 1-18: The relative deviations in the branching fraction for $H \rightarrow J/\psi \gamma$ as function of κ_c [18].

674 This event signature can be utilized to design kinematic requirements such as the
 675 angular separation ΔR^4 to reject backgrounds.

676 Fig. 1-19 shows the distributions of key variables at the generator level. All the
 677 distributions shown in the figure are normalized to unity. One can see that, the
 678 momenta of muons cover a wide range: the transverse momentum p_T of trailing
 679 muon⁵ can be less than 10 GeV, while that of leading muon can be greater than 40
 680 and 60 GeV in the Z and Higgs boson decay respectively. The photon can have
 681 high transverse energy. The muons and the photon distribute mostly in the central
 682 region. The high- E_T photon is back-to-back to the dimuon system, while the two
 683 muons are close to each other spatially.

684 1.2.3 Previous results from the ATLAS and CMS Collaborations

685 The $Z \rightarrow J/\psi \gamma$ decay was searched for by the ATLAS Collaboration using the
 686 data set collected at $\sqrt{s} = 8$ TeV [86]. An observed (expected) upper limit on the

⁴The coordinate system will be introduced in the next chapter.

⁵In the analysis, two muons will be selected in the final state. The one with higher p_T is referred to as leading muon, and the other one is then referred to as trailing or subleading muon.

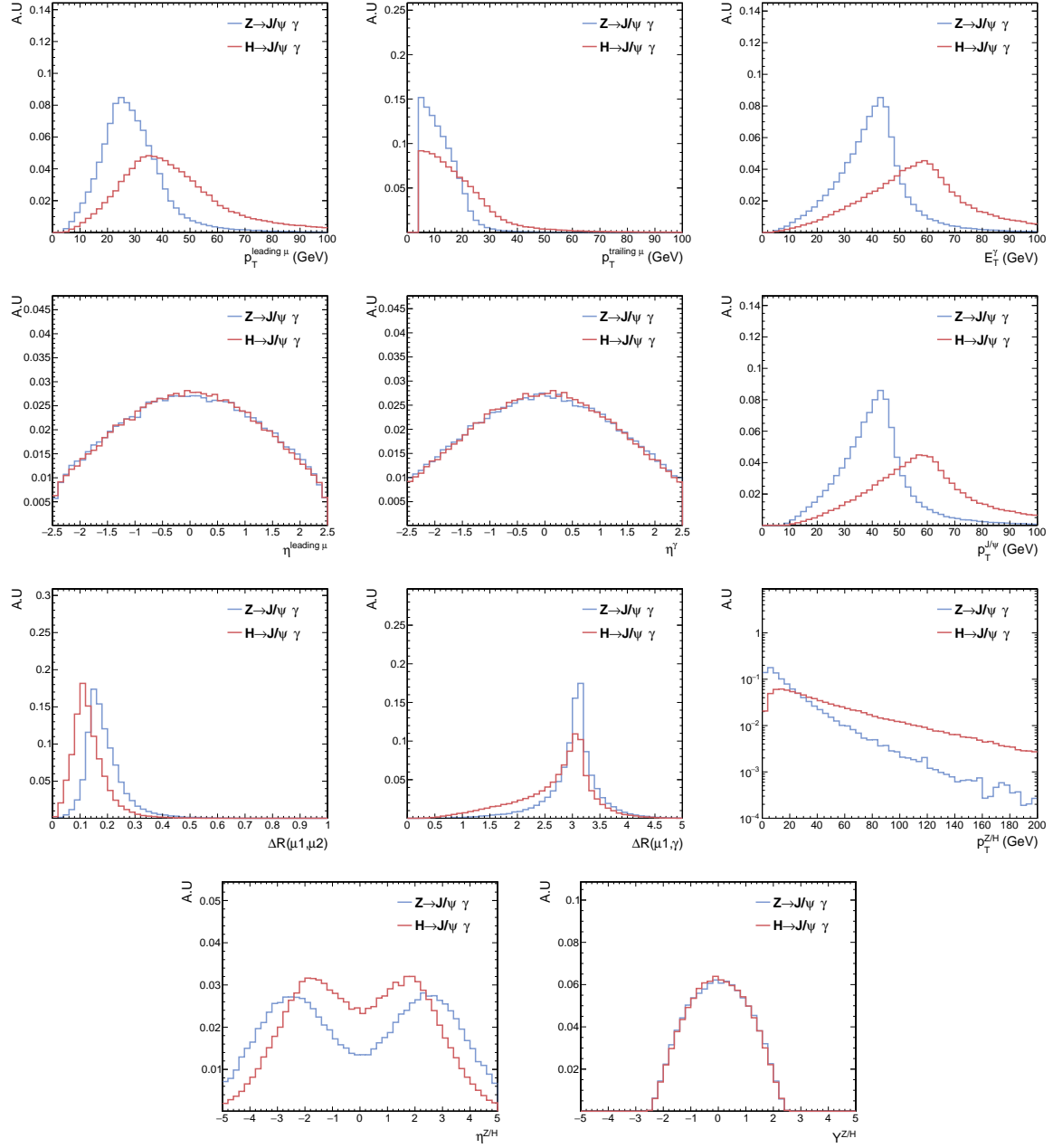


Figure 1-19: The distributions of key variables at generator level in both the Z and Higgs boson decays: p_T and E_T of the leading, trailing muon and the photon, pseudorapidity η of the leading muon and the photon, p_T of the J/ψ meson , angular separation ΔR between muons, ΔR between the leading muon and the photon, p_T of the Z and Higgs boson, η of the Z and Higgs boson, and the rapidity Y of the Z and Higgs boson

branching fraction of $2.6 (2.0^{+1.0}_{-0.6}) \times 10^{-6}$ was reported. Searches for the $H \rightarrow J/\psi \gamma$ decay have been performed by the ATLAS and CMS Collaborations using the data set collected at $\sqrt{s} = 8$ TeV respectively [86, 87]. Observed (expected) limits on the branching fraction were $1.5 (1.2^{+0.6}_{-0.3}) \times 10^{-3}$ from the ATLAS Collaboration and $1.5 (1.6^{+0.8}_{-0.8}) \times 10^{-3}$ from the CMS Collaborations. Fig. 1-20 shows the three-body invariant mass $m_{\mu\mu\gamma}$ and $p_T^{\mu\mu\gamma}$ distributions, along with the signal-plus-background fit to observed data collected at $\sqrt{s} = 8$ TeV from ATLAS results. Fig. 1-21 shows the non-resonant background fit to the $m_{\mu\mu\gamma}$ distributions observed in data collected at $\sqrt{s} = 8$ TeV with CMS search. Recently, ATLAS provides results with data collected in 2016 for both decays. An observed (expected) upper limit on the branching fraction of $Z \rightarrow J/\psi \gamma$ decay is set at $2.3 (1.1^{+0.5}_{-0.3}) \times 10^{-6}$, and of the $H \rightarrow J/\psi \gamma$ is at $3.5 (3.0^{+1.4}_{-0.8}) \times 10^{-4}$ [88]. Fig. 1-22 shows the recent results from ATLAS Collaboration.

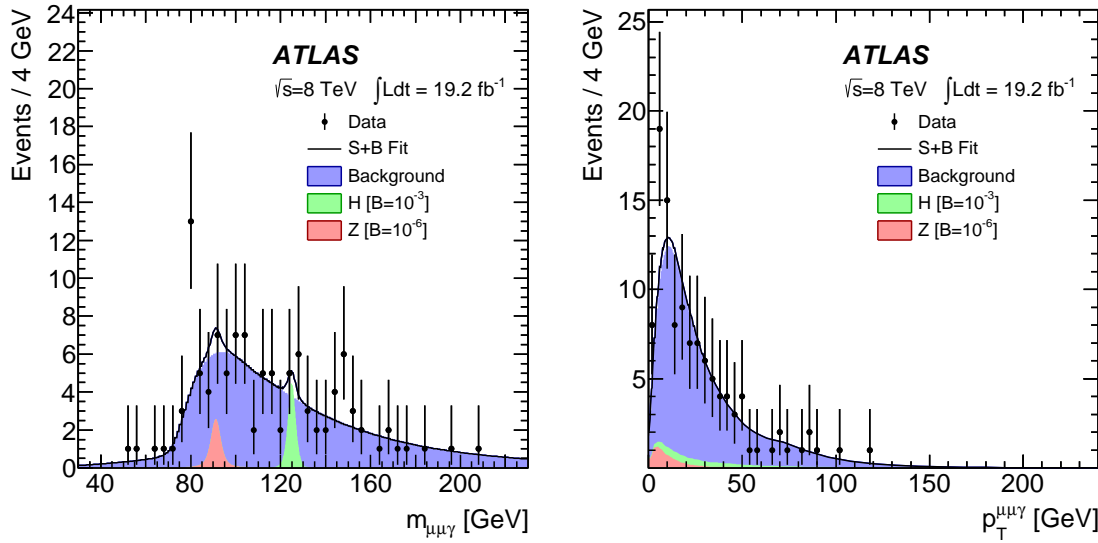


Figure 1-20: Previous result of Z (H) $\rightarrow J/\psi \gamma$ decay search from the ATLAS Collaboration. The three-body invariant mass $m_{\mu\mu\gamma}$ and $p_T^{\mu\mu\gamma}$ distributions, along with the results of signal-plus-background fit to observed data collected at $\sqrt{s} = 8$ TeV [86].

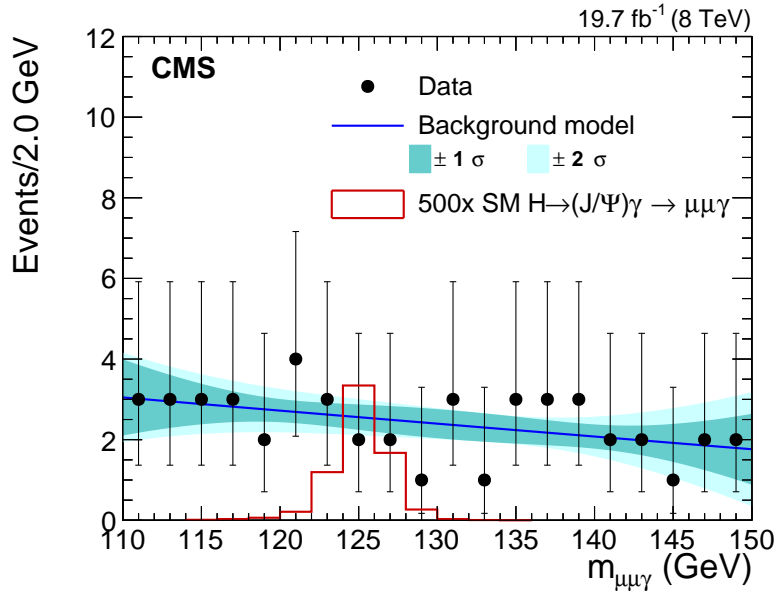


Figure 1-21: Previous result of $H \rightarrow J/\psi \gamma$ decay search from the CMS Collaboration. Non-resonant background fit to the $m_{\mu\mu\gamma}$ distributions observed in data collected at $\sqrt{s} = 8$ TeV [86].

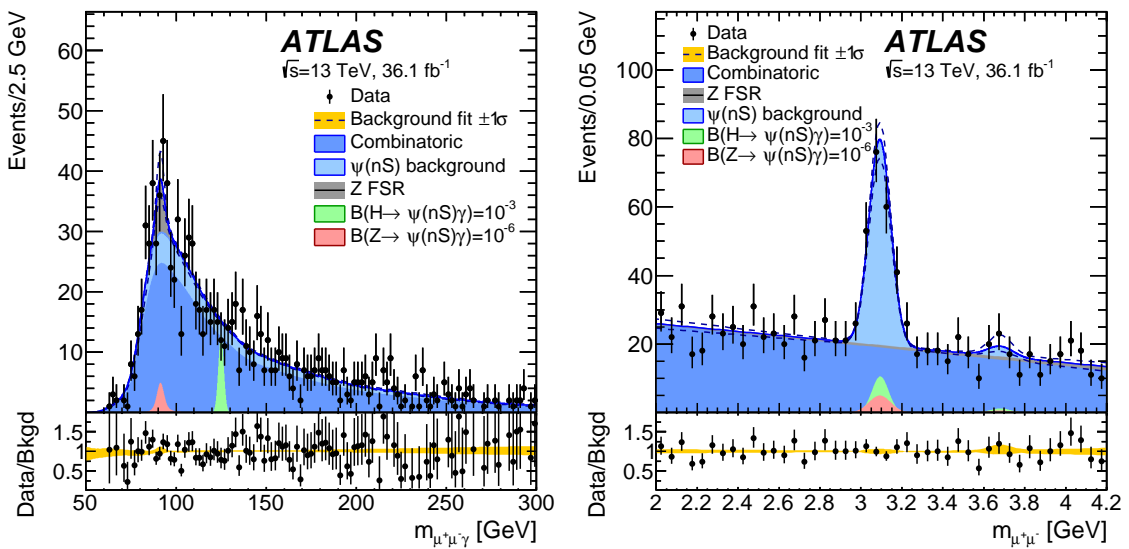


Figure 1-22: Result of Z (H) $\rightarrow J/\psi \gamma$ decay search from the ATLAS Collaboration with data collected at $\sqrt{s} = 13$ TeV in 2016 [88].

700 **Chapter 2**

701 **Experimental apparatus**

702 In this chapter, the overview of the Large Hadron Collider (LHC) and the Com-
703 pact Muon Solenoid (CMS) will be introduced. The object reconstruction will be
704 summarized in the last section, as it is closely related to the detectors.

705 **2.1 Large Hadron Collider**

706 The LHC is so far the largest particle accelerator that human have ever built, and
707 currently hosted by the Europe Organization of Nuclear Research (CERN). It pos-
708 sses a 26.7 km of ring and is placed more than 100 m deep beneath Geneva
709 and France. Such large circumference makes it able to provide high energy col-
710 lisions, and enables us to examine the validity of the SM and explore the physics
711 such as the existence of the Higgs boson, supersymmetry particles (SUSY), extra-
712 dimension, or even dark matter (DM). The ring consists of two individual and
713 parallel beam pipes, in which protons (or heavy-ions) circulate in opposite direc-
714 tions.

715 The protons are grouped together into 2808 bunches, and each bunch contains
716 1.15×10^{11} protons. The time interval between two bunches is 25 ns, corresponding
717 to a collision rate of 40 MHz. A series of machines then successively accelerate and
718 bring proton beams to higher energy. Each beam is accelerated up to an energy of
719 6.5 TeV when it finally arrives at the LHC beam line.

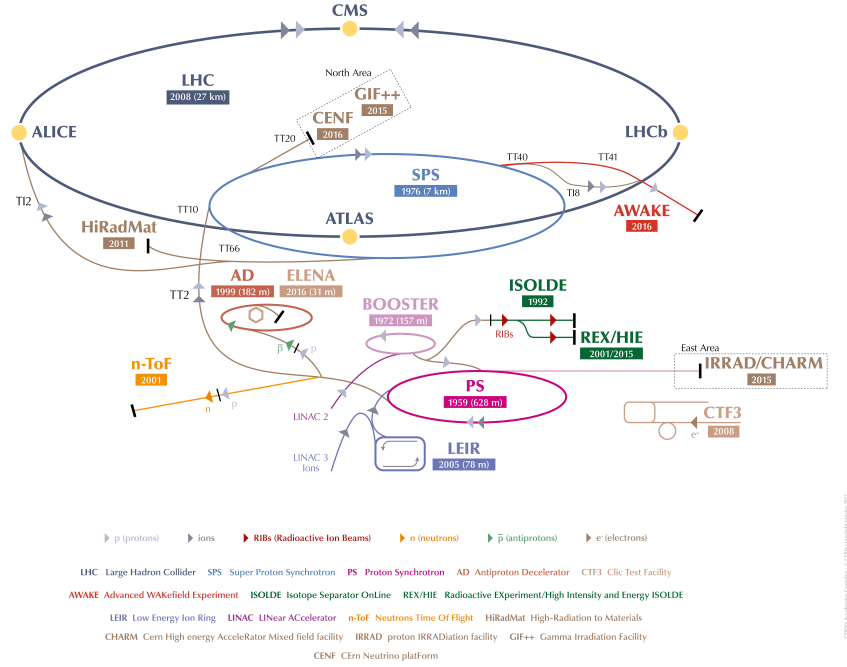


Figure 2-1: The CERN accelerator complex. The protons are accelerated from the LINAC2, PSB, PS, SPS, and finally to LHC [89].

720 Fig. 2-1 shows the whole system of the CERN complex [89].

721 An important quantity in the collider physics is the luminosity \mathcal{L} . The instant-
722 taneous luminosity is defined as:

$$\frac{dN}{dt} = \sigma_{\text{event}} \frac{d\mathcal{L}}{dt} \quad (2.1)$$

723 The $\frac{dN}{dt}$ is the event production rate, and σ_{event} is the interaction cross section. The
724 integrated luminosity \mathcal{L}_{Tot} is the integral of the instantaneous luminosity over a
725 period of time. The \mathcal{L}_{Tot} is a measure of the amount of data. Fig. 2-2 shows the
726 integrated luminosity that CMS recorded in each data-taking year [90].

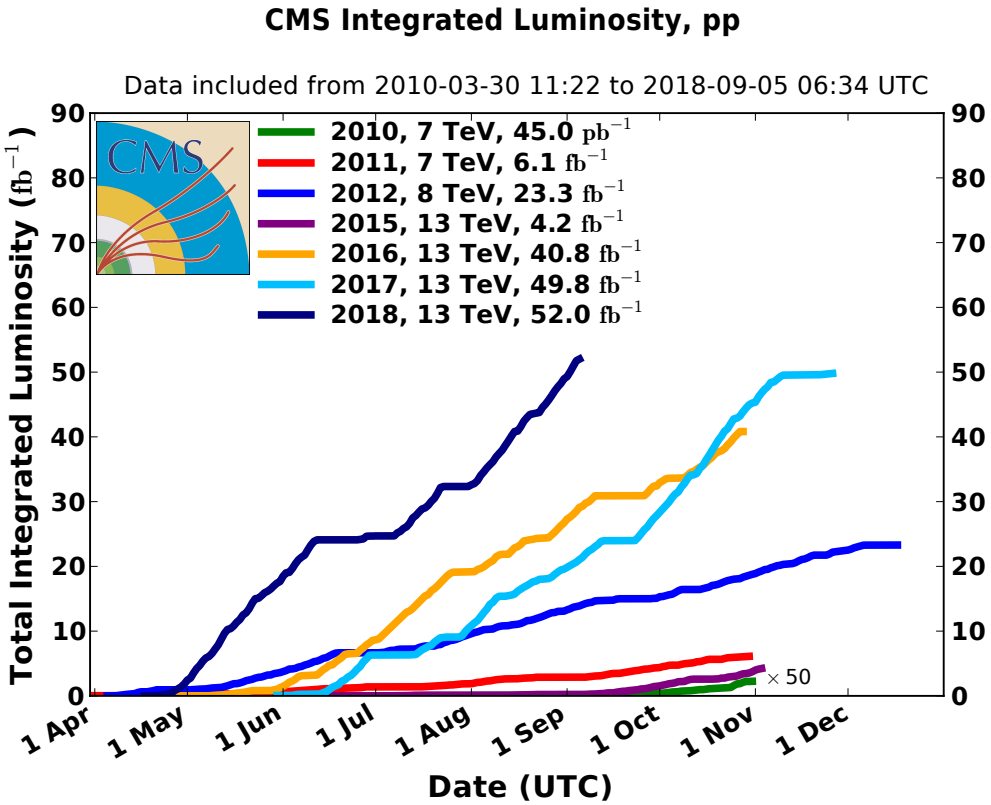


Figure 2-2: Cumulative luminosity versus day delivered to CMS during stable beams for pp collisions at nominal center-of-mass energy. This is shown for data-taking in 2010 (green), 2011 (red), 2012 (blue), 2015 (purple), 2016 (orange), 2017 (light blue), and 2018 (deep blue) [90].

727 2.2 Compact Muon Solenoid

728 Compact Muon Solenoid is one of the general purpose detectors located at the
 729 LHC ring. The central feature of the CMS apparatus is a superconducting solenoid
 730 of 13 m in length and 6 m in internal diameter, providing an axial magnetic field
 731 of 3.8 T. Within the solenoid volume are a silicon pixel and strip tracker, a lead
 732 tungstate crystal electromagnetic calorimeter (ECAL), and a brass and scintillator
 733 hadron calorimeter (HCAL), each composed of a barrel and two endcap sections.
 734 Forward calorimeters extend the pseudorapidity (η) coverage provided by the bar-
 735 rel and endcap detectors. Muons are detected in gas-ionization chambers embed-
 736 ded in the steel flux-return yoke outside the solenoid.

737 The adopted coordinate system, as shown in Fig. 2-3 has the origin at the nom-
 738 inal collision point inside CMS detector, where the y-axis pointing vertically up-
 739 ward, the x-axis pointing radially inward toward the center of the LHC, and the
 740 z-axis pointing along the beam direction. The azimuthal angle ϕ is measured from
 741 the x-axis in the x-y plane, while the polar angle θ is measured from the z-axis. Ra-
 742 pidity, Y , is defined as $Y \equiv \frac{1}{2} \ln \left(\frac{E+p_z c}{E-p_z c} \right)$, where E is the energy of the particle and
 743 p_z is the momentum in the z direction. This Lorentz invariant quantity indicates
 744 the angle between the x-y plane and the direction of the measured particle. For
 745 the highly relativistic particles, the other quantity called pseudorapidity, defined
 746 as $\eta = -\ln \tan(\theta/2)$, is used, where θ is the angle between the particle trajectory
 747 and the z-axis (beam pipe).

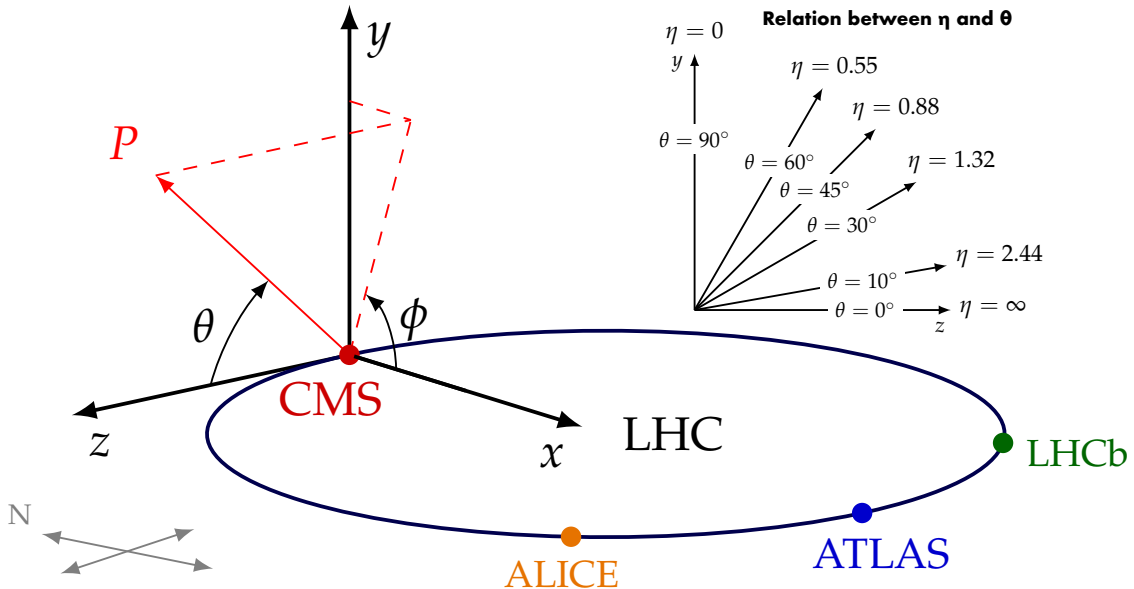


Figure 2-3: The adopted coordinate system in CMS.

748 The momentum and energy transverse to the beam direction, denoted by p_T
 749 and E_T , respectively, are computed from the x and y components.

750 Fig. 2-4 shows a global view of the CMS detector [91]. Brief description of each
 751 sub-detector is summarized as follows.

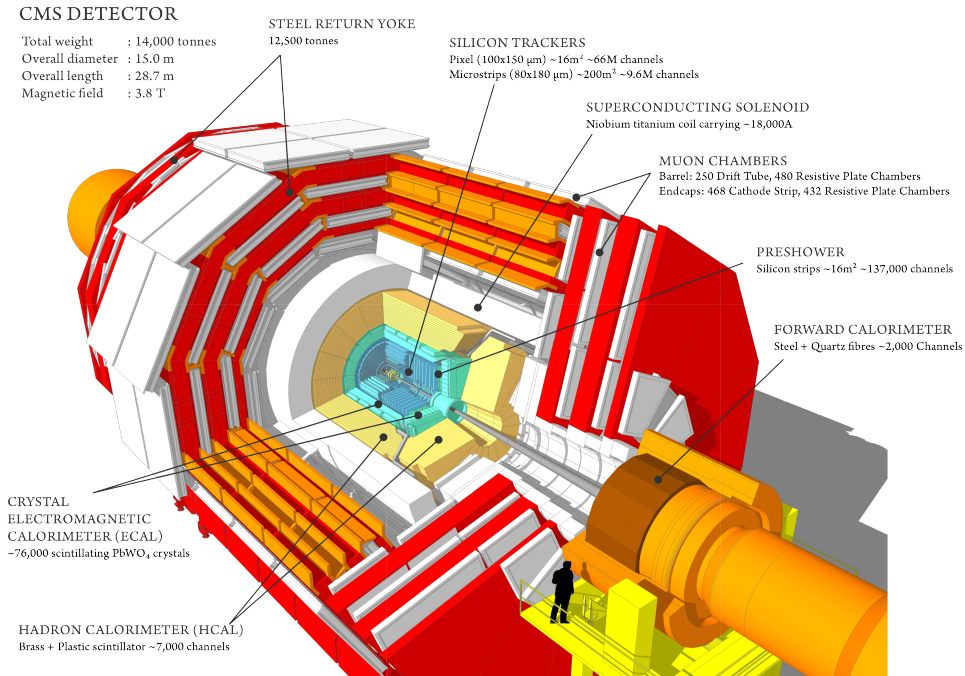


Figure 2-4: A cutaway view of the CMS detector [91].

752 Superconduction magnet

753 The superconducting solenoid magnet, formed by a cylindrical coil of supercon-
754 ducting fibers, was originally designed to provide a magnetic field of 4 Tesla (T),
755 while in the actual operation it produces a 3.8 T of field. Such large bending power
756 enables us to measure the momentum of high energy charged particles precisely.
757 The magnetic field is confined to the volume of the detector. This is done by the
758 steel yoke, consisting five layers for barrel part and three layers for each endcap.

759 Silicon tracker

760 The CMS tracker is composed of two systems: a pixel detector (for a total of 1440
761 silicon pixel modules) with three barrel layers, and a silicon strip tracker (for a
762 total of 15148 silicon strip modules) with ten barrel detection layers, four layers of
763 tracker inner barrel (TIB) and six layers of tracker outer barrel (TOB), extending
764 outwards. Each system is completed by endcaps, which consist of two disks in the

765 pixel detector, three tracker inner disks (TID) and nine disks of tracker endcaps
 766 (TEC) in the strip tracker on each side of the barrel. The acceptance of the whole
 767 tracker system extends up to a $|\eta| < 2.5$. Fig. 2-5 shows the schematic view of
 768 the silicon tracker in the r-z plane. The upper plot is the cross section through the
 769 tracker, and the lower one is one quarter of the tracker, where the paths of the laser
 770 rays (R), the alignment tubes (A) and the beam splitters (B) of the laser alignment
 771 system are illustrated.

772 For non-isolated particles with transverse momentum, p_T , between 1 and 10 GeV
 773 and $|\eta| < 1.4$, the track resolutions are typically 1.5% in p_T and 25–90 (45–150) μm
 774 in the transverse (longitudinal) impact parameter [92].

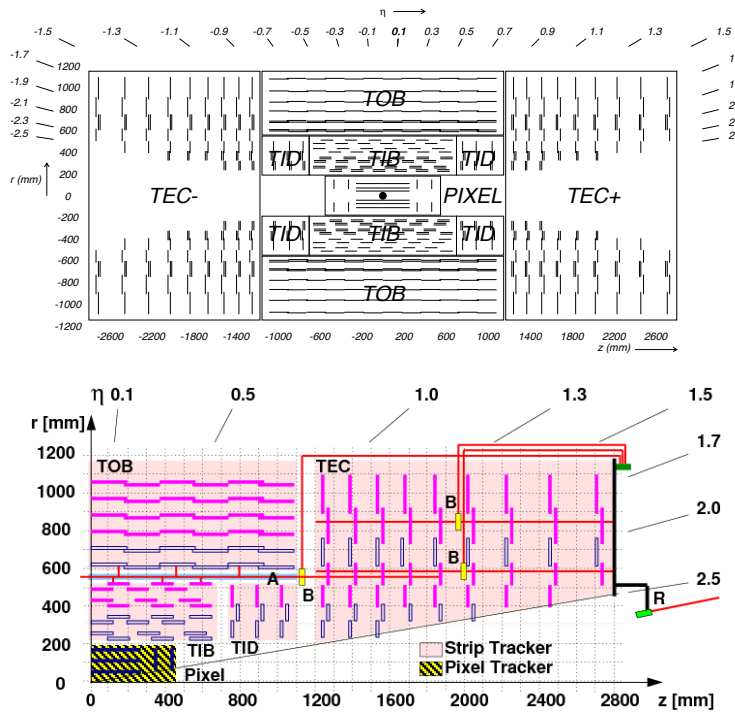


Figure 2-5: Schematic view of one quarter of the silicon tracker in the r-z plane [93].

775 Electromagnetic calorimeter

776 The electromagnetic calorimeter (ECAL) is a homogeneous calorimeter made of
 777 61200 lead tungstate (PbWO_4) crystals in the barrel part ($0 < |\eta| < 1.48$) and 7324

778 crystals in each of endcaps ($1.48 < |\eta| < 3.0$). The high density (8.28 g/cm^3) and
 779 short radiation length X_0^{-1} (0.89 cm) of the crystal result in a compact calorimeter
 780 with fast response, fine granularity, and strong resistance to the radiation. A sam-
 781 pling calorimeter, preshower detector (ES), is placed in front of the endcap crystals
 782 and covers the range of $1.65 < |\eta| < 2.6$. It consists of two planes of silicon sen-
 783 sors interleaved with a total of $3X_0$ of lead. The main task of this detector is to
 784 help on distinguishing between single high-energy photons and the close pairs of
 785 low-energy photons, usually from the decay of neutral pion. The ES also improves
 786 the ability of identifying electrons against minimum ionizing particles and the po-
 787 sition determination of electrons and photons . Fig. 2-6 shows layout of the CMS
 ECAL.

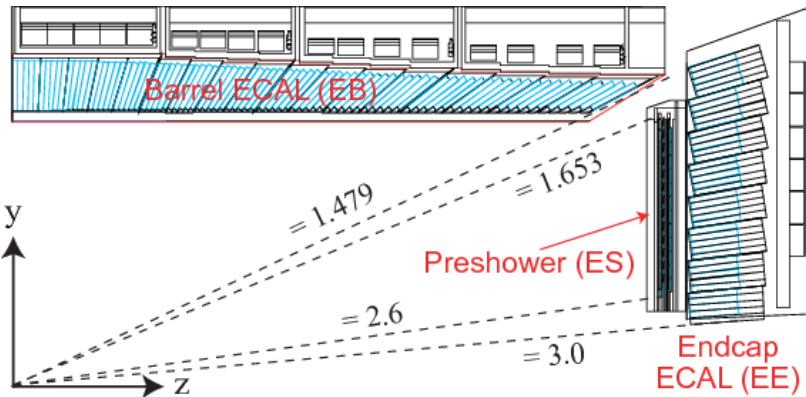


Figure 2-6: Layout of the ECAL [94].

788

789 Hadron calorimeter

790 The hadron calorimeters (HCAL), a sampling calorimeter, measures the energy
 791 of hadron jets and provides indirect measurement of missing transverse energy,
 792 which can be neutrinos or exotic particles that do not interact with matters. Fig. 2-
 793 7 shows the longitudinal view of the CMS detector with the dashed lines repre-
 794 senting fixed η values. The HCAL consists four parts: the HCAL barrel (HB), the

¹One radiation length of a given material is defined as the distance after which the electron loose $1/e$ of its original energy.

795 HCAL endcap (HE), the HCAL outer (HO), and the HCAL forward (HF). The HB,
 796 covering the range of $|\eta| < 1.3$, is placed radially between the outer extent of the
 797 ECAL and the inner extent of the magnet coil. The HO sits outside the solenoid
 798 complementing the barrel part, and ensure the leakage of the energy not detected
 799 by HB to be minimal. The HE covers the range of $1.3 < |\eta| < 3.0$, a region con-
 800 taining about 34% of the particles produced in the final state. The HF is place at
 801 the range of $|\eta| > 3.0$, where much higher energy will be deposited compared to
 other sub-detectors.

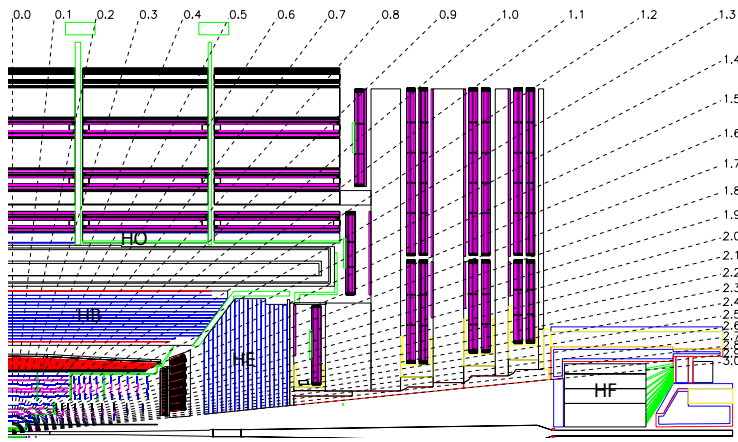


Figure 2-7: Longitudinal view of the CMS detector showing the locations of the hadron barrel (HB), endcap (HE), outer (HO) and forward (HF) calorimeters [93].

802

803 Muon system

804 The muon system is located outside the solenoid and covers the range $|\eta| < 2.4$.
 805 It is composed of three types of gaseous detectors, drift tubes (DTs), cathode strip
 806 chambers (CSCs), and resistive plate chambers (RPCs), sandwiched among the
 807 layers of the steel yoke. The DTs are segmented into drift cells; the position of the
 808 muon is determined by measuring the drift time to an anode wire of a cell with a
 809 shaped electric field. The CSCs operate as standard multi-wire proportional coun-
 810 ters but with a finely segmented cathode strip readout, which yields an accurate

measurement of the position of the bending plane ($R - \phi$) coordinate at which the muon crosses the gas volume. The DT and CSC chambers are located in the regions $|\eta| < 1.2$ and $0.9 < |\eta| < 2.4$, respectively, and are complemented by RPCs in the range $|\eta| < 1.9$. Three regions are defined and referred to as the barrel ($|\eta| < 0.9$), overlap ($0.9 < |\eta| < 1.2$), and endcap ($1.2 < |\eta| < 2.4$) regions [95]. Fig. 2-8 shows the arrangement of the muon system.

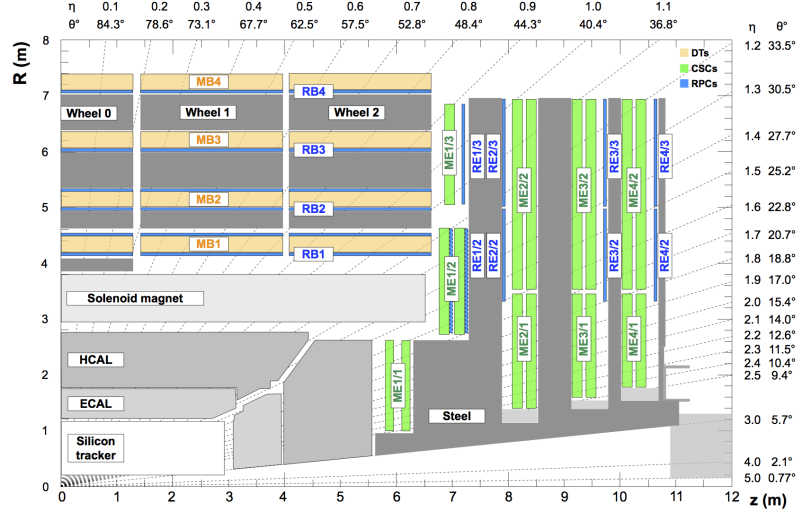


Figure 2-8: An R-z cross section of the muon station. The drift tube stations (DTs) are labeled MB ("Muon Barrel") and the cathode strip chambers (CSCs) are labeled ME ("Muon Endcap"). Resistive plate chambers (RPCs) are mounted in both the barrel and endcaps of CMS, where they are labeled RB and RE, respectively [95].

816

817 Trigger and data acquisition system

The LHC provides pp and heavy-ion collisions at high interaction rate. This corresponds to an enormous amount of data that are currently not able to be completely stored. Furthermore, most of these interactions would be low-energy glancing collisions, rather than energetic and head-on interactions where processes of interest may occur. The trigger system is designed to reduce the rate and to start the physics event selection process. Fig. 2-9 shows the schematic diagram of the trigger architecture and data acquisition system. The level-1 trigger (L1) consists of custom-designed and programmable electronics. Information from muon system

826 (including DTs, CSCs, and RPCs), ECAL, HCAL, and HF is used to reconstruct
 827 candidate trigger objects, and these quantities are combined and forwarded to the
 828 Global Trigger (GT), which calculates the trigger decision and sends out the signal
 829 if it is "L1 Accept (L1S)". This step reduces the data rate from the 40 MHz of the
 830 LHC bunch crossing rate down to a maximum of 100 kHz. In case of a positive
 831 L1 decision all data for the corresponding bunch crossing time is read out from
 832 the CMS detector and transferred to the HLT, which consists of a software system
 833 implemented in a filter farm. The high level trigger algorithm (HLT) performs a
 834 full reconstruction of events using a faster version of offline software and writes
 data out to permanent storage at a typical rate of several hundred Hz.

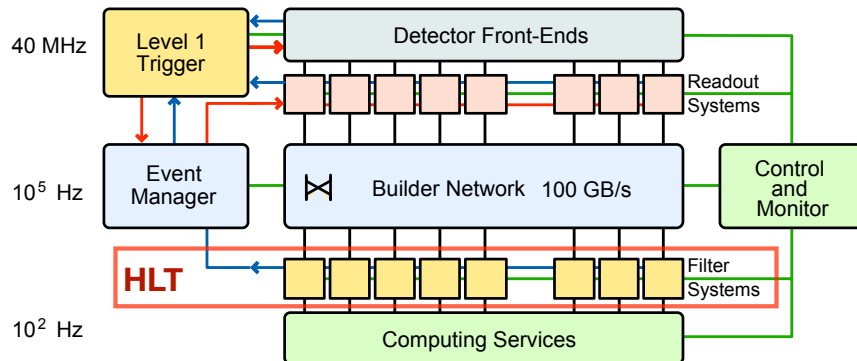


Figure 2-9: A schematic diagram of the trigger system [93].

835

836 2.3 Object reconstruction

837 2.3.1 Particle-Flow algorithm

838 The core concept of this algorithm is to optimally correlate tracks or clusters from
 839 all sub-detectors and combines the information to reconstruct final state particles.
 840 In order to have PF algorithm as efficient as possible, the magnetic field should be
 841 strong enough to maximize the separation between charged and neutral particles,
 842 and the detector should have fine spatial granularity layers that can distinguish

843 merged particles, especially those in jets. The CMS meets all of these advantages
844 to use PF reconstruction as a global event description.

845 The ECAL energy clusters without being associated to extrapolated tracks from
846 tracker are reconstructed as photons. Electrons are reconstructed by tracks in the
847 tracker system with associated energy deposits in the ECAL. The bremsstrahlung
848 emission and energy losses when traveling through tracker materials are properly
849 accounted for. Muons tracks can be reconstructed in tracker, in muon system, or
850 the combination of the two. Charged hadrons are reconstructed by the tracks not
851 identified as electrons or muons with energy cluster in HCAL. The energy clusters
852 that correspond to excesses of energy with respect to charged hadrons and not
853 linked to charged particle trajectories are reconstructed as neutral hadrons.

854 In this analysis, photon and muons are selected as final states particles. Hence,
855 their reconstructions are described in detail in the following paragraphs.

856 Photon reconstruction

857 Photons are reconstructed from energy deposits in the ECAL. The algorithms,
858 without any hypothesis as to whether the particle from the interaction point is
859 a photon or an electron, identify the energy clusters and constrains them to the ex-
860 pected sizes and shapes, based on the study of simulation. The measurements of
861 photon trigger, reconstruction, and identification efficiencies and energy scale and
862 resolution can therefore utilize the electrons from $Z \rightarrow e^+e^-$ events with a well
863 defined invariant mass.

864 The clustering algorithms are used to sum over all energy deposits in crystals
865 in the same electromagnetic shower. A basic cluster (BC) is chosen to be the lo-
866 cal maximum among the energy deposits. Several BCs are combined to construct
867 a supercluster (SC). The radiated energies, such as the conversions of photons or
868 bremsstrahlung from electrons, are corrected and recovered for their correspond-
869 ing SC. The energy of the photon is determined by summing the amplitude in
870 channels A_i over the crystals i in the supercluster where the photon leaves energy,

871 corrected by the intercalibration c_i and light monitoring $S_i(t)$ constants. The pro-
872 cedure can be summarized in a formula,

$$E_{fl} = \left[\sum_i \left(S_i(t) \times c_i \times A_i \right) \times G(\eta) + E_{ES} \right] \times F_{fl} \quad (2.2)$$

873 where $G(\eta)$ is the ADC to GeV factor.

874 Independent methods are used to calculate the intercalibration constants (ICs),
875 and the combined factor is obtained from the mean of the individual IC at a fixed
876 value of η , weighted by their respective precisions. A light monitoring system,
877 consisting of a system of lasers that inject light to crystals, is used to monitor the
878 time dependence of response in the ECAL resulting from the decreases in crystal
879 transparency in radiation exposure. The difference between input and read laser
880 amplitudes are then used to calculate correction factors $S_i(t)$. For photon in the re-
881 gion $1.65 < |\eta| < 2.6$ the energy deposits in the preshower E_{ES} are also accounted
882 for. The cluster corrections F_{fl} is applied to take the variation of shower contain-
883 ment in the clustered crystals and the shower losses of photons that convert before
884 reaching the calorimeter into account. The correction factors are computed with
885 a multivariate regression technique that estimates the energy of the photon and
886 its uncertainty simultaneously. The resolution of photon energy is optimized after
887 applying the factors.

888 The ECAL energy resolution was measured in beam tests, and found to be:

$$\frac{\sigma_E}{E} = \frac{2.8\%}{\sqrt{E \text{ (GeV)}}} \oplus \frac{12\%}{E \text{ (GeV)}} \oplus 0.3\%. \quad (2.3)$$

889 The first contribution is the stochastic term, which represents the event to event
890 fluctuations in the lateral shower containment. The second term comes from the
891 electronic noise. The last one is the constant term, characterizing the resolution at
892 high energy region.

893 The energy scale and resolution is further measured and calibrated using a high
894 purity $Z \rightarrow e^+ e^-$ samples with 2% of background contamination, estimated from

895 simulation. An unbinned maximum likelihood fit to the invariant mass distribu-
 896 tion is performed. A Breit-Wigner distribution convolved with a Crystal Ball (CB)
 897 function [?] is used.

$$CB(m - \Delta m) = \begin{cases} e^{-\frac{1}{2}(\frac{m-\Delta m}{\sigma_{CB}})^2}, & \frac{m-\Delta m}{\sigma_{CB}} > \alpha \\ (\frac{\gamma}{\alpha})^\gamma \cdot e^{-\frac{\alpha^2}{2}} \cdot \left(\frac{\gamma}{\alpha} - \alpha - \frac{m-\Delta m}{\sigma_{CB}} \right)^{-\gamma}, & \frac{m-\Delta m}{\sigma_{CB}} < \alpha \end{cases} \quad (2.4)$$

898 where the parameter Δm quantifies the displacement of the peak with respect to
 899 the nominal Z boson mass; σ_{CB} is the width of the Gaussian component of the
 900 CB function and serves as a measure of the energy resolution; the parameters α and
 901 γ describe the tail part of CB, accounting for electrons of which energy is not fully
 902 retained after the clustering algorithms. In this step, the ADC to GeV factor $G(\eta)$
 903 is also adjusted and determined such that the peak value from the fit to $Z \rightarrow e^+e^-$
 904 distribution agrees with that of the simulation, independently for the barrel and
 905 endcap. There are still unknown effects that make the resolution of $Z \rightarrow e^+e^-$ dis-
 906 tribution in data worse than that in simulation. These residual discrepancies are
 907 corrected by adding a Gaussian smearing, where the parameters of smearing func-
 908 tion are determined by a comparison between the lineshapes of $Z \rightarrow e^+e^-$ in data
 909 and simulation. As a result, the corrections to the energy scale vary in time, $|\eta|$
 910 and R_9 variable, which is defined as the energy sum of the 3×3 crystals centered
 911 on the most energetic crystal in the candidate electromagnetic cluster divided by
 912 the energy of the candidate. The amount of smearing required changes from about
 913 0.1% to about 2.7%, depending on the same categories as the energy scale correc-
 914 tions. The comparison of the dielectron invariant mass distributions in data and
 915 simulation after energy smearing are shown in Fig. 2-10.

916 In the barrel section of the ECAL, an energy resolution of about 1% is achieved
 917 for unconverted or late-converting photons in the tens of GeV energy range. The
 918 remaining barrel photons have a resolution of about 1.3% up to a pseudorapidity
 919 of $|\eta| = 1$, rising to about 2.5% at $|\eta| = 1.4$. In the endcaps, the resolution of
 920 unconverted or late-converting photons is about 2.5%, while the remaining endcap

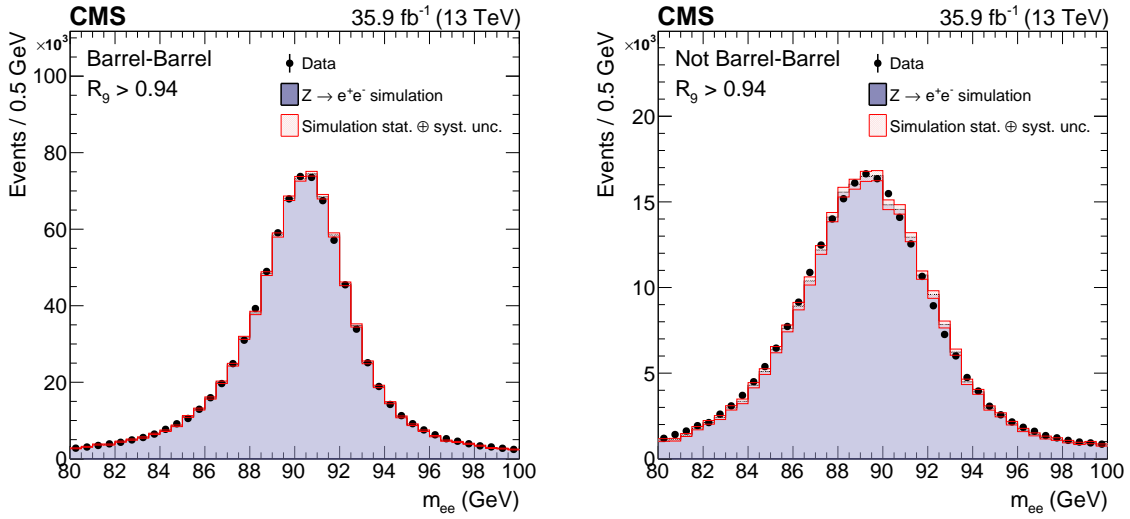


Figure 2-10: The comparison of the dielectron invariant mass distributions in data and simulation after energy smearing [43].

photons have a resolution between 3 and 4% [96].

Muon reconstruction

The muon reconstruction starts with hits in DTs, CSCs and RPCs. Those hits are combined to form segments. This step is called local reconstruction. Three collections of muons reconstructed by different methods are described as follows:

- **Standalone Muon reconstruction.** The segments are used to generate the seeds including the information of positions, directions, and estimated muon p_T . The segments and hits from DTs, CSCs and RPCs with the seeds are then fitted by the Kalman-filter technique [97]. The resulting objects are referred to as standalone muon.
- **Global Muon reconstruction.** Each standalone muon track is matched 'outside-in' to a tracker track (also referred to as inner track or silicon track). This global muon track is then fitted by combining the hits from both tracker and standalone tracks using Kalman-filter technique.
- **Tracker Muon reconstruction.** Tracker tracks with $p_T > 0.5 \text{ GeV}$ and total

momentum $p > 2 \text{ GeV}$ are matched ‘inside-out’ to the muon system, with bending effect from magnetic field, multiple scattering and expected energy losses while traveling through the detector materials taking into account. The extrapolated track will be considered as tracker muon if it matches to at least one muon segment, formed by hits within each DT and CSC.

In general, tracker muon reconstruction is more efficient than the global muon reconstruction at low momenta $p \leq 5 \text{ GeV}$, as it merely requires a single muon segment in the muon system. The downside is that the hadron shower with high energy may “punch through” the calorimeter and reach the innermost muon station, which is then misidentified as a tracker muon. As for the global muon reconstruction, high efficiency is maintained for muons with higher p_T , which can traverse through more than one muon station. As a result, around 99% of muons within the acceptance of the muon system can be well reconstructed either as global muon or tracker muon, and usually as both. For those only reconstructed as standalone muon, they are usually not used in physics analyses as they have worse momentum resolution and are more probable from cosmic-ray.

The ensemble of reconstructed muons (abbreviated as reco muon) is used as ingredient by the PF event reconstruction. In the PF algorithm, some of identification requirements together with the measurement of energy in the calorimeter are optimized to identify muons with high efficiency and low fake rate, especially those in jets as fake or missed reconstructed (identified) muons can bias measurements of jets and missing transverse energy E_T^{miss} . Consequently, this selection is able to retain not only isolated muons but also non-isolated muons, and those from decay products of hadron that typically treated as background.

Three sets of requirements are imposed to label reco muons as “isolated”, “pf-tight”, and “pf-loose”, and are grouped as particle-flow muons. Reco muons are considered to be isolated if the sum of the p_T of the tracks and of the transverse energy of the calorimeter hits calculated in a cone of size $\Delta R = 0.3$ centered on the muon is less than 10% of the muon p_T . The pf-tight and pf-loose selections, tuned to identify muons in jets, are applied to the remaining reco muons. The pf-tight

966 criteria requires the muon track to have a certain number of hits with compatibility
 967 with the muon segment and the energy deposited in calorimeter, defined by a
 968 template-based simulation. In the pf-loose selection the required number of hits
 969 are relaxed and the compatibility requirements are simply replaced to a matching
 970 of the track to hits in the muon stations.

971 Matching muons to tracks measured in the silicon tracker results in a relative
 972 transverse momentum resolution, for muons with p_T up to 100 GeV, of 1% in the
 973 barrel ($|\eta| < 0.9$) and 3% in the endcaps ($|\eta| > 0.9$). The p_T resolution in the barrel
 974 is better than 7% for muons with p_T up to 1 TeV [95]. The improvement compared
 975 to the 2010 results [98] is primarily due to the improvement to the tracker align-
 976 ment [99].

977 2.3.2 Pile-up & Primary vertex

978 The high instantaneous luminosity of the LHC results in multiple proton-proton
 979 interactions per bunch crossing, which is often referred to as event pile-up. In
 980 13 TeV collisions in 2016 data-taking period, there was on average 27 interactions
 981 per bunch crossing, as shown in Fig. 2-11 [90].

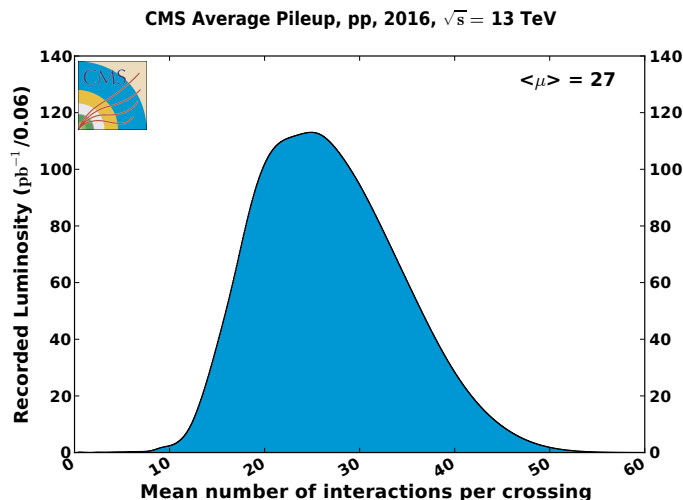


Figure 2-11: Mean number of interactions per bunch crossing for the 2016 pp run
 at 13 TeV [90].

982 The reconstructed vertex with the largest value of summed physics-object p_T^2

is taken to be the primary pp interaction vertex. The physics objects are the jets, clustered using the jet finding algorithm [100, 101] with the tracks assigned to the vertex as inputs, and the associated missing transverse momentum, taken as the negative vector sum of the p_T of those jets. The simulated $t\bar{t}$ events (inclusive decays) are used to validate the performance of the vertexing algorithm. Consequently, a resolution, defined as the difference between the position of the reconstructed vertex and the true vertex along the z direction, better than 1 mm can be achieved, and a harder p_T threshold ($p_{T,\min}$) for a track to be taken into account does not result in a significantly degradation of the resolution. The efficiency of reconstructing the primary vertex within 5 mm of the true vertex is $\sim 97\%$. Restricting it to be within 1 mm of the generated vertex, the efficiency is about 90% for $p_{T,\min} = 2 \text{ GeV}$, and remains at $\sim 86\%$ with $p_{T,\min} = 5 \text{ GeV}$ [102].

995 **Chapter 3**

996 **Analysis procedures**

997 **3.1 Data and simulated samples**

998 **3.1.1 Data sample**

999 The MuonEG February re-reco dataset collected in 2016 at $\sqrt{s} = 13$ TeV, corre-
1000 sponding to a total integrated luminosity of 35.9 fb^{-1} , is used. The data for each
1001 run period is summarized in Table 3.1. The official Golden JSON file is used to se-
1002 lect the luminosity sections recorded when all sub-detectors running under good
condition.

Dataset Name	Luminosity(fb^{-1})
/MuonEG/Run2016B-03Feb2017_ver2-v2/MINIAOD	5.8
/MuonEG/Run2016C-03Feb2017-v1/MINIAOD	2.6
/MuonEG/Run2016D-03Feb2017-v1/MINIAOD	4.2
/MuonEG/Run2016E-03Feb2017-v1/MINIAOD	4.0
/MuonEG/Run2016F-03Feb2017-v1/MINIAOD	2.7
/MuonEG/Run2016F-03Feb2017-v1/MINIAOD	0.4
/MuonEG/Run2016G-03Feb2017-v1/MINIAOD	7.5
/MuonEG/Run2016H-03Feb2017_ver2-v1/MINIAOD	8.4
/MuonEG/Run2016H-03Feb2017_ver3-v1/MINIAOD	0.2

Table 3.1: Summary of data sample used in the analysis.

1004 **3.1.2 Simulated samples**

1005 **Signal samples**

1006 The $H \rightarrow J/\psi \gamma \rightarrow \mu\mu\gamma$ sample, with $m_H = 125$ GeV, is produced with POWHEG
 1007 v2.0 [103, 104] for ggF, VBF, VH, and ttH productions. The generator is inter-
 1008 faced with PYTHIA 8.212 [105, 106] for hadronization and fragmentation with tune
 1009 CUETP8M1 [107]. The parton distribution function PDF set used is NNPDF3.0 [108].
 1010 The samples used, with the cross-section for each production mode taken from
 1011 Ref. [12], are summarized in the Table 3.2. The cross sections for all the produc-
 1012 tions are calculated with QCD and electroweak (EW) corrections. The EW correc-
 1013 tion for each mode includes the calculation up to next-to-leading order (NLO). The
 1014 QCD correction for the ggF is calculated at next-to-next-to-next-to-leading order,
 1015 at next-to-next-to-leading order (NNLO) for the VBF and VH , and at NLO for the
 ttH.

Dataset name	Production	Cross-section(pb)	Order
/ggH_HToJPsiG*/RunII Summer16/*	ggF	48.6	N3LO QCD & NLO EW
/VBFH_HToJPsiG*/RunII Summer16/*	VBF	3.78	NNLO QCD & NLO EW
/ZH_HToJPsiG*/RunII Summer16/*	ZH	0.884	NNLO QCD & NLO EW
/WpHJ_HToJPsiG*/RunII Summer16/*	W^+H	0.840	NNLO QCD & NLO EW
/WmHJ_HToJPsiG*/RunII Summer16/*	W^-H	0.538	NNLO QCD & NLO EW
/ttH_HToJPsiG*/RunII Summer16/*	ttH	0.507	NLO QCD & NLO EW
	Total	55.1	

Table 3.2: Summary of Higgs boson signal samples.

1016
 1017 The $Z \rightarrow J/\psi \gamma \rightarrow \mu\mu\gamma$ sample, with $m_Z = 91.2$ GeV [65], is produced with
 1018 the PYTHIA 8.226 generator for hadronization and fragmentation with underly-
 1019 ing event tune CUETP8M1. The SM Z boson production cross section includes
 1020 the NNLO contribution, QCD and electroweak corrections from FEWZ 3.1 using
 1021 the NLO PDF set NNPDF3.0. To account for the potential mismodeling of the
 1022 Z p_T distribution and the missing γ^* contribution in the sample, we apply the
 1023 Z p_T reweighting. We use the Drell-Yan jets samples (with $m_{ll} > 50$ GeV) as
 1024 references to do Z p_T reweighting, one generated with MADGRAPH5_aMC@NLO
 1025 matrix-element generator and the other one with POWHEG generator. In both sam-
 1026 ples, the NLO contribution, the interference, and the contribution of the γ^* dia-

grams are included. The left plot of Fig. 3-1 shows the Z p_T distributions at generator level of the $Z \rightarrow J/\psi \gamma$ and Drell-Yan jets samples. The interference between diagrams at NLO in *aMC@NLO* sample are properly handled. We take the ratio of the two p_T distributions "Drell-Yan jets (*aMC@NLO*)" to " $Z \rightarrow J/\psi \gamma$ " as binned weight, as shown in the right plot of Fig. 3-1.

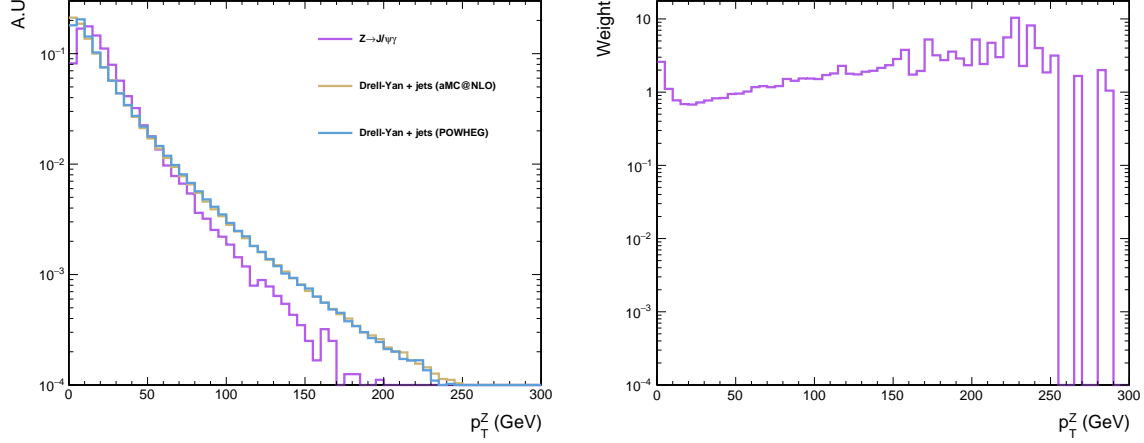


Figure 3-1: The right plot shows the Z p_T distributions at generator level of the $Z \rightarrow J/\psi \gamma$ and Drell-Yan jets samples. The left plot shows the ratio of the two p_T distributions "Drell-Yan jets(*aMC@NLO*)" to " $Z \rightarrow J/\psi \gamma$ ", as binned weight to be applied to the PYTHIA sample.

1031

1032 J/ψ polarization

1033 The Higgs boson is now commonly believed to be a spin-0 particle, and the J/ψ
 1034 from its decay is therefore transversely polarized (with $J_Z = \pm 1$). However, this
 1035 polarization is not correctly simulated in the PYTHIA. The distribution of $\cos\theta$ was
 1036 checked, where θ is the angle between the muon and the direction of J/ψ , and is
 1037 derived at the generator level. The angle θ is calculated without kinematic require-
 1038 ment and in the rest frame of J/ψ , where the direction of J/ψ is obtained from the
 1039 center-of-mass (CM) frame of the Higgs boson. The $H \rightarrow J/\psi \gamma$ samples are there-
 1040 fore reweighted using weight $w = 3/4 \times (1 + (\cos\theta)^2)$ per event. This reweighting
 1041 preserves the total number of events in the samples, however, results in a decrease

1042 of the signal acceptance by 7.0%. No systematic uncertainty is assigned for this
 1043 procedure since the reweighting is done via exact formula, and the angular dis-
 1044 tribution after reweighting is the one we expect. Figs. 3-2 shows the distributions
 1045 of the $H \rightarrow J/\psi \gamma$ samples before (green), after (blue) reweighting, and of the
 1046 $H \rightarrow \gamma^* \gamma$ sample (red) where the polarization of γ^* is correctly simulated.

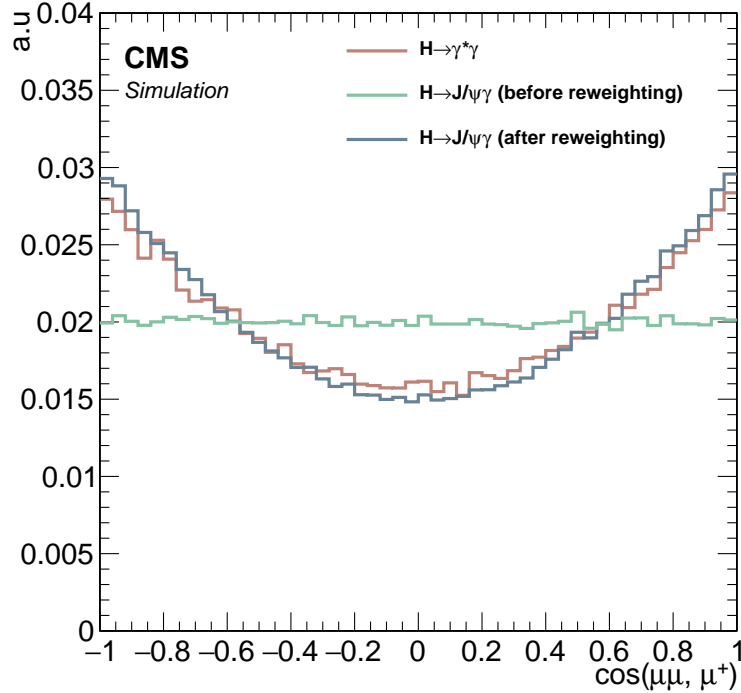


Figure 3-2: Distributions of $\cos\theta$ of $J/\psi \rightarrow \mu\mu$ and $\gamma^* \rightarrow \mu\mu$. The green distribution is the $H \rightarrow J/\psi \gamma$ sample before reweighting; the red distribution is from $H \rightarrow \gamma^* \gamma$; the blue distribution is $H \rightarrow J/\psi \gamma$ sample after reweighting.

1047 The Z boson is a spin-1 particle, the J/ψ from its decay can be transversely
 1048 (with $J_Z = \pm 1$) or longitudinally polarized (with $J_Z = 0$), depending on the po-
 1049 larization of the Z boson. Figs. 3-3 shows the distributions resulting from different
 1050 polarization scenarios. Table 3.3 summarizes the reweight formulae and effects on
 1051 acceptance from different polarization scenarios.

1052 The central value of the final results is to assume the J/ψ to be unpolarized.
 1053 Variations resulting from the extreme scenarios (complete transverse or longitu-

1054 nal) will be quoted and shown.

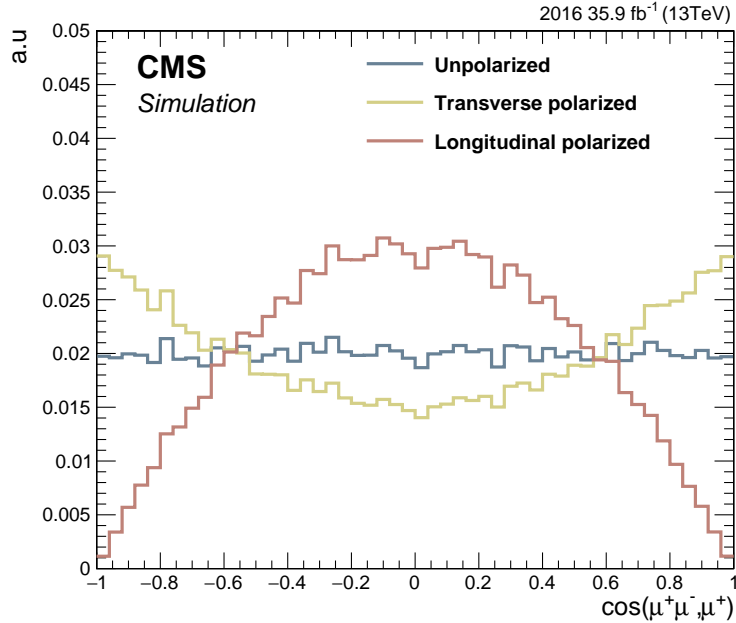


Figure 3-3: Distributions of $\cos\theta$ of $J/\psi \rightarrow \mu\mu$ resulting from different polarization scenarios. The blue distribution is the unpolarized scenario; the earthy yellow distribution is fully transversely polarized scenario; the red distribution is fully longitudinal polarized scenario.

J_Z	Polarization scenario	Formula	Effect on acceptance
± 1	Transverse	$3/4 \times (1 + (\cos\theta)^2)$	-7.8%
0	Longitudinal	$3/2 \times (1 - (\cos\theta)^2)$	+15.6%

Table 3.3: Summary of the reweight formulae and effects on acceptance from different polarization scenarios.

1055 **Background**

1056 The Higgs boson Dalitz decay [109], $H \rightarrow \gamma^*\gamma \rightarrow \mu\mu\gamma$, results in the same final
1057 state as the signal. This process exhibits a peak in the three-body invariant mass
1058 $m_{\mu\mu\gamma}$ at the Higgs boson mass, and is therefore referred to as a peaking, or reso-
1059 nant, background. It is taken into account when deriving the upper limit on the

1060 branching fraction for $Z \rightarrow J/\psi \gamma$. The diagrams for $H \rightarrow \gamma^*\gamma$ process are shown
 1061 in Fig. 3-4. Samples of Higgs boson Dalitz decays, produced in ggF, VBF, VH for
 1062 $m_H = 125\text{ GeV}$, are simulated at NLO using the MADGRAPH5_aMC@NLO 2.6.0
 1063 matrix element generator [110], interfaced with PYTHIA 8.212 for parton showering and hadronization. The dimuon invariant mass $m_{\mu\mu}$ in the ggF sample is restricted to be less than 50 GeV, while in VBF and VH samples it is less than 60 GeV.
 1064 The contribution of the ttH is accounted for by scaling the VBF signal to the ttH
 1065 production cross section. The branching fraction for $H \rightarrow \gamma^*\gamma$ is obtained from
 1066 MCFM 7.0.1 program [111]. The other source of peaking background comes from
 1067 the decay of a Higgs boson into two muons, with a photon radiated from one of
 1068 the muons. Fig. 3-5 shows the distributions of some kinematic variables for the
 1069 $H \rightarrow \mu\mu$ and the $H \rightarrow J/\psi \gamma$ decays. As one can see, the event signatures of the de-
 1070 cay are different from those of the $H \rightarrow J/\psi \gamma$, the contribution of this background
 1071 is found to be negligible after the event selection.

Dataset name	$\mathcal{B}_{SM}(H \rightarrow \gamma^*\gamma \rightarrow \mu\mu\gamma)$
/GluGluHToMuMuG_M125_mll-0To50*/RunII Summer16*/MINIAODSIM	3.83×10^{-5}
/VBFHToMuMuG_M125_MLL-0To60*/RunII Summer16*/MINIAODSIM	3.92×10^{-5}
/ZHToMuMuG_M125_MLL-0To60*/RunII Summer16*/MINIAODSIM	3.92×10^{-5}
/WHToMuMuG_M125_MLL-0To60*/RunII Summer16*/MINIAODSIM	3.92×10^{-5}

Table 3.4: Summary of Higgs Dalitz decay samples.

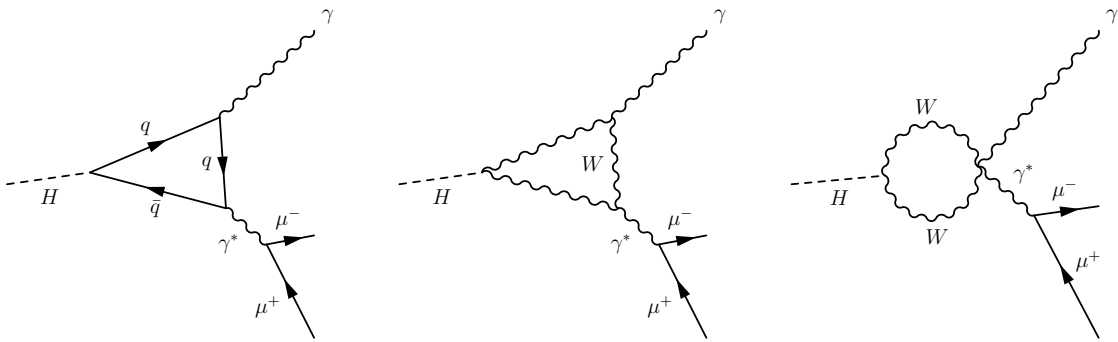


Figure 3-4: Main diagrams for the Higgs Dalitz decay, $H \rightarrow \gamma^*\gamma \rightarrow \mu\mu\gamma$.

1074 Similarly, the Drell–Yan process, $pp \rightarrow Z \rightarrow \mu\mu\gamma$ is a peaking background for
 1075 $Z \rightarrow J/\psi \gamma$. The diagrams for the $pp \rightarrow Z \rightarrow \mu\mu\gamma$ process are shown in Fig. 3-6.

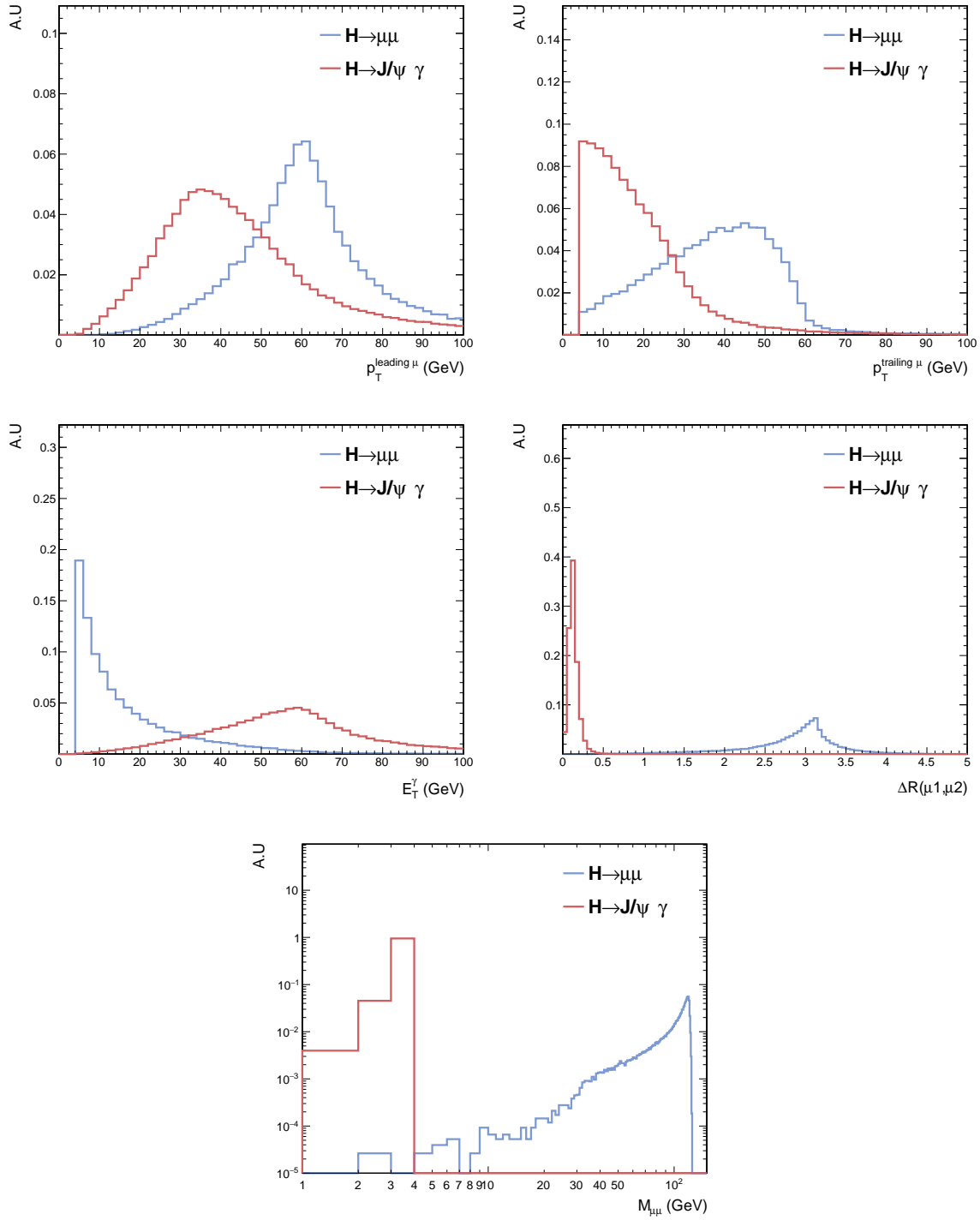


Figure 3-5: Distributions of kinematic variables for the $H \rightarrow \mu\mu$ and the $H \rightarrow J/\psi \gamma$ decays. (Top left) p_T of the leading muon; (Top middle) p_T of the trailing muon; (Top right) E_T of the photon; (Bottom left) angular separation ΔR between muons; (Bottom right) dimuon mass $M_{\mu\mu}$.

1076 The MADGRAPH5_aMC@NLO 2.6.0 generator at leading order with the NNPDF3.0
 1077 PDF set, interfaced with PYTHIA 8.226 for parton showering and hadronization
 1078 with tune CUETP8M1, is used to generate a sample of these resonant background
 1079 events. The photons in these events are all produced in final-state radiation from
 1080 the $Z \rightarrow \mu\mu$ decay and therefore the $m_{\mu\mu\gamma}$ distribution peaks at the Z boson mass
 1081 and there is no continuum contribution. Kinematic requirements, such as $2 <$
 1082 $m_{\mu\mu} < 15 \text{ GeV}$ and $E_T^\gamma > 20 \text{ GeV}$, are imposed when generating the sample, and
 results in an inclusive cross section of 93.0 pb. The additional photons added by

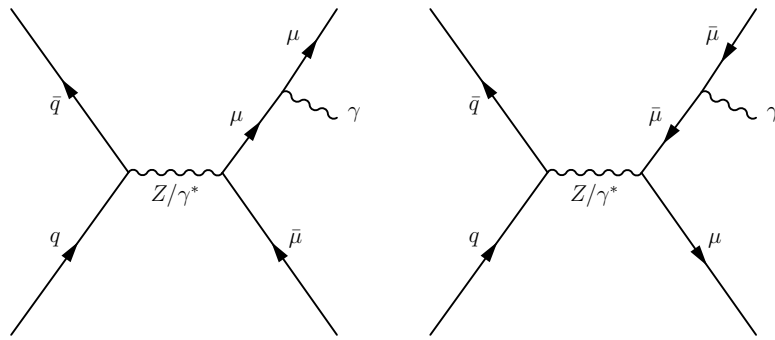


Figure 3-6: Main diagrams for the Drell-Yan process, $\text{pp} \rightarrow Z \rightarrow \mu\mu\gamma$.

1083
 1084 PYTHIA may modify the photon E_T modeling in the sample. The effect is checked
 1085 by using generator level information. Figs. 3-7 shows two distributions, one is the
 1086 E_T of the photons which are prompt final states¹(in blue) and the other one is the
 1087 E_T of the photons added by the PYTHIA8 when it is interfaced with *aMC@NLO* (in
 1088 red). The number of photons with $E_T > 33 \text{ GeV}$ added by PYTHIA8 is only 0.3% of
 1089 those from hard scattering. Therefore, the interface with PYTHIA has minimal effect
 1090 on the overall photon E_T spectrum, and no additional uncertainty is assigned.

1091 There are also background processes that do not give resonance peaks in the
 1092 three-body invariant mass spectrum. These are referred to as non-peaking (non-
 1093 resonant) backgrounds. These processes include

- 1094 • The Drell-Yan FSR process: $\text{pp} \rightarrow Z + \gamma_{\text{FSR}} \rightarrow \mu\mu\gamma_{\text{FSR}}$, where $m_{\mu\mu\gamma}$ is within

¹A particle is labeled as prompt if it is from the hard process in an interaction.

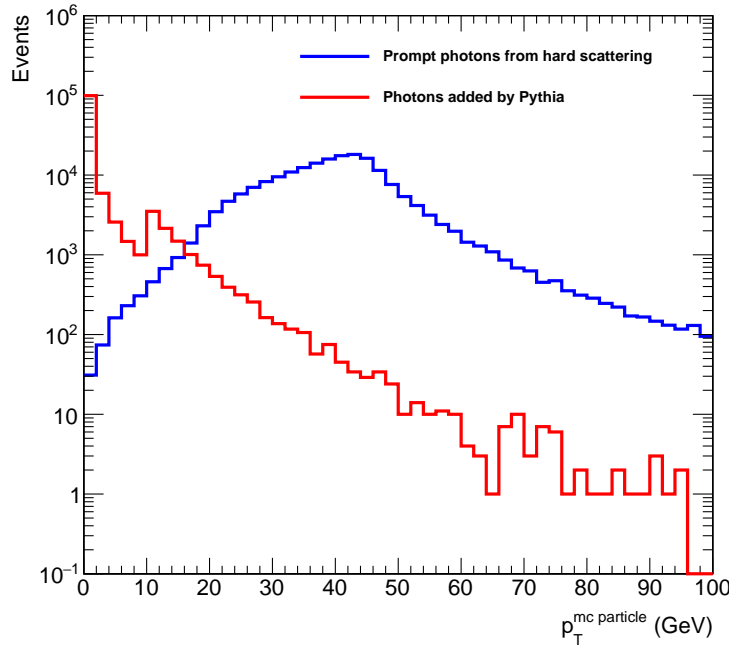


Figure 3-7: The E_T of the photons which are prompt final state (in blue) and the other one is the E_T of the photons added by the PYTHIA when it is interfaced with *aMC@NLO* (in red).

1095 the Higgs (Z) mass window.

- 1096 • The Drell-Yan ISR process: $pp \rightarrow Z/\gamma^* + \gamma_{\text{ISR}} \rightarrow \mu\mu\gamma_{\text{ISR}}$, where $m_{\mu\mu}$ is
1097 within the J/ψ mass window and $m_{\mu\mu\gamma}$ is within the Higgs (Z) mass window.
- 1098 • $pp \rightarrow Z/\gamma^*(\rightarrow \mu\mu) + \text{jets}$, where a jet is misidentified as an energetic photon
1099 which can fire the trigger and pass the event requirements.
- 1100 • $pp \rightarrow \gamma + \text{jets}$, where the muons can come from the jets.
- 1101 • Inclusive quarkonium production with a jet reconstructed as a photon $pp \rightarrow J/\psi + \text{jets}/\gamma$, where the muons come from the quarkonium, J/ψ , in our cases.
- 1103 Since currently no proper simulated samples for those processes are available,
1104 these non-resonant backgrounds are modeled using the fits to $m_{\mu\mu\gamma}$ in data, which
1105 will be introduced in Sec. 3.5.

1106 **Pile-up reweighting**

1107 The simulated sample is reweighted in analysis level using minimum bias events
1108 with cross section of 69.2mb. The corresponding systematic uncertainties are de-
1109 scribed in Sec. 3.7, and are estimated to be less than 1.5% on the expected yields of
1110 the signal for both the Higgs and Z boson decays.

1111 **3.2 Trigger**

1112 The HLT_Mu17_Photon30_CaloIdL_L1ISO trigger is used in this analysis. At the
1113 L1 (L1_Mu5IsoEG18), the trigger requires the presence of a muon with p_T greater
1114 than 5 GeV and an isolated electromagnetic object with p_T greater than 18 GeV. The
1115 main HLT requires a muon and a photon with p_T greater than 17 GeV and 30 GeV,
1116 respectively. No isolation requirement is imposed on the muon by the fact that the
1117 small angular separation between muons in the final state.

1118 **The choice of the trigger**

1119 A study is made to compare the resulting signal efficiency with different triggers.
1120 In the single muon trigger, the p_T threshold on muon is high and there is isolation
1121 requirement calculated in the cone $\Delta R = 0.3$. For the double muon trigger, the
1122 p_T cut of 8 GeV is imposed on the subleading muon, and there are requirements
1123 on the isolation calculated using tracker information. Among the triggers used
1124 in analyses associated with heavy flavor or quarkonium physics, most of them
1125 are pre-scaled and target at different physics content. The only suitable choice is
1126 the HLT_Dimuon20_Jpsi_v6. The L1 seed of this quarkonium trigger requires two
1127 muons of p_T greater than 13 and 6 GeV respectively.

1128 Fig. 3-8 shows the trigger efficiency in the $H \rightarrow J/\psi \gamma$ signal as function of p_T of
1129 the leading muon, p_T of the dimuon system, photon E_T , angular separation (ΔR)
1130 between the muons, invariant mass of the dimuon system $m_{\mu\mu}$, and the number
1131 of vertex. As one can see, the muon-photon trigger preserves the highest signal

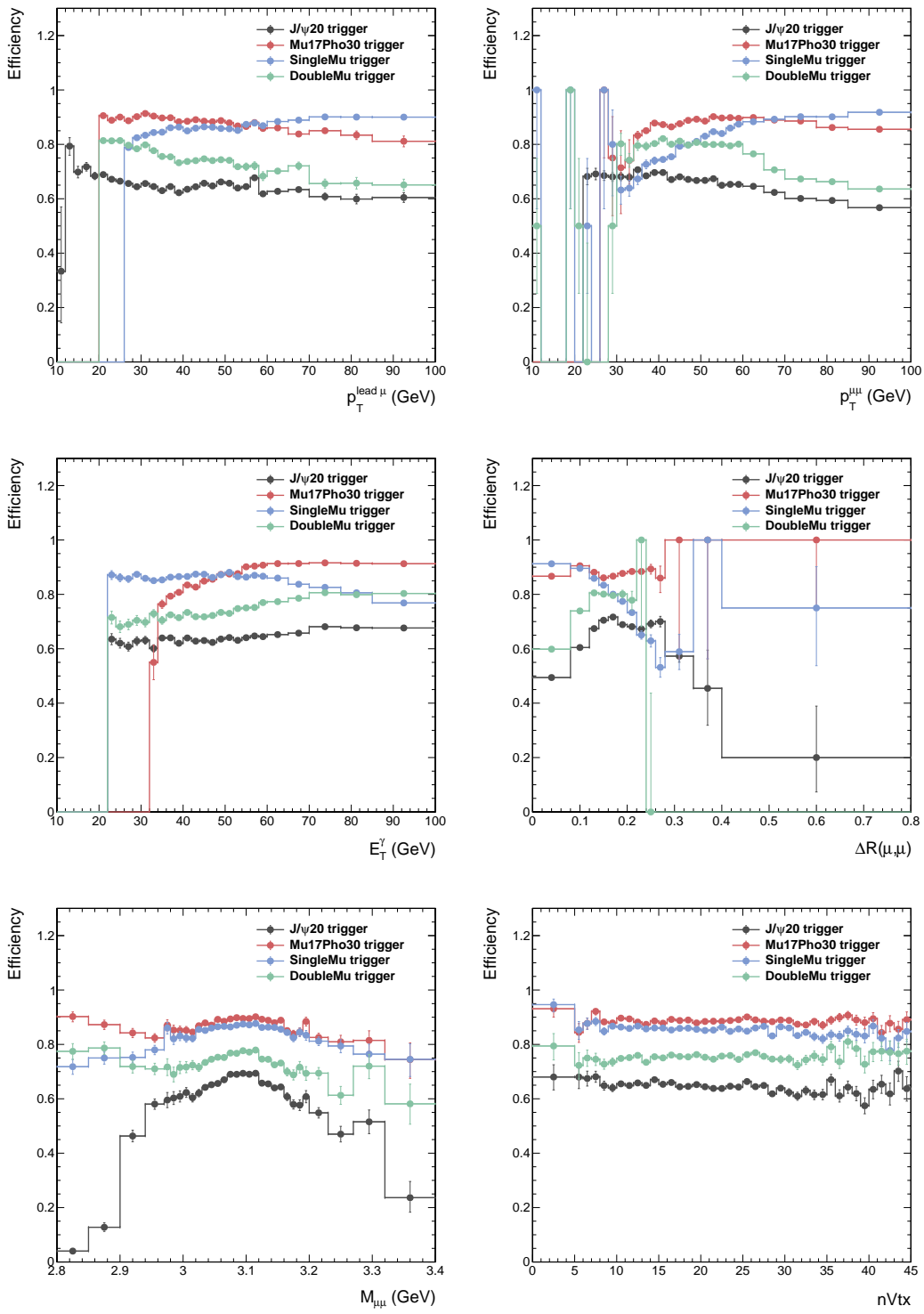


Figure 3-8: The trigger efficiency in the $H \rightarrow J/\psi \gamma$ signal as function of leading muon p_T (top left), p_T of the dimuon system (top right), photon E_T (middle left), angular separation ΔR between the muons (middle right), invariant mass of the dimuon system $M_{\mu\mu}$ (bottom left), and the number of vertex (bottom right).

Trigger path
Single muon trigger
HLT_IsoMu24_v* OR
HLT_IsoTkMu24_v*
Double muon trigger
HLT_Mu17_TrkIsoVVL_Mu8_TrkIsoVVL_v* OR
HLT_Mu17_TrkIsoVVL_TkMu8_TrkIsoVVL_v* OR
HLT_Mu17_TrkIsoVVL_Mu8_TrkIsoVVL_DZ_v* OR
HLT_Mu17_TrkIsoVVL_TkMu8_TrkIsoVVL_DZ_v
Muon-Photon trigger
HLT_Mu17_Photon30_CaloIdL_L1ISO_v*
Quarkonium trigger
HLT_Dimuon20_Jpsi_v*

Table 3.5: Triggers used in the signal efficiency study.

efficiency. The inefficiencies of double muon and quarkonium triggers are responsible for that both triggers are not specifically designed for the muons with small separation. The efficiency of single muon trigger is slightly lower than that of the muon-photon trigger, which may be due to the isolation requirement and high p_T threshold. Consequently, the muon-photon trigger is chosen.

In the actual signal events, the trigger efficiency is 89.2 (84.2)% in the Higgs (Z) boson decay. The trigger efficiency is measured in the control sample, and found to be 81.5 (83.3)% in data (simulation). The method of this measurement is described in the next section.

Trigger efficiency measurement

Trigger efficiency in data is measured using $Z \rightarrow \mu\mu\gamma$ control sample in the dataset collected by single muon trigger, while in the simulated events the Drell-Yan jets with $m_{ll} > 50$ GeV sample is used. Events must have at least two muons and one photon in the final state, and are required to pass at least one of the two single muon triggers, HLT_MuIso24 or HLT_MuTkIso24. The muon that fires one or both triggers is considered as the tag muon, and is further required to pass Tight Muon ID and relative isolation requirement [95]. One muon and one photon are then

1149 selected as probe objects, and are required to pass the kinematic selections listed
1150 below, which ensure that they come from the Z decay with a final-state-radiated
1151 (FSR) photon.

1152 • $0.1 < \Delta R(\mu, \gamma) < 0.8$, where the lower bound of 0.1 rejects events where
1153 the selected photon picks up the track from one of the muons, and the upper
1154 bound of 0.8 rejects events where neither muons emitted the photon

1155 • $m_{\mu\mu} + m_{\mu\mu\gamma} < 180 \text{ GeV}$ to reject contribution from initial-state-radiated (ISR)
1156 photons

1157 • $60 < m_{\mu\mu\gamma} < 120 \text{ GeV}$, the mass window cut used to identify the Z boson.

1158 If there are two muons passing tag selections simultaneously, we could choose
1159 between two possible tag muons. In this case, both choices are considered and
1160 tested, and the event is counted twice. This is to avoid underestimating the effi-
1161 ciency and the potential bias on the measurement.

1162 The Z boson candidate mass distribution in data and MC obtained through this
1163 method are shown in Fig. 3-9. Offline selection requirements of the analysis are
1164 applied in order to factorize the selection efficiency. The events passing all these
1165 selections are counted as the denominator of the trigger efficiency. For the numer-
1166 ator, the probe muon (photon) is tested to see if it can fire the muon (photon) leg
1167 of the muon-photon trigger used in the analysis. The filters in the muon-photon
1168 trigger are listed in Table 3.6. (The filters checked for the muon and photon legs
1169 are different between runs B to E and F to H. The filters in the MC sample are the
1170 same as those in run F to H in data) The filters marked in red color are used for
1171 testing the muon leg, while those in blue are for the photon leg.

1172 There is almost no Run-dependency in trigger efficiency (except for period B),
1173 as shown in the red points in Fig. 3-10 as well as the constant fits and the re-
1174 sulting χ^2/ndf . The black points shown here, which serve as a reference, are the
1175 efficiencies with the standard loose muon ID with additional d_Z and d_{xy} cuts used
1176 previously in this analysis.

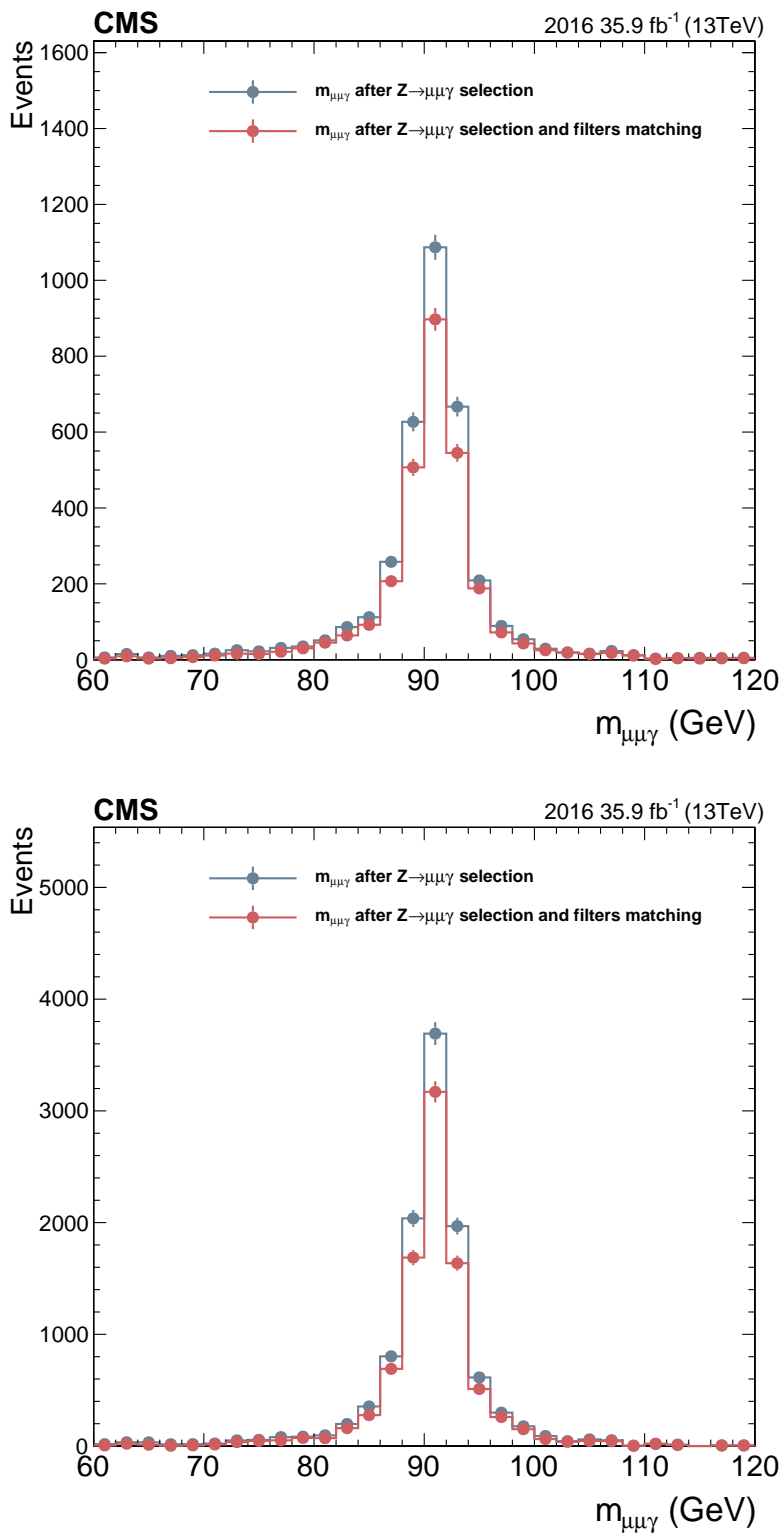


Figure 3-9: The Z boson candidate mass after selection in data (top) and MC (bottom).

HLT_Mu17_Photon30_CaloIdL_L1ISO_v6	
Run B~E	
Filters	hltL1sMu5IsoEG18 hltPreMu17Photon30CaloIdLL1ISO hltL1fL1sMu5IsoEG18L1Filtered5 hltL2fL1sL1Mu5IsoEG18L1f5L2Filtered7 hltL3fL1sL1Mu5IsoEG18L1f5L2f7L3Filtered17 hltEgammaCandidates hltEGL1Mu5IsoEG18Filter hltMu17Photon30CaloIdLL1ISOEtFilter hltEgammaClusterShape hltMu17Photon30CaloIdLL1ISOClusterShapeFilter hltEgammaHoverE hltMu17Photon30CaloIdLL1ISOHEFilter
HLT_Mu17_Photon30_CaloIdL_L1ISO_v9	
RunF~H, MC samples	
Filters	hltL1sMu5IsoEG18IorMu5IsoEG20 hltPreMu17Photon30CaloIdLL1ISO hltL1fL1sMu5IsoEG18ORMu5IsoEG20L1Filtered5 hltL2fL1sL1Mu5IsoEG18ORL1Mu5IsoEG20L1f5L2Filtered7 hltL3fL1sL1Mu5IsoEG18ORL1Mu5IsoEG20L1f5L2f7L3Filtered17 hltEgammaCandidates hltEGL1Mu5IsoEG18ORMu5IsoEG20Filter hltMu17Photon30CaloIdLL1ISOOREtFilter hltEgammaClusterShape hltMu17Photon30CaloIdLL1ISOORClusterShapeFilter hltEgammaHoverE hltMu17Photon30CaloIdLL1ISOORHEFilter

Table 3.6: Filters in the muon-photon trigger, listed in sequence. The filters marked in red color are used for testing the muon leg, while those in blue are for the photon leg.

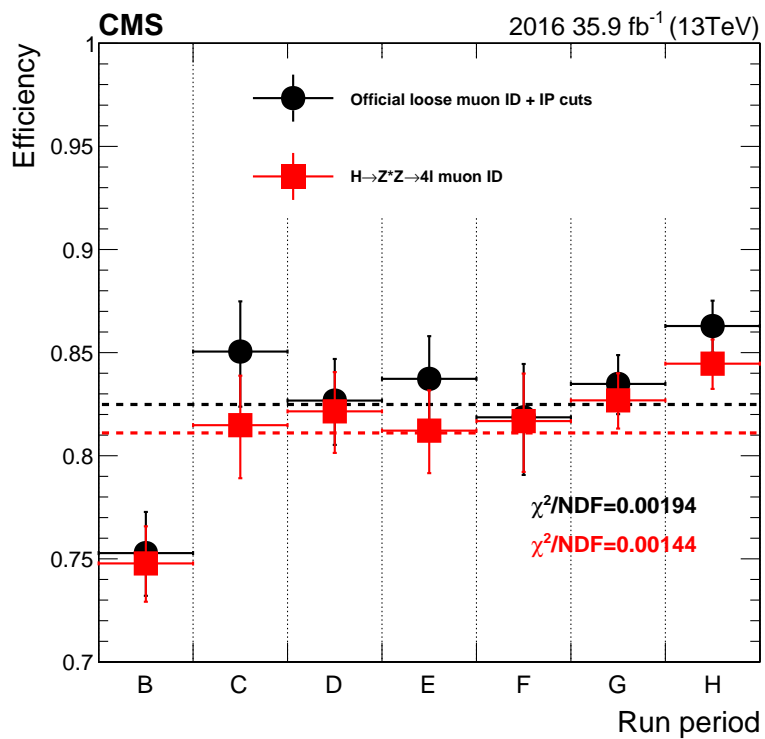


Figure 3-10: Trigger efficiency in each run period. Points in black correspond to the efficiencies measured when using the standard loose muon ID with additional d_Z and d_{xy} cuts used previously in this analysis, while red points correspond to the efficiencies measured using the muon ID optimized for $H \rightarrow ZZ^* \rightarrow 4l$ analysis that is currently used.

Trigger efficiency as a function of probe photon E_T , probe muon p_T , probe muon pseudorapidity η^μ , and probe photon supercluster pseudorapidity η_{SC}^γ are shown in Fig. 3-11. The efficiency as function of probe muon p_T is made with the probe photon $E_T > 33 \text{ GeV}$. Similarly, the plot as function of probe photon E_T is made with the probe muon $p_T > 20 \text{ GeV}$.

The trigger efficiency scale factors – the ratio of Data/MC efficiencies – are to be applied to simulated samples. They are derived in bins of probe muon p_T and probe photon E_T in 2 photon supercluster eta η_{SC} regions : Ecal Barrel (EB) region ($0 < \eta_{SC} < 1.4442$) and Ecal Endcap (EE) region ($1.566 < \eta_{SC} < 2.5$). When applying the trigger efficiency scale factors to MC samples, it is assumed that the leading muon is the one that fires the muon leg of the trigger, so the leading muon p_T and photon E_T are used to determine which trigger efficiency bin to apply on an event. Results for the trigger efficiency measurement are shown in Fig. 3-12 and the scale factors are shown in Fig. 3-13. The uncertainty of each bin on Fig. 3-12 only includes statistical uncertainty, while uncertainties shown in Fig. 3-13 are total systematic uncertainties, which will be detailed in Section 3.7.

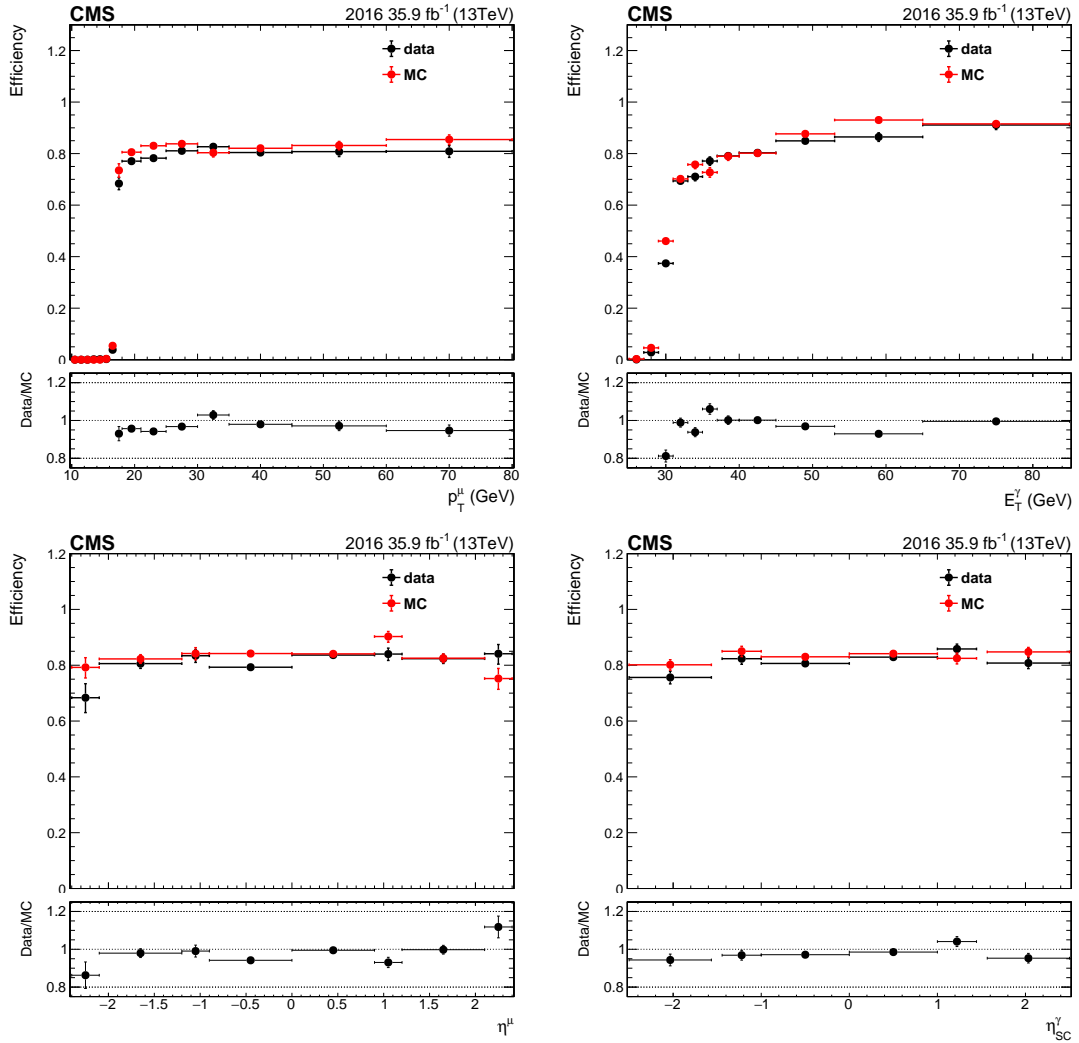


Figure 3-11: Trigger efficiency as a function of probe muon p_T (top left), probe photon E_T (top right), probe muon p_T (bottom left), and probe photon η_{SC}^{γ} (Bottom right).

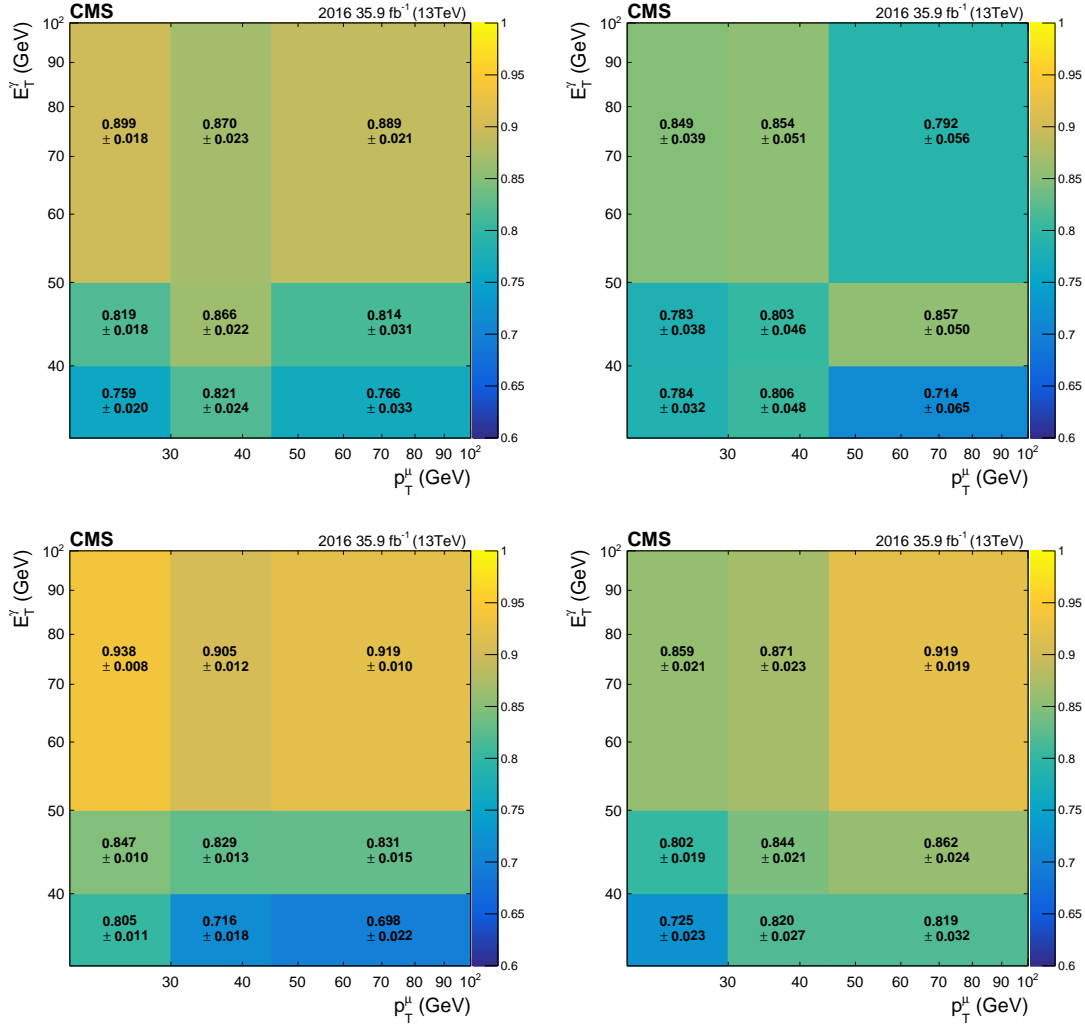


Figure 3-12: Trigger efficiency in bins of muon p_T vs photon E_T for data with the photon in EB region (top left) and in EE region (top right), and for MC with the photon in EB region (bottom left) and in EE region (bottom right).

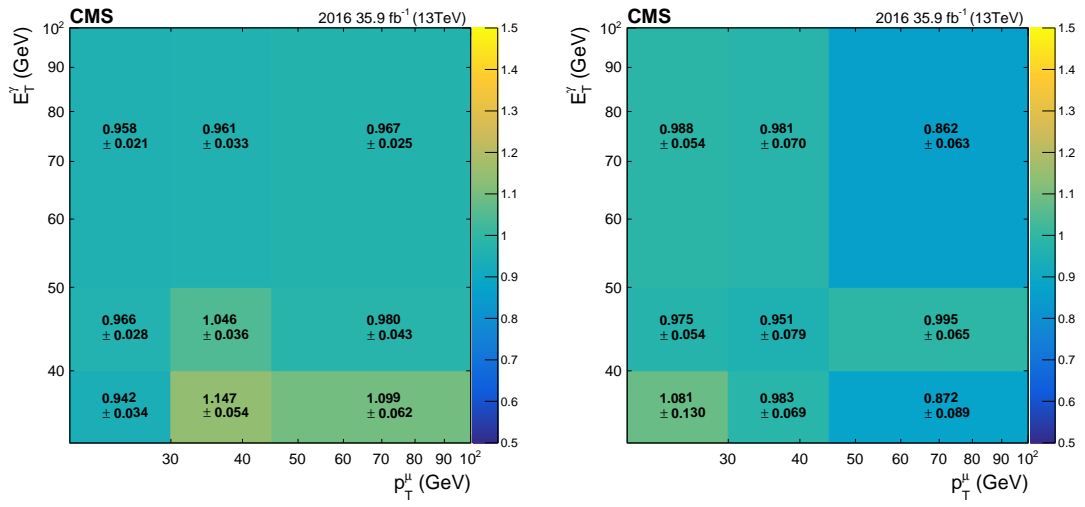


Figure 3-13: Trigger efficiency scale factors in bins of photon p_T vs muon p_T for the selected photon in ECAL EB region (left), for the selected photon in ECAL EE region (right).

₁₁₉₃ **3.3 Object identification**

₁₁₉₄ **3.3.1 Muon identification**

₁₁₉₅ It was observed in 2016 data that a single muon may be incorrectly reconstructed
₁₁₉₆ as two or more muons. To deal with this situation, the “ghost cleaning” procedure
₁₁₉₇ is performed. Tracker muons matched to segments in at least two muons stations
₁₁₉₈ are retained. If there are two muons sharing more than 50% of their segments, the
₁₁₉₉ one with lower reconstruction quality is removed.

₁₂₀₀ Two opposite-sign muons are selected with the identification requirements which
₁₂₀₁ are motivated by $H \rightarrow ZZ^* \rightarrow 4\ell$ analysis [40] and are listed as follows:

₁₂₀₂ • Muons must be reconstructed as particle-flow muons, and can either be global
₁₂₀₃ muons or tracker muons. Those only reconstructed as standalone muon are
₁₂₀₄ rejected.

₁₂₀₅ • $p_T > 4, |\eta| < 2.4$

₁₂₀₆ • Muons must have $d_{xy} < 0.5$ cm, $d_z < 1$ cm, where d_{xy} and d_z are defined as
₁₂₀₇ the closest distance between the track of the muon and the PV in the ϕ plane
₁₂₀₈ and the z direction respectively.

₁₂₀₉ • Significance of the impact parameter in 3-dimensional space $SIP_{3D} = |IP/\sigma_{IP}| <$
₁₂₁₀ 4, where IP is the closest distance between the track of the muon and the
₁₂₁₁ event vertex, σ_{IP} is the uncertainty of the IP.

₁₂₁₂ The usage of impact parameter cuts suppresses the muons from the decays of
₁₂₁₃ heavy-flavor hadrons or products of cosmic ray. If the muon p_T is greater than
₁₂₁₄ 200 GeV, it is selected if it passes Tracker High- p_T ID. After the whole set of selec-
₁₂₁₅ tion, there is no event with the muon p_T greater than 200 GeV in both Higgs and Z
₁₂₁₆ boson searches.

₁₂₁₇ In order to discriminate prompt muons from Higgs (Z) boson decays from those
₁₂₁₈ from electroweak decays of hadrons within jets, the Particle-Flow isolation require-

1219 ment is applied. In this analysis, the relative isolation is calculated for the leading
 1220 muon.

$$\mathcal{I}^\mu \equiv \frac{\sum p_T^{\text{charged}} + \max \left[0, \sum E_T^{\text{neutral}} + \sum E_T^\gamma - p_T^{\text{PU}}(\mu) \right]}{p_T^\mu} \quad (3.1)$$

1221 A cone of size $\Delta R = \sqrt{(\Delta\eta)^2 + (\Delta\phi)^2} = 0.3$ is constructed around the direction
 1222 of muon momentum. The $\sum p_T^{\text{charged}}$ is the scalar sum of the transverse momenta
 1223 of charged hadrons originating from the chosen primary vertex of the event. The
 1224 $\sum E_T^{\text{neutral}}$ and $\sum E_T^\gamma$ are the scalar sums of the transverse energy for neutral hadrons
 1225 and photons, respectively. Since the isolation variable is sensitive to energy de-
 1226 posits from pileup interactions, the $p_T^{\text{PU}}(\mu)$ contribution is subtracted. The pileup
 1227 contribution $p_T^{\text{PU}}(\mu) \equiv 0.5 \sum_i p_T^{\text{PU},i}$, where i runs over the momenta of the charged
 1228 hadron PF candidates not originating from the primary vertex, and the factor of
 1229 0.5 corrects for the different fraction of charged and neutral particles in the cone.
 1230 These momentum and energy sums do not include the contribution from the muon
 1231 itself. $\Delta\beta$ correction is applied, where $\Delta\beta \equiv 0.5 \sum_{\text{PU}}^{\text{charged hadron}} p_T$ is the estimation
 1232 of the energy deposit of neutral hadrons and photons from other pileup vertices.
 1233 The isolation is required to be less than 0.35 for the leading muon, corresponding
 1234 to $\sim 96\%$ of signal efficiency and $\sim 81\%$ of background rejection power.

1235 The reason that the isolation is not calculated for the trailing muon is that the
 1236 ΔR for most of selected muon pairs are less than 0.3 (as can be seen from Fig. 3-
 1237 26, 3-27, and 3-28), which means that the trailing muon is within the isolation cone
 1238 defined with the leading muon. The Isolation efficiencies as functions of $p_T^{\text{leading } \mu}$,
 1239 $p_T^{\text{trailing } \mu}$, $\eta^{\text{leading } \mu}$, $\eta^{\text{trailing } \mu}$, and $p_T^{\mu\mu}$ are shown in Fig. 3-14. Applying isolation on
 1240 both muons is about 7% less efficient than applying it only on the leading muon,
 1241 which is due to the fact that the trailing muon p_T is not significantly greater than
 1242 other activities in the defined cone.

1243 When the subleading muon is in the isolation cone of the leading muon, its p_T
 1244 contribution is subtracted in the isolation sum of the leading muon, and vice versa.
 1245 This can be verified by looking at the isolation of the leading muon divided by

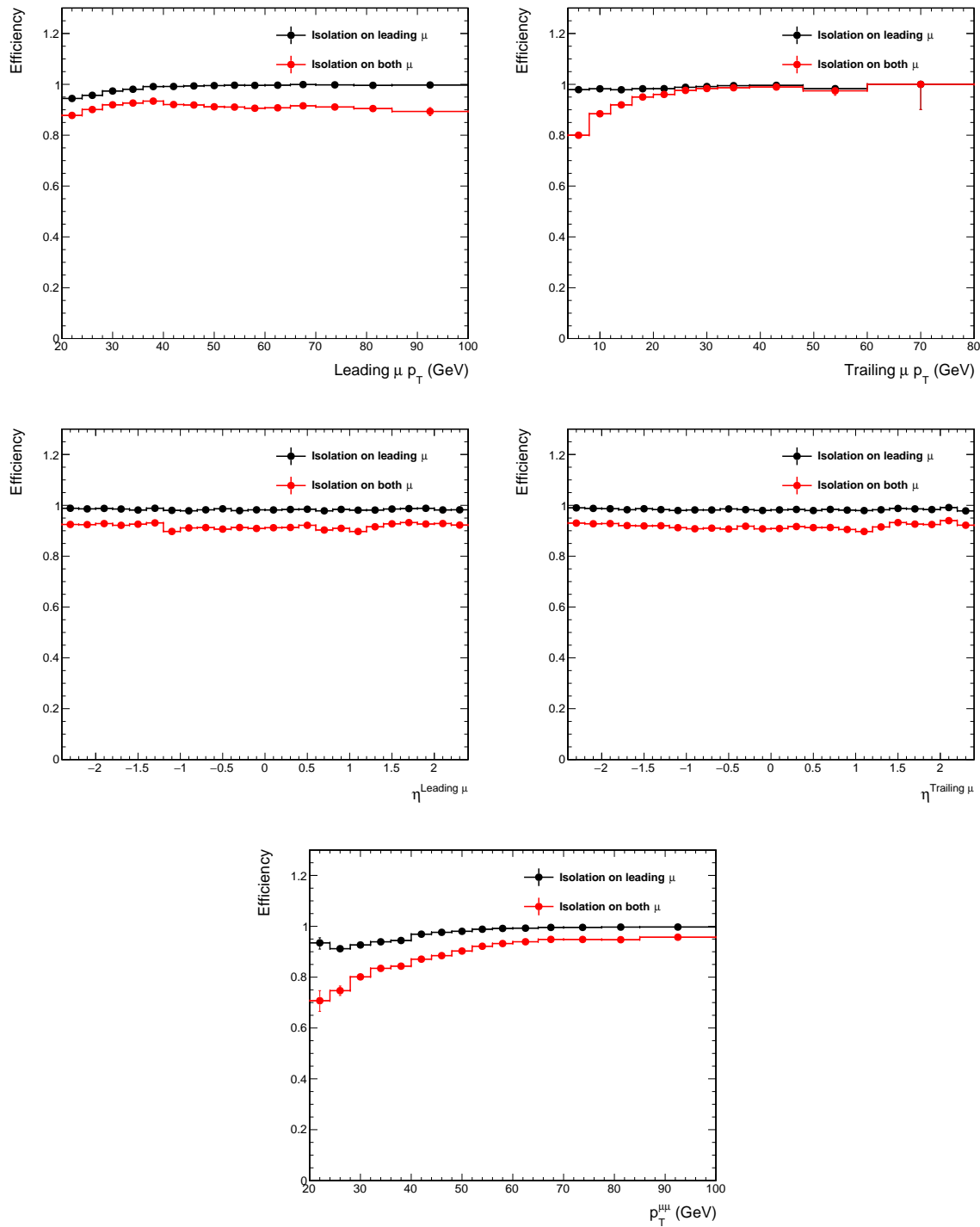


Figure 3-14: Relative isolation efficiency for muon as function of $p_T^{\text{leading } \mu}$ (top left), $p_T^{\text{trailing } \mu}$ (top right), $\eta^{\text{leading } \mu}$ (bottom left), $p_T^{\mu\mu}$ (bottom right).

1246 the p_T of the trailing muon in each sample with isolation requirement relaxed, as
 1247 shown in Fig. 3-15. All the distributions are normalized to unity. If the subleading
 1248 muon is not excluded in the isolation of the leading muon, then it is expected that
 1249 there will be a peak at ~ 1 on the distribution, which is not seen.

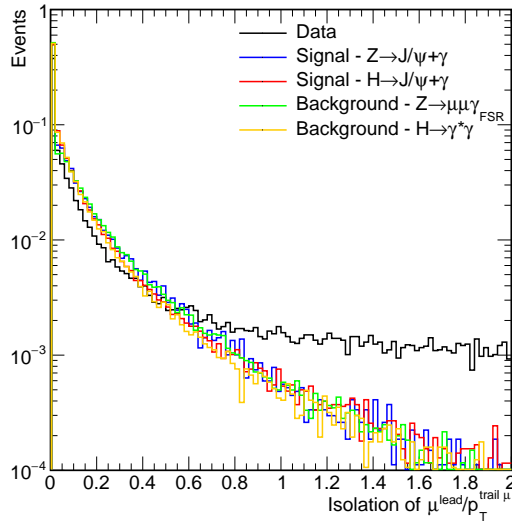


Figure 3-15: The isolation of the leading muon divided by the p_T of the trailing muon in each sample. All the distributions are normalized to unity.

1250 Fig. 3-16 shows the $m_{\mu\mu}$ distributions of the events selected with isolation re-
 1251 quirement (left) and without isolation requirement (right). Muons from J/ψ decay
 1252 must be true muons, so the fake muons should mostly fall in the continuum back-
 1253 ground but not form in J/ψ peak. Therefore, the numbers of background, Nbkg,
 1254 from the fit can roughly tell us how many fake muons will be selected if no isolat-
 1255 tion requirement is imposed. By removing the isolation cut, Nbkg changes from
 1256 ~ 492 to ~ 756 , meaning that fake muons roughly decrease by 34.9%.

1257 The other information that can be extracted here is that, lots of events from
 1258 QCD background can be removed by applying the isolation, based on the fact that
 1259 the J/ψ in the distributions are from QCD events rather than from actual signal
 1260 $H(Z) \rightarrow (J/\psi)\gamma$. Whether the isolation is applied or not has negligible impact on
 1261 the expected signal yields (less than 1%).

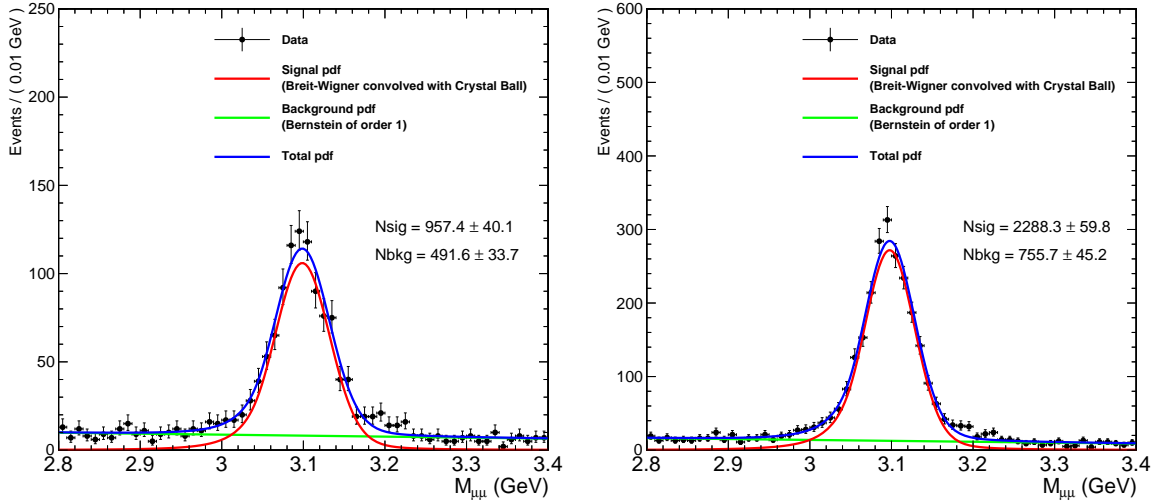


Figure 3-16: The $m_{\mu\mu}$ distributions of the events selected with isolation requirement (left) and without isolation requirement (right). By removing the isolation cut, the fake muons roughly decrease by 34.9%.

1262 Muon momentum calibration

1263 In this analysis, Rochester Muon Momentum Corrections [112] derived for 2016
 1264 dataset are applied. Biases in the measurement of muon momenta in hadron col-
 1265 lider experiments can originate from several sources such as misalignment of the
 1266 detectors, the deficiency in the software reconstruction, and uncertainties in mag-
 1267 netic field. Corrections are developed to remove such biases. The momentum
 1268 scale corrections are extracted using the average of $1/p_T$ ($< 1/p_T >$) spectra of
 1269 muons from Z decay, while the resolution corrections and scale factors are derived
 1270 by comparing the $m_{\mu\mu}$ distributions between data and MC. The corrections are
 1271 then applied to correct the momentum scale in data events and resolution in simu-
 1272 lated events. We validate whether the Rochester correction would give consistent
 1273 energy scale and resolution between data and MC for the muons from decay of
 1274 J/ ψ candidates in $H \rightarrow (J/\psi)\gamma$ events. In this validation study, the events are
 1275 required to satisfy the nominal selection requirements with relaxed dimuon and
 1276 photon transverse momenta ($p_T^{\mu\mu}, E_T^\gamma / m_{\mu\mu\gamma} > 0.16(20/125)$). To quantify the scale
 1277 and resolution, a Breit-Wigner convolved with a Crystal Ball function (Eq. 3.2) is

1278 used to fit the distribution for the signal events. For the data events, Breit-Wigner
 1279 convolved with a Crystal Ball function in addition of the Bernstein 1_{st} polynomial
 1280 (Eq. 3.3) is used as model. As can be seen in Fig. 3-17, the $m_{\mu\mu}$ distribution in MC
 1281 is smeared, while the scale of the $m_{\mu\mu}$ distribution in data is shifted.

$$f_{J/\psi-MC} = \text{BW}(m, \Delta) \otimes \text{CB}(0, \sigma_{CB}, \alpha, n) \quad (3.2)$$

$$f_{J/\psi-\text{data}} = N_{sig} \times f_{J/\psi-MC} + N_{bkg} \times \text{Bern.1st}(p1) \quad (3.3)$$

1282 Associated systematic uncertainty is quoted and will be detailed in Sec ??.

1283 Muon efficiency measurements

1284 A “tag-and-probe” method [113] based on samples of $Z \rightarrow \mu\mu$ and $J/\psi \rightarrow \mu\mu$
 1285 events in data and simulation is used to measure the efficiency, and is found to
 1286 be between 94–98 (92–97)% in the barrel (endcap), depending on muon p_T and
 1287 η . The isolation efficiency is measured with $Z \rightarrow \mu\mu$ events, and found to be p_T
 1288 dependent and between 90 (92) and 100% in the barrel (endcap).

1289 The difference in the efficiencies measured in simulation and data, which on
 1290 average is 1% per muon, is used to rescale the selection efficiency in the simulated
 1291 samples. The products of all the data to simulation scale factors for muon tracking,
 1292 reconstruction, identification, impact parameter and isolation requirements and
 1293 corresponding uncertainties are shown in Fig. 3-18.

Reconstruction and identification	$p_T > 20 \text{ GeV}$	$Z \rightarrow \mu\mu$ events are used
	$p_T < 20 \text{ GeV}$	$J/\psi \rightarrow \mu\mu$ events are used
Impact parameter	$Z \rightarrow \mu\mu$ events are used for the whole p_T range	
Isolation	$Z \rightarrow \mu\mu$ events are used for the whole p_T range	
Tracking	$Z \rightarrow \mu\mu$ events are used for the whole p_T range	

Table 3.7: The summary table of muon efficiencies and scale factors measurement.

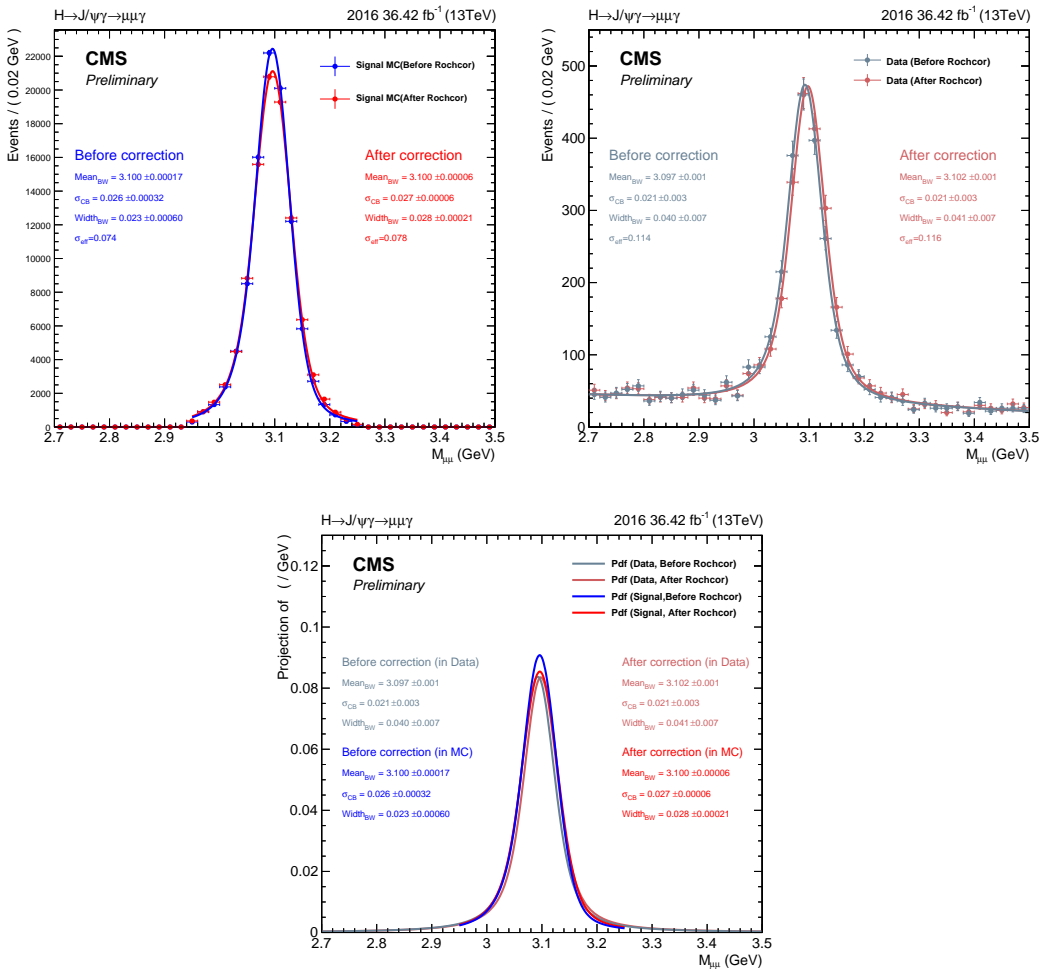


Figure 3-17: Comparisons between the dimuon mass $m_{\mu\mu}$ distributions with and without the corrections in both data and signal MC.

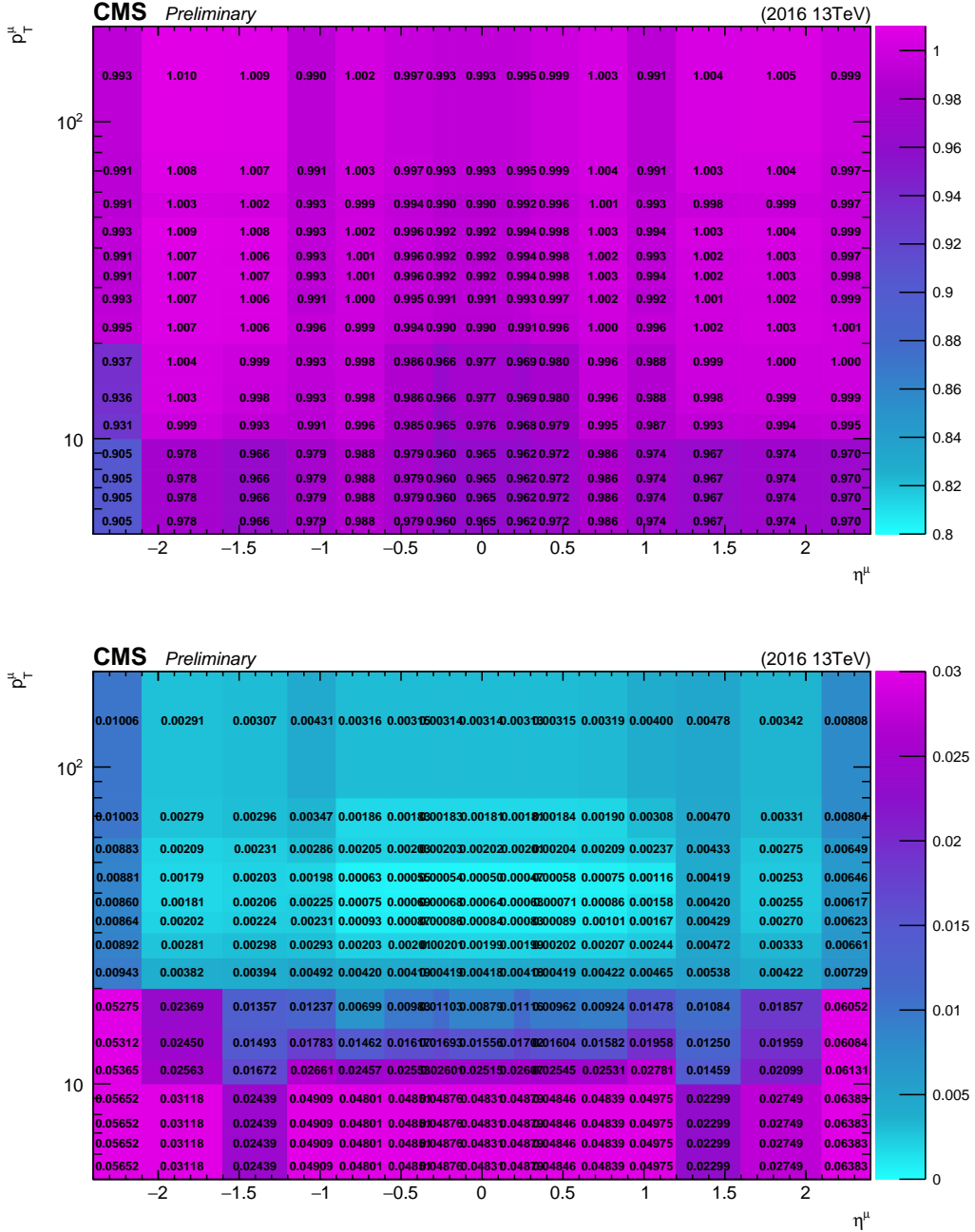


Figure 3-18: The histograms of overall data to simulation scale factors (reconstruction, identification, impact parameter and isolation requirements and tracking SF) and corresponding uncertainty.

1294 3.3.2 Photon identification

1295 MVA based ID with working point (W.P) 90% is used. This ID is trained on a sam-
 1296 ple of simulated $\gamma + \text{jet}$ events, where the photon candidates matching the prompt
 1297 photon are used as signal, and photon candidates not matching the prompt pho-
 1298 ton are identified as background. The input variables for the photon MVA training
 1299 include the shower shapes variables, photon isolation, and charged hadron isolat-
 1300 ion. The general purpose MVA has two categories, one for photons in barrel (EB)
 1301 region and the other for those in endcap (EE) region. The suggested cut values,
 1302 0.2 for both categories, result in 95.2% (93.9%) of signal efficiency for $Z \rightarrow J/\psi \gamma$
 1303 events and 60.3% (67.3%) of background rejection power, defined as $1 - \epsilon_{\text{Bkg}}$, for
 1304 the EB (EE) region. Here, the events selected in data are treated as background.
 1305 Fig. 3-19 shows the ROC curves for photon MVA ID obtained from $Z \rightarrow J/\psi \gamma$
 1306 signal events and data events (treated and labeled as background in the plots), the
 1307 point corresponding to the 90% W.P for each category is shown as red solid star.

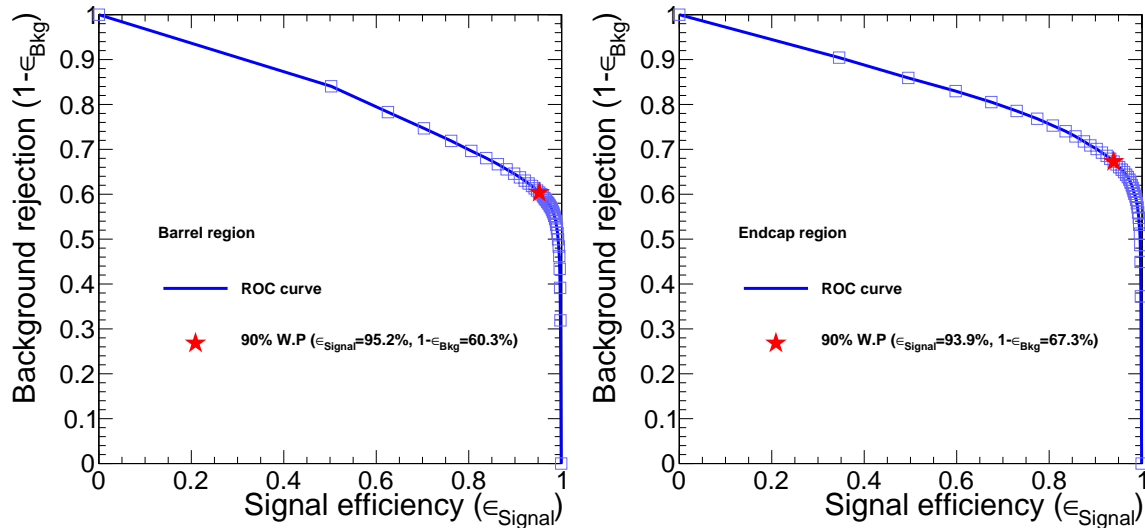


Figure 3-19: The ROC curves for photon MVA ID obtained from $Z \rightarrow J/\psi \gamma$ signal events and data events for EB (left) and EE (right) category. The red solid star corresponds to the efficiency for 90% W.P.

1308 The contamination of fake photons is estimated by checking the ratio of the
 1309 $Z + \text{jets}$ yields to the $Z + \gamma$ yields. This gives a rough idea on the performance

1310 of photon ID. It is found that the ratio of $Z + \text{jets}/Z\gamma$ events is $\sim 30\%$ for photon
 1311 E_T between 33 and 40 GeV, and $\sim 20\%$ for photon E_T between 60 and 80 GeV.
 1312 The ratios of $Z + \text{jets}/Z\gamma$ events in different photon E_T regions are summarized in
 1313 Table 3.8.

photon E_T	$Z+\text{jets}/Z\gamma$ (in %)
$33 < E_T^\gamma < 40 \text{ GeV}$	30
$40 < E_T^\gamma < 50 \text{ GeV}$	28
$50 < E_T^\gamma < 60 \text{ GeV}$	22
$60 < E_T^\gamma < 80 \text{ GeV}$	21

Table 3.8: The ratios of $Z+\text{jets}/Z\gamma$ events in different photon E_T regions.

1314 Conversion safe electron veto (CSEV) is used to reject photons from electron
 1315 conversions by requiring that there be no charged-particle track with a hit in the
 1316 inner layer of the pixel detector associated to the photon cluster in the ECAL. The
 1317 small number of inoperative sensors and possible cases where a track can pass be-
 1318 tween the first layer of sensors without leaving a hit are accounted for. The photon
 1319 inefficiency is largely reduced and the residual comes from photons converting in
 1320 the beam pipe. Up to 99.1% (97.8%) of photon in EB (EE) can pass CSEV, and 5.3%
 1321 (19.6%) of electrons in EB (EE) can also satisfy this requirement. The efficiency of
 1322 the photon identification is measured from $Z \rightarrow ee$ events using tag-and-probe
 1323 techniques, and found to be between 84 and 91% (77 and 94%), depending on the
 1324 transverse energy E_T , in the barrel (endcap). The electron veto efficiencies are mea-
 1325 sured with $Z \rightarrow \mu\mu\gamma$ events, where the photon is produced by final-state radiation,
 1326 and found to be 98 (94%) in the barrel (endcap). The scale factors for the photon
 1327 ID in bins of photon E_T and η_{SC} are shown in Fig. 3-20, and those for the CSEV are
 1328 shown in Fig.3-21.

1329 3.4 Event Selection

1330 In addition to the object identification and isolation, kinematic selections are ap-
 1331 plied to further discriminate the background.

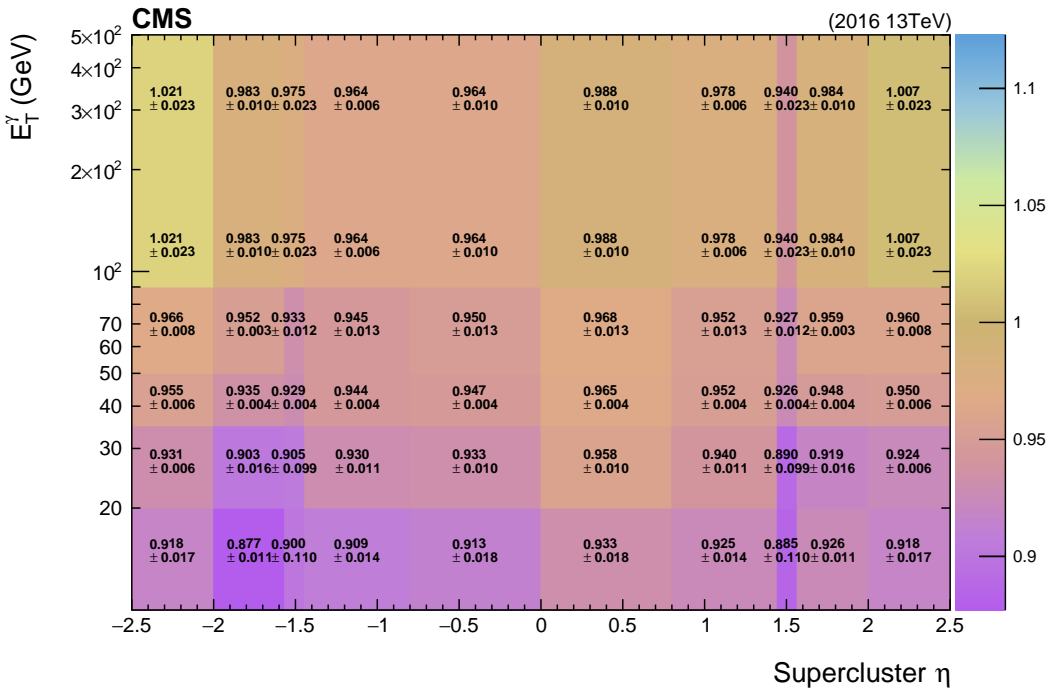


Figure 3-20: The scale factors in bins of photon E_T and η_{SC} .

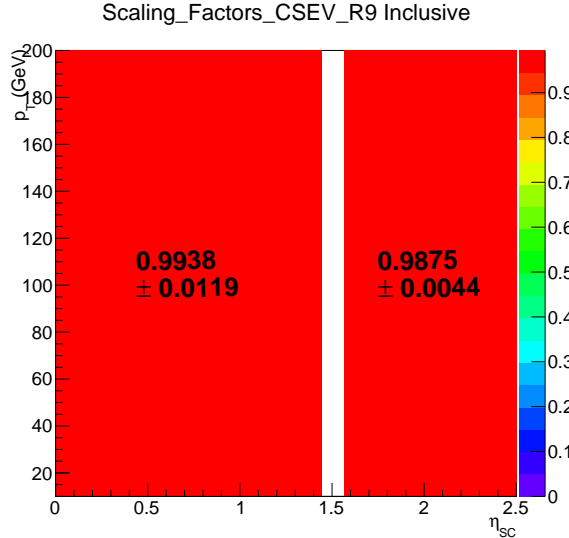


Figure 3-21: The scale factors of SCEV in bins of photon η_{SC} .

- 1332 • Two opposite charged muons with $p_T^{\mu_1} > 20$ GeV, $p_T^{\mu_2} > 4$ GeV, $|\eta^\mu| < 2.4$.
1333 The p_T cut value on the leading muon is driven by the trigger threshold.
- 1334 • J/ψ candidate selection $3.0 < m_{\mu\mu} < 3.2$ GeV.

- 1335 • $E_T^\gamma > 33 \text{ GeV}$, $|\eta_{SC}^\gamma| < 2.5$, excluding the Barrel-Endcap transition region at
 1336 $1.4442 < |\eta_{SC}^\gamma| < 1.566$. The E_T cut value on the photon is driven by the
 1337 trigger threshold.

 1338 • $\Delta R(\mu_1, \gamma) > 1$, $\Delta R(\mu_2, \gamma) > 1$, $\Delta R(\mu\mu, \gamma) > 2$, and $|\Delta\phi(\mu\mu, \gamma)| > 1.5$. The
 1339 angular separation ΔR cuts on each muon and the photon are imposed to
 1340 suppress Drell-Yan process with FSR photon. As we do not have proper back-
 1341 ground MC samples, the cut values are determined such that a higher total
 1342 signal efficiency is kept.

 1343 • $p_T^{\mu\mu}, E_T^\gamma / m_{\mu\mu\gamma} > 0.28$ (35/125) for $H \rightarrow J/\psi \gamma$, 0.384 (35/91.2) for $Z \rightarrow J/\psi \gamma$.
 1344 If a hard cut on E_T or $p_T^{\mu\mu}$ is imposed, there will be an obvious turn-on at the
 1345 Z mass region, as shown in Fig. 3-22, which will complicate the background
 1346 model. This ratio cut also helps to reject the $\gamma^* + \text{jet}$ and $\gamma + \text{jet}$ backgrounds.
 1347 As for the cut value, 91.2 and 125.0 GeV are the nominal mass of the Z and
 1348 Higgs boson respectively.

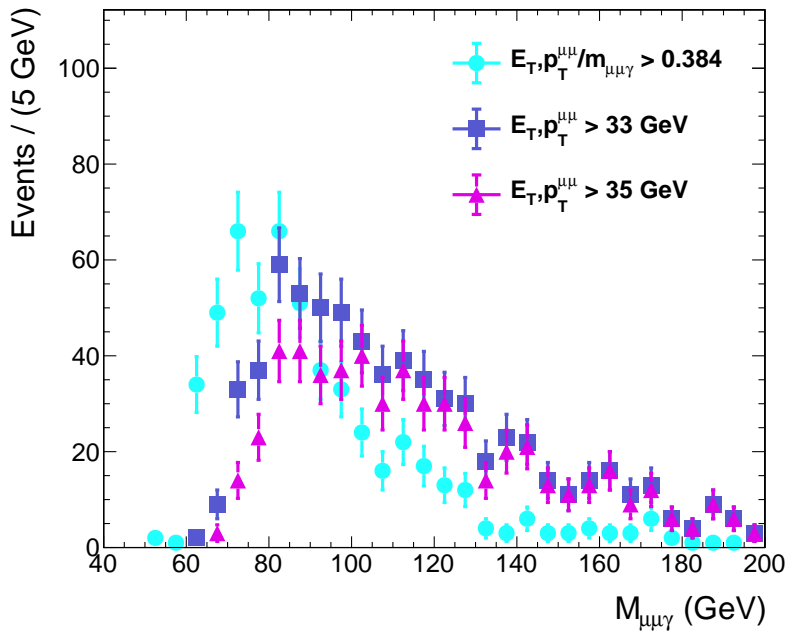


Figure 3-22: $m_{\mu\mu\gamma}$ distributions with different forms of p_T or E_T cuts.

Table 3.9 summarizes event selections in this analysis

Trigger : HLT_Mu17_Photon30_CaloIdL_L1ISO_v
Muon identification, Particle Flow Isolation in cone 0.3 for $\mu_{\text{lead}} < 0.35$
$p_T^{\mu_{\text{lead}}} > 20 \text{ GeV}$, $p_T^{\mu_{\text{trai}}} > 4 \text{ GeV}$, $ \eta_\mu < 2.4$
Photon MVA ID(90% WP), $E_T^\gamma > 33 \text{ GeV}$
$ \eta_{SC}^\mu < 2.5$, excluding those in Barrel-Endcap transition region of ECAL.
$\Delta R(\mu_1, \gamma) > 1$, $\Delta R(\mu_2, \gamma) > 1$, $\Delta R(\mu\mu, \gamma) > 2$, and $ \Delta\phi(\mu\mu, \gamma) > 1.5$
$3.0 < m_{\mu\mu} < 3.2 \text{ GeV}$
$p_T^{\mu\mu}/m_{\mu\mu\gamma} > 0.384(0.28)$, $E_T^\gamma/m_{\mu\mu\gamma} > 0.384(0.28)$ for the Z (H) $\rightarrow J/\psi \gamma$.

Table 3.9: The selection requirements in this analysis, including ID, isolation and kinematic selection.

1350 In the $Z \rightarrow J/\psi \gamma$ search, selected events are classified into mutually exclusive
 1351 categories in order to enhance the sensitivity of the search. The categorization is
 1352 based on the η of the photon and the photon R_9 variable (defined as the energy sum
 1353 of 3×3 ECAL crystals centered on the most energetic crystal in the supercluster
 1354 divided by the energy of the supercluster). Unconverted photons have high values
 1355 of R_9 and a threshold of 0.94 is used to classify reconstructed photons with high
 1356 R_9 (thus with a better resolution) and low R_9 (worse resolution). The background
 1357 is larger in the converted photon category. The three categories are: photon in
 1358 the barrel region with a high R_9 value (referred to as EB high R_9); photon in the
 1359 barrel region with low R_9 value (referred to as EB low R_9); photon in the endcap
 1360 region (referred to as EE). The EE category is not divided into high/low R_9 because
 1361 there are few events in this category. By this categorization, this improvement on
 1362 the search limit is $\sim 2.0\%$. In the $H \rightarrow J/\psi \gamma$ search events are not divided into
 1363 categories. The possibility of splitting the EE category was investigated, but this
 1364 did not result in a significant improvement.

1365 The exact definition of the three event categories in $Z \rightarrow J/\psi \gamma$ search are shown
 1366 in Table 3.10. The table includes the fractions of expected events in each category
 1367 for signal and of the observed events for data. The σ_{eff} of the $m_{\mu\mu\gamma}$ distribution of
 1368 each category is also included.

1369 Table 3.11 summarizes the expected number of events from signals and ob-
 1370 served yields in data in steps of event selection of both the Higgs and Z boson

	Category 1 $0 < \eta_\gamma^{\text{SC}} < 1.4442$ $R_9 > 0.94$	Category 2 $0 < \eta_\gamma^{\text{SC}} < 1.4442$ $R_9 > 0.94$	Category 3 $1.566 < \eta_\gamma^{\text{SC}} < 2.5$ -
Data	40.3%	36.2%	23.5%
Signal	49.0%	30.6%	20.3%
σ_{eff}	3.58 GeV	3.86 GeV	4.08 GeV

Table 3.10: Definition of the three event classes in $Z \rightarrow J/\psi \gamma$ and the fraction of selected events in signal and data. The expected mass resolution on the signal are also shown.

1371 decays. For the Z boson decays, the numbers are with the unpolarized J/ψ as-
 1372 sumption and p_T reweighting. Table 3.12 shows the impacts of different polariza-
 1373 tion scenarios and the Z p_T reweighting. The variations on the yields resulting
 1374 from the extreme polarization assumption is -7.8% (transverse) to +16% (longitu-
 1375 dinal), corresponding to the total signal efficiency varying from 13.1% to 16.4%.
 1376 The Z p_T reweighting, with weights derived from the *aMC@NLO* sample, results in
 1377 +2.3% of increase on the expected yields of the Z decay. The difference between the
 1378 yield with weights derived from the *aMC@NLO* sample and that from *POWHEG* is
 1379 only 0.13%, and no additional uncertainty is assigned. In both Z and Higgs decays
 1380 the number of events coming from the peaking background H ($Z \rightarrow \mu\mu\gamma$) is large
 1381 compared to signal processes. On the other hand, it is small compared to the total
 1382 background. Hence, it has minimal effect on the upper limit on $\mathcal{B}(H(Z) \rightarrow J/\psi \gamma)$.
 1383 With the constraint 100 (70) $< m_{\mu\mu\gamma} < 150$ (120) GeV, the total signal efficiency,
 1384 including kinematic acceptance, trigger and reconstruction efficiencies, and p_T
 1385 reweighting for the Z boson decay, of about 22.6% and 14.2% in Higgs and Z boson
 1386 decays. The difference in the total signal efficiency between the Higgs and the Z
 1387 boson decay is mostly due to the kinematic acceptance, which comes from the dif-
 1388 ference in p_T distributions of muons and photon given that the Z boson is lighter
 1389 than the Higgs boson.

1390 Fig. 3-23 and 3-24 show the $m_{\mu\mu}$ distributions in $H \rightarrow J/\psi \gamma$ (top plots in Fig. 3-
 1391 23), Cat1 of $Z \rightarrow J/\psi \gamma$ (bottom plots in Fig. 3-23), Cat2 of $Z \rightarrow J/\psi \gamma$ (top plots in
 1392 Fig. 3-24), and Cat3 of $Z \rightarrow J/\psi \gamma$ (bottom plots in Fig. 3-24). The black points with

	$H \rightarrow J/\psi \gamma$			$Z \rightarrow J/\psi \gamma$		
	Data	$H \rightarrow J/\psi \gamma$ signal	$H \rightarrow \gamma^* \gamma$ background	Data	$Z \rightarrow J/\psi \gamma$ signal	$Z \rightarrow \mu\mu\gamma$ background
Total (Before selection)	170M	0.350	91.7	170M	10.8	3335
HLT	30.3M	0.190	51.3	30.3M	4.24	1932
Muon selection	650K	0.136	35.9	650K	2.67	1317
Photon selection	152K	0.116	30.7	152K	2.17	1066
$\Delta R, \Delta\phi$	59.4K	0.101	23.5	59.4K	2.09	1020
$m_{\mu\mu}$	1088	0.0929	0.274	1088	1.93	5.29
$m_{\gamma\mu\gamma}$	363	0.0928	0.273	637	1.90	5.37
$p_T^{\mu\mu}, E_T^{\gamma}/m_{\mu\mu\gamma}$	279	0.0884	0.257	384	1.58	4.57
Expected signal yields (with the pileup weight, all the scale factors and efficiencies)						
All	279	0.0765	0.207	384	1.54	4.47
Cat1	-	-	-	148	0.770	2.14
Cat2	-	-	-	144	0.468	1.20
Cat3	-	-	-	92	0.299	1.12

Table 3.11: The expected signal yield and the number of selected events in data, for the integrated luminosity of 35.9 fb^{-1} .

	Inclusive Yield	Inclusive Difference (in %)
unpolarized & with p_T reweighting	1.54	
transversely polarized & with p_T reweighting	1.42	-7.86
longitudinally polarized & with p_T reweighting	1.78	+15.7
unpolarized & without p_T reweighting	1.50	-2.24
transversely polarized & without p_T reweighting	1.38	-9.85
longitudinally polarized & without p_T reweighting	1.74	+13.0

Table 3.12: Summary of the impacts of different polarization scenarios and the Z p_T reweighting.

1393 error bars are distributions in data, while the filled histograms are distributions in
1394 signal events. Plots on the left hand side are with the $m_{\mu\mu}$ constraint, while those
1395 on the right hand side are not. The peak at the J/ψ mass in data shows that real
1396 J/ψ candidates are reconstructed and selected. These events come from inclusive
1397 quarkonium production, for which no simulation is available. The backgrounds
1398 from $H \rightarrow \gamma^* \gamma$ and $Z \rightarrow \mu\mu\gamma$ events, for which there is a simulation, are much
1399 smaller than that from inclusive quarkonium production and they are scaled to
1400 make it visible. Figures 3-25, 3-26, 3-27, 3-28 show the distributions of kinematic
1401 variables in $H \rightarrow J/\psi \gamma$, Cat1, Cat2, and Cat3 of $Z \rightarrow J/\psi \gamma$. The variables shown
1402 are : p_T of leading muon, p_T of trailing muon, E_T of photon, η of leading muon, η
1403 of trailing muon, η_{SC} of photon, p_T of reconstructed dimuon system, ΔR between
1404 two muons, and ΔR between leading muon and photon.

	$H \rightarrow J/\psi \gamma$ signal					
	ggF	VBF	ZH	W^+H	W^-H	ttH
Total (Before selection)	0.307	0.0240	0.00596	0.00565	0.00360	0.00334
HLT	0.167	0.0132	0.00303	0.00279	0.00193	0.00226
Muon selection	0.119	0.00939	0.00216	0.00198	0.00139	0.00168
Photon selection	0.103	0.00803	0.00178	0.00161	0.00114	0.00125
$\Delta R, \Delta\phi$	0.0925	0.00480	0.00110	0.00100	0.000742	0.000510
$m_{\mu\mu}$	0.0858	0.00442	0.000938	0.000784	0.000594	0.000351
$m_{\mu\mu\gamma}$	0.0858	0.00442	0.000932	0.000776	0.000589	0.000330
$p_T^{\mu\mu}, E_T^\gamma/m_{\mu\mu\gamma}$	0.0820	0.00401	0.000855	0.000714	0.000541	0.000305
Expected signal yields (with the pileup weight, all the scale factors and efficiencies)	0.0710	0.00352	0.000711	0.000597	0.000454	0.000266

Table 3.13: The expected signal yield for each Higgs production mode.

1405 The normalization of each distribution from data events is the number of events
 1406 selected in the corresponding category. The number of events in distributions from
 1407 signal simulated events are normalized to 750 (40) times the SM prediction for
 1408 Higgs (Z) decays. The number of events in distributions from peaking background
 1409 MC events are normalized to 150 (5) times their SM expectation for Higgs (Z) de-
 1410 cays. These scale factors in the plots are chosen to give better visualization.

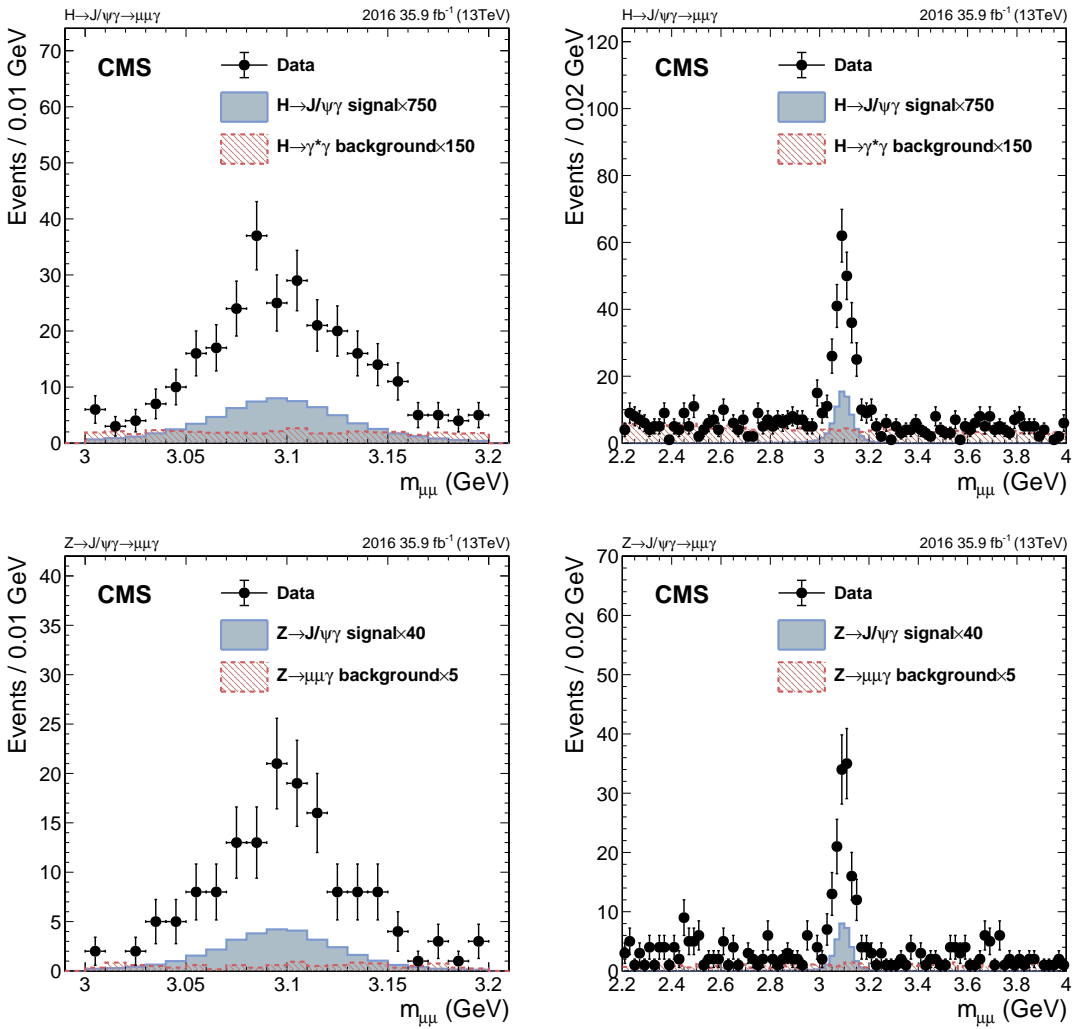


Figure 3-23: The $m_{\mu\mu}$ distributions from data and signal events of: $H \rightarrow J/\psi \gamma$ (top), Cat1 of $Z \rightarrow J/\psi \gamma$ decay (bottom).

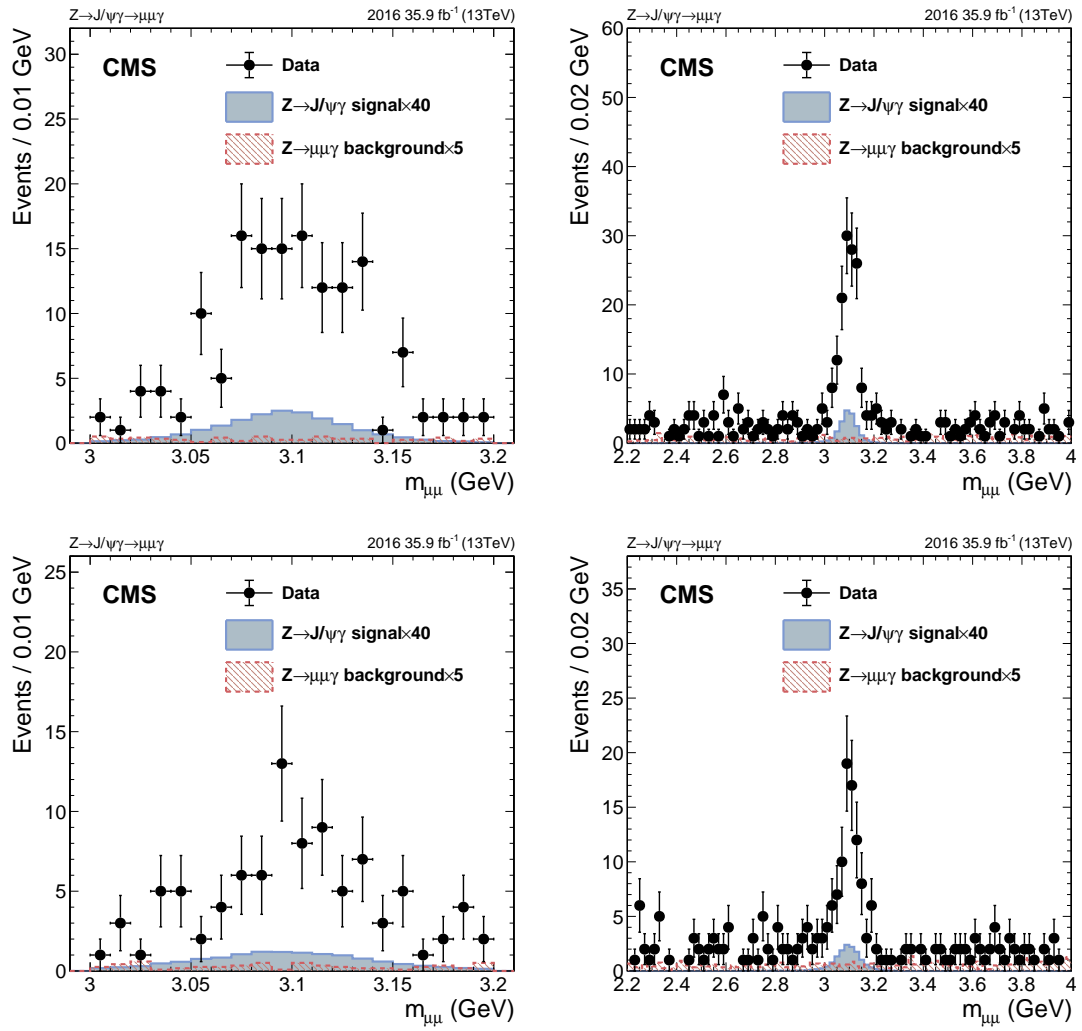


Figure 3-24: The $m_{\mu\mu}$ distributions from data and signal events of: Cat2 of $Z \rightarrow J/\psi \gamma$ decay (top), and Cat3 of $Z \rightarrow J/\psi \gamma$ decay (bottom).

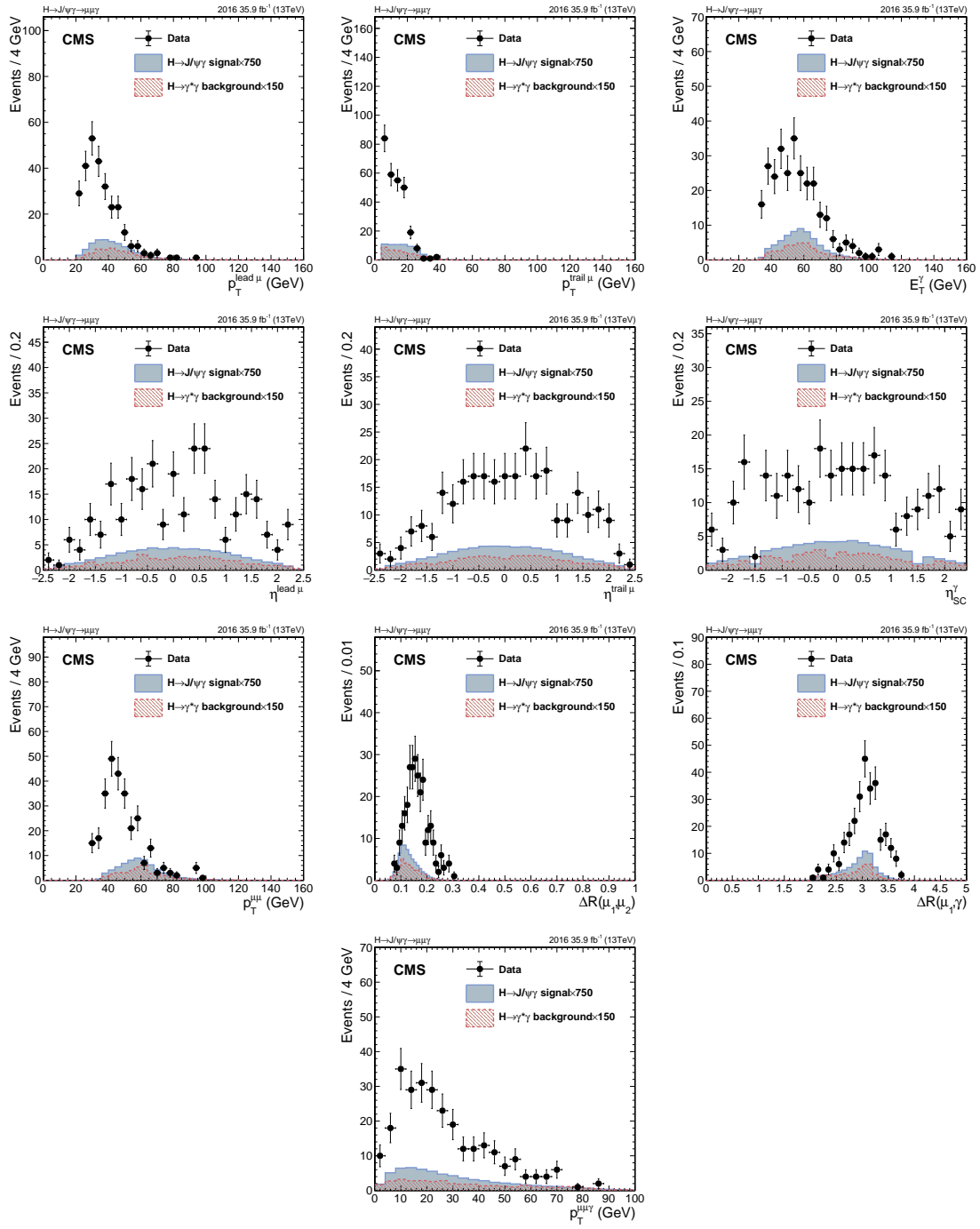


Figure 3-25: Distributions of the key variables from data and signal events in $H \rightarrow J/\psi \gamma$ decay. Transverse momenta of the muons and the photon; pseudorapidity of the muons and the photon; transverse momenta of the dimuon system; distances ΔR between the two muons and between the leading muon and the photon; the transverse momenta of the three-body system, $p_T^{\mu\mu\gamma}$

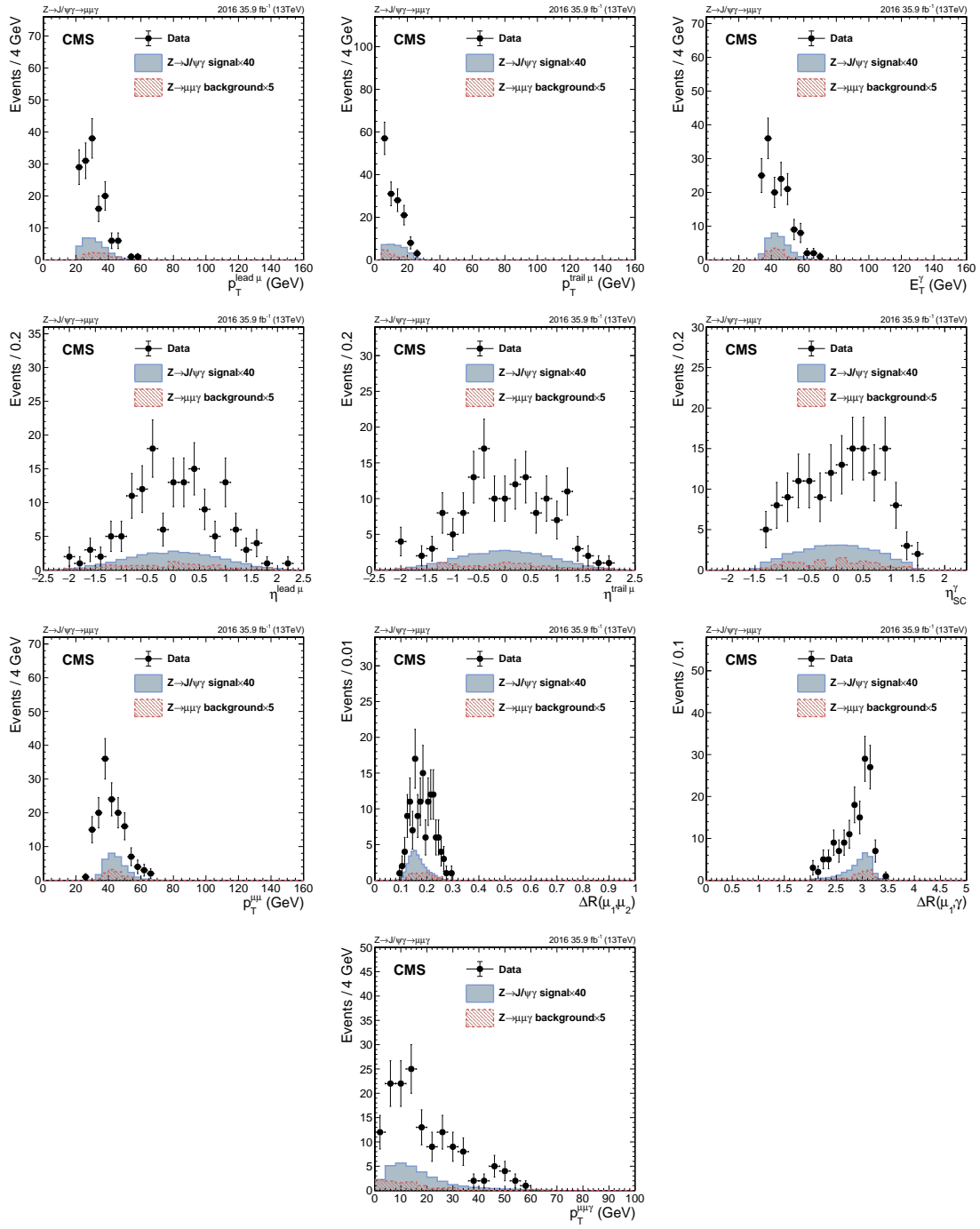


Figure 3-26: Distributions of the key variables from data and signal events of Cat1 in $Z \rightarrow J/\psi \gamma$ decay. Transverse momenta of the muons and the photon; pseudorapidity of the muons and the photon; Transverse momenta of the dimuon system; distances ΔR between the two muons and between the leading muon and the photon; the transverse momenta of the three-body system, $p_T^{\mu\mu\gamma}$.

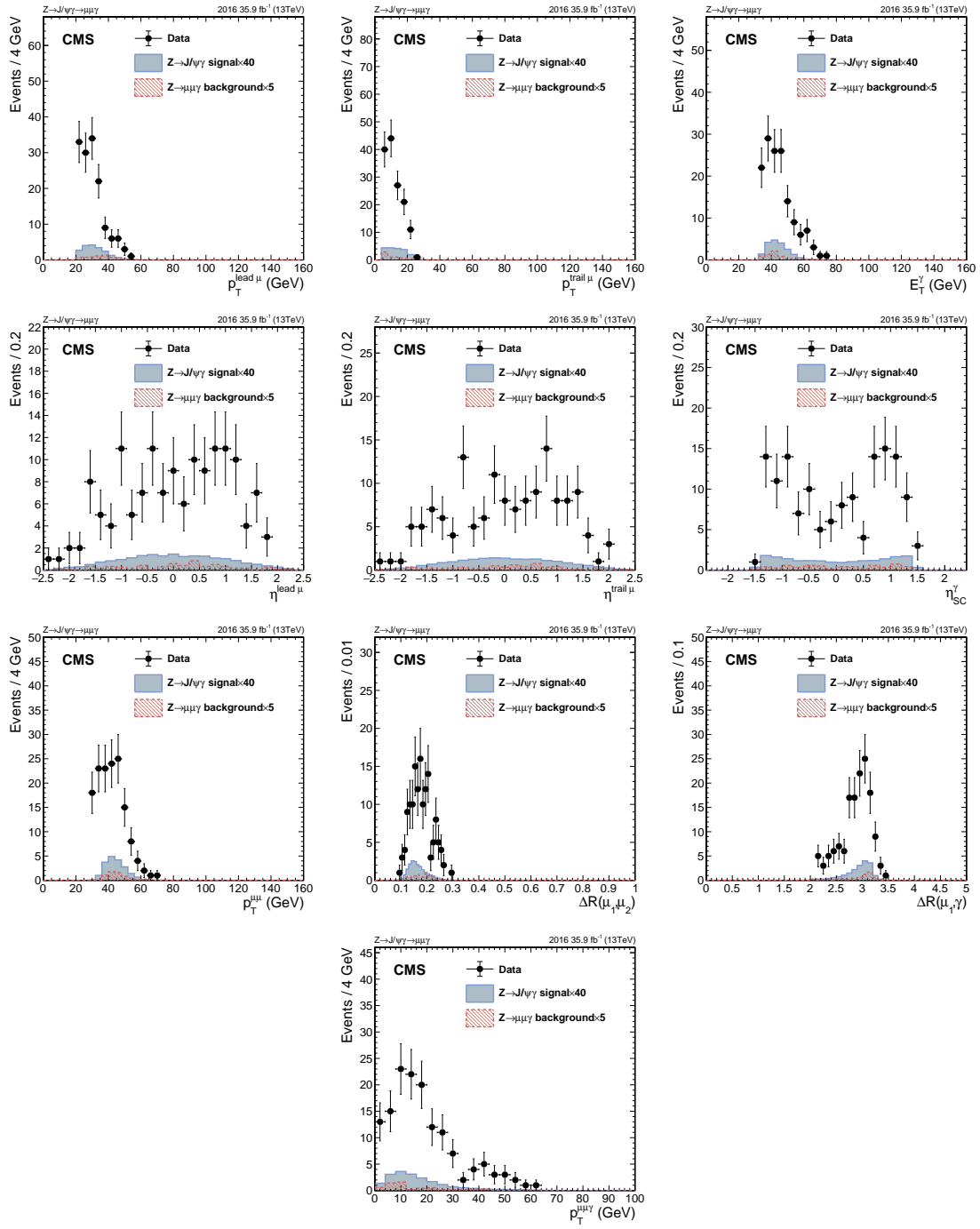


Figure 3-27: Distributions of the key variables from data and signal events of Cat2 in $Z \rightarrow J/\psi \gamma$ decay. Transverse momenta of the muons and the photon; pseudorapidity of the muons and the photon; Transverse momenta of the dimuon system; distances ΔR between the two muons and between the leading muon and the photon; the transverse momenta of the three-body system, $p_T^{\mu\mu\gamma}$.

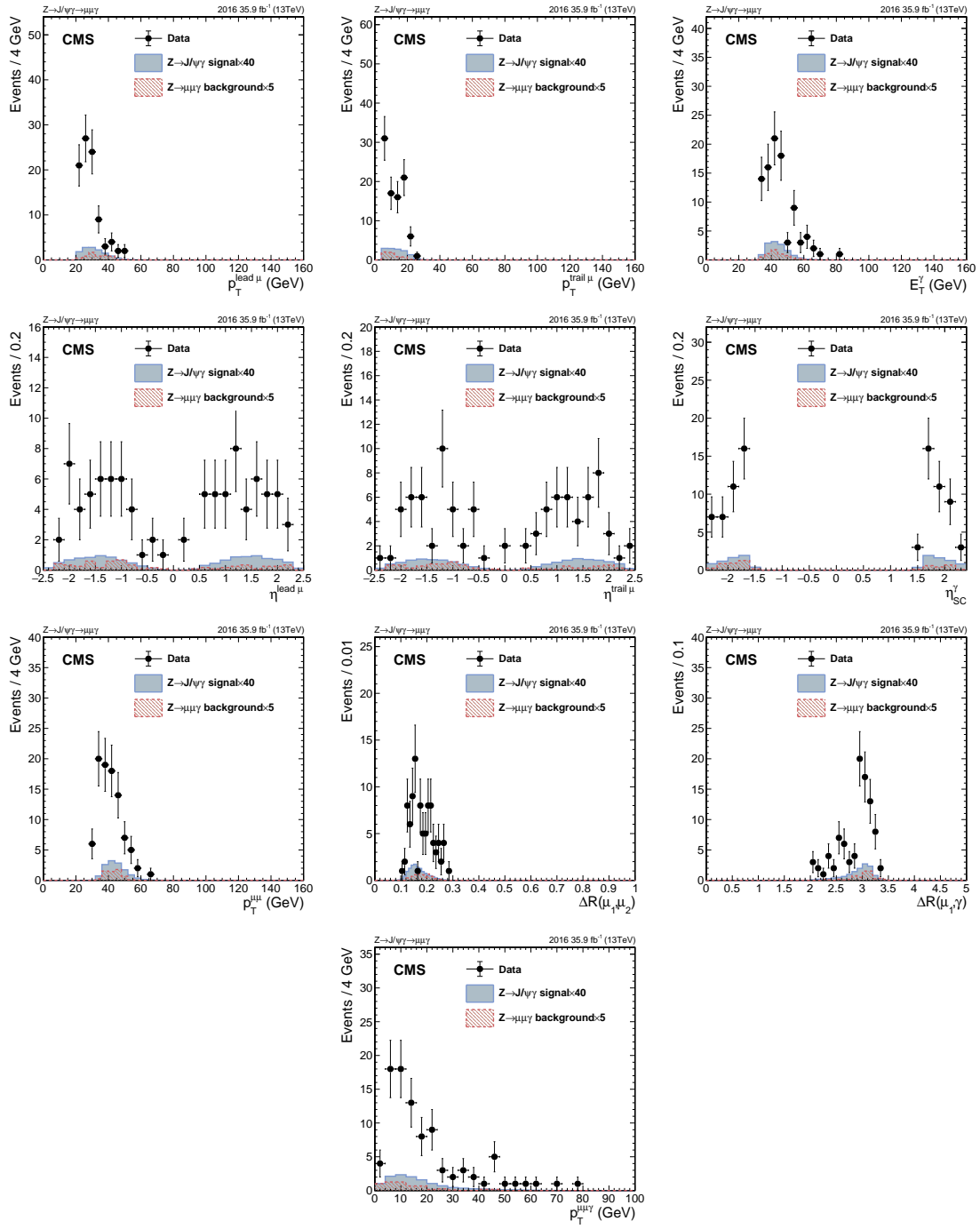


Figure 3-28: Distributions of the key variables from data and signal events of Cat3 in $Z \rightarrow J/\psi \gamma$ decay. Transverse momenta of the muons and the photon; pseudorapidity of the muons and the photon; Transverse momenta of the dimuon system; distances ΔR between the two muons and between the leading muon and the photon. the transverse momenta of the three-body system, $p_T^{\mu\mu\gamma}$.

1411 A study of the muon vertex is done to ensure whether the reconstructed J/ψ
1412 after the full selection are promptly produced at the pp interaction point, referred
1413 to as “prompt J/ψ ”, and not from the displaced heavy hadron decays, referred to
1414 as “non-prompt J/ψ ”. It is expected that in signal events the J/ψ are produced
1415 promptly since the lifetimes of the Z and Higgs boson are very short.

1416 Vertex-related variables examined in this study are:

- 1417 • Dimuon vertex position (x, y and z coordinates)
- 1418 • The transverse decay length $L_{xy} = \frac{\vec{r}_T \cdot \vec{p}_T^{J/\psi}}{|\vec{p}_T^{J/\psi}|}$, where \vec{r}_T is the vector from PV
1419 to the dimuon vertex in transverse plane.
- 1420 • $R_{xy} = |L_{xy}|$
- 1421 • $SL_{xy} = |L_{xy}|/\sigma(L_{xy})$. The significance of the L_{xy} is defined as the absolute
1422 value of L_{xy} divided by its error $\sigma(L_{xy})$.
- 1423 • $\text{Cos}(\alpha)$, where α is defined as the angle between the reconstructed momen-
1424 tum vector of the dimuon system and the vector from the PV to the dimuon
1425 vertex.
- 1426 • Dimuon vertex χ^2 , one of the indicators of the goodness of the fit
- 1427 • Dimuon vertex probability, which is the chi-square probability given the dimuon
1428 vertex χ^2 and the number of degree of freedom in the fit.
- 1429 • Validity of the dimuon vertex. The vertex returned may not be valid in some
1430 cases. The status of the vertex will be invalid when the maximum number of
1431 iterations is exceeded or the fitted position is out of the tracker bounds.
- 1432 • Proper decay time $t = \frac{m_{J/\psi}}{p_T^{J/\psi}} \cdot L_{xy}$, where the $m_{J/\psi}$ is the mass of the recon-
1433 structed J/ψ candidate

1434 The distributions of the vertex-related variables from data (in black points with
1435 error bars) and signal (filled histograms) for the Higgs and Z boson searches are
1436 shown in Figs. 3-30, 3-31, 3-32, and 3-33. These distributions are normalized to the

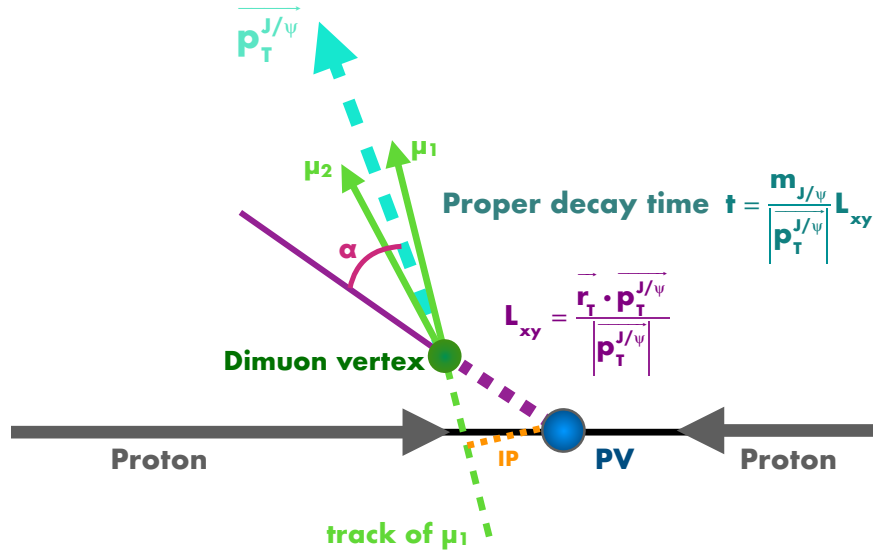


Figure 3-29: Schematic figure for vertex variables.

1437 number of selected events in data to enable a comparison between the shapes of
 1438 the distributions for the simulated signals and the data. The distributions suggest
 1439 that the J/ψ candidates reconstructed in data, like the signal events, are produced
 1440 promptly at the pp interaction point, rather than coming from displaced heavy
 1441 hadron decays. Based on the above-mentioned argument, no additional require-
 1442 ment associated with these vertex variables is imposed any, since the d_{xy} , d_z , and
 1443 the SIP_{3D} cuts already reject non-prompt J/ψ .

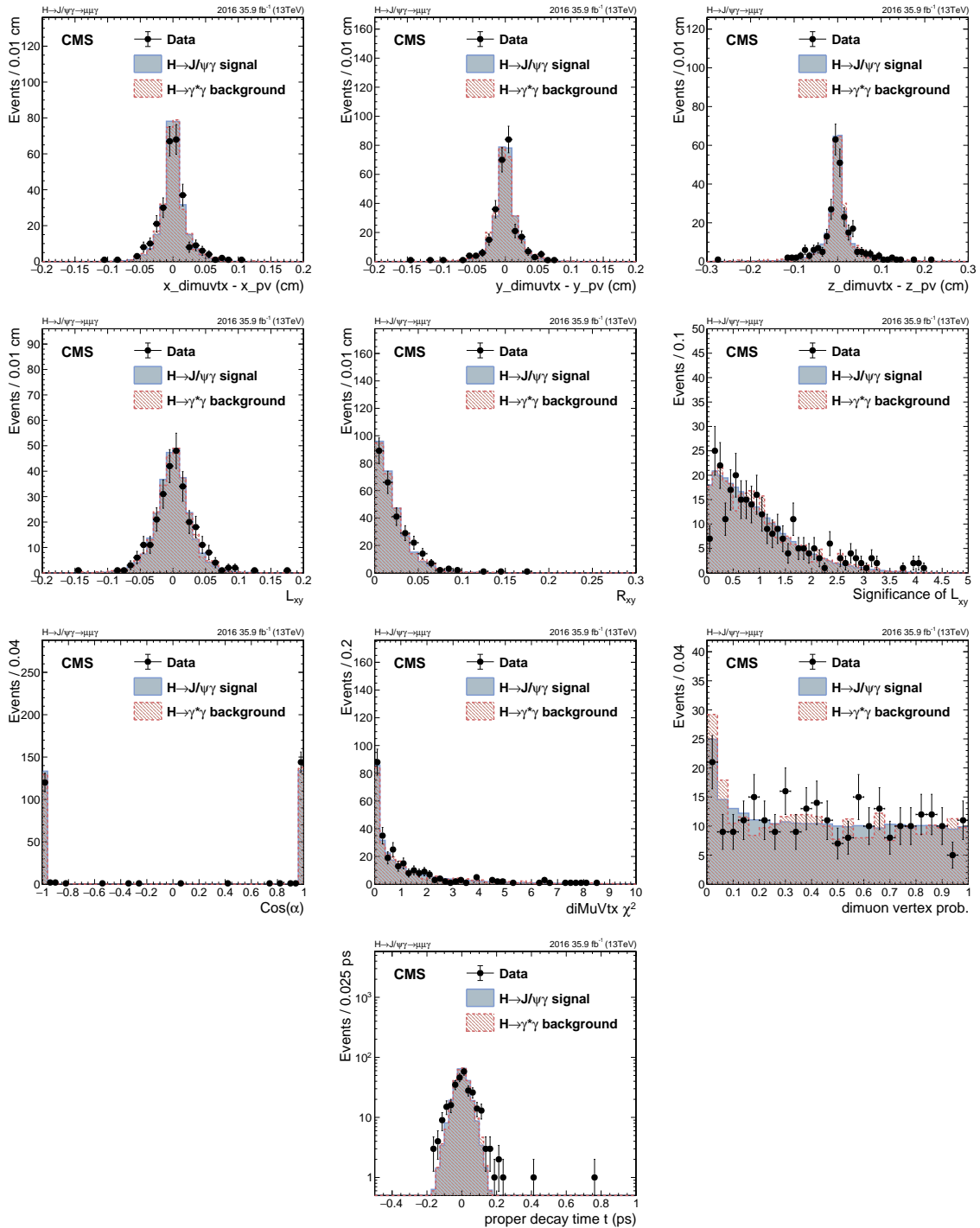


Figure 3-30: Distributions of the vertex-related variables from data and signal events in $H \rightarrow J/\psi \gamma$ decay.

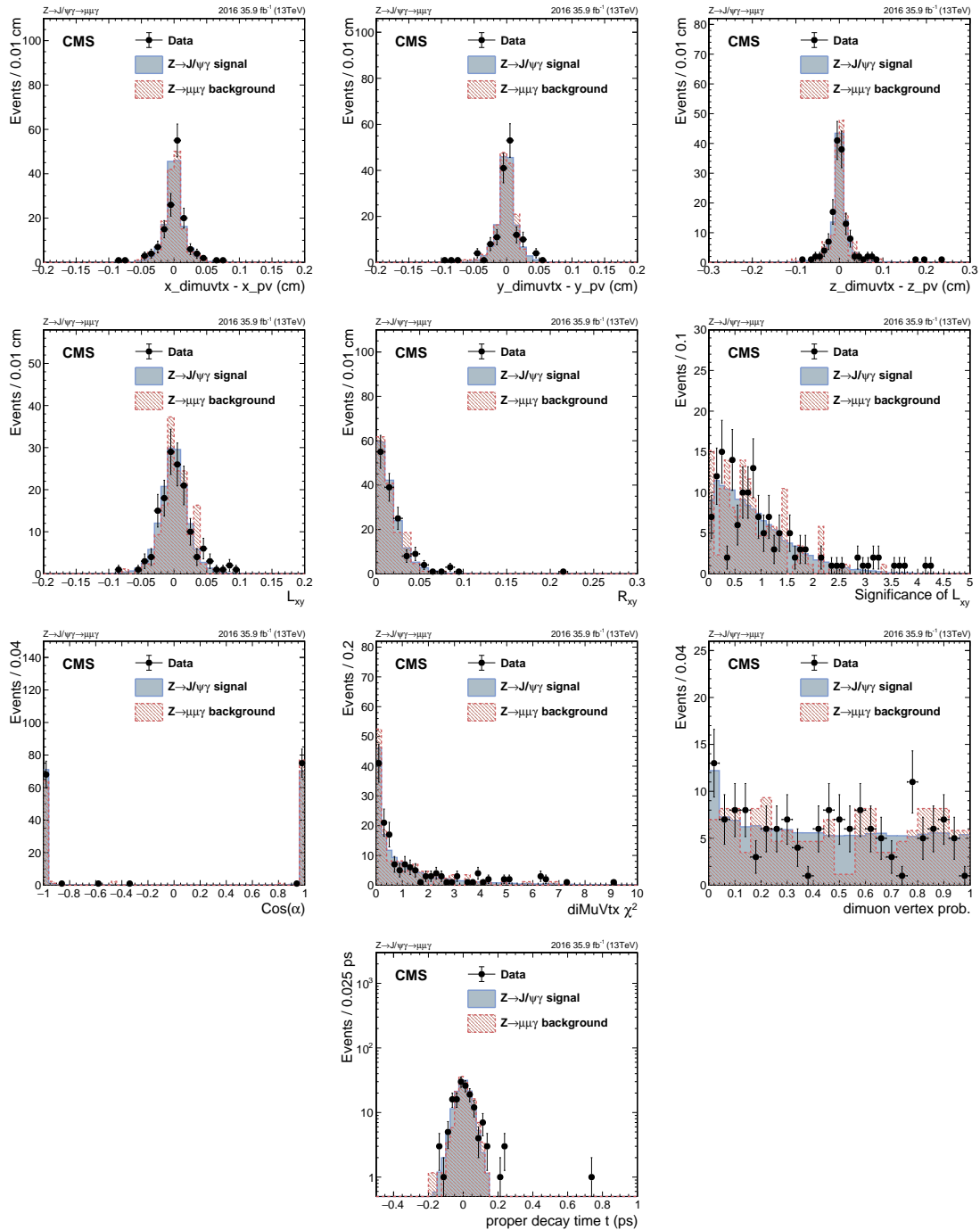


Figure 3-31: Distributions of the vertex-related variables from data and signal events of Cat1 in $Z \rightarrow J/\psi \gamma$ decay.

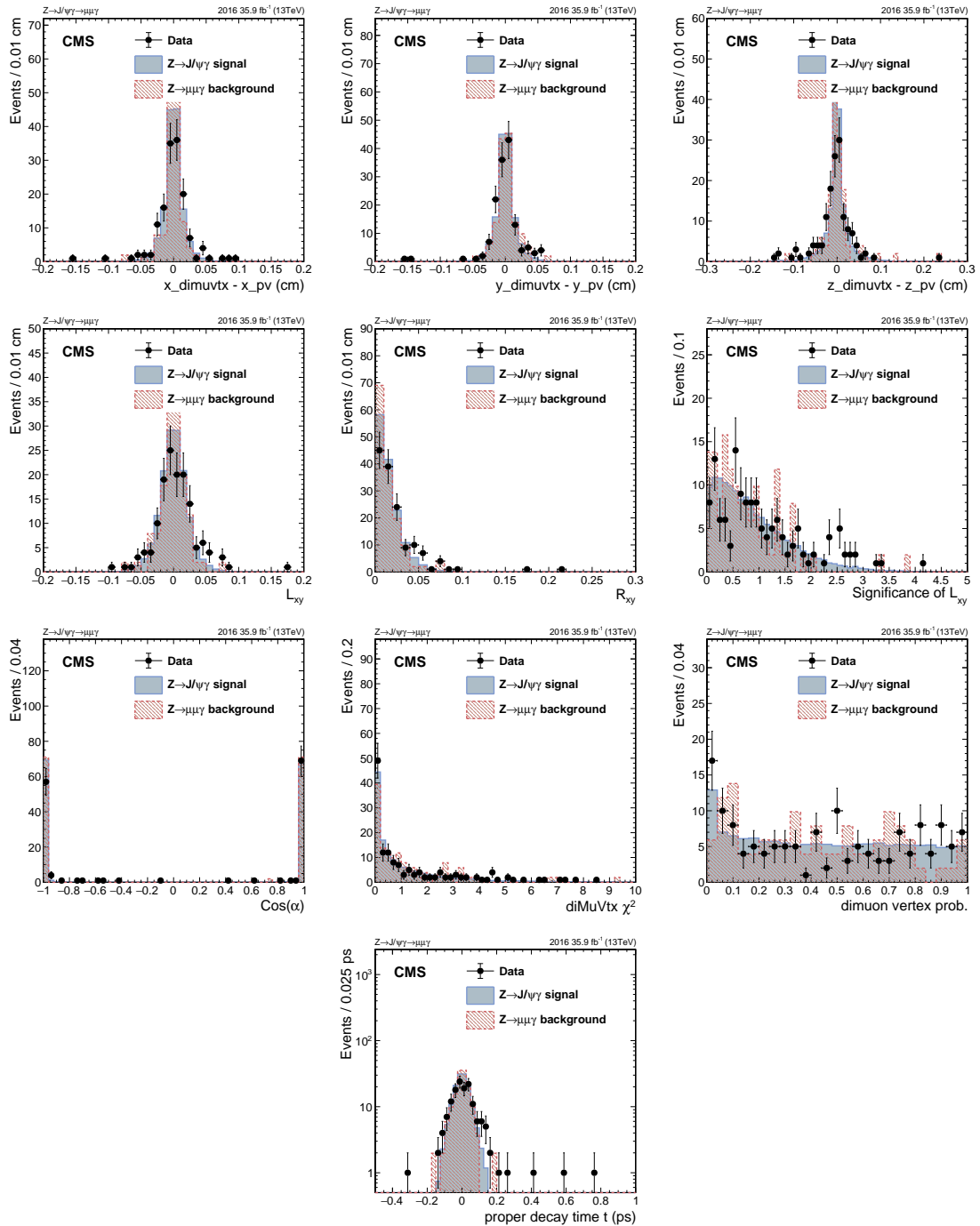


Figure 3-32: Distributions of the vertex-related variables from data and signal events of Cat2 in $Z \rightarrow J/\psi \gamma$ decay.

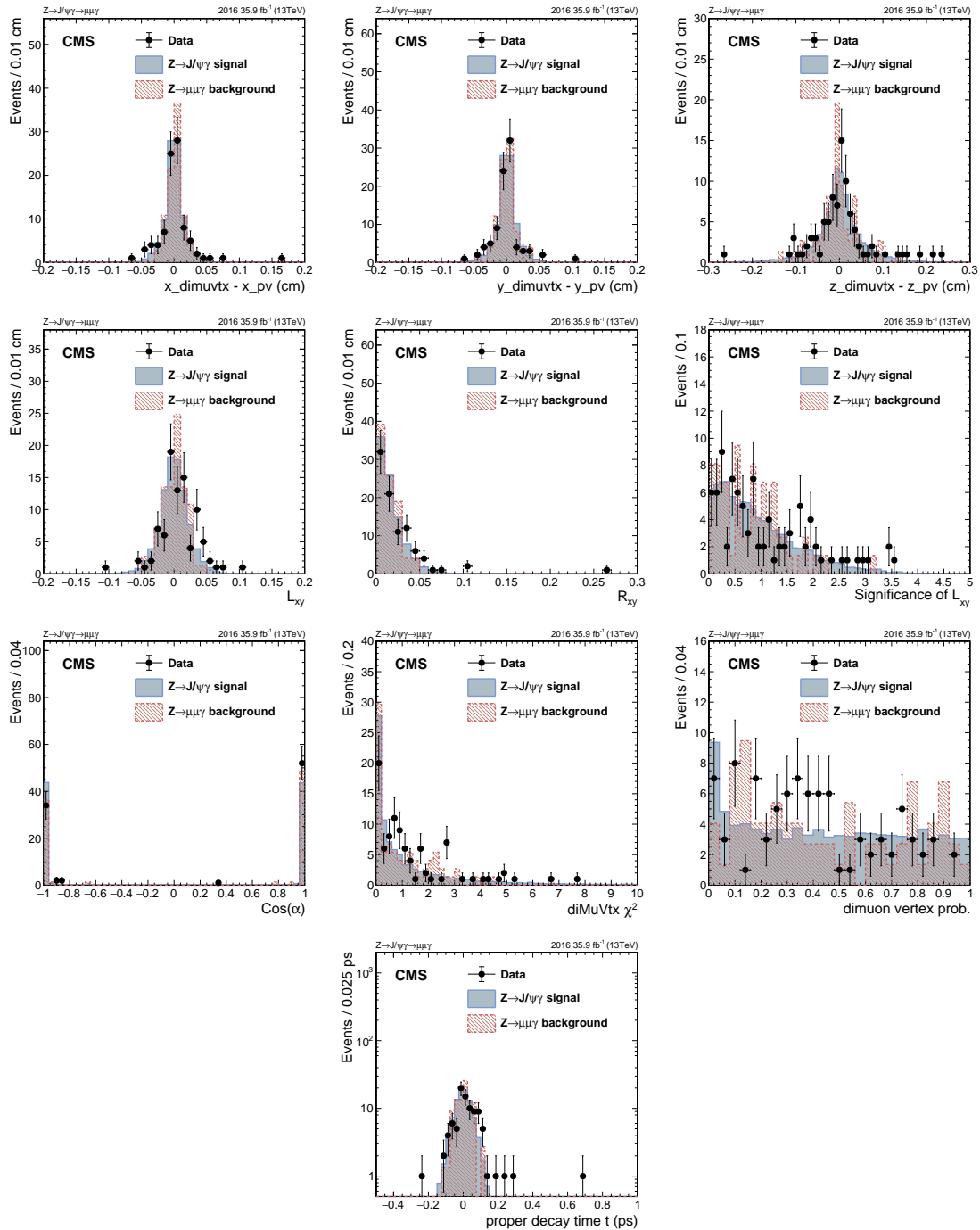


Figure 3-33: Distributions of the vertex-related variables from data and signal events of Cat3 in $Z \rightarrow J/\psi\gamma$ decay.

1444 3.5 Background modeling

1445 While the sub-dominant, peaking, backgrounds are estimated from the simulated
 1446 samples, the dominant continuum background of each category of both the Z and
 1447 Higgs boson decays is estimated and modeled from data by fitting parameteric
 1448 functions to the $m_{\mu\mu\gamma}$ distributions. An un-binned maximum likelihood fit is per-
 1449 formed over the range 70 (100) $< m_{\mu\mu\gamma} < 120$ (150) GeV for the Z (H) $\rightarrow J/\psi \gamma$
 1450 search.

1451 The following functions are considered:

- 1452 • Bernstein polynomials of order N (NPol)

$$\text{Bern}_N(m_{\mu\mu\gamma}) = \sum_{i=1}^N f_i^2 \binom{N}{i} m_{\mu\mu\gamma}^i (1 - m_{\mu\mu\gamma})^{N-i} \quad (3.4)$$

1453 with N free parameters.

- 1454 • A sum of N exponential functions

$$N\text{Exp}(m_{\mu\mu\gamma}) = \sum_{i=1}^N f_i e^{p_i (m_{\mu\mu\gamma})} \quad (3.5)$$

1455 with $2N - 1$ free parameters: $p_i < 0$ and f_i . The lowest order considered has
 1456 $N = 1$, i.e. one term.

- 1457 • The sum of N power-functions

$$N\text{Pow}(m_{\mu\mu\gamma}) = \sum_{i=1}^N f_i (m_{\mu\mu\gamma})^{p_i}, \quad (3.6)$$

1458 with $2N - 1$ free parameters $p_i < 0$ and f_i . The lowest order considered has
 1459 $N = 1$, i.e. one term.

- 1460 • Laurent series with 2, 3 and 4 terms

$$2\text{Lau}(m_{\mu\mu\gamma}) = f_2 (m_{\mu\mu\gamma})^{-4} + f_3 (m_{\mu\mu\gamma})^{-5}, \quad (3.7)$$

$$3\text{Lau}(m_{\mu\mu\gamma}) = f_1(m_{\mu\mu\gamma})^{-3} + f_2(m_{\mu\mu\gamma})^{-4} + f_3(m_{\mu\mu\gamma})^{-5}, \quad (3.8)$$

1461 and

$$4\text{Lau}(m_{\mu\mu\gamma}) = f_1(m_{\mu\mu\gamma})^{-3} + f_2(m_{\mu\mu\gamma})^{-4} + f_3(m_{\mu\mu\gamma})^{-5} + f_4(m_{\mu\mu\gamma})^{-6}, \quad (3.9)$$

1462 with N free parameters $f_1 \dots f_4$.

1463 Fits to the $m_{\mu\mu\gamma}$ distributions in data from the Higgs and Z boson decays using
1464 different functions are shown on Fig.3-34. To choose the best fit function out of the
1465 above-mentioned families of functions, a F-test is performed and follows with the
1466 bias study. F-test is performed for all the functions except for Bernstein polyno-
1467 mials. For Bernstein family, the bias study is performed all the orders up to order
1468 6.

1469 3.5.1 F-test

1470 To choose the best fit order from a family of functions, a F-test on data is per-
1471 formed. First, for a given family, the lowest order function in that family is fit to
1472 a single category. Then, the next order function is fit to the data in the same cat-
1473 egory. The difference of twice the negative log-likelihood(NLL) between the two
1474 fits, $2\Delta NLL_{N+1} = 2(NLL_{N+1} - NLL_N)$, indicates the improvement of the fit and
1475 whether or not the data support the hypothesis of the higher order function. This
1476 argument is made by the fact that the $2\Delta NLL_{N+1}$ should be distributed as a χ^2 dis-
1477 tribution of M degrees of freedom, where M is the difference in the number of free
1478 parameters in the $(N+1)_{th}$ -order function and N_{th} -order function. For example,
1479 for exponential family, $M = [2(N+1) - 1] - [2(N) - 1] = 2$, while for the Bern-
1480 stein polynomials $M = (N+1) - (N) = 1$. A p-value is defined and calculated
1481 as

$$\text{p-value} = p(2\Delta NLL > 2\Delta NLL_{N+1} | \chi^2(M)). \quad (3.10)$$

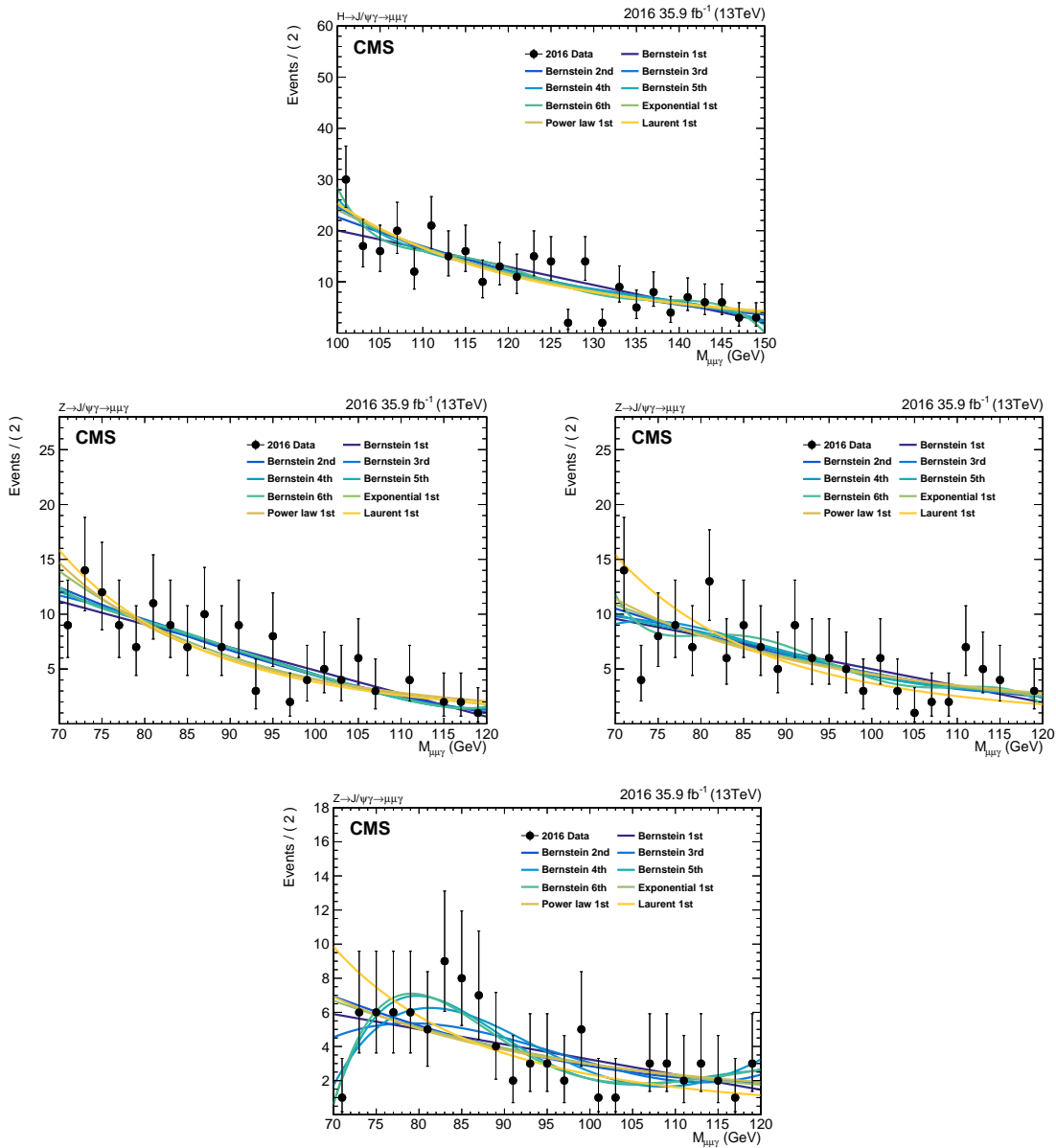


Figure 3-34: Fits on the three-body invariant mass $m_{\mu\mu\gamma}$ distributions of data for $H \rightarrow J/\psi \gamma$ (top), $Z \rightarrow J/\psi \gamma$ Cat1 (middle left), $Z \rightarrow J/\psi \gamma$ Cat2 (middle right), and $Z \rightarrow J/\psi \gamma$ Cat3 (bottom).

1482 If the p-value is less than 0.05, the higher order function is supported by the
 1483 data since the probability of obtaining a NLL with $(N + 1)_{th}$ order function being
 1484 greater or equal to a NLL with N_{th} function is small. The procedure then continues
 1485 to test the next higher order function in the family. If the p-value is more than 0.05,
 1486 meaning that an additional increase of parameters does not result in a significant
 1487 improvement of the fit. Therefore the higher order function is considered to be too
 1488 flexible for the given $m_{\mu\mu\gamma}$ distribution in data. The procedure terminates, and the
 1489 highest order of function in a family is found.

1490 As a result, the functions with 1 degree of freedom of exponential, power law,
 1491 and Laurent form are picked up by the F-test. These 3 functions with Bernstein
 1492 polynomials from 1st to 6th order will be tested in the bias study.

Table 3.14 shows the functions to be used in the bias study.

Category	Bernstein polynomial	Exponential	Power-law	Laurent
$H \rightarrow J/\psi \gamma$				
Inclusive	1st - 6th	1Exp	1Pow	1Lau
$Z \rightarrow J/\psi \gamma$				
Cat1, EB_HR9	1st - 6th	1Exp	1Pow	1Lau
Cat2, EB_LR9	1st - 6th	1Exp	1Pow	1Lau
Cat3, EE	1st - 6th	1Exp	1Pow	1Lau

Table 3.14: The functions to be used in the bias study for both Higgs and Z decays.

1493

1494 3.5.2 Bias study

1495 Bias study is performed to determine the best function out of those resulting from
 1496 the F-test. The procedures of bias study are as follows. One of the functions listed
 1497 in Table 3.14 is chosen to fit to $m_{\mu\mu\gamma}$ distribution from data events. Pseudo-events
 1498 are randomly generated by using the resulting fit (referred to as the true func-
 1499 tion) as background model to simulate possible experiment results. Signal events
 1500 with signal strength μ_{True} are introduced when generating the pseudo-events. We
 1501 should note that $\mu_{True} = 1$ corresponds to injecting $1 \times (\text{expected signal yield})$
 1502 events on top of the background. A fit is made to the distribution using one of the

functions in the four families combined with a signal model, where the normalization of the signal in this step is allowed to be negative. This procedure is repeated many times, and it's expected that ideally on average the signal strength predicted by the fit μ_{Fit} will be equal to μ_{True} . A pull value, defined as $(\mu_{\text{Fit}} - \mu_{\text{True}}) / \sigma_{\text{Fit}}$, where σ_{Fit} is the error on μ_{Fit} , is calculated for each pseudo-event. The criteria used to determine the unbiased fit is that, the distribution of the pull value $(\mu_{\text{Fit}} - \mu_{\text{True}}) / \sigma_{\text{Fit}}$ from all pseudo-events with a given combination of true and fit function should be a Gaussian with a mean value less than 0.20 and width around 1. The criteria of 0.20 ensures that a possible bias is at least 20% times smaller than the statistical fluctuation, hence can be neglected. This also implies that the error on the frequentist coverage of the quoted measurement in the analysis is less than 1%, where the coverage is defined as the fraction of experiments in which the true value is contained within the confidence interval. Since the bias introduced by the unbiased fit is negligible, no additional uncertainty is assigned for the background modeling.

The 2-D bias maps of the study with true function (used to generate the toys) on the X-axis and the fitted function (used to fit the toys) on the Y-axis of $H \rightarrow J/\psi \gamma$ (Fig 3-35), Cat1 in $Z \rightarrow J/\psi \gamma$ (Fig. 3-36), Cat2 in $Z \rightarrow J/\psi \gamma$ (Fig. 3-37), and Cat3 in $Z \rightarrow J/\psi \gamma$ (Fig. 3-38) are shown. For the $H \rightarrow J/\psi \gamma$, the table with $\mu_{\text{True}} = 300$ is shown. For all the three categories of $Z \rightarrow J/\psi \gamma$, the tables with $\mu_{\text{True}} = 200$ are shown.

The pull-value distributions are shown in Fig. 3-39, 3-40, 3-41, and 3-42. Some of the pseudo-events generated in this study are shown in Appendix A.

For the $H \rightarrow J/\psi \gamma$ channel, the lowest order satisfying the criteria of bias 20% is Bernstein polynomial of 2nd order. For the $Z \rightarrow J/\psi \gamma$ channel, the lowest order satisfying the criteria for all three categories are Bernstein polynomial of 3rd order.

The background fits with the best fit functions for both Higgs and Z boson are shown in Fig 3-43 (Top: $H \rightarrow J/\psi \gamma$; Middle left: Cat1 of $Z \rightarrow J/\psi \gamma$); Middle right: Cat2 of $Z \rightarrow J/\psi \gamma$; Bottom: Cat3 of $Z \rightarrow J/\psi \gamma$).

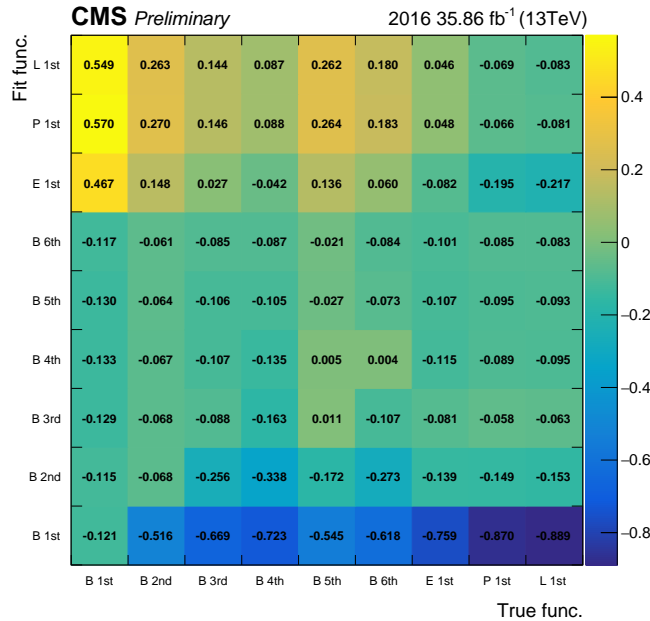


Figure 3-35: The 2-D bias maps of the study for $\mu_{\text{True}} = 300$ with true function (used to generate the toys) on the X-axis and the fitted function (used to fit the toys) on the Y-axis of $H \rightarrow J/\psi \gamma$

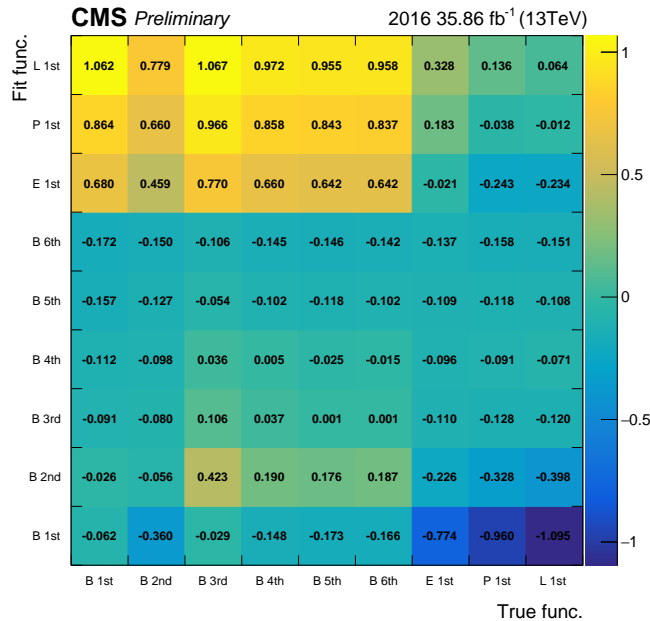


Figure 3-36: The 2-D bias maps of the study for $\mu_{\text{True}} = 200$ with true function (used to generate the toys) on the X-axis and the fitted function (used to fit the toys) on the Y-axis of Cat1 in $Z \rightarrow J/\psi \gamma$

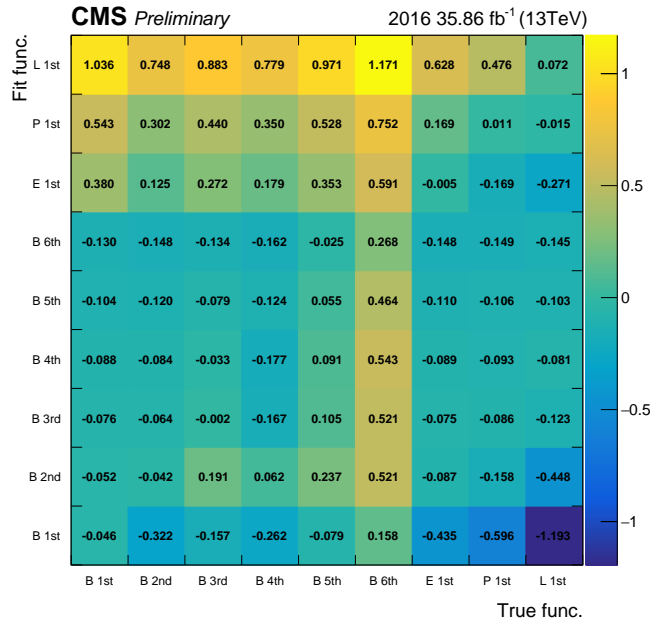


Figure 3-37: The 2-D bias maps of the study for $\mu_{\text{True}} = 200$ with true function (used to generate the toys) on the X-axis and the fitted function (used to fit the toys) on the Y-axis of Cat2 in $Z \rightarrow J/\psi \gamma$

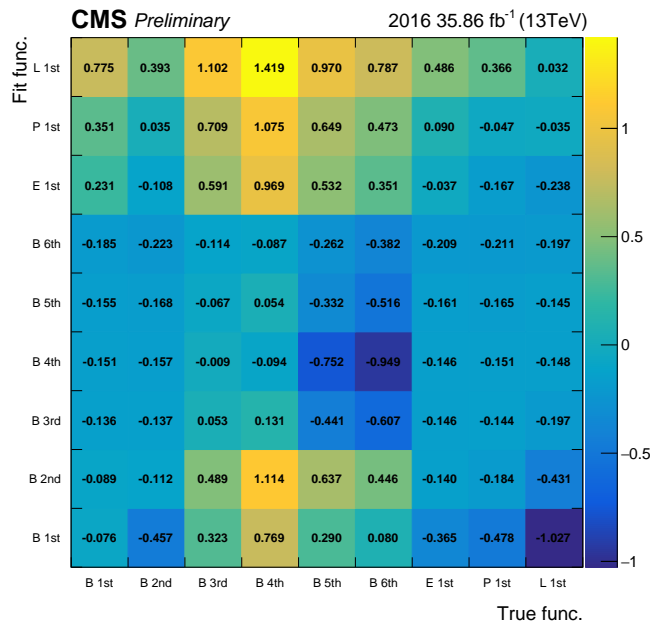


Figure 3-38: The 2-D bias maps of the study for $\mu_{\text{True}} = 200$ with true function (used to generate the toys) on the X-axis and the fitted function (used to fit the toys) on the Y-axis of Cat3 in $Z \rightarrow J/\psi \gamma$

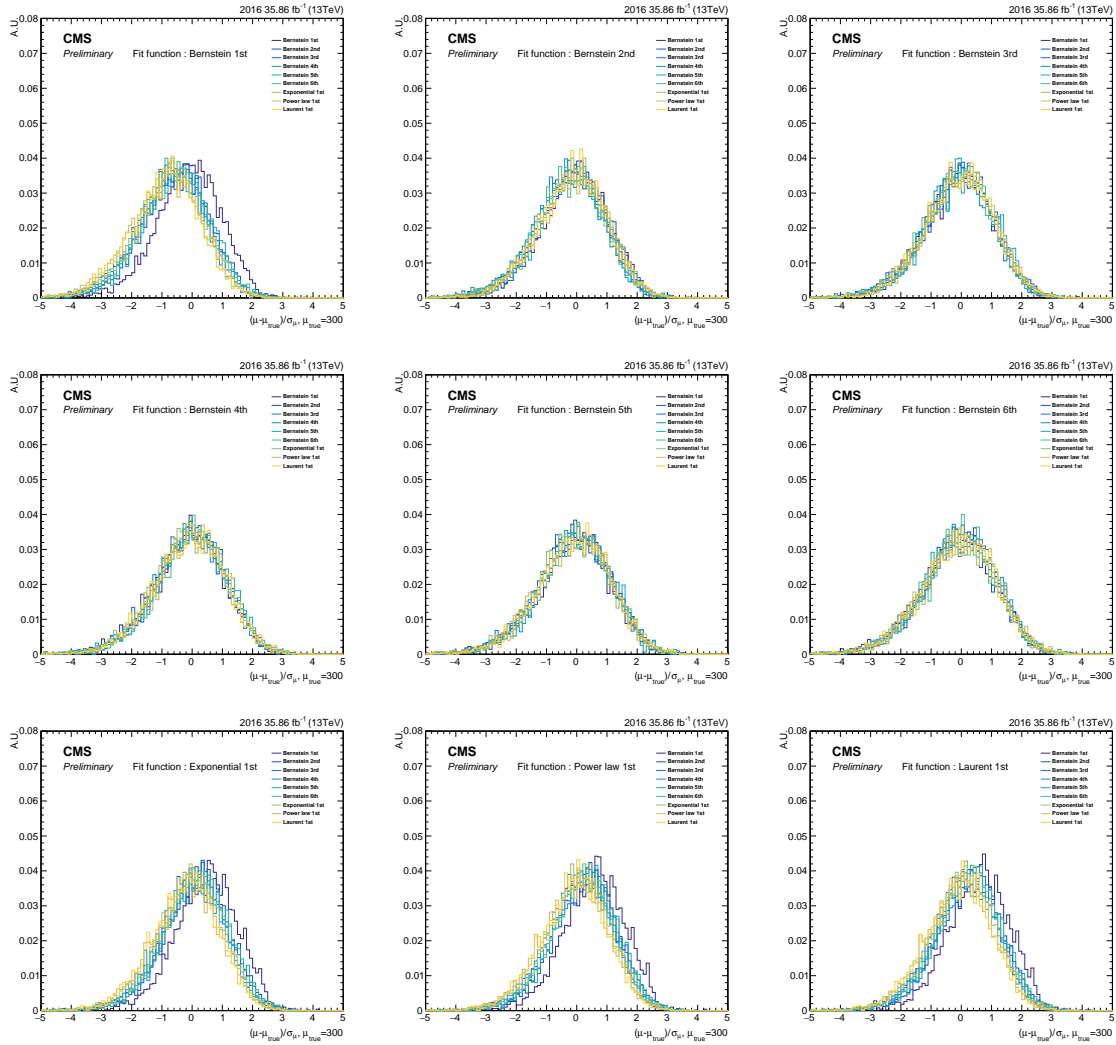


Figure 3-39: The pull-value distributions of bias study in the Higgs boson search. In these plots, the legend labels the distributions using different true functions. The fit function of each plots is: (Top left) Bernstein of 1st order; (Top middle) Bernstein of 2nd order; (Top right) Bernstein of 3rd orderl; (Middle left) Bernstein of 4th order; (Middle central) Bernstein of 5th order; (Middle right) Bernstein of 6th order; (Bottom left) Exponential with 1 d.o.f (1Exp); (Bottom middle) Power law with 1 d.o.f (1Pow); (Bottom right) Laurent series with 2 terms (1Lau).

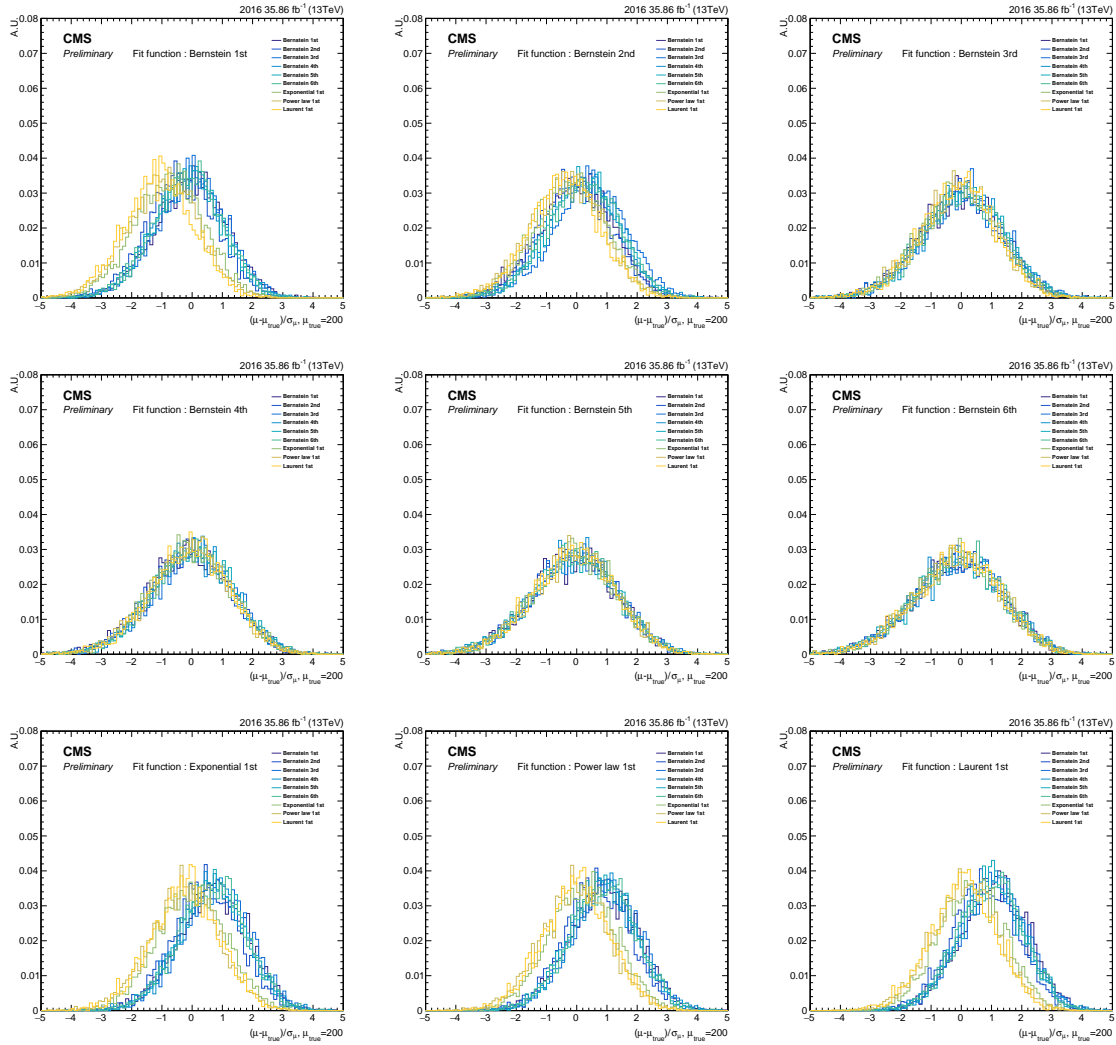


Figure 3-40: The pull-value distributions of bias study of Cat1 in the Z boson search. In these plots, the legend labels the distributions using different true functions. The fit function of each plots is: (Top left) Bernstein of 1st order; (Top middle) Bernstein of 2nd order; (Top right) Bernstein of 3rd order; (Middle left) Bernstein of 4th order; (Middle central) Bernstein of 5th order; (Middle right) Bernstein of 6th order; (Bottom left) Exponential with 1 d.o.f (1Exp); (Bottom middle) Power law with 1 d.o.f (1Pow); (Bottom right) Laurent series with 2 terms (1Lau).

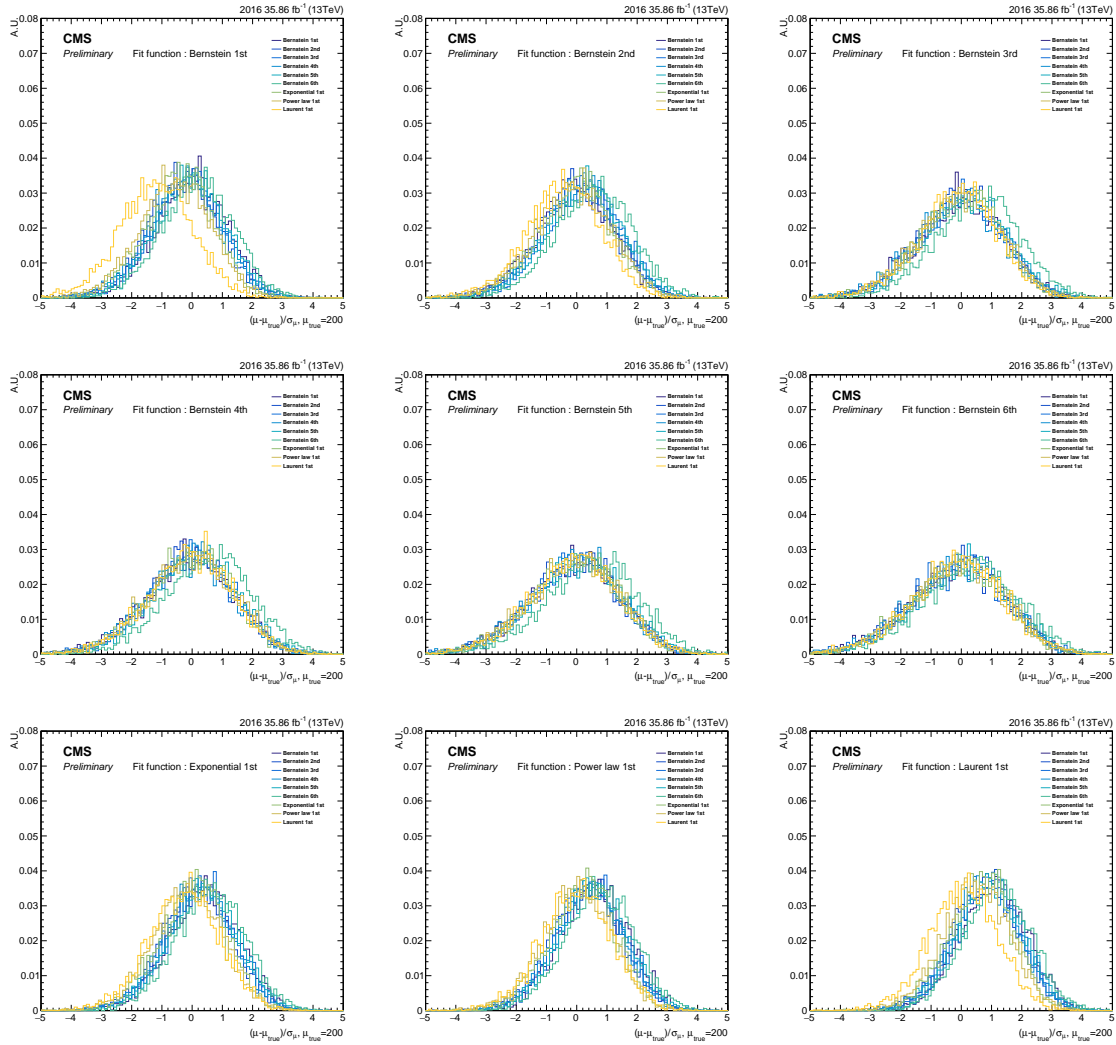


Figure 3-41: The pull-value distributions of bias study of Cat2 in the Z boson search. In these plots, the legend labels the distributions using different true functions. The fit function of each plots is: (Top left) Bernstein of 1st order; (Top middle) Bernstein of 2nd order; (Top right) Bernstein of 3rd order; (Middle left) Bernstein of 4th order; (Middle central) Bernstein of 5th order; (Middle right) Bernstein of 6th order; (Bottom left) Exponential with 1 d.o.f (1Exp); (Bottom middle) Power law with 1 d.o.f (1Pow); (Bottom right) Laurent series with 2 terms (1Lau).

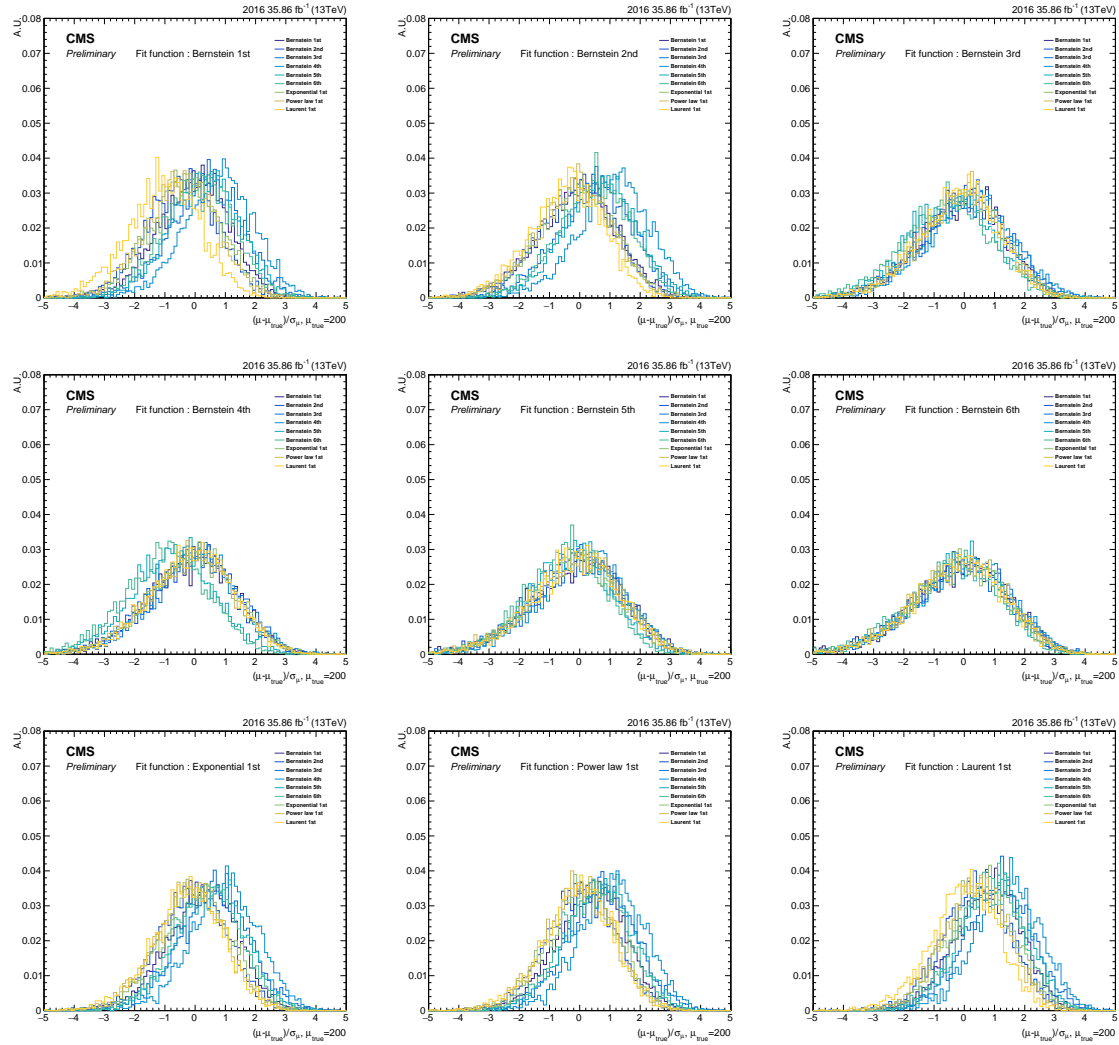


Figure 3-42: The pull-value distributions of bias study of Cat3 in the Z boson search. In these plots, the legend labels the distributions using different true functions. The fit function of each plots is: (Top left) Bernstein of 1st order; (Top middle) Bernstein of 2nd order; (Top right) Bernstein of 3rd order; (Middle left) Bernstein of 4th order; (Middle central) Bernstein of 5th order; (Middle right) Bernstein of 6th order; (Bottom left) Exponential with 1 d.o.f (1Exp); (Bottom middle) Power law with 1 d.o.f (1Pow); (Bottom right) Laurent series with 2 terms (1Lau).

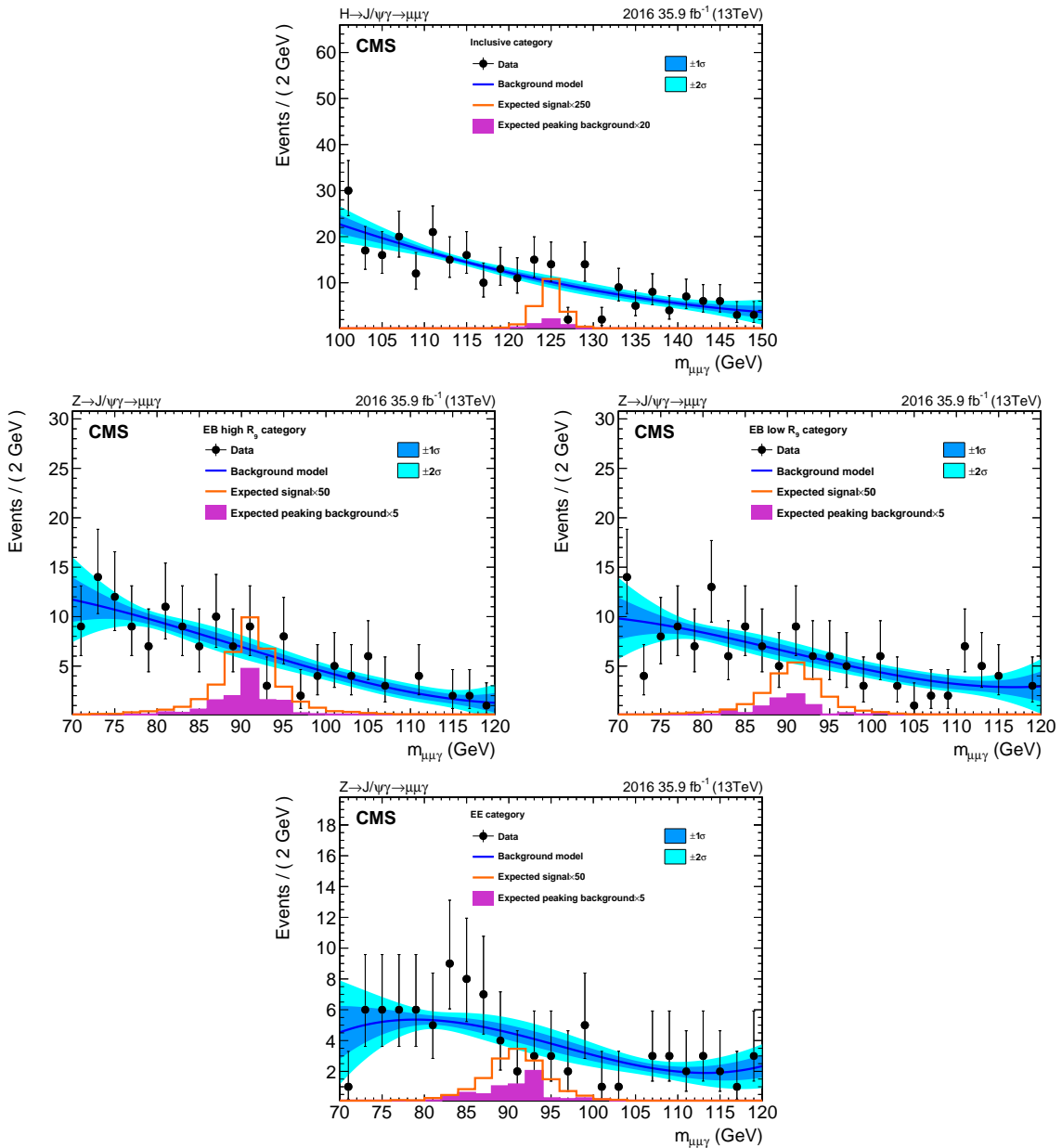


Figure 3-43: Non-resonant background fits with the lowest order unbiased functions to the three-body invariant mass $m_{\mu\mu\gamma}$ distributions observed in data for the $Z \rightarrow J/\psi\gamma$ channel in the EB high R_9 category (top left), the EB low R_9 category (top right), the EE category (bottom left), as well as the $H \rightarrow J/\psi\gamma$ channel (bottom right).

1532 **Motivation of B-only fit**

1533 Here we show the plots comparing background-only (B-only) with signal-plus-
1534 background (B+S) fit to motivate that including signal region in B-only fits does
1535 not change the background model significantly. 2 sets of comparisons are made.
1536 Fig. 3-44 shows the s+b fit where signal component is fixed to be the expected yield
1537 in each category. Fig. 3-45 shows the s+b fit where signal component is allowed to
1538 float when the fit is performed.

1539 Here, an argument is made that the B+S fit in the “full mass” range is actu-
1540 ally not too much different from B-only fit in sidebands in combination to signal
1541 shape, where the signal shape takes care the region, say, $\pm 2\sigma$ of the signal distribu-
1542 tion (that is, the range containing 95% of signal events). Then based on the plots
1543 attached previously, the conclusion can be drawn that the difference between the
1544 background model resulting from sideband region and that from the whole range
1545 is not significant at all.

1546 Another study is made with binned fit. Fig. 3-46 shows the sideband-only fit
1547 (in red) and the sideband-plus-signal region fit (in blue) to the event in $H \rightarrow J/\psi \gamma$
1548 search. The χ^2/NDF of each fit is also shown in the legend. The reasonable as-
1549 sumption in this study is that the resulting function forms from binned fit and
1550 un-binned fit are similar.

1551 As one can see, neither including the signal component in the fit does not have
1552 significant impact on the overall shape. Whether a sideband-only fit or not will not
1553 affect the background model much.

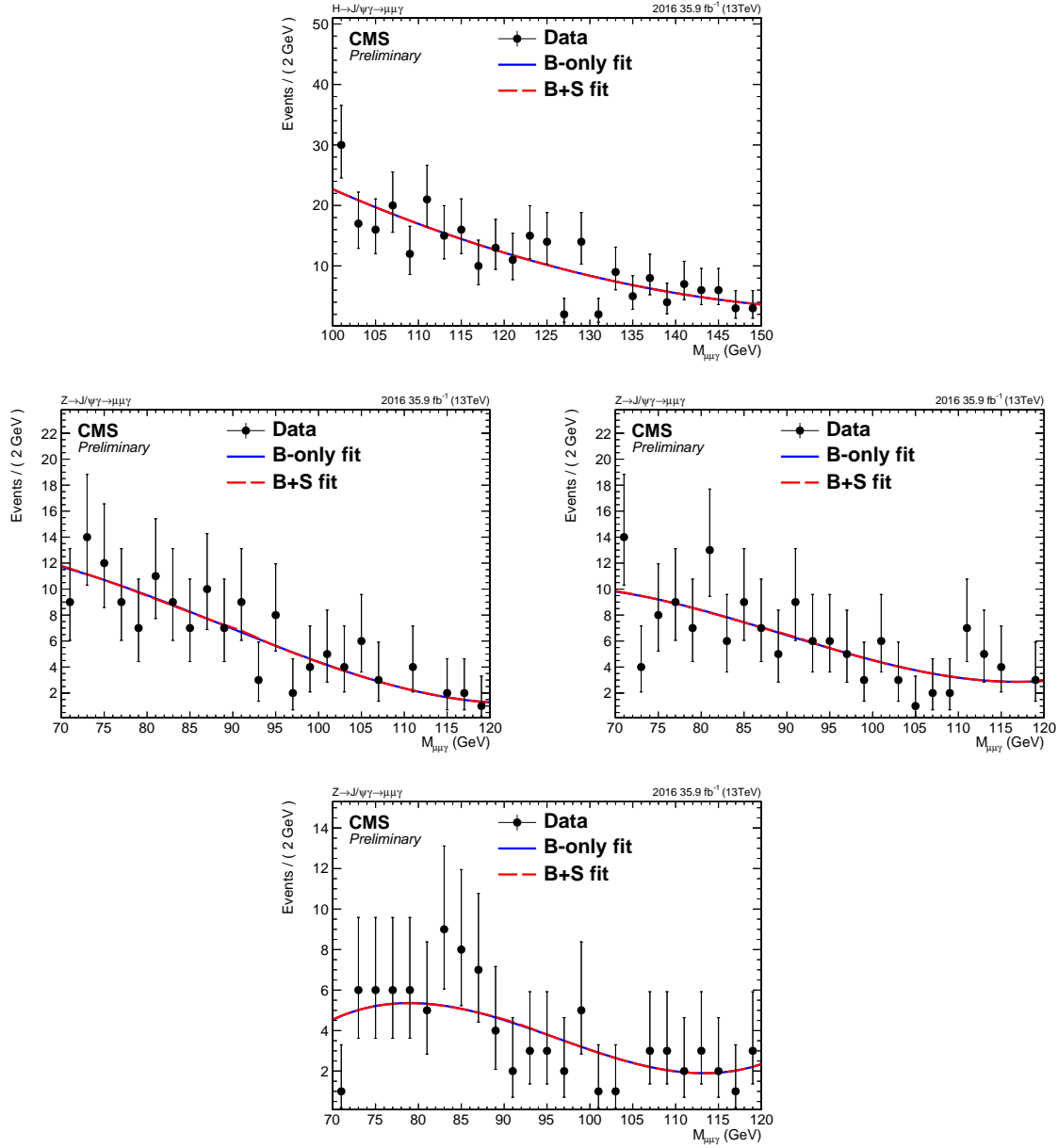


Figure 3-44: B+S fits, where signal component is fixed to be the expected yield in each category, with lowest order unbiased functions on the three-body invariant mass $m_{\mu\mu\gamma}$ distributions of data for $H \rightarrow (J/\psi)\gamma$ (top), $Z \rightarrow (J/\psi)\gamma$ Cat1 (middle left), $Z \rightarrow (J/\psi)\gamma$ Cat2 (middle right), and $Z \rightarrow (J/\psi)\gamma$ Cat3 (bottom).

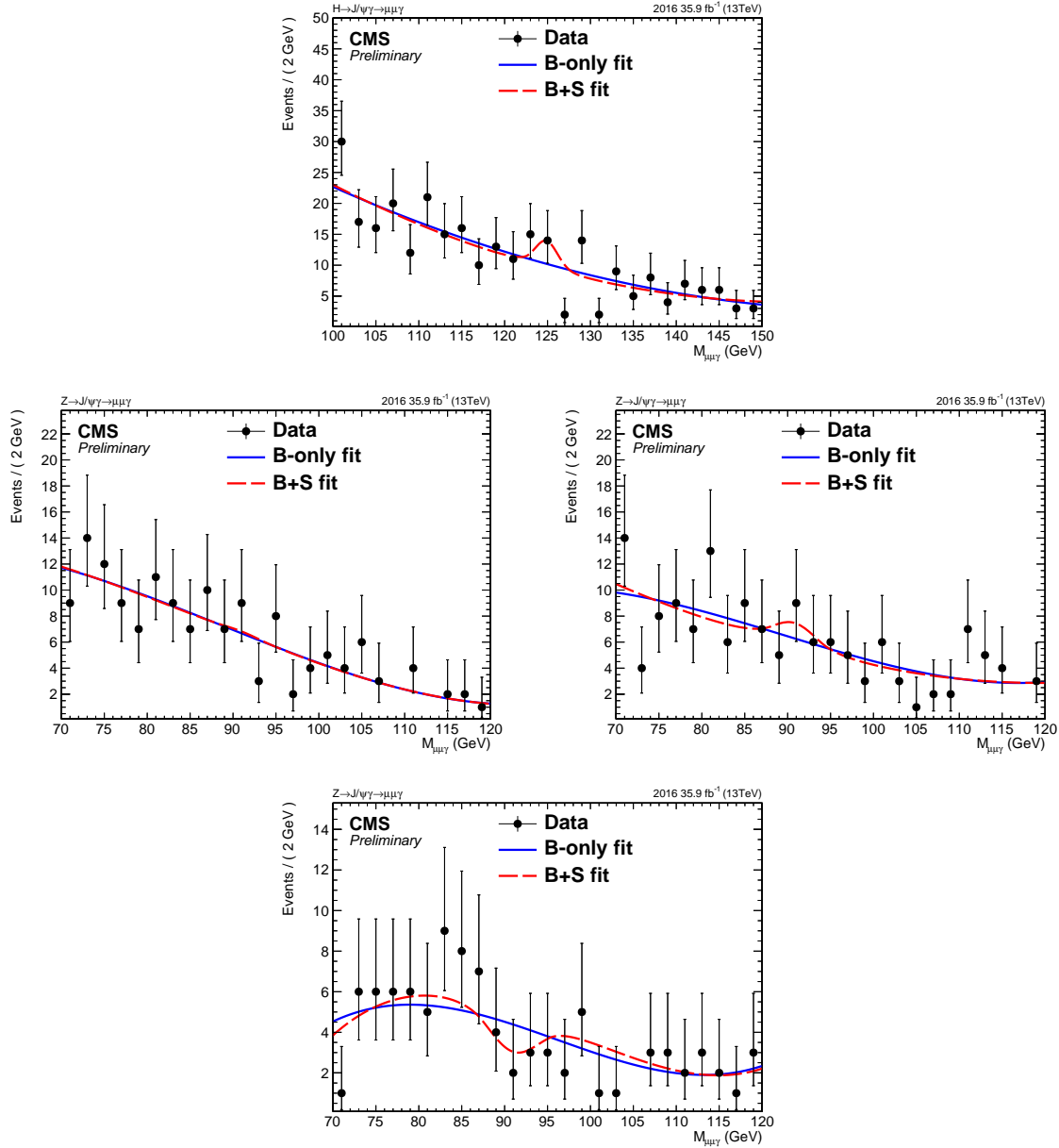


Figure 3-45: B+S fits, where signal component is allowed to float, with lowest order unbiased functions on the three-body invariant mass $m_{\mu\mu\gamma}$ distributions of data for $H \rightarrow (J/\psi)\gamma$ (top), $Z \rightarrow (J/\psi)\gamma$ Cat1 (middle left), $Z \rightarrow (J/\psi)\gamma$ Cat2 (middle right), and $Z \rightarrow (J/\psi)\gamma$ Cat3 (bottom).

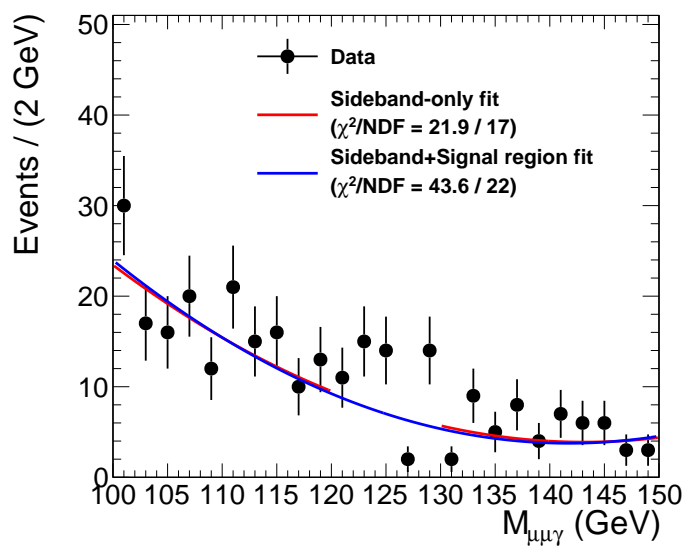


Figure 3-46: The binned fit with sideband-only fit (in red) and with sideband-plus-signal region fit (in blue).

1554 3.6 Signal modeling

1555 For the $H \rightarrow J/\psi \gamma$ decay, a Gaussian function in addition to a Crystal Ball func-
1556 tion with common mean value is used. It is a 6-parameter fit (CB: power, α , σ_{CB} ;
1557 Gaussian: σ_{Gau} ; mean value; fraction of the Gaussian and the Crystal Ball func-
1558 tion). For the Higgs Dalitz background, a Crystal Ball function is used to model
1559 the shape. For the $Z \rightarrow J/\psi \gamma$, we use a double-sided Crystal Ball function. It has
1560 6 parameters: mean, σ , n_1 , n_2 , α_1 , and α_2 . For the $Z \rightarrow \mu\mu\gamma$ background, we take
1561 the $Z \rightarrow J/\psi \gamma$ signal shape, since the events after full selections are not enough
1562 to give reasonable fits. The signal fits for both Higgs and Z boson are shown in
1563 Fig. 3-47 and 3-49. The Higgs Dalitz background shapes for the Higgs decay are
1564 shown in Fig. 3-48.

1565 3.7 Systematic uncertainties

1566 Systematic uncertainties arising from incomplete knowledge of the detector sim-
1567 ulation and theoretical prediction on signal production mechanism may affect the
1568 results. Uncertainties for the simulated signal are evaluated by varying contribut-
1569 ing sources within their corresponding uncertainties and propagating to the signal
1570 yield or shape.

1571 The background modeling and prediction is purely derived from data, so only
1572 statistical uncertainties are considered, which are translated into uncertainty on
1573 each parameter of the fit function. Besides, the bias study mentioned in previous
1574 section is performed to ensure the bias on the choice of the background function is
1575 negligible. Hence, no additional systematic uncertainty is assigned.

1576 In both Higgs and Z boson decays, the uncertainties can be classified into two
1577 classes, one affecting the predicted signal yields and the other affecting the shape
1578 of the signal model.. They are described separately in the following subsections.

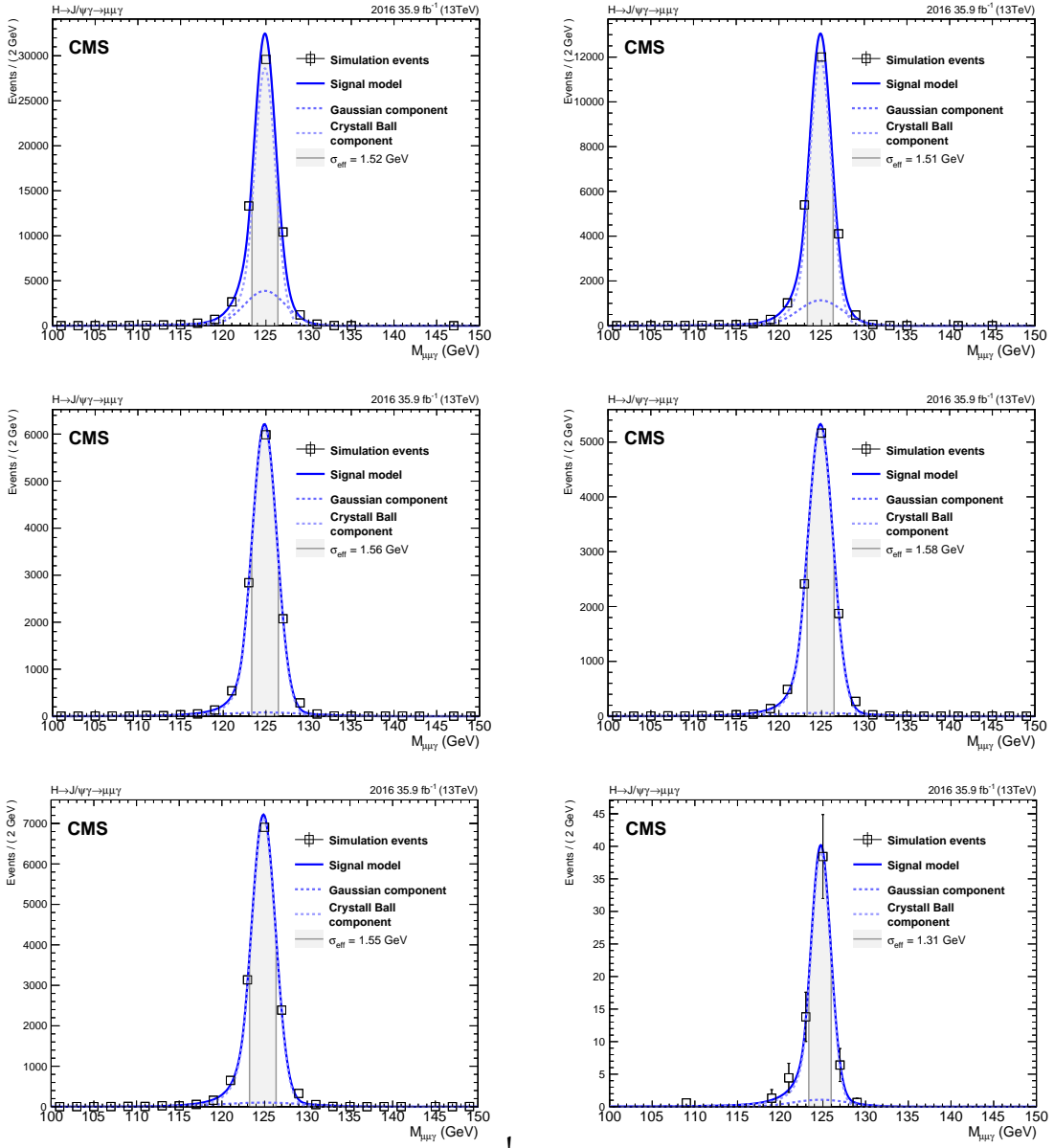


Figure 3-47: Signal model of $H \rightarrow J/\psi \gamma$ for each production mode. (Top left) gluon fusion; (Top right) vector-boson fusion; (Middle left) ZH production; (Middle right) W^+H production; (Bottom left) W^-H production; (Bottom right) associated top quark production ttH .

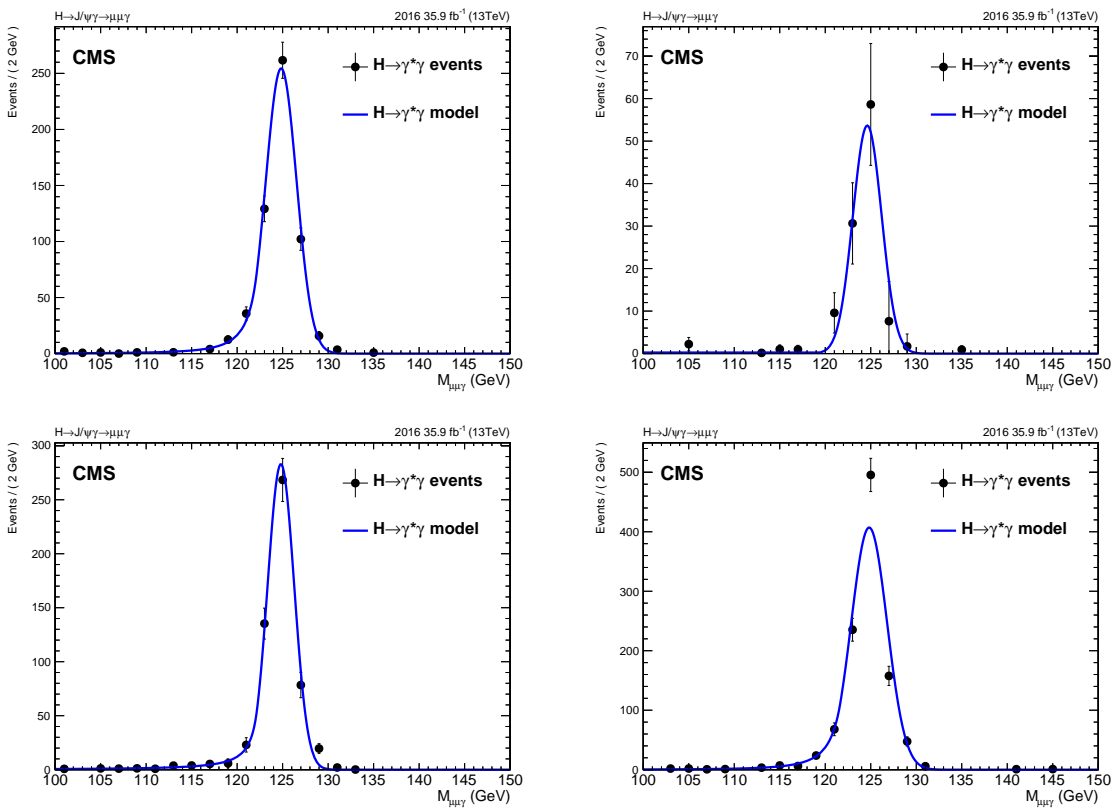


Figure 3-48: The shape of peaking background $H \rightarrow \gamma^*\gamma$ for ggF (top left), VBF (top right), ZH (bottom left), and W^+H (bottom right).

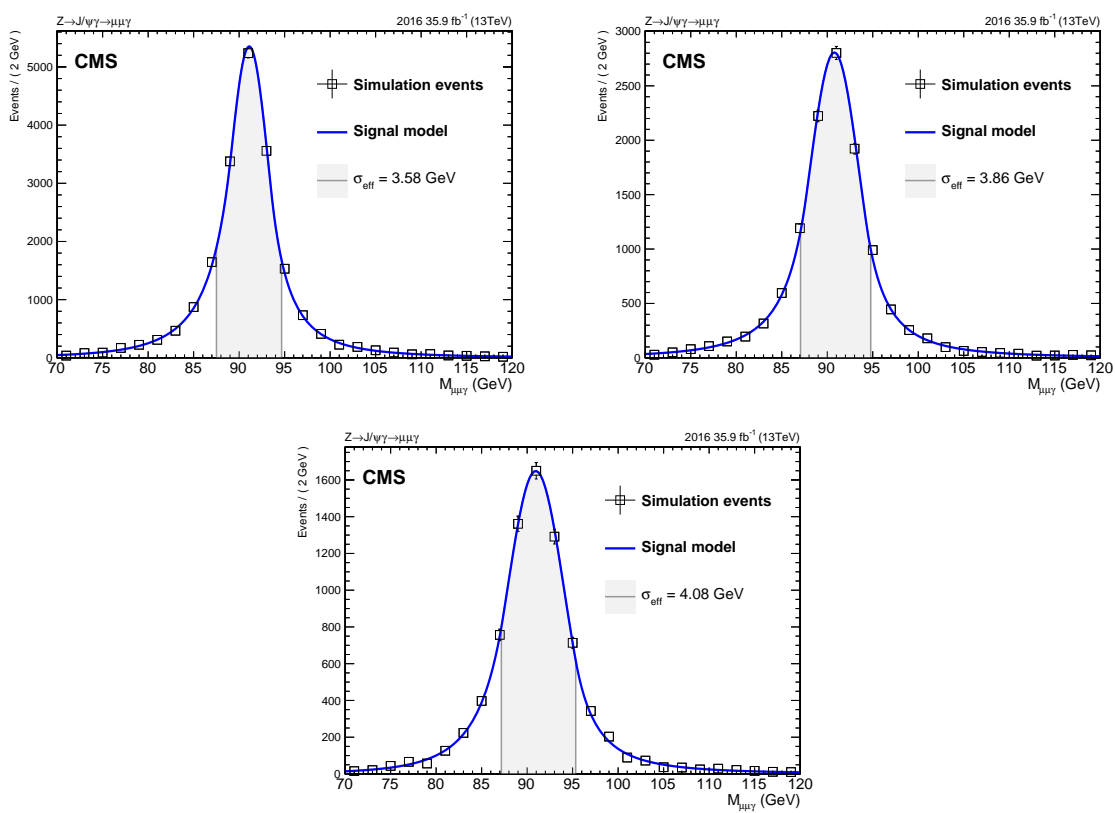


Figure 3-49: Signal model of each category of $Z \rightarrow J/\psi \gamma$.

1579 **Uncertainties affecting the predicted signal yields**

- 1580 • **Luminosity measurement** [114]. The recommended value of 2.5% is used.
- 1581 • **ID and isolation of the objects.** For the muons and photon MVA ID, the
1582 uncertainties are derived from three sources:
- 1583 1. Different signal and background functions used in tag-and-probe method
1584 to obtain the scale factors
- 1585 2. Different tag requirements
- 1586 3. Compute the passing and failing probes by simply counting in the sim-
1587 ulated events

1588 For the photon CSEV, the uncertainties come from

- 1589 1. Different pileup reweighting references
- 1590 2. Adding background simulated events
- 1591 3. Different generators used to generate the signal events
- 1592 • **Trigger.** Uncertainties in the measurement of trigger efficiency scale factors
1593 are derived by adding background simulated samples for the computation of
1594 the scale factors and by varying the pileup weight references. The systematic
1595 uncertainty from each source is taken to be the difference between the nomi-
1596 nal value of scale factors and values obtained after varying these parameters.
1597 These two were estimated separately and added in quadrature along with
1598 the statistical uncertainty to give total uncertainties.
- 1599 • **Pileup.** The minimum bias cross-section of 69.2 mb for pileup reweighting
1600 is used in the analysis. The analysis is run with varied weights, $\pm 4.6\%$ with
1601 respect to the nominal one. The largest difference in the yields is quoted as
1602 the uncertainty.
- 1603 • **Theoretical sources.** These include

- 1604 1. The effects of the parton density function (PDF) choice on the signal
1605 cross-section and strong coupling constant α_s [48, 108, 115]

1606 2. The lack of higher-order calculations for the cross-section and renormal-
1607 ization scale [116, 117, 118, 119, 120]

1608 3. The prediction of the decay branching fraction [121]

1609 **Uncertainties affecting the shape of the signal model**

1610 Since the energy resolution of simulated events is better than that in real data,
1611 smearing corrections are applied on simulated events. The energy scale in real
1612 data is corrected to match the simulated event.

1613 • **Muon momentum scale and resolution.** Rochester correction derived for
1614 full 2016 dataset is used in the analysis. There are several sources contribut-
1615 ing to the uncertainties, including statistical uncertainty, the effect of correc-
1616 tion without reweighting reference to data, varied profile mass windows, and
1617 varied fitting mass windows. For each source, the analysis is run many times,
1618 varying the members given in the package. Different corrections on the p_T
1619 are applied to muons, and the differences on muon p_T are then propagated
1620 to $m_{\mu\mu\gamma}$. Fits to the resulting $m_{\mu\mu\gamma}$ distributions are done using previously
1621 mentioned signal model to obtain the mean and width of the Gaussian com-
1622 ponent of the signal model σ , which are measures of the scale and resolution
1623 uncertainties. When the mean values are to be obtained, the parameters of
1624 the signal model are fixed except for the mean value. Similarly, when the σ
1625 values are to be obtained, all other parameters than σ are fixed. The largest
1626 variation on the mean/ σ among the members in each source is quoted. The
1627 uncertainties from these four sources are added in quadrature and assigned
1628 as total systematic uncertainty for the scale and resolution.

1629 • **Photon energy scale.** The uncertainty in the photon energy scale is estimated
1630 by varying the energy correction. Three sources are considered: statistical

uncertainties, systematic uncertainties (cut-based selection, R_9 categorization, etc.), and gain switch uncertainties. Each of the sources contains up and down corrections. The analysis is run with these six variations and varied $m_{\mu\mu\gamma}$ distributions are obtained. The signal model with all parameters fixed except for the mean is fitted to varied distributions. The largest variation on the mean value of the fit with respect to the nominal one is taken as systematic uncertainty on the photon energy scale.

- Photon energy resolution. The smearing of the photon energy is done with two parameters, rho and phi, corresponding to constant term and E_T dependent term. Each of them contains up and down corrections. Similar to what has been done for photon energy scale, the analysis is run with these four variations and varied $m_{\mu\mu\gamma}$ distributions are obtained. Alternatively, the signal model with all parameters fixed except the σ is fitted to varied distributions. The largest variation on the σ value of the fit with respect to the nominal one is taken as systematic uncertainty on the photon energy resolution.

Table 3.15, 3.16, and 3.17 show the sources of the all systematic uncertainties in both Higgs and Z analyses and the pre-fit value of each source.

Source	Pre-fit value (in %)					
	$H \rightarrow J/\psi \gamma$ signal					
	ggF	VBF	ZH	W^+H	W^-H	$t\bar{t}H$
Integrated luminosity						
Theoretical uncertainties						
Cross section (scale)				+4.6	-6.7	
Cross section (PDF + α_s)				3.2		
Detector simulation, reconstruction:						
Pileup reweighting	0.686	0.684	0.927	0.606	0.907	1.509
Trigger (per event)	3.92	4.05	4.12	4.23	4.12	4.05
Muon ID/Isolation	2.08	2.04	2.05	2.06	2.06	2.16
Photon ID	1.21	1.18	1.18	1.22	1.17	1.13
Electron veto	1.05	1.05	1.04	1.02	1.04	1.07
Signal model fits:						
Mean (scale)	0.0966	0.0884	0.0804	0.0927	0.0953	0.112
Sigma (resolution)	4.95	4.30	3.35	4.61	3.79	14.1

Table 3.15: Systematic uncertainties for the $H \rightarrow J/\psi \gamma$ signal.

Source	Pre-fit value (in %)			
	$H \rightarrow \gamma^*\gamma$ background			
	ggF	VBF	ZH	WH
Integrated luminosity	2.5			
Theoretical uncertainties				
SM H boson cross section (scale)	+4.6 -6.7			
SM H boson cross section (PDF + α_s)	3.2			
SM BR($H \rightarrow \gamma^*\gamma$)	6.0			
Detector simulation, reconstruction:				
Pileup reweighting	1.71	0.103	1.80	1.39
Trigger (per event)	4.10	4.09	4.09	4.29
Muon ID/Isolation	2.50	2.63	2.49	2.20
Photon ID	1.18	1.10	1.17	1.19
Electron veto	1.04	1.11	1.04	1.01

Table 3.16: Systematic uncertainties for the $H \rightarrow \gamma^*\gamma$ background.

Source	Pre-fit value (in %)					
	$Z \rightarrow J/\psi \gamma$			$Z \gamma \rightarrow \mu\mu\gamma$		
	Cat1	Cat2	Cat3	Cat1	Cat2	Cat3
Integrated luminosity	2.5					
Theoretical uncertainties						
SM Z boson XS (scale)	3.5			5.0		
SM Z boson XS (PDF + α_s)	1.73			5.0		
Detector simulation, reconstruction						
Pileup reweighting	0.990	0.200	1.34	0.940	1.45	4.38
Trigger (per event)	3.30	3.30	6.50	3.41	3.40	6.52
Muon ID/Isolation	2.92	2.95	3.01	3.31	3.42	3.58
Photon ID	1.12	1.11	1.11	1.08	1.08	1.14
Electron veto	1.20	1.20	0.450	1.20	1.92	0.446
Signal model						
Mean (scale)	0.0495	0.0767	0.0685	—		
Sigma (resolution)	0.990	0.690	1.45	—		

Table 3.17: Systematic uncertainties in the Z boson decay.

₁₆₄₉ $\psi(2S)$ feed-down

₁₆₅₀ The decay $\psi(2S) \rightarrow J/\psi(\rightarrow \mu\mu) + X$, where X can be anything, contributes as a
₁₆₅₁ background source. Currently there is no theoretical reference on the branching
₁₆₅₂ ratio of the $Z \rightarrow \psi(2S)\gamma$, so here an assumption is made,

$$\frac{N(Z \rightarrow J/\psi \gamma)}{N(Z \rightarrow \psi(2S)\gamma)} \simeq \frac{N(Z \rightarrow J/\psi + ll)}{N(Z \rightarrow \psi(2S) + ll)} \simeq 3.5 \quad (3.11)$$

₁₆₅₃ By taking the branching ratio of the $\psi(2S) \rightarrow J/\psi(\rightarrow \mu\mu) + X$ into account,

$$\frac{N(Z \rightarrow J/\psi \gamma)}{N(Z \rightarrow \psi(2S)\gamma[\rightarrow J/\psi(\rightarrow \mu\mu) + X])} \simeq \frac{N(Z \rightarrow J/\psi + ll)}{N(Z \rightarrow \psi(2S) + ll[\rightarrow J/\psi(\rightarrow \mu\mu) + X])} \simeq 5.7 \quad (3.12)$$

1654 we then expect to have $1.54/5.7 \sim 0.270$ events from the $\psi(2S)$ decay, where 1.54
1655 is the expected yield of $Z \rightarrow J/\psi \gamma$. This is negligible amount compared to the total
1656 background, 384.

1657 The mass shapes of this background at the generator level are shown in Fig. 3-
1658 50, where $m_{\mu\mu\gamma}$ distributions from the $Z \rightarrow (\psi(2S) \rightarrow J/\psi + X) \gamma$ are in blue
1659 and from the $Z \rightarrow J/\psi \gamma$ are in red. The distribution in solid line is without the
1660 kinematic cuts used in the selection, while the filled distribution in dashed line
1661 is after imposing the kinematic cuts. The distribution without kinematic cuts is
1662 normalized to 1, while the one with kinematic cuts is normalized to the fraction of
1663 the events passing kinematic cuts. As one can see, the $Z \rightarrow (\psi(2S) \rightarrow J/\psi + X) \gamma$
1664 actually contributes as peaking background, with the peak shifts around 10 GeV
1665 toward lower value. Since it is estimated to be 1/6 of signal and small compared
1666 to total background, it will be taken care by the background fit. Further more,
1667 from the red dashed distribution the range containing $\sim 68\%$ of events is of 87.4
1668 to 94.6 GeV, which corresponds to 17.3% of events of $Z \rightarrow \psi(2S) \gamma$ after kinematic
1669 selection. It is less than 2.9% of the $Z \rightarrow J/\psi \gamma$ yield for which are relevant at limit
1670 calculation.

1671 3.8 Statistical method

1672 The model-independent limit is set on the signal cross section times branching
1673 ratio ($\sigma \times \mathcal{BR}$) with procedures followed from Ref. [122, 123, 124, 125].

1674 First, a likelihood function is constructed as:

$$\mathcal{L}(\text{data} \mid \mu, \theta) = \text{Poisson}(\text{data} \mid \mu \cdot s(\theta_{\text{sig}}) + b(\theta_{\text{bkg}})) \cdot p(\tilde{\theta} \mid \theta), \quad (3.13)$$

1675 where “data” can either be actual experiment observation or pseudo-events; μ is

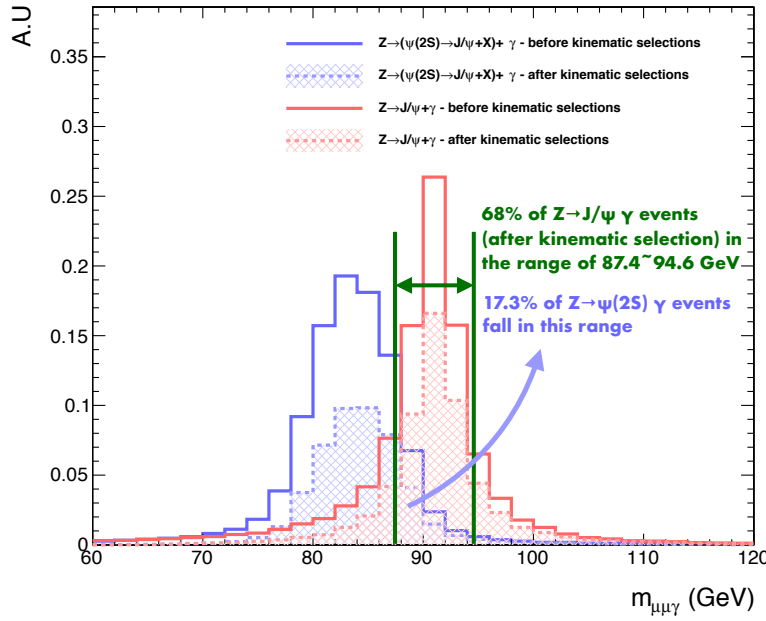


Figure 3-50: The comparison of the $m_{\mu\mu\gamma}$ distributions between the $Z \rightarrow (\psi(2S) \rightarrow J/\psi + X) \gamma$ (blue) and the $Z \rightarrow J/\psi \gamma$ (red) at the generator level.

the signal strength modifier, defined as $\sigma \times \mathcal{BR}/(\sigma \times \mathcal{BR})_{\text{SM}}$; $\theta_{\text{sig(bkg)}}$ represents the set of nuisance parameters associated with the signal and background model. Systematic uncertainties are treated as nuisance parameters which are of uninterested in the analysis but can affect results, and handle by introducing probability distribution functions (pdfs) $p(\tilde{\theta}|\theta)$. Here θ stands for the whole set of nuisance in the analysis, and $\tilde{\theta}$ represents the set of default values of the nuisance parameter, which reflecting our knowledge or belief on what values of these parameters can be. There are different choices of pdfs for nuisance parameters.

- Gaussian pdf is used for parameters that can be either positive or negative.

$$p(\tilde{\theta}|\theta) = \frac{1}{\sqrt{2}} \exp \left(-\frac{(\tilde{\theta} - \theta)^2}{2\sigma^2} \right), \quad (3.14)$$

The uncertainties in the parameter of the signal model belong to this class. Two multiplicative factors $\kappa_m \equiv 1 \pm \delta\kappa_m$ and $\kappa_\sigma \equiv 1 \pm \delta\kappa_\sigma$ are introduced

1687 such that the mean and width of the signal model are modified as

$$m' = \kappa_m \cdot m, \sigma' = \kappa_\sigma \cdot \sigma, \quad (3.15)$$

1688 where m and σ are original parameters.

1689 • **Log-normal** pdf is an alternative pdf for positively defined parameters.

$$p(\tilde{\theta}|\theta) = \frac{1}{\sqrt{2\pi} \ln(w)} \exp\left(-\frac{(\ln(\tilde{\theta}/\theta))^2}{2(\ln(w))^2}\right) \frac{1}{\tilde{\theta}}, \quad (3.16)$$

1690 where w characterizes the width of the log-normal pdf. This distribution has
1691 a longer tail than the Gaussian and goes to zero at $\theta = 0$. This class includes
1692 uncertainties in luminosity, cross-section, efficiency measurements.

1693 • The parameters for background model are allowed to freely float across their
1694 ranges and not Gaussian constrained.

1695 The unbinned likelihood is computed as,

$$k^{-1} \prod_i (\mu S f_s(x_i) + B f_b(x_i)) \cdot e^{-(\mu S + B)}. \quad (3.17)$$

1696 $f_{s(b)}(x_i)$ are pdfs (models) of signal and background of observable(s) x_i , and S and
1697 B are event yields for signal and background. The observable used in this analysis
1698 is the three-body invariant mass $m_{\mu\mu\gamma}$.

1699 The likelihood function can be used to represent *background-only* (*b-only*) hy-
1700 pothesis, $\mathcal{L}_b = \mathcal{L}(\mu = 0)$, and *signal plus background* (*s+b*) hypothesis, $\mathcal{L}_{s+b} = \mathcal{L}(\mu)$.
1701 For the nominal SM hypothesis $\mu = 1$.

1702 Based on the Neyman & Pearson lemma [126], the likelihood ratio $\frac{\mathcal{L}_{s+b}}{\mathcal{L}_b}$ provides
1703 the most powerful test for hypothesis test. Hence, it is used as *test statistic*,

$$t(\mu) = \frac{\mathcal{L}_{s+b}}{\mathcal{L}_b} = \frac{\mathcal{L}(\mu, \theta)}{\mathcal{L}(0, \theta)}. \quad (3.18)$$

1704 However, since the expected signal yields from the SM prediction are small,

1705 \mathcal{L}_{s+b} and \mathcal{L}_b are not well separated. In other words, we are not sensitive to determine the presence of the signal yet. Instead, an upper limit on the μ is set, and a different test statistic is used.

$$\tilde{\lambda}(\mu) = \begin{cases} \frac{\mathcal{L}(\mu, \hat{\theta}_\mu)}{\mathcal{L}(\hat{\mu}, \hat{\theta})} & \text{if } \hat{\mu} \geq 0 \\ \frac{\mathcal{L}(\mu, \hat{\theta}_\mu)}{\mathcal{L}(0, \hat{\theta}_{\mu=0})} & \text{if } \hat{\mu} < 0 \end{cases}$$

1708 where $\hat{\theta}_\mu$ is the value of θ that maximizes \mathcal{L} for a specific μ ; the $\mathcal{L}(\hat{\mu}, \hat{\theta})$ is the global 1709 (unconditional) maximum of the likelihood function, where $\hat{\mu}$ and $\hat{\theta}$ are values 1710 such that the likelihood function is maximized. In the second part where $\hat{\mu} < 0$, 1711 the definition of $\tilde{\lambda}(\mu)$ is determined to constrain the signal yield to be positive.

1712 Apart from the negative signal rate constraint, upward fluctuations of the data 1713 such that $\hat{\mu} > \mu$ are not considered as evidence against the signal hypothesis μ . 1714 Based on this argument, the test statistic is modified as,

$$\tilde{q}_\mu = \begin{cases} -2 \ln \tilde{\lambda}(\mu) & \text{if } 0 \leq \hat{\mu} \leq \mu \\ 0 & \text{if } \hat{\mu} \geq \mu \end{cases}$$

1715 The *observed* value of the test statistic \tilde{q}_μ for a given signal strength μ under test 1716 \tilde{q}_μ^{obs} , as well as the value of nuisance parameters $\hat{\theta}_0^{obs}$ and $\hat{\theta}_\mu^{obs}$ that maximize the 1717 likelihood for *b-only* and *s+b* hypotheses respectively, can be found. Next, pseudo- 1718 events are generated, based on the pdfs for signal and background, to construct 1719 pdfs for \tilde{q}_μ for *b-only* and *s+b* hypotheses, $f(\tilde{q}_\mu | \mu, \hat{\theta}_\mu^{obs})$ and $f(\tilde{q}_\mu | 0, \hat{\theta}_0^{obs})$. 1720 Example distributions are shown in Fig. 3-51.

1721 Having $f(\tilde{q}_\mu | \mu, \hat{\theta}_\mu^{obs})$ and $f(\tilde{q}_\mu | 0, \hat{\theta}_0^{obs})$ distributions, two p-values are defined 1722 to be associated with the actual observation for *s+b* and *b-only* hypotheses, p_μ and

1723 p_b ,

$$p_\mu = P(\tilde{q}_\mu \geq \tilde{q}_\mu^{obs} | s + b) = \int_{\tilde{q}_\mu^{obs}}^{\infty} f(\tilde{q}_\mu | \mu, \hat{\theta}_\mu^{obs}) d\tilde{q}_\mu^{obs} \quad (3.19)$$

1724

$$p_b = P(\tilde{q}_\mu \geq \tilde{q}_\mu^{obs} | b - only) = \int_{\tilde{q}_\mu^{obs}}^{\infty} f(\tilde{q}_\mu | 0, \hat{\theta}_0^{obs}) d\tilde{q}_\mu^{obs} \quad (3.20)$$

1725 and $CL_s(\mu)$ is defined as a ratio of these two p-values

$$CL_s(\mu) = \frac{p_\mu}{1 - p_b}. \quad (3.21)$$

1726 To quote the 95% confidence level (C.L) upper limit on μ , denoted as $\mu^{95\%CL}$,
 1727 the μ value is adjusted until the $CL_s(\mu) = 0.05$. The derived limit is called *observed*
 1728 limit.²

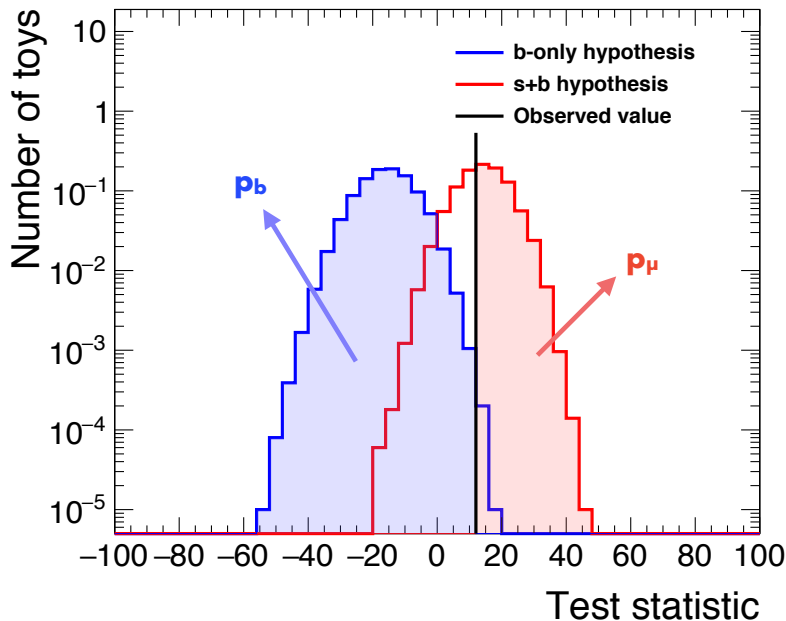


Figure 3-51: Test statistic distributions for pseudo-events generated with signal+background and background-only hypotheses.

²If ,for example, $\mu = 1$ and $CL_s \leq \alpha$, we would state that "The SM Higgs/Z boson decay is excluded with $(1 - \alpha)CL_s$ confidence level (C.L)." .

1729 The traditional way to compute the *expected* limit for *b-only* hypothesis is to
 1730 generate a large number of pseudo-events based on the pdfs of the signal and
 1731 background, without using the true data, treat them as real data, and calculate
 1732 the CL_s and $\mu^{95\%CL}$ for each of them. A pdf for the $\mu^{95\%CL}$ and corresponding
 1733 cumulative probability distribution (or cumulative distribution function, CDF) can
 1734 be obtained. An example is shown in Fig. 3-52. The point where the CDF crosses
 1735 50% of entries is the median expected value. The $\pm 1\sigma$ (68%) band is defined as
 1736 points crossings of the 16% and 84% entries. Points crossings at 2.5% and 97.5%
 1737 define the $\pm 2\sigma$ (95%) band.

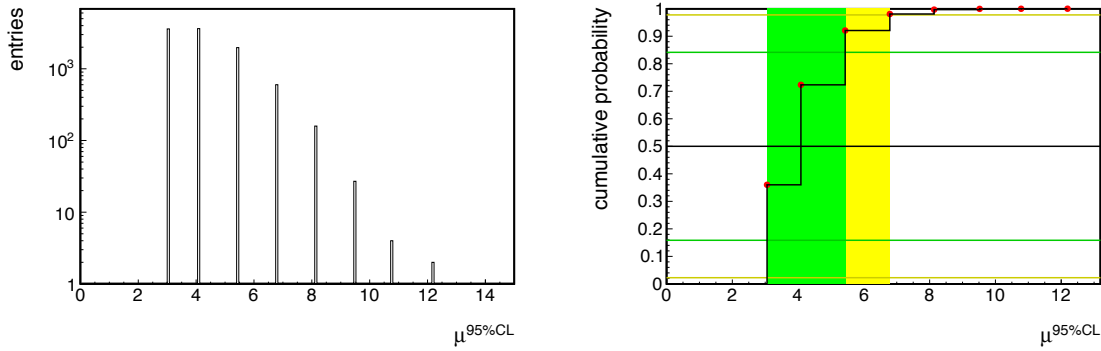


Figure 3-52: An example of distribution of $\mu^{95\%CL}$ for the *b-only* hypothesis (left), and the corresponding CDF with horizontal lines indicating the 2.5%, 16%, 50%, 84%, and 97.5% quantiles, and vertical green and yellow bands show the $\pm 1\sigma$ and $\pm 2\sigma$ ranges of $\mu^{95\%CL}$ [124].

1738 Instead, in this analysis *expected* limits are set with the *asymptotic* method. The
 1739 detail discussion of the method is described in Ref. [125], here a brief summary is
 1740 shown. It is found that with the large data sample size (asymptotic regime)³, the
 1741 modified test statistic \tilde{q}_μ is in the form,

$$\tilde{q}_\mu = \begin{cases} \frac{\mu^2}{\sigma^2} - \frac{2\mu\hat{\mu}}{\sigma^2} & \text{if } \hat{\mu} < 0 \\ \frac{(\mu - \hat{\mu})^2}{\sigma^2} & \text{if } 0 \leq \hat{\mu} \leq \mu \\ 0 & \text{if } \hat{\mu} > \mu \end{cases}$$

1742 where σ is a factor that characterizes effects from all nuisance parameters. The pdf

₁₇₄₃ $f(\tilde{q}_\mu | \mu)$ is found to follow a well defined formula (here the θ is drop as the σ takes
₁₇₄₄ care of their effects)

$$f(\tilde{q}_\mu | \mu) = \frac{1}{2} \delta(\tilde{q}_\mu) + \begin{cases} \frac{1}{2} \frac{1}{\sqrt{2\pi}} \frac{1}{\sqrt{\tilde{q}_\mu}} e^{-\tilde{q}_\mu/2} & \text{if } 0 < \tilde{q}_\mu \leq \mu^2/\sigma^2 \\ \frac{1}{\sqrt{2\pi}(2\mu/\sigma)} \exp\left(-\frac{1}{2} \frac{(\tilde{q}_\mu + \mu^2/\sigma^2)^2}{(2\mu/\sigma)^2}\right) & \text{if } \tilde{q}_\mu > \mu^2/\sigma^2 \end{cases}$$

₁₇₄₅ where

$$\sigma^2 = \frac{\mu^2}{q_{\mu,A}}. \quad (3.22)$$

₁₇₄₆ $q_{\mu,A}$ is the test statistic evaluated with the expected background and nominal nui-
₁₇₄₇ sance parameters. A in the $q_{\mu,A}$ stands for the Asimov data set⁴. The same con-
₁₇₄₈ struction can also be used for $f(\tilde{q}_\mu | b - \text{only})$. A novel result states that, by as-
₁₇₄₉ suming the large sample size, one can obtain the exact formulae for $f(\tilde{q}_\mu | \mu)$ and
₁₇₅₀ $f(\tilde{q}_\mu | 0)$, whose parameter σ can be extracted from a single representative Asimov
₁₇₅₁ data set. The median expected limits and their bands are therefore easily obtained
₁₇₅₂ using this data set, without performing any generation of pseudo experiments.
₁₇₅₃ The median expected CL_s limit, $\mu_{\text{up}}^{\text{med}}$ is expressed as

$$\mu_{\text{up}}^{\text{med}} = \hat{\mu} + \sigma \Phi^{-1}(1 - 0.5\alpha), \quad (3.23)$$

₁₇₅₄ and the $\pm n\sigma$ band is given by

$$\text{Band}_{n\sigma} = \hat{\mu} + \sigma (\Phi^{-1}(1 - \alpha) \pm n), \quad (3.24)$$

₁₇₅₅ where Φ^{-1} is the inverse of the cumulative distribution of the standard Gaussian.

³This is a critical assumption, which enables us to factorize the test statistic into Gaussian and non-Gaussian part. In the large data sample limit, the contribution from the non-Gaussian component is negligible.

⁴The Asimov data set is defined such that when maximizing the likelihood associated to this data set, one would get the maximum likelihood estimators of the parameters to be the assumed (true) values of the parameters.

₁₇₅₆ The $\alpha = 0.05$ is chosen corresponding to the 95% CL.

1757

Chapter 4

1758

Results and conclusion

1759

4.1 Limits on decay branching fraction

1760 The distributions in $m_{\mu\mu\gamma}$ observed in the data are in agreement with the SM ex-
1761 expectation of the background-only hypothesis. The results are used to derive upper
1762 limits on the branching fractions, $\mathcal{B}(Z \rightarrow J/\psi \gamma)$ and $\mathcal{B}(H \rightarrow J/\psi \gamma)$ for the Z and
1763 Higgs boson.

1764 The observed (expected) exclusion upper limit on the cross-section times the
1765 branching fraction at 95% CL for the $H \rightarrow J/\psi \gamma$, where the J/ψ meson is fully
1766 transversely polarized, is,

$$\sigma(pp \rightarrow H) \times \mathcal{B}(H \rightarrow J/\psi \gamma \rightarrow \mu\mu\gamma) < 2.5 (1.7^{+0.8}_{-0.5}) \text{ fb}, \quad (4.1)$$

1767 where upper and lower bounds for 68% of interval of expected limits are shown
1768 as superscript and subscript. With the known values of $\sigma(pp \rightarrow H) = 55.1 \text{ pb}$ and
1769 $\mathcal{B}(J/\psi \rightarrow \mu\mu) = 0.059$, the above result can be interpreted in terms of limit on the
1770 branching fraction,

$$\mathcal{B}(H \rightarrow J/\psi \gamma) < 7.6 (5.2^{+2.4}_{-1.6}) \times 10^{-4}. \quad (4.2)$$

1771 which corresponds to 260 (170) times the SM prediction.

₁₇₇₂ For the Z boson decay, with the unpolarized J/ ψ meson assumption ,the ob-
₁₇₇₃ served (expected) upper limit on the cross-section times the branching fraction is,

$$\sigma(pp \rightarrow Z) \times \mathcal{B}(Z \rightarrow J/\psi \gamma \rightarrow \mu\mu\gamma) < 4.6 (5.3^{+2.3}_{-1.6}) \text{ fb}, \quad (4.3)$$

₁₇₇₄ With the known value $\sigma(pp \rightarrow Z) = 5.71 \times 10^4 \text{ pb}$, the observed (expected) upper
₁₇₇₅ limit in branching fraction is

$$\mathcal{B}(Z \rightarrow J/\psi \gamma) < 1.4 (1.6^{+0.7}_{-0.5}) \times 10^{-6}. \quad (4.4)$$

₁₇₇₆ , corresponding to 15 (18) times the SM prediction.

₁₇₇₇ Extreme polarization scenarios give rise to variations from $-13.6 (-13.5)\%$,
₁₇₇₈ for a fully longitudinally polarized J/ ψ , to $+8.6 (+8.2)\%$, for a fully transversely
₁₇₇₉ polarized J/ ψ meson, in the observed (expected) branching fraction. The observed
₁₇₈₀ (expected) exclusion limits on the cross sections and branching fractions at 95%
₁₇₈₁ confidence level for the Z and Higgs boson decays are summarized in Table 4.1.

Channel	Polarization scenario	σ (fb)	$\mathcal{B}(Z (H) \rightarrow J/\psi \gamma)$	$\frac{\mathcal{B}(Z (H) \rightarrow J/\psi \gamma)}{\mathcal{B}_{SM}(Z (H) \rightarrow J/\psi \gamma)}$
$Z \rightarrow J/\psi \gamma$	Unpolarized	$4.6 (5.3^{+2.3}_{-1.6})$	$1.4 (1.6^{+0.7}_{-0.5}) \times 10^{-6}$	15 (18)
	Transverse	$5.0 (5.9^{+2.5}_{-1.7})$	$1.5 (1.7^{+0.7}_{-0.5}) \times 10^{-6}$	16 (19)
	Longitudinal	$3.9 (4.6^{+2.0}_{-1.4})$	$1.2 (1.4^{+0.6}_{-0.4}) \times 10^{-6}$	13 (15)
$H \rightarrow J/\psi \gamma$	Transverse	$2.5 (1.7^{+0.8}_{-0.5})$	$7.6 (5.2^{+2.4}_{-1.6}) \times 10^{-4}$	260 (170)

Table 4.1: Upper observed (expected) limits on cross sectiona $\sigma(pp \rightarrow Z (H) \rightarrow (J/\psi \rightarrow \mu\mu)\gamma)$ (fb) and branching fractions of $Z (H) \rightarrow J/\psi \gamma$ decays, where the latter are computed assuming SM cross section of the Z (H) boson. Variations of the branching fractions of the Z decay for complete transverse and longitudinal polarizations for J/ ψ are also shown. The upper and lower bounds of the expected 68% confidence level interval for the expected limits are shown as superscripts and subscripts respectively.

1782 **Combination with 8 TeV result**

1783 The results of the $H \rightarrow J/\psi \gamma$ are combined with the results of a similar search
1784 performed by the CMS Collaboration using data recorded with pp collisions at
1785 $\sqrt{s} = 8$ TeV, corresponding to an integrated luminosity of 19.7 fb^{-1} [87]. The com-
1786 bination results in an upper limit corresponding to 220 (160) times the SM predic-
1787 tion. All systematic uncertainties are assumed to be uncorrelated in the combi-
1788 nation, apart from the theoretical calculations for the cross section and branching
1789 fractions.

1790 **4.2 Conclusion**

1791 A search is performed for decays of the standard model (SM) Z and Higgs bosons
1792 into a J/ψ meson and a photon with the J/ψ meson subsequently decaying into $\mu\mu$.
1793 Data from pp collisions at $\sqrt{s} = 13$ TeV, corresponding to an integrated luminosity
1794 of 35.9 fb^{-1} is used. No excess has been observed above the predicted background.
1795 The observed (expected) exclusion limit at 95% CL on the branching fraction of
1796 the Higgs boson is set at $\mathcal{B}(H \rightarrow J/\psi \gamma) < 7.6 (5.2) \times 10^{-4}$, corresponding to 260
1797 (170) times the SM value. The 68% confidence level interval ranges from 3.6 to
1798 7.6×10^{-4} . The limit on the branching fraction of the Z boson decay in the unpo-
1799 larized scenario is set at $\mathcal{B}(Z \rightarrow J/\psi \gamma) < 1.4 (1.6)$, corresponding to 15 (18) times
1800 the SM prediction. The 68% confidence level interval ranges from 1.1 to 2.3×10^{-6} .
1801 Extreme polarization scenarios give rise to variations from $-13.6 (-13.5)\%$, for a
1802 fully longitudinally polarized J/ψ meson, to $+8.6 (+8.2)\%$, for a fully transversely
1803 polarized J/ψ meson, in the observed (expected) branching fraction. The results
1804 for the Higgs boson channel are combined with the results obtained by a similar
1805 search performed at $\sqrt{s} = 8$ TeV by the CMS Collaboration, yielding an observed
1806 (expected) upper limit on the branching fraction for the decay $H \rightarrow J/\psi \gamma$ of 220
1807 (160) times the SM prediction.

1808 **4.3 Outlook**

1809 Improvements can be done in order to make the analysis more advanced. The
1810 proper simulation of the background processes is of the first priority. The diffi-
1811 culty is mainly due to the large cross sections of the low mass dimuon system in
1812 the final states, and therefore efficient ways to produce such samples should be
1813 developed. The background samples will enable us to have better understand-
1814 ing of the background composition and make the optimization of the event selec-
1815 tion feasible. Furthermore, the multivariate analysis (MVA) or the matrix element
1816 method¹(MEM) can be exploited to better discriminate the signal and background.
1817 The analysis can be extended to include the decay of $Z(H) \rightarrow Y(nS)\gamma$, where the
1818 $Y(nS)$ mesons decay to a muon pair. The one dimension fit in the $m_{\mu\mu\gamma}$ space to
1819 estimate the background in this analysis will need to be modified to cope with the
1820 non-negligible contribution of the peaking background $Z \rightarrow \mu\mu\gamma$. A two dimen-
1821 sion (in the $m_{\mu\mu}$ and $m_{\mu\mu\gamma}$ space) or multi-dimension fit is suggested. The back-
1822 ground composition can also be estimated by this data-driven method, and in turn
1823 can be used to validate the background simulation samples. The development of
1824 the identification and reconstruction of merged electrons can be used in the elec-
1825 tron channel. The projection study is performed, and the expected distributions
1826 of $m_{\mu\mu\gamma}$ with 3000 fb^{-1} of data from both decay channels are shown in Fig. 4-1.
1827 The upper limit on $\mathcal{BR}(Z \rightarrow J/\psi \gamma)$ is around 2 times its SM value, while that on
1828 the $\mathcal{BR}(H \rightarrow J/\psi \gamma)$ is expected to be less than 20 times its SM prediction. With
1829 the addition of the electron channel and foreseeable improvements, the $Z \rightarrow J/\psi \gamma$
1830 would be sensitive to it's current SM predicted rate after the high luminosity run of
1831 the LHC, possibly leading to the first observation of this rare decay of the Z boson.

¹For example, the Matrix Element Likelihood Analysis (MELA) used in the $H \rightarrow ZZ^* \rightarrow 4l$ analysis.

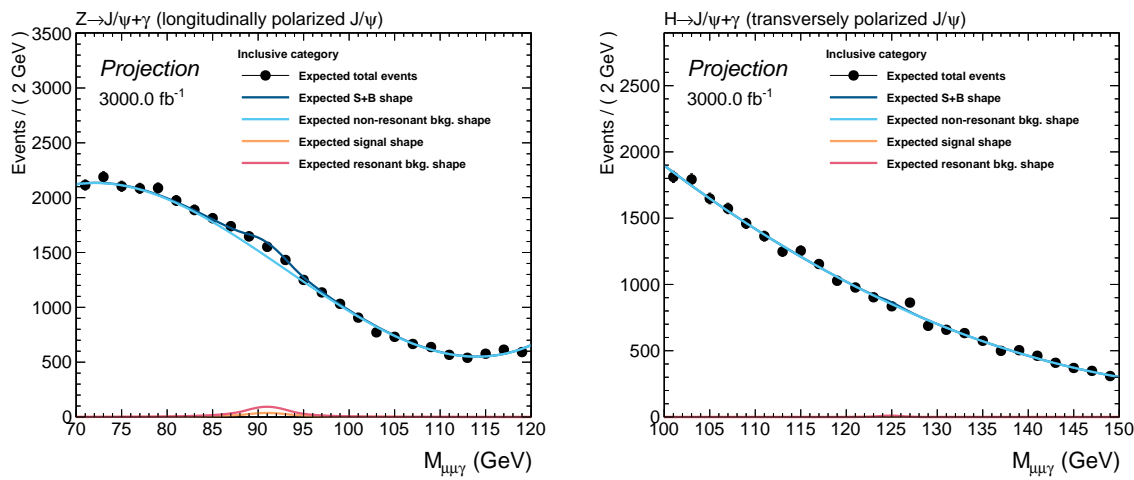


Figure 4-1: The expected distributions of $m_{\mu\mu\gamma}$ at 3000 fb^{-1} of data from both decay channels.

¹⁸³² Appendix A

¹⁸³³ Additional materials for the bias ¹⁸³⁴ study

¹⁸³⁵ A.1 Linearity

¹⁸³⁶ It was suggested to do the bias study with more signal events introduced when
¹⁸³⁷ generating the pseudo-event. Following plots show how the mean and width of
¹⁸³⁸ the pull distribution evolve as more signal events are introduced.

A.1.1 $H \rightarrow J/\psi \gamma$

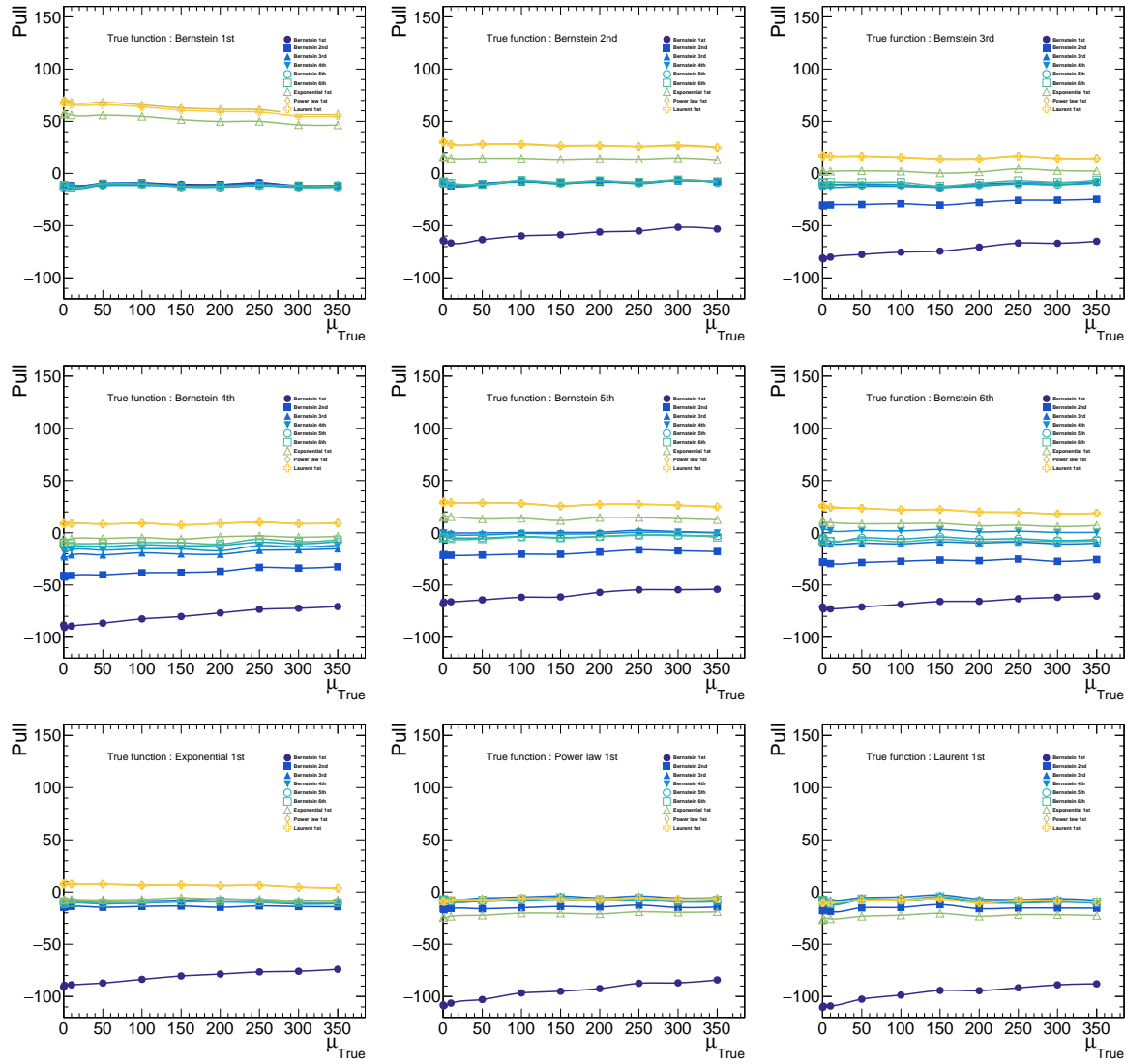


Figure A-1: The evolution of the mean of the pull value distribution as more signal events are introduced in the Higgs decay.

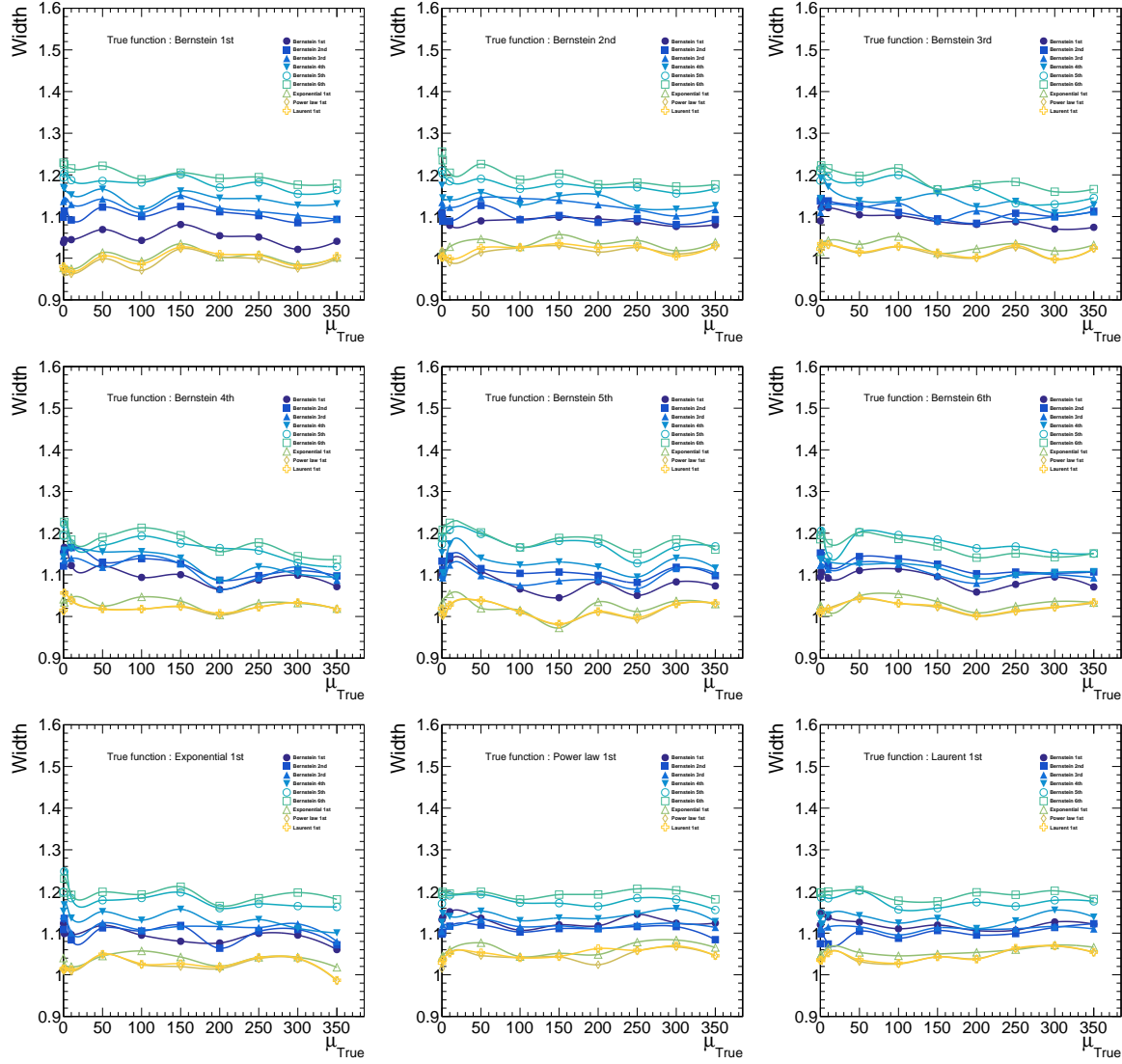


Figure A-2: The evolution of the width of the pull value distribution as more signal events are introduced in the Higgs decay.

1840 A.1.2 $Z \rightarrow J/\psi \gamma$ Cat1

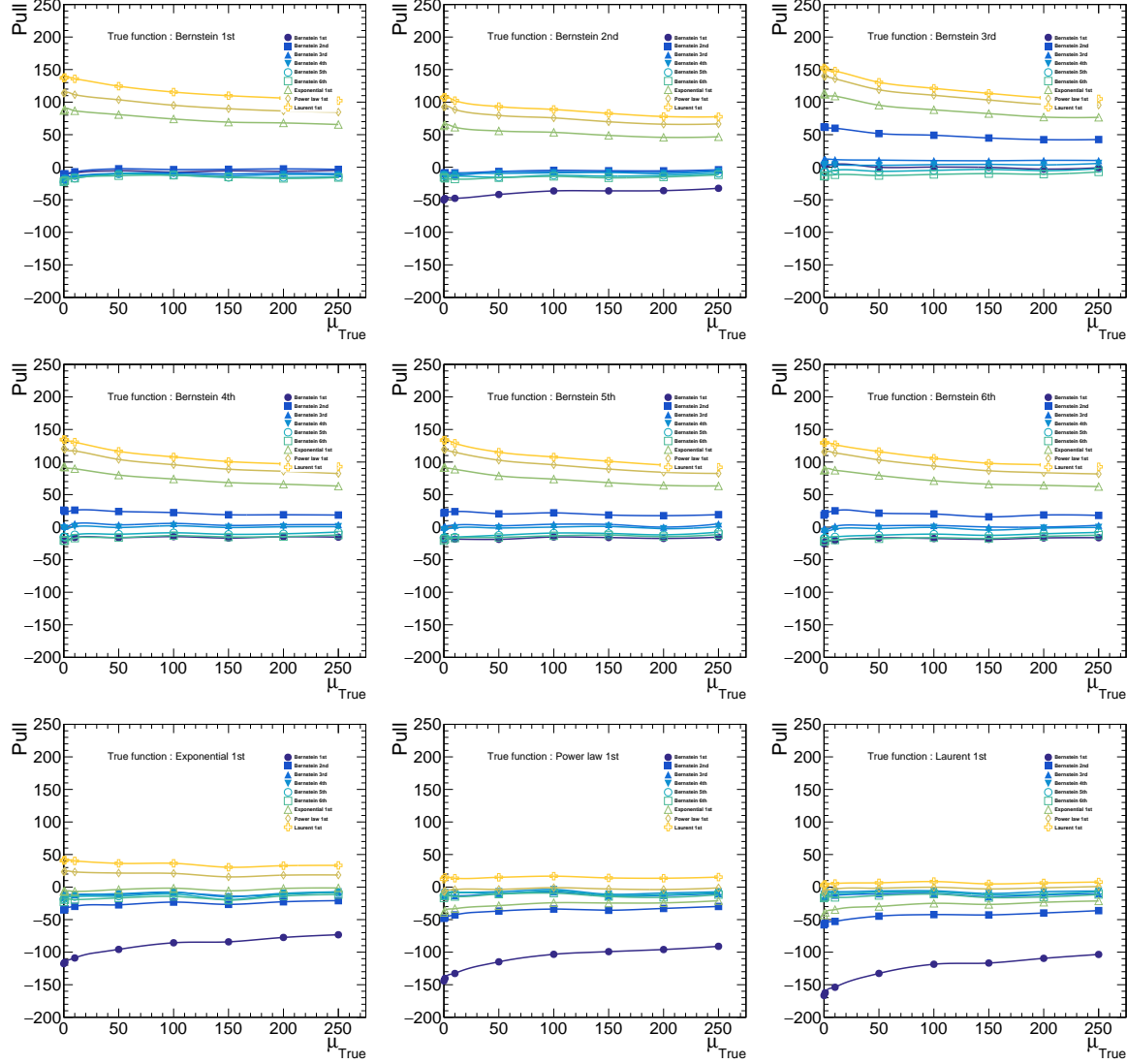


Figure A-3: The evolution of the mean of the pull value distribution as more signal events are introduced in the Cat1 of the Z decay.

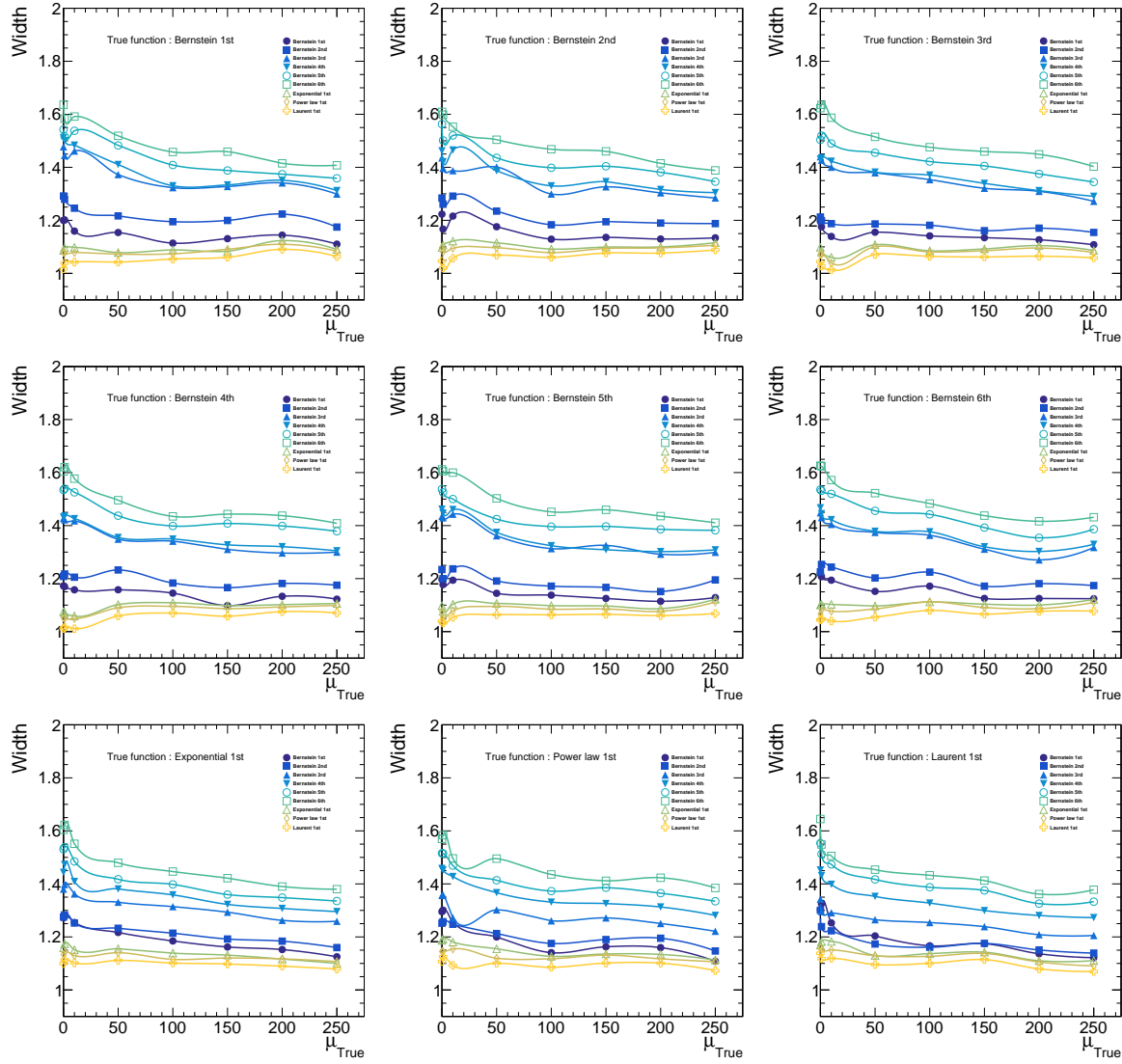


Figure A-4: The evolution of the width of the pull value distribution as more signal events are introduced in the Cat1 of the Z decay.

1841 A.1.3 $Z \rightarrow J/\psi \gamma$ Cat2

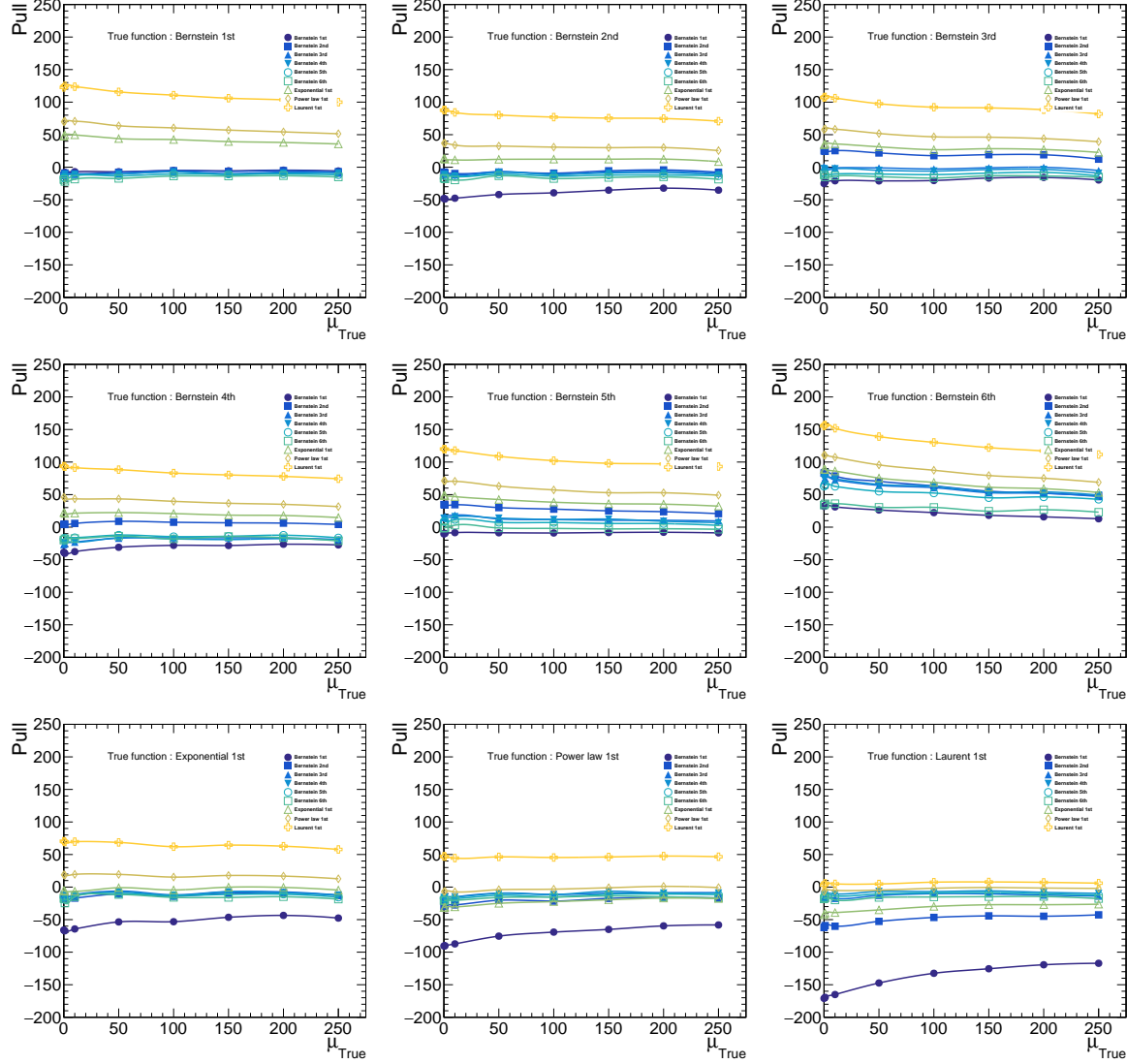


Figure A-5: The evolution of the mean of the pull value distribution as more signal events are introduced in the Cat2 of the Z decay.

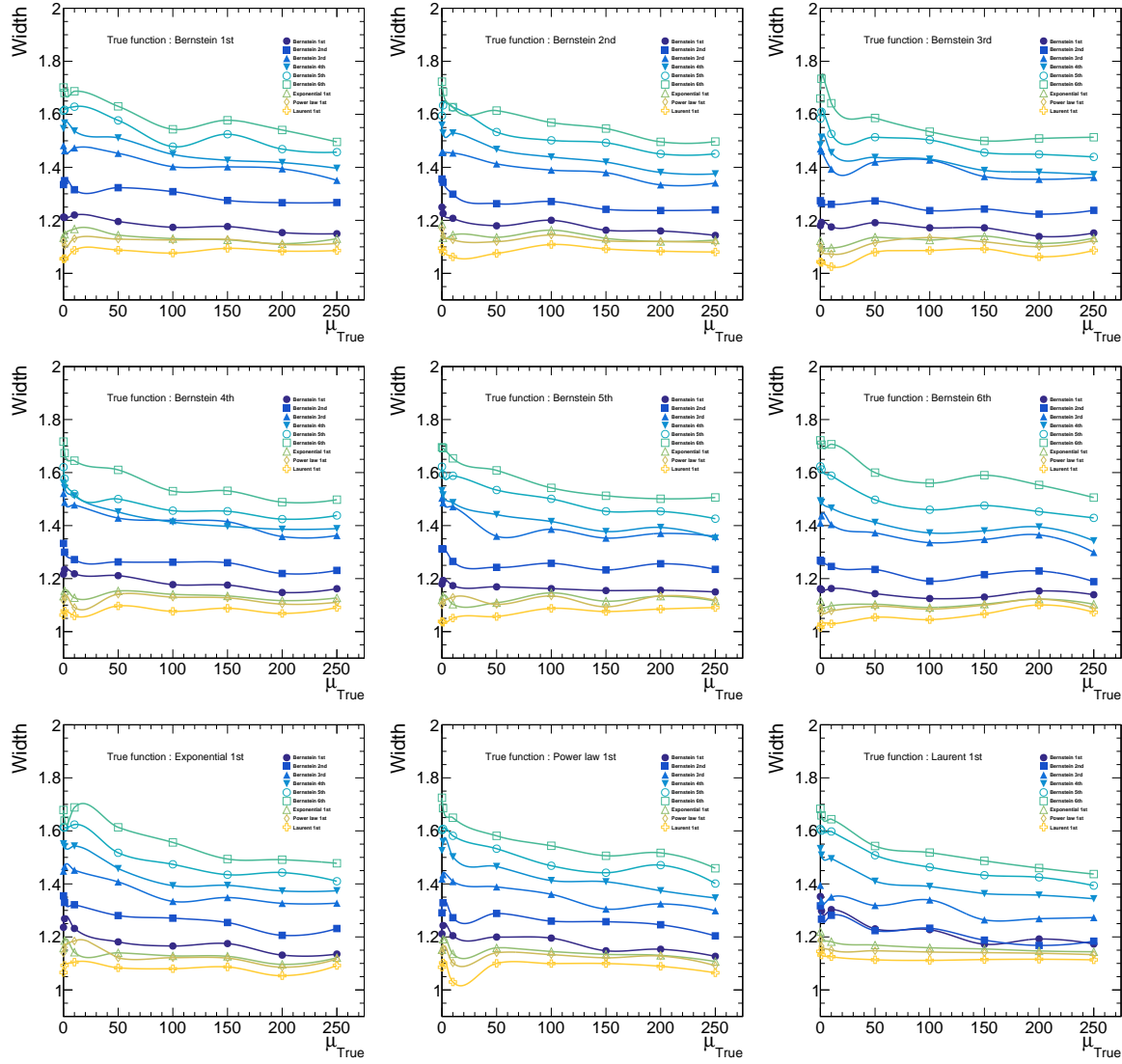


Figure A-6: The evolution of the width of the pull value distribution as more signal events are introduced in the Cat2 of the Z decay.

1842 A.1.4 $Z \rightarrow J/\psi \gamma$ Cat3

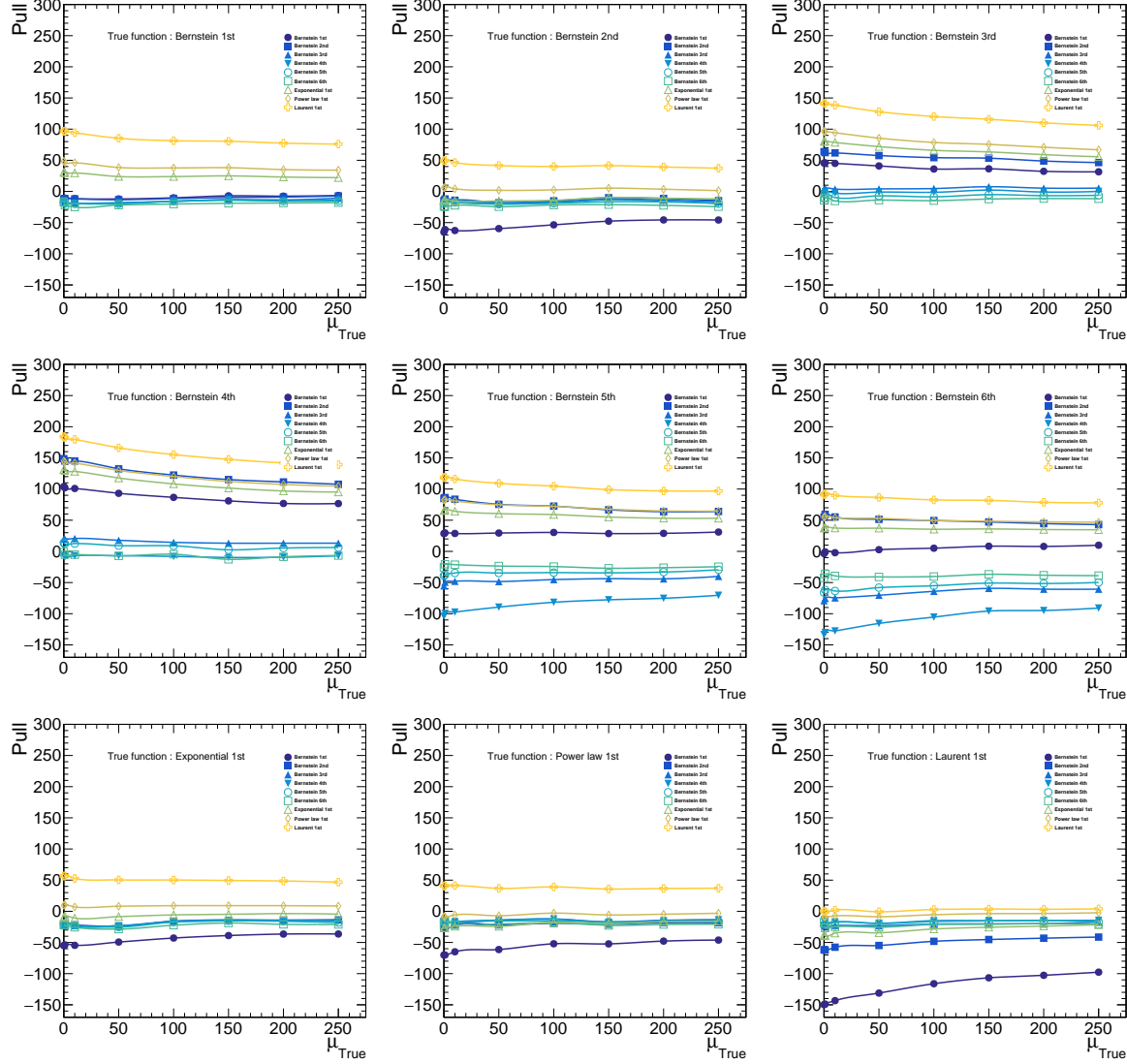


Figure A-7: The evolution of the mean of the pull value distribution as more signal events are introduced in the Cat3 of the Z decay.

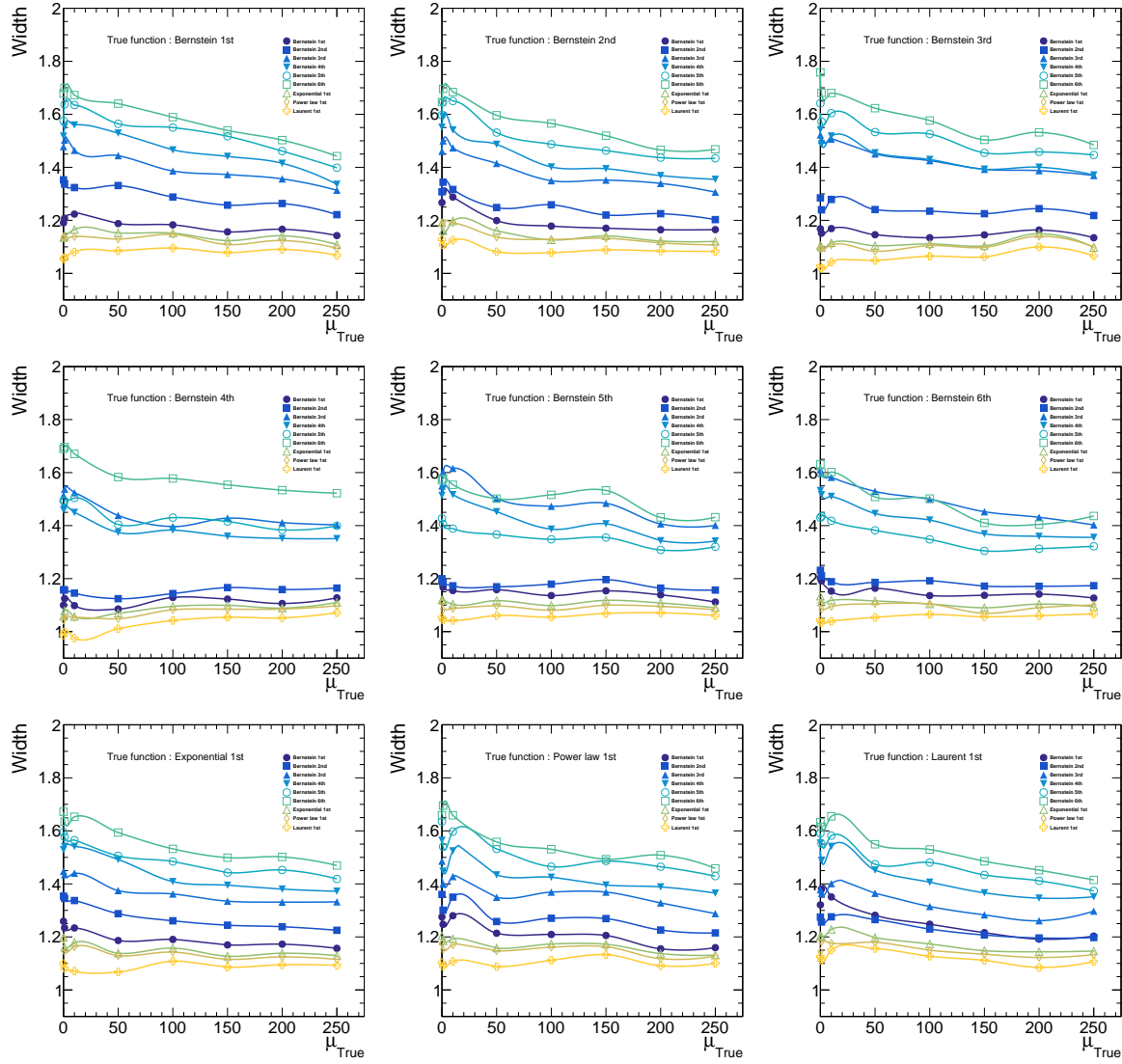


Figure A-8: The evolution of the width of the pull value distribution as more signal events are introduced in the Cat3 of the Z decay.

1843 **A.2 Pseudo-event**

1844 Examples of pseudo-events for the Higgs and all the three categories of Z boson
1845 searches are shown in this section. The pseudo-events are generated from the least-
1846 bias functions for each category. The fits using the least-bias functions are also
1847 shown in the plots, where the green one is the signal component of the resulting
1848 fit, red one is the background component, and the blue one is the combination of
1849 the signal and background component.

A.2.1 Pseudo-events for $H \rightarrow J/\psi \gamma$

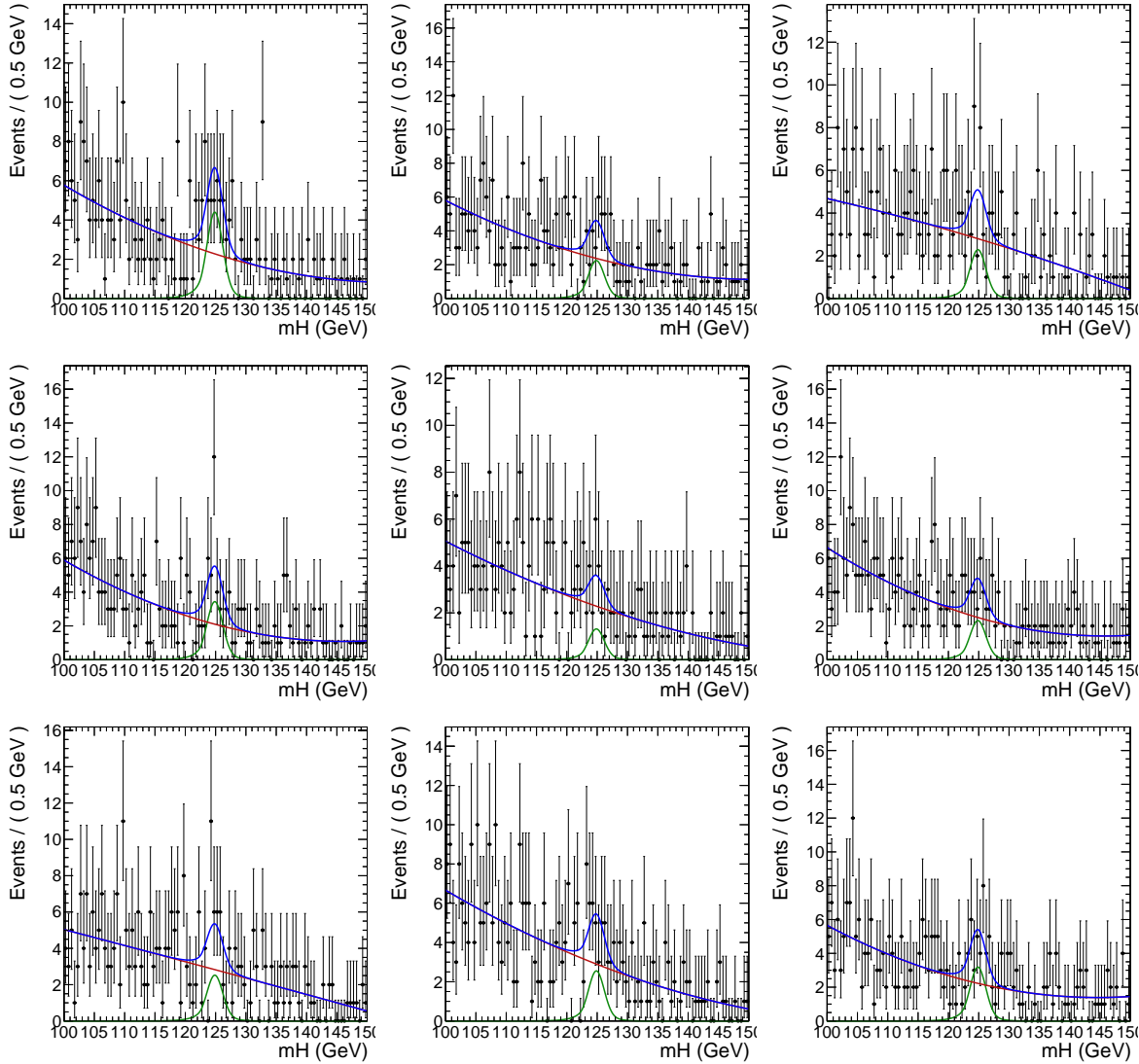


Figure A-9: Examples of the pseudo-events for bias study in Higgs search. The toys are generated from Bernstein polynomial of 2nd order, and the background fit (red line) is the Bernstein polynomial of 2nd order.

A.2.2 Pseudo-events for Cat1 of $Z \rightarrow J/\psi \gamma$

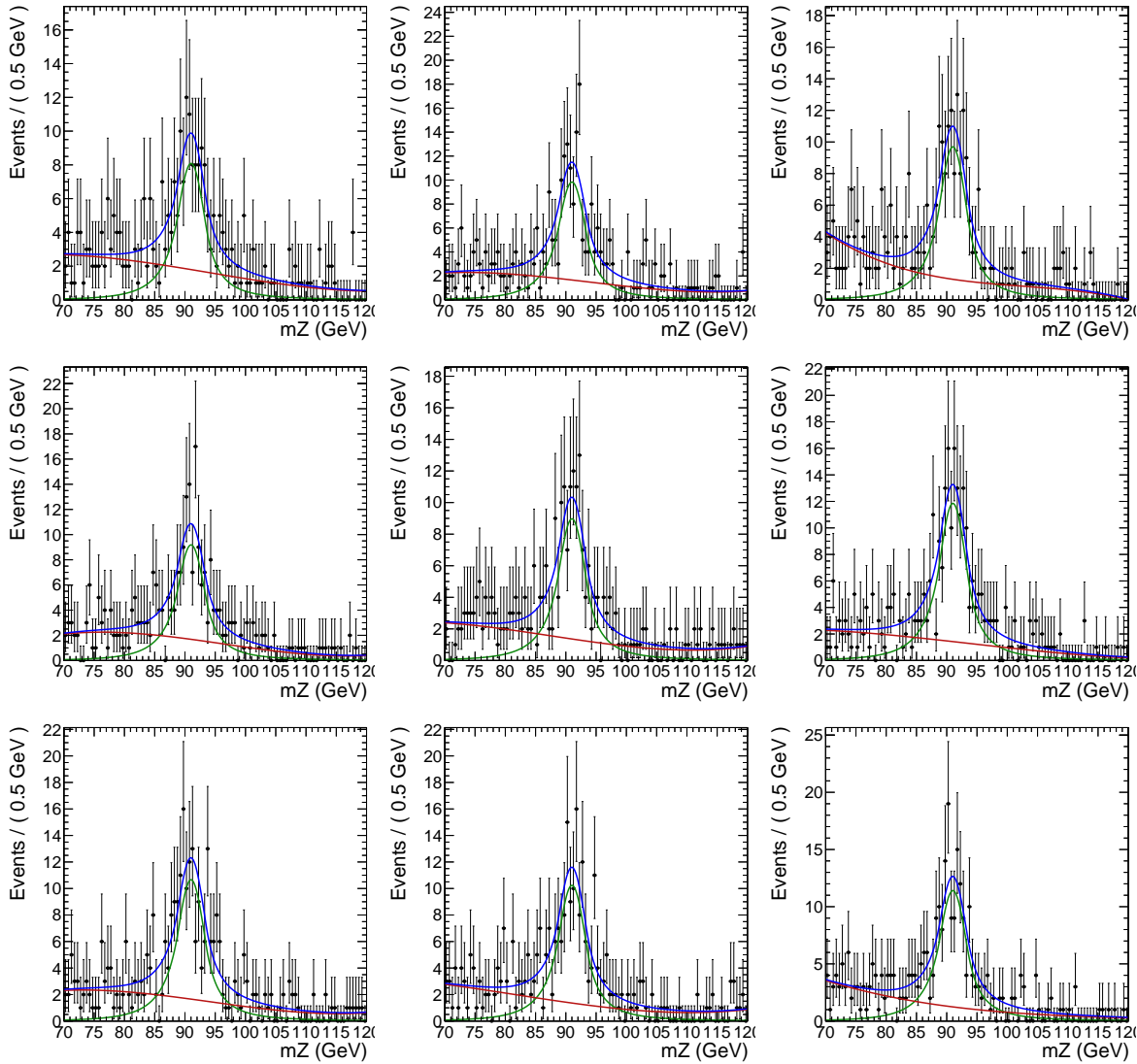


Figure A-10: Examples of the pseudo-events for bias study in Cat1 of Z search. The toys are generated from Bernstein polynomial of 3rd order, and the background fit (red line) is the Bernstein polynomial of 3rd order.

A.2.3 Pseudo-events for Cat2 of $Z \rightarrow J/\psi \gamma$

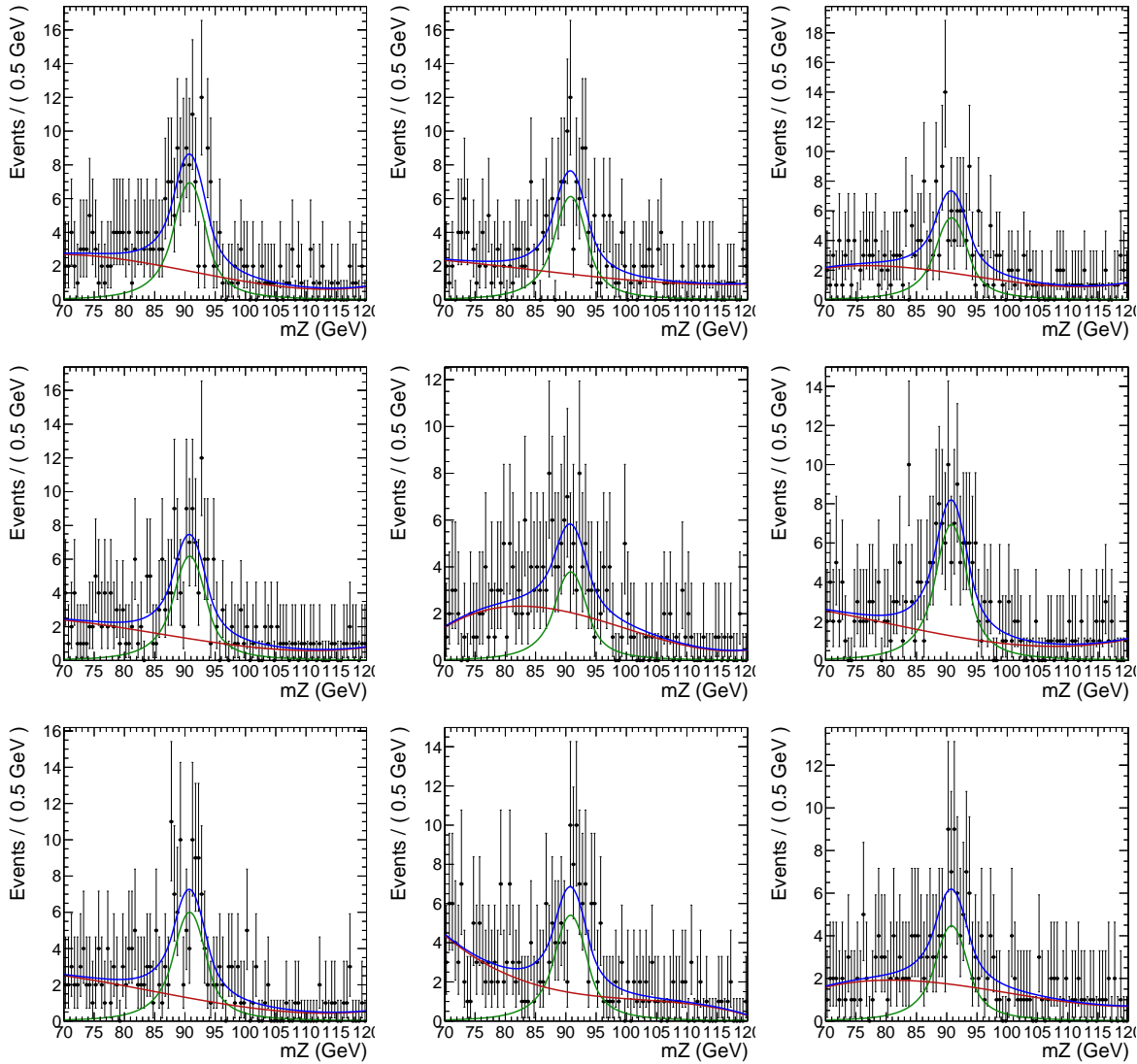


Figure A-11: Examples of the pseudo-events for bias study in Cat2 of Z search. The toys are generated from Bernstein polynomial of 3rd order, and the background fit (red line) is the Bernstein polynomial of 3rd order.

A.2.4 Pseudo-events for Cat3 of $Z \rightarrow J/\psi \gamma$

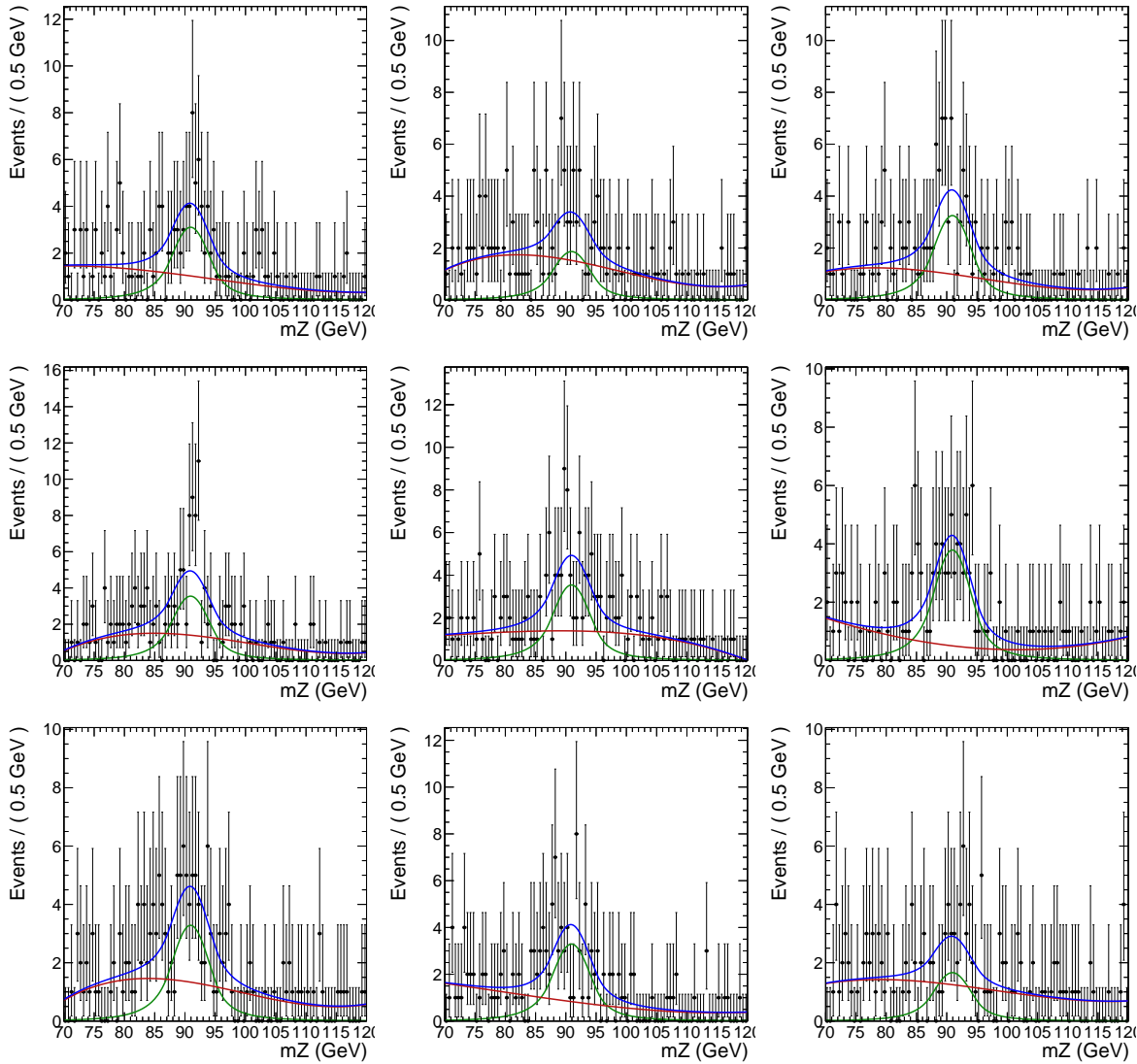


Figure A-12: Examples of the pseudo-events for bias study in Cat3 of Z search. The toys are generated from Bernstein polynomial of 3rd order, and the background fit (red line) is the Bernstein polynomial of 3rd order.

1855 **Appendix B**

1856 **Discussion on the systematic
uncertainties**

1858 Comments and discussions on systematic uncertainties are summarized as fol-
1859 lows.

1860 • **Pileup.** The uncertainty in the Cat2 in the Z decay is small compared to other
1861 categories. No weird behavior in the pileup weights of all three categories is
1862 found, no mistake is made when the pileup weights are evaluated and ap-
1863 plied. Table B.1 shows the detail numbers that give the final uncertainties in
1864 all the categories. Fig. B-1 shows the distributions of the difference between
1865 the up (down) variation and the nominal pileup weight of all the three cate-
1866 gorizes in the Z decay. Fig. B-2 shows the 2D distributions of the difference
1867 between the up (down) variation and the nominal pile-up weight versus the
1868 photon R_9 value. In Fig. B-3, the x-axis is the event number while the y-axis
1869 is the difference with respect to the sum of nominal pile-up weight over all
1870 events. This plot clearly shows how the difference evolves with the events in
1871 each category. As one can see, such small uncertainty in EBLR9 category is
1872 due to the cancellation of positive and negative weights.

	[1]	[2]	fraction [1]/[2] (in %)	[3]	[4]	[5]	Uncertainty (in %)
EBHR9	4423	5447	44.8	589.0	-687.3	10050.1	-0.98
EBLR9	2898	3257	47.1	387.2	-399.7	6213.0	-0.20
EE	1800	2287	44.0	234.7	-290.9	4196.7	-1.34
	[1]	[2]	fraction [1]/[2] (in %)	[3]	[4]	[5]	Uncertainty (in %)
EBHR9	4956	4914	50.2	728.8	-629.1	10050.1	0.99
EBLR9	2910	3245	47.3	418.6	-413.0	6213.0	0.091
EE	2074	2013	50.7	307.9	-254.1	4196.7	1.28

[1]: number of events where $(\text{puwei_up}/\text{down} - \text{puwei}) > 0$
 [2]: number of events where $(\text{puwei_up}/\text{down} - \text{puwei}) < 0$
 [3]: sum over positive value of $(\text{puwei_up}/\text{down} - \text{puwei})$
 [4]: sum over negative value of $(\text{puwei_up}/\text{down} - \text{puwei})$
 [5]: sum over all puwei

Table B.1: The uncertainties in pile-up weight of each category.

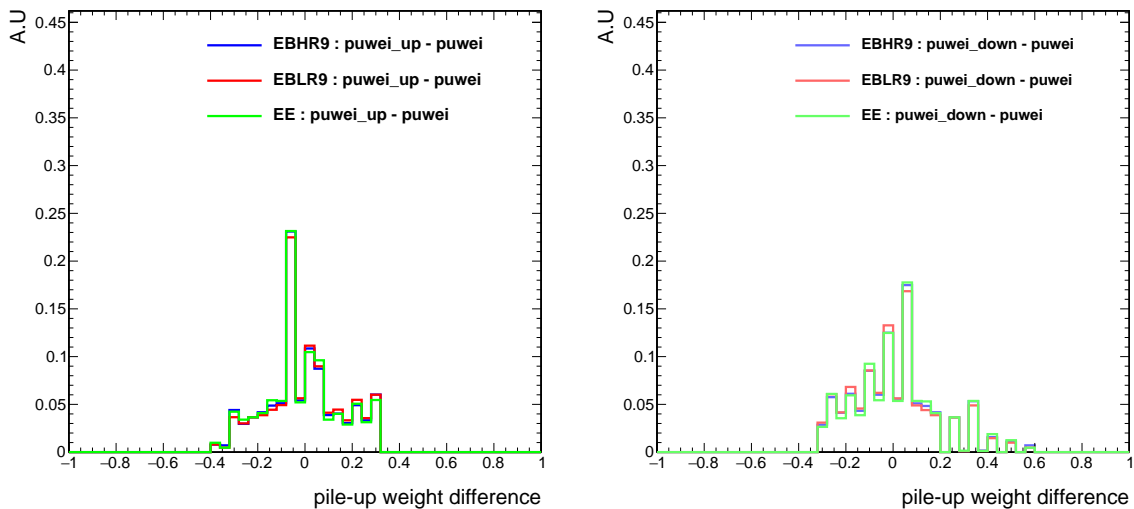


Figure B-1: The 1D distributions of the difference between the up(down) variation and the nominal pile-up weight of all the 3 categorizes in the Z decay.

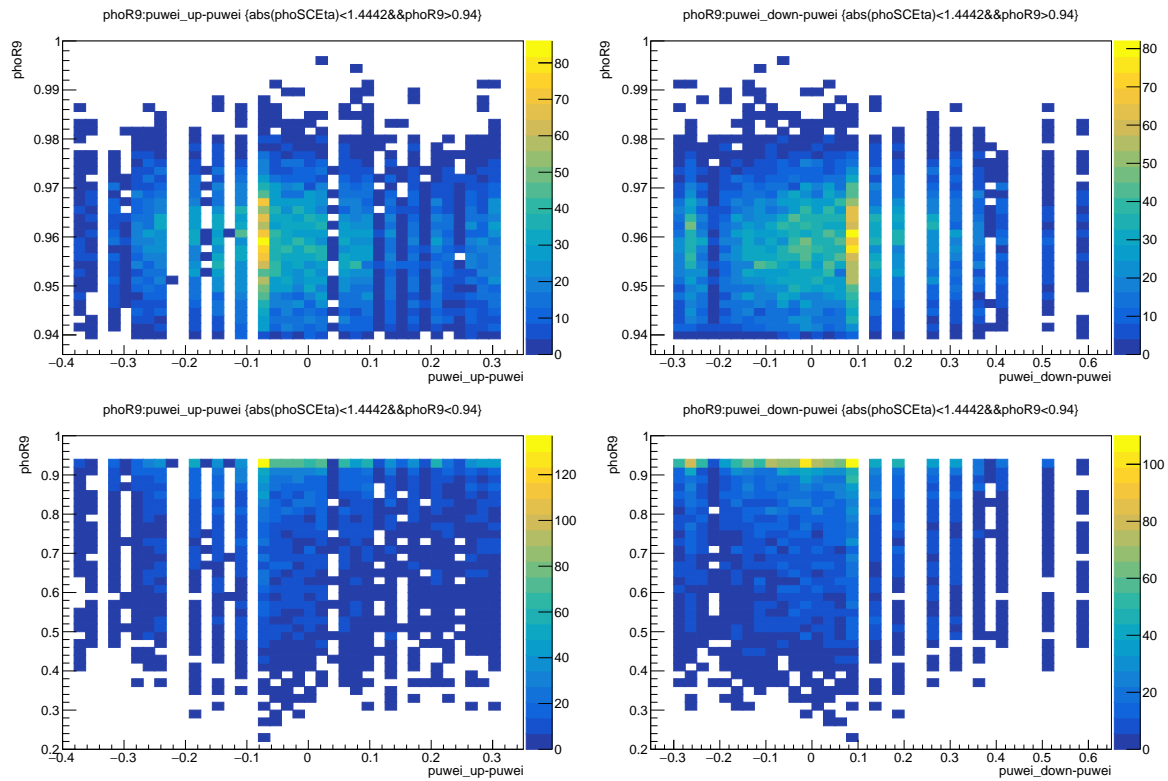


Figure B-2: The 2D distributions of the difference between the up(down) variation and the nominal pile-up weight versus the photon R_9 value. (Top left) (puwei_up - puwei) v.s photon R_9 in EBHR9; (Top right) (puwei_down - puwei) v.s photon R_9 in EBHR9; (Bottom left) (puwei_up - puwei) v.s photon R_9 in EBLR9; (Bottom right) (puwei_down - puwei) v.s photon R_9 in EBLR9

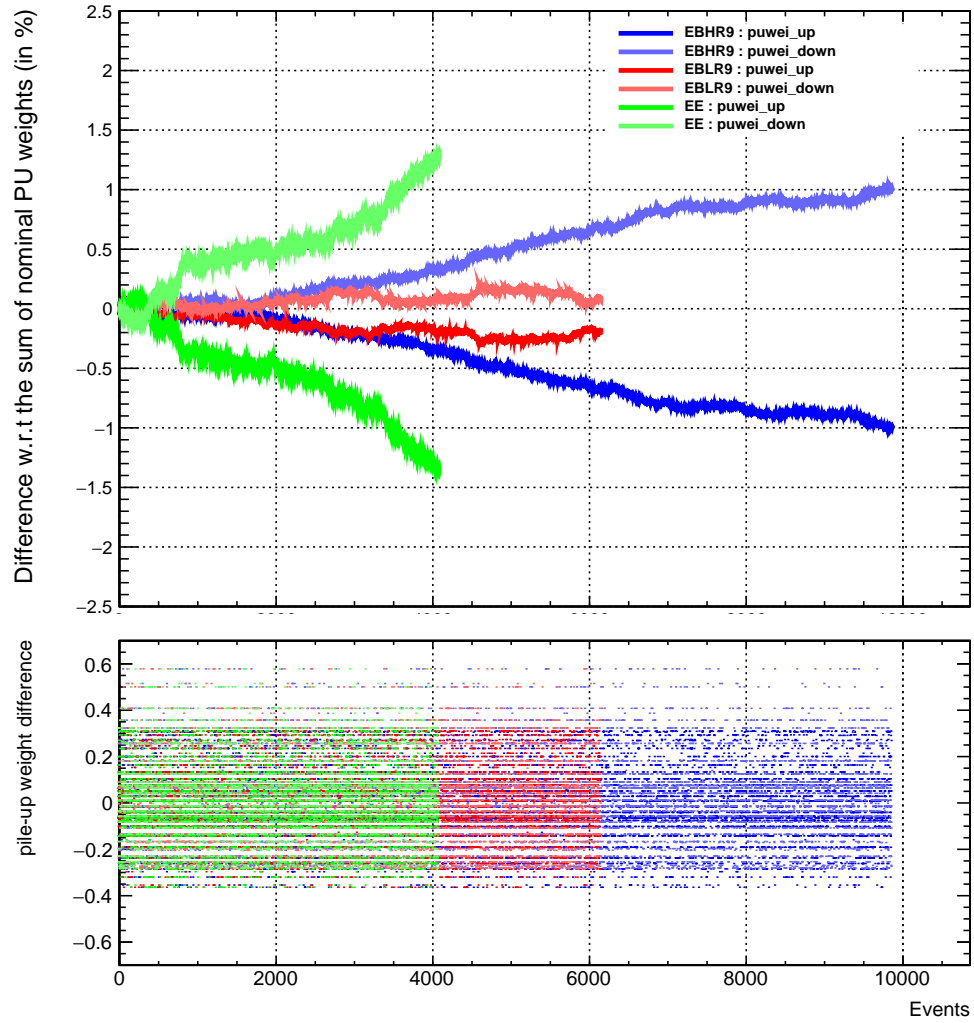


Figure B-3: The evolution of the difference with respect to the sum of nominal pile-up weights of all the 3 categories in the Z decay.

- **Muon ID/Isolation.** Muons from Z boson decay are softer than those from the Higgs boson decay, which can be seen in Fig. 3-25, 3-26, 3-27, 3-28. The p_T of muons from the Z boson decay distribute mostly in the range of 20~30 GeV, while those from the Higgs boson decay are mostly in the range of 30~40 GeV, and from the Fig. 3-18, one can see that uncertainties in the range of 20~30 GeV are slightly higher than those in 30~40 GeV. Consequently, uncertainties in muon ID and isolation in the Z boson decay are higher than those in the Higgs boson decay.
- **Electron veto.** As shown in the Fig. 3-21, the uncertainty of photons in endcap region is smaller than that of the photon in barrel region by a factor of $0.0044/0.0119 = 0.37(37\%)$. The ratio of the uncertainty on the yields in categories of barrel and endcap should be comparable to this number, $0.450/1.200.375$ (37.5%). Therefore, the difference of uncertainties between barrel and endcap region is reasonable.
- **Scale uncertainty in the signal modeling.** The individual uncertainty from each source in each category of the Z boson decay is shown in Table B.2. There are four sets of variation in the muon momentum correction and three sets in the photon energy correction. The final uncertainty in each category are summed in quadrature over the muon and photon part.
- **Resolution uncertainty in the signal modeling.** The uncertainties in the σ of the signal model are larger in the Higgs boson decays than in the Z decay. No unusual behaviors in the distributions of $m_{\mu\mu\gamma}$ resulting from different sets of correction is found, and fits are all reasonable. The difference may come from the correction itself, for which individual analysis cannot do much. The natural width of the Z boson itself is larger, and so relative uncertainty becomes smaller compared to the Higgs boson case. In addition, for the Z decay the first two categories for barrel photons where the uncertainties are smaller, while in Higgs all events are combined and uncertainties from different kinematic regime are averaged. Uncertainties in the muon and

1902 photon correction separately are summarized in Table B.3 and B.4. The total
 1903 uncertainty is derived by summing the uncertainties in the muon and photon
 1904 parts in quadrature.

Table B.2: The uncertainties in the mean of the signal model from muon and photon correction.

	Cat1 EBHR9		Cat2 EBLR9		Cat3 EE	
	Scale	Uncertainty (in %)	Scale	Uncertainty (in %)	Scale	Uncertainty (in %)
Nominal	91.002		90.768		90.950	
Muon - Set1	91.004	0.00220	90.785	0.0187	90.966	0.0176
Muon - Set2	90.997	0.00549	90.782	0.0154	90.961	0.0121
Muon - Set4	90.992	0.0110	90.785	0.0187	90.956	0.00660
Muon - Set5	90.997	0.00549	90.782	0.0154	90.957	0.00770
Muon - Total		0.0136		0.0343		0.0236
Photon - gain up	90.995	0.00769	90.772	0.00441	90.995	0.00769
Photon - gain down	90.995	0.00769	90.772	0.00441	90.995	0.00769
Photon - stat. up	90.996	0.00659	90.772	0.00441	91.000	0.00220
Photon - stat. down	90.994	0.00879	90.772	0.00441	90.991	0.0121
Photon - syst. up	91.030	0.0308	90.830	0.0683	91.046	0.0484
Photon - syst. down	90.960	0.0462	90.713	0.0606	90.945	0.0626
Photon - Total		0.0476		0.0686		0.0643
Total uncertainty		0.0495		0.0767		0.0685

Table B.3: The uncertainties in the sigma of the signal model from muon and photon correction in the H decay. The total uncertainty is derived by summing the uncertainties in the muon and photon parts in quadrature. The numbers in the table are in percentage.

	$H \rightarrow (J/\psi)\gamma$					
	ggF	VBF	ZH	W^+H	W^-H	$t\bar{t}H$
muon	1.69	1.27	1.60	1.38	2.00	2.97
photon	4.65	4.15	2.95	4.40	3.22	13.8
Total	4.94	4.30	3.35	4.61	3.79	14.1

Table B.4: The uncertainties in the sigma of the signal model from muon and photon correction in the Z decay. The total uncertainty is derived by summing the uncertainties in the muon and photon parts in quadrature. The numbers in the table are in percentage.

	$Z \rightarrow (J/\psi)\gamma$		
	Cat1	Cat2	Cat3
muon	0.44	0.38	0.49
photon	0.89	0.57	1.37
Total	0.99	0.69	1.45

Bibliography

- [1] Peter Skands. Introduction to QCD. 2013.
- [2] The ALEPH, DELPHI, L3, OPAL Collaborations, the LEP Electroweak Working Group. Electroweak Measurements in Electron-Positron Collisions at W-Boson-Pair Energies at LEP. *Phys. Rept.*, 532:119, 2013.
- [3] Steven Weinberg. A Model of Leptons. *Phys. Rev. Lett.*, 19:1264–1266, Nov 1967.
- [4] G. Arnison et al. Experimental observation of isolated large transverse energy electrons with associated missing energy at $\sqrt{s}=540$ GeV. *Phys. Lett. B*, 122(1):103 – 116, 1983.
- [5] G. Arnison et al. Observation of muonic Z_0 -decay at the pp collider. *Phys. Lett. B*, 147(1):241 – 248, 1984.
- [6] Michał Szleper. The Higgs boson and the physics of WW scattering before and after Higgs discovery. 2014.
- [7] F. Englert and R. Brout. Broken Symmetry and the Mass of Gauge Vector Mesons. *Phys. Rev. Lett.*, 13:321–323, Aug 1964.
- [8] Peter W. Higgs. Broken Symmetries and the Masses of Gauge Bosons. *Phys. Rev. Lett.*, 13:508–509, Oct 1964.
- [9] G. S. Guralnik, C. R. Hagen, and T. W. B. Kibble. Global Conservation Laws and Massless Particles. *Phys. Rev. Lett.*, 13:585–587, Nov 1964.
- [10] Murray Gell-Mann, Pierre Ramond, and Richard Slansky. Complex Spinors and Unified Theories. *Conf. Proc.*, C790927:315–321, 1979.
- [11] Mohapatra, Rabindra N. and Senjanović, Goran. Neutrino Mass and Spontaneous Parity Nonconservation. *Phys. Rev. Lett.*, 44:912–915, Apr 1980.
- [12] LHC Higgs Cross Section Working Group. History: r294.
- [13] LHCTopWG Summary Plots. History: r52.

- [14] Georges Aad et al. Measurements of the Higgs boson production and decay rates and constraints on its couplings from a combined ATLAS and CMS analysis of the LHC pp collision data at $\sqrt{s} = 7$ and 8 TeV. *JHEP*, 08:045, 2016.
- [15] Morad Aaboud et al. Observation of Higgs boson production in association with a top quark pair at the LHC with the ATLAS detector. 2018.
- [16] Albert M Sirunyan et al. Observation of $t\bar{t}H$ production. *Phys. Rev. Lett.*, 120(23):231801, 2018.
- [17] Search for the associated production of a Higgs boson and a single top quark in pp collisions at $\sqrt{s} = 13$ TeV. Technical Report CMS-PAS-HIG-18-009, CERN, Geneva, 2018.
- [18] Geoffrey T. Bodwin, Frank Petriello, Stoyan Stoynev, and Mayda Velasco. Higgs boson decays to quarkonia and the $H\bar{c}c$ coupling. *Phys. Rev. D*, 88:053003, 2013.
- [19] T. Aaltonen, A. Buzatu, B. Kilminster, Y. Nagai, and W. Yao. Improved b -jet energy correction for $H \rightarrow b\bar{b}$ searches at CDF. 2011.
- [20] Vardan Khachatryan et al. Search for the associated production of a Higgs boson with a single top quark in proton-proton collisions at $\sqrt{s} = 8$ TeV. *JHEP*, 06:177, 2016.
- [21] Georges Aad et al. Search for the $b\bar{b}$ decay of the Standard Model Higgs boson in associated $(W/Z)H$ production with the ATLAS detector. *JHEP*, 01:069, 2015.
- [22] Albert M Sirunyan et al. Evidence for the Higgs boson decay to a bottom quark-antiquark pair. *Phys. Lett. B*, 780:501–532, 2018.
- [23] Observation of $H \rightarrow b\bar{b}$ decays and VH production with the ATLAS detector. Technical Report ATLAS-CONF-2018-036, CERN, Geneva, Jul 2018.
- [24] Georges Aad et al. Test of CP Invariance in vector-boson fusion production of the Higgs boson using the Optimal Observable method in the ditau decay channel with the ATLAS detector. *Eur. Phys. J.*, C76(12):658, 2016.
- [25] Stefan Berge, Werner Bernreuther, and Sebastian Kirchner. Prospects of constraining the Higgs boson's CP nature in the tau decay channel at the LHC. *Phys. Rev. D*, 92:096012, 2015.
- [26] Cross-section measurements of the Higgs boson decaying to a pair of tau leptons in proton–proton collisions at $\sqrt{s} = 13$ TeV with the ATLAS detector. Technical Report ATLAS-CONF-2018-021, CERN, Geneva, Jun 2018.

- [27] Albert M Sirunyan et al. Observation of the Higgs boson decay to a pair of τ leptons with the CMS detector. *Phys. Lett. B*, 779:283–316, 2018.
- [28] Measurement of gluon fusion and vector boson fusion Higgs boson production cross-sections in the $H \rightarrow WW^* \rightarrow e\nu\mu\nu$ decay channel in pp collisions at $\sqrt{s} = 13$ TeV with the ATLAS detector. Technical Report ATLAS-CONF-2018-004, CERN, Geneva, Mar 2018.
- [29] Albert M Sirunyan et al. Measurements of properties of the Higgs boson decaying to a W boson pair in pp collisions at $\sqrt{s} = 13$ TeV. *Submitted to: Phys. Lett. B*, 2018.
- [30] Serguei Chatrchyan et al. Measurement of the properties of a Higgs boson in the four-lepton final state. *Phys. Rev. D*, 89(9):092007, 2014.
- [31] Serguei Chatrchyan et al. Study of the mass and spin-parity of the Higgs boson candidate via its decays to Z Boson pairs. *Phys. Rev. Lett.*, 110(8):081803, 2013.
- [32] Vardan Khachatryan et al. Constraints on the spin-parity and anomalous HVV couplings of the Higgs boson in proton collisions at 7 and 8 TeV. *Phys. Rev. D*, 92(1):012004, 2015.
- [33] Georges Aad et al. Measurements of Higgs boson production and couplings in the four-lepton channel in pp collisions at center-of-mass energies of 7 and 8 TeV with the ATLAS detector. *Phys. Rev. D*, 91(1):012006, 2015.
- [34] Georges Aad et al. Study of the spin and parity of the Higgs boson in diboson decays with the ATLAS detector. *Eur. Phys. J.*, C75(10):476, 2015. [Erratum: *Eur. Phys. J.* C76,no.3,152(2016)].
- [35] Vardan Khachatryan et al. Constraints on the Higgs boson width from off-shell production and decay to Z-boson pairs. *Phys. Lett. B*, B736:64–85, 2014.
- [36] Vardan Khachatryan et al. Limits on the Higgs boson lifetime and width from its decay to four charged leptons. *Phys. Rev. D*, 92(7):072010, 2015.
- [37] Georges Aad et al. Constraints on the off-shell Higgs boson signal strength in the high-mass ZZ and WW final states with the ATLAS detector. *Eur. Phys. J.*, C75(7):335, 2015.
- [38] Measurements of properties of the Higgs boson in the four-lepton final state at $\sqrt{s} = 13$ TeV. Technical Report CMS-PAS-HIG-18-001, CERN, Geneva, 2018.
- [39] Measurements of the Higgs boson production, fiducial and differential cross sections in the 4ℓ decay channel at $\sqrt{s} = 13$ TeV with the ATLAS detector. Technical Report ATLAS-CONF-2018-018, CERN, Geneva, Jun 2018.

- [40] Albert M Sirunyan et al. Measurements of properties of the Higgs boson decaying into the four-lepton final state in pp collisions at $\sqrt{s} = 13$ TeV. *JHEP*, 11:047, 2017.
- [41] Vardan Khachatryan et al. Observation of the diphoton decay of the Higgs boson and measurement of its properties. *Eur. Phys. J.*, C74(10):3076, 2014.
- [42] Georges Aad et al. Measurement of Higgs boson production in the diphoton decay channel in pp collisions at center-of-mass energies of 7 and 8 TeV with the ATLAS detector. *Phys. Rev. D*, 90(11):112015, 2014.
- [43] Albert M Sirunyan et al. Measurements of Higgs boson properties in the diphoton decay channel in proton-proton collisions at $\sqrt{s} = 13$ TeV. 2018.
- [44] Albert M Sirunyan et al. Measurement of inclusive and differential Higgs boson production cross sections in the diphoton decay channel in proton-proton collisions at $\sqrt{s} = 13$ TeV. 2018.
- [45] Morad Aaboud et al. Measurements of Higgs boson properties in the diphoton decay channel with 36 fb^{-1} of pp collision data at $\sqrt{s} = 13$ TeV with the ATLAS detector. 2018.
- [46] Albert M Sirunyan et al. Search for the decay of a Higgs boson in the $\ell\ell\gamma$ channel in proton-proton collisions at $\sqrt{s} = 13$ TeV. *Submitted to: JHEP*, 2018.
- [47] M. Aaboud et al. Searches for the $Z\gamma$ decay mode of the Higgs boson and for new high-mass resonances in pp collisions at $\sqrt{s} = 13$ TeV with the ATLAS detector. *JHEP*, 10:112, 2017.
- [48] D. de Florian et al. Handbook of LHC Higgs Cross Sections: 4. Deciphering the Nature of the Higgs Sector. 2016.
- [49] Albert M Sirunyan et al. Search for the Higgs boson decaying to two muons in proton-proton collisions at $\sqrt{s} = 13$ TeV. 2018.
- [50] A search for the rare decay of the Standard Model Higgs boson to dimuons in pp collisions at $\sqrt{s} = 13$ TeV with the ATLAS Detector. Technical Report ATLAS-CONF-2018-026, CERN, Geneva, Jul 2018.
- [51] Gilad Perez, Yotam Soreq, Emmanuel Stamou, and Kohsaku Tobioka. Constraining the charm Yukawa and Higgs-quark coupling universality. *Phys. Rev. D*, 92(3):033016, 2015.
- [52] Gilad Perez, Yotam Soreq, Emmanuel Stamou, and Kohsaku Tobioka. Prospects for measuring the Higgs boson coupling to light quarks. *Phys. Rev. D*, 93(1):013001, 2016.

- [53] M. Aaboud et al. Search for the Decay of the Higgs Boson to Charm Quarks with the ATLAS Experiment. *Phys. Rev. Lett.*, 120(21):211802, 2018.
- [54] Georges Aad et al. Combined measurement of the Higgs boson mass in pp collisions at $\sqrt{s} = 7$ and 8 TeV with the ATLAS and CMS experiments. *Phys. Rev. Lett.*, 114:191803, 2015.
- [55] Georges Aad et al. Observation of a new particle in the search for the Standard Model Higgs boson with the ATLAS detector at the LHC. *Phys. Lett. B*, 716:1–29, 2012.
- [56] Serguei Chatrchyan et al. Observation of a new boson at a mass of 125 GeV with the CMS experiment at the LHC. *Phys. Lett. B*, 716:30–61, 2012.
- [57] Serguei Chatrchyan et al. Observation of a new boson with mass near 125 GeV in pp collisions at $\sqrt{s} = 7$ and 8 TeV. *JHEP*, 06:081, 2013.
- [58] Georges Aad et al. Measurements of the Higgs boson production and decay rates and coupling strengths using pp collision data at $\sqrt{s} = 7$ and 8 TeV in the ATLAS experiment. *Eur. Phys. J.*, C76(1):6, 2016.
- [59] Vardan Khachatryan et al. Precise determination of the mass of the Higgs boson and tests of compatibility of its couplings with the standard model predictions using proton collisions at 7 and 8 TeV. *Eur. Phys. J.*, C75(5):212, 2015.
- [60] Georges Aad et al. Evidence for the spin-0 nature of the Higgs boson using ATLAS data. *Phys. Lett. B*, 726:120–144, 2013.
- [61] Combined measurements of the Higgs boson’s couplings at $\sqrt{s} = 13$ TeV. Technical Report CMS-PAS-HIG-17-031, CERN, Geneva, 2018.
- [62] J R Andersen et al. Handbook of LHC Higgs Cross Sections: 3. Higgs Properties. 2013.
- [63] John Ellis and Tevong You. Global analysis of the Higgs candidate with mass 125 GeV. *JHEP*, 09:123, 2012.
- [64] John Ellis and Tevong You. Updated Global Analysis of Higgs Couplings. *JHEP*, 06:103, 2013.
- [65] C et al. Patrignani. Review of Particle Physics, 2016-2017. *Chin. Phys. C*, 40(10):100001. 1808 p, 2016.
- [66] Fady Bishara, Ulrich Haisch, Pier Francesco Monni, and Emanuele Re. Constraining Light-Quark Yukawa Couplings from Higgs Distributions. *Phys. Rev. Lett.*, 118(12):121801, 2017.

- [67] Combined measurement and interpretation of differential Higgs boson production cross sections at $\sqrt{s}=13$ TeV. Technical Report CMS-PAS-HIG-17-028, CERN, Geneva, 2018.
- [68] Cédric Delaunay, Tobias Golling, Gilad Perez, and Yotam Soreq. Enhanced Higgs boson coupling to charm pairs. *Phys. Rev. D*, 89(3):033014, 2014.
- [69] W. Buchmuller and D. Wyler. Effective Lagrangian analysis of new interactions and flavor conservation. *Nucl. Phys. B*, 268:621, 1986.
- [70] Steven Weinberg. Effective gauge theories. *Phys. Lett. B*, 91:51, 1980.
- [71] Roberto Contino, Margherita Ghezzi, Christophe Grojean, Margarete Muhlleitner, and Michael Spira. Effective Lagrangian for a light Higgs-like scalar. *JHEP*, 07:035, 2013.
- [72] Michael Trott and Mark B. Wise. On theories of enhanced CP violation in $B_{s,d}$ meson mixing. *JHEP*, 11:157, 2010.
- [73] Martin Jung, Antonio Pich, and Paula Tuzon. Charged-Higgs phenomenology in the Aligned two-Higgs-doublet model. *JHEP*, 11:003, 2010.
- [74] G. F. Giudice, C. Grojean, A. Pomarol, and R. Rattazzi. The strongly-interacting light Higgs. *JHEP*, 06:045, 2007.
- [75] Cédric Delaunay, Thomas Flacke, J. Gonzalez-Fraile, Seung J. Lee, Giuliano Panico, and Gilad Perez. Light non-degenerate composite partners at the LHC. *JHEP*, 02:055, 2014.
- [76] B. Guberina and J.H. Kühn and R.D. Peccei and R. Rückl. Rare decays of the Z^0 . *Nuclear Physics B*, 174:317, 1980.
- [77] Ting-Chung Huang and Frank Petriello. Rare exclusive decays of the Z-boson revisited. *Phys. Rev. D*, 92:014007, 2015.
- [78] Yuval Grossman, Matthias König, and Matthias Neubert. Exclusive radiative decays of W and Z bosons in QCD factorization. *JHEP*, 04:101, 2015.
- [79] Geoffrey T. Bodwin, Hee Sok Chung, June-Haak Ee, and Jungil Lee. Addendum: New approach to the resummation of logarithms in Higgs-boson decays to a vector quarkonium plus a photon [Phys. Rev. D 95, 054018 (2017)]. *Phys. Rev. D*, 96:116014, 2017.
- [80] Geoffrey T. Bodwin, Hee Sok Chung, June-Haak Ee, and Jungil Lee. Z-boson decays to a vector quarkonium plus a photon. *Phys. Rev. D*, 97(1):016009, 2018.
- [81] Geoffrey T. Bodwin, Eric Braaten, and G. Peter Lepage. Rigorous QCD analysis of inclusive annihilation and production of heavy quarkonium. *Phys. Rev. D*, 51:1125–1171, Feb 1995.

- [82] G. Peter Lepage and Stanley J. Brodsky. Exclusive processes in perturbative quantum chromodynamics. *Phys. Rev. D*, 22:2157–2198, Nov 1980.
- [83] Chernyak, V. L. and Zhitnitsky, A. R. Asymptotic Behavior of Exclusive Processes in QCD. *Phys. Rept.*, 112:173, 1984.
- [84] C. N. Yang. Selection Rules for the Dematerialization of a Particle into Two Photons. *Phys. Rev.*, 77:242–245, Jan 1950.
- [85] Ye Li and Frank Petriello. Combining QCD and electroweak corrections to dilepton production in FEWZ. *Phys. Rev. D*, 86:094034, 2012.
- [86] Georges Aad et al. Search for Higgs and Z Boson decays to $J/\psi\gamma$ and $\Upsilon(nS)\gamma$ with the ATLAS detector. *Phys. Rev. Lett.*, 114:121801, 2015.
- [87] Vardan Khachatryan et al. Search for a Higgs boson decaying into $\gamma^*\gamma \rightarrow \ell\ell\gamma$ with low dilepton mass in pp collisions at $\sqrt{s} = 8$ TeV. *Phys. Lett. B*, 753:341, 2016.
- [88] Morad Aaboud et al. Searches for exclusive Higgs and Z boson decays into $J/\psi\gamma$, $\psi(2S)\gamma$, and $\Upsilon(nS)\gamma$ at $\sqrt{s} = 13$ TeV with the ATLAS detector. 2018.
- [89] Esma Mobs. The CERN accelerator complex. Complex des accélérateurs du CERN. Jul 2016. General Photo.
- [90] CMS Luminosity - Public Results. History: r140.
- [91] Tai Sakuma and Thomas McCauley. Detector and event visualization with SketchUp at the CMS experiment. Technical Report CMS-CR-2013-379. arXiv:1311.4942, CERN, Geneva, Oct 2013. Comments: 5 pages, 6 figures, Proceedings for CHEP 2013, 20th International Conference on Computing in High Energy and Nuclear Physics.
- [92] Serguei Chatrchyan et al. Description and performance of track and primary-vertex reconstruction with the CMS tracker. *JINST*, 9:P10009, 2014.
- [93] S. Chatrchyan et al. The CMS Experiment at the CERN LHC. *JINST*, 3:S08004, 2008.
- [94] A. Benaglia. The CMS ECAL performance with examples. *JINST*, 9:C02008, 2014.
- [95] A. M. Sirunyan et al. Performance of the CMS muon detector and muon reconstruction with proton-proton collisions at $\sqrt{s} = 13$ TeV. *JINST*, 13(06):P06015, 2018.
- [96] Vardan Khachatryan et al. Performance of photon reconstruction and identification with the CMS detector in proton-proton collisions at $\sqrt{s} = 8$ TeV. *JINST*, 10:P08010, 2015.

- [97] R. Fruhwirth. Application of Kalman filtering to track and vertex fitting. *Nucl. Instrum. Meth. A*, 262:444–450, 1987.
- [98] Serguei Chatrchyan et al. Performance of CMS muon reconstruction in pp collision events at $\sqrt{s} = 7\text{ TeV}$. *JINST*, 7:P10002, 2012.
- [99] Serguei Chatrchyan et al. Alignment of the CMS tracker with LHC and cosmic ray data. *JINST*, 9:P06009, 2014.
- [100] Matteo Cacciari, Gavin P. Salam, and Gregory Soyez. The anti- k_t jet clustering algorithm. *JHEP*, 04:063, 2008.
- [101] Matteo Cacciari, Gavin P. Salam, and Gregory Soyez. FastJet user manual. *Eur. Phys. J. C*, 72:1896, 2012.
- [102] D Contardo, M Klute, J Mans, L Silvestris, and J Butler. Technical proposal for the Phase-II upgrade of the CMS detector. Technical Report CERN-LHCC-2015-010. LHCC-P-008. CMS-TDR-15-02, Geneva, Jun 2015. Upgrade Project Leader Deputies: Lucia Silvestris (INFN-Bari), Jeremy Mans (University of Minnesota) Additional contacts: Lucia.Silvestris@cern.ch, Jeremy.Mans@cern.ch.
- [103] Simone Alioli, Paolo Nason, Carlo Oleari, and Emanuele Re. NLO Higgs boson production via gluon fusion matched with shower in POWHEG. *JHEP*, 04:002, 2009.
- [104] Paolo Nason and Carlo Oleari. NLO Higgs boson production via vector-boson fusion matched with shower in POWHEG. *JHEP*, 02:037, 2010.
- [105] Torbjorn Sjöstrand, Stephen Mrenna, and Peter Z. Skands. A brief introduction to PYTHIA 8.1. *Comput. Phys. Commun.*, 178:852, 2008.
- [106] Torbjörn Sjöstrand, Stefan Ask, Jesper R. Christiansen, Richard Corke, Nishita Desai, Philip Ilten, Stephen Mrenna, Stefan Prestel, Christine O. Rasmussen, and Peter Z. Skands. An introduction to PYTHIA 8.2. *Comput. Phys. Commun.*, 191:159, 2015.
- [107] Vardan Khachatryan et al. Event generator tunes obtained from underlying event and multiparton scattering measurements. *Eur. Phys. J. C*, 76:155, 2016.
- [108] Richard D. Ball et al. Parton distributions for the LHC Run II. *JHEP*, 04:040, 2015.
- [109] Ali Abbasabadi, David Bowser-Chao, Duane A. Dicus, and Wayne W. Repko. Radiative Higgs boson decays $H \rightarrow ff\gamma$. *Phys. Rev. D*, 55:5647, 1997.
- [110] J. Alwall, R. Frederix, S. Frixione, V. Hirschi, F. Maltoni, O. Mattelaer, H.-S. Shao, T. Stelzer, P. Torrielli, and M. Zaro. The automated computation of tree-level and next-to-leading order differential cross sections, and their matching to parton shower simulations. *JHEP*, 07:079, 2014.

- [111] John M. Campbell and R. Ellis. MCFM for the Tevatron and the LHC. *Nucl. Phys. Proc. Suppl.*, 205:10, 2010.
- [112] A. Bodek, A. van Dyne, J. Y. Han, W. Sakumoto, and A. Strelnikov. Extracting muon momentum xcale corrections for hadron collider experiments. *Eur. Phys. J.*, C72:2194, 2012.
- [113] Serguei Chatrchyan et al. Measurement of the inclusive W and Z production cross sections in pp collisions at $\sqrt{s} = 7$ TeV. *JHEP*, 10:132, 2011.
- [114] CMS Luminosity measurements for the 2016 data taking period. Technical Report CMS-PAS-LUM-17-001, 2017.
- [115] Jon Butterworth et al. PDF4LHC recommendations for LHC Run II. *J. Phys. G*, 43:023001, 2016.
- [116] A. D. Martin, W. J. Stirling, R. S. Thorne, and G. Watt. Parton distributions for the LHC. *Eur. Phys. J. C*, 63:189, 2009.
- [117] Hung-Liang Lai, Marco Guzzi, Joey Huston, Zhao Li, Pavel M. Nadolsky, Jon Pumplin, and C.-P. Yuan. New parton distributions for collider physics. *Phys. Rev. D*, 82:74024, 2010.
- [118] Sergey Alekhin et al. The PDF4LHC Working Group Interim Report. 2011.
- [119] Michiel Botje, Jon Butterworth, Amanda Cooper-Sarkar, Albert de Roeck, Joel Feltesse, Stephano Forte, Alexander Glazov, Joey Huston, Ronan McNulty, and Sjöstrand. The PDF4LHC Working Group Interim Recommendations. 2011.
- [120] Richard D. Ball, Valerio Bertone, Francesco Cerutti, Luigi Del Debbio, Stefano Forte, Alberto Guffanti, Jose I. Latorre, Juan Rojo, and Maria Ubiali. Impact of heavy quark masses on parton distributions and LHC phenomenology. *Nucl. Phys. B*, 849:296, 2011.
- [121] Giampiero Passarino. Higgs boson production and decay: Dalitz sector. *Phys. Lett. B*, 727:424, 2013.
- [122] Thomas Junk. Confidence level computation for combining searches with small statistics. *Nucl. Instrum. Meth. A*, 434:435, 1999.
- [123] Alexander L. Read. Presentation of search results: The CL_s technique. *J. Phys. G*, 28:2693, 2002.
- [124] ATLAS and CMS Collaborations, The LHC Higgs combination group. Procedure for the LHC Higgs boson search combination in Summer 2011. Technical Report CMS-NOTE-2011-005. ATL-PHYS-PUB-2011-11, 2011.

- [125] Glen Cowan, Kyle Cranmer, Eilam Gross, and Ofer Vitells. Asymptotic formulae for likelihood-based tests of new physics. *Eur. Phys. J. C*, 71:1554, 2011. [Erratum: Eur. Phys. J.C 73,2501(2013)].
- [126] J. Neyman and E. S. Pearson. *On the Problem of the Most Efficient Tests of Statistical Hypotheses*, pages 73–108. Springer New York, New York, NY, 1992.